Development and Applications of a Laser-Wakefield X-ray Source (updated)

Gallardo Gonzalez, Isabel

2019

Document Version:
Publisher's PDF, also known as Version of record

Development and Applications of a Laser-Wakefield X-ray Source

ISABEL GALLARDO GONZÁLEZ
FACULTY OF ENGINEERING | LUND UNIVERSITY

Development and Applications of a Laser-Wakefield X-ray Source

Isabel Gallardo González

Modified on June 28, 2019

LUND
UNIVERSITY

Akademisk avhandling som för avläggande av teknologie doktorsexamen vid tekniska fakulteten vid Lunds universitet kommer att offentligen försvaras den 7 december 2018, kl. 9.15 i Rydbergssalen, på Fysiska institutionen, Professorsgatan 1, Lund.
Fakultetsopponent: Prof. Dr. Malte C. Kaluza
Friedrich-Schiller-University Jena, Tyskland

Academic dissertation which, by due permission of the Faculty of Engineering at Lund University, will be publicly defended on December 7, 2018, at 9.15 a.m. in the Rydberg hall, at the Department of Physics, Professorsgatan 1, Lund, for the degree of Doctor of Philosophy in Engineering.
Faculty opponent: Prof. Dr. Malte C. Kaluza
Friedrich-Schiller-University Jena, Germany

Organization
LUND UNIVERSITY

Atomic Physics
Department of Physics
P.O. Box 118
SE-112 00 Lund
Sweden

Author(s)
Isabel Gallardo González

Document name
DOCTORAL DISSERTATION

Date of disputation
7th December 2018

Sponsoring organization

Title and subtitle
Development and Applications of a Laser-Wakefield X-ray Source

Abstract
In laser-wakefield acceleration (LWFA), a femtosecond laser pulse is tightly focused in a gas to intensities exceeding 10^{18} W/cm^2. The laser radiation ionizes the medium and excites a plasma wave that travels behind the laser pulse. Electrons can be trapped in the oscillations in the plasma density, where electric fields of the order of several hundreds of GV/m accelerate them to relativistic energies. Together with the longitudinal accelerating fields, transverse electromagnetic forces keep the electrons oscillating in the three-dimensional plasma structure around the direction of propagation of the laser. These betatron oscillations cause the emission of X-ray pulses with a broadband spectrum and femtosecond duration.

The emission of such relativistic electron beams and ultrashort X-ray pulses, due to the high accelerating fields that can be sustained in the plasma, promises a new generation of compact electron accelerators. However, the complexity of the nonlinear laser–plasma interaction that produces LWFA poses challenges in the reproducibility and control of both the electron beams and the X-ray pulses.

The main goals of the present work are the optimization and application of a LWFA-based X-ray source. The mechanism through which the electrons are trapped and accelerated in the plasma wave influences the final parameters governing both the electrons and X-rays. Several trapping mechanisms have been investigated: using gas mixtures, a plasma density down-ramp and a combination of the two. The advantages of these approaches were a general improvement in the shot-to-shot reproducibility and some control of the electron beam charge and spectrum. It is shown that an increase in the dopant concentration of the gas also affects the acceleration process, as it increases the contribution to the electron energy from direct laser acceleration (DLA), where the overlap of the laser fields with the charge trapped in the plasma wave led to higher transverse and longitudinal electron momenta. By the intersection of two laser pulses in the plasma, the merging of two laser wakefields is experimentally observed, producing the emission of one single electron beam and X-rays in the forward direction. Due to their effect on the electron transverse momentum, DLA and wakefield merging are expected to increase the total emission of X-rays produced by LWFA.

Regarding potential uses of the X-ray source, several experiments presented here demonstrated the applicability of betatron X-rays for scientific studies in different disciplines. Phase-contrast imaging of an insect and an alloy demonstrated the resolution of a few micrometres that is possible with betatron radiation. The source was also used to test an X-ray absorption spectrometer designed for a femtosecond time-resolved study of hot plasmas with a LWFA-based X-ray source.

Key words
Laser-wakefield acceleration, betatron radiation, ionization-induced trapping, direct laser acceleration, laser-wakefield merging, phase-contrast imaging, warm dense matter

Classification system and/or index terms (if any)

Supplementary bibliographical information

Language
English

ISSN and key title

ISBN
978-91-7753-886-8(print)
978-91-7753-887-5(pdf)

Recipient's notes

Number of pages
234

Price

Security classification

Signature _____ Date 12 November 2018

Development and Applications of a Laser-Wakefield X-ray Source

Isabel Gallardo González

Modified on June 28, 2019

Doctoral Thesis
2018

LUND
UNIVERSITY

Development and Applications of a
Laser-Wakefield X-ray Source

Department of Physics
Faculty of Engineering
Lund University

Lund Reports on Atomic Physics, LRAP-550 (2018)
ISBN (print): 978-91-7753-886-8
ISBN (pdf): 978-91-7753-887-5
ISSN: 0281-2762

Printed in Sweden by Media-Tryck, Lund 2018

And there is nothing better than imagining,
and there is nothing better than composing
without guitar or paper,
and there is nothing better than formulating,
listening and hearing at the same time.
Physics is a pleasure.

Antonio Vega

A mi madre, porque nena, tú vales mucho.

Abstract

In laser-wakefield acceleration (LWFA), a femtosecond laser pulse is tightly focused in a gas to intensities exceeding 10^{18} W/cm^2. The laser radiation ionizes the medium and excites a plasma wave that travels behind the laser pulse. Electrons can be trapped in the oscillations in the plasma density, where electric fields of the order of several hundreds of GV/m accelerate them to relativistic energies. Together with the longitudinal accelerating fields, transverse electromagnetic forces keep the electrons oscillating in the three-dimensional plasma structure around the direction of propagation of the laser. These betatron oscillations cause the emission of X-ray pulses with a broadband spectrum and femtosecond duration.

The emission of such relativistic electron beams and ultrashort X-ray pulses, due to the high accelerating fields that can be sustained in the plasma, promises a new generation of compact electron accelerators. However, the complexity of the nonlinear laser–plasma interaction that produces LWFA poses challenges in the reproducibility and control of both the electron beams and the X-ray pulses.

The main goals of the present work are the optimization and application of a LWFA-based X-ray source. The mechanism through which the electrons are trapped and accelerated in the plasma wave influences the final parameters governing both the electrons and X-rays. Several trapping mechanisms have been investigated: using gas mixtures, a plasma density down-ramp and a combination of the two. The advantages of these approaches were a general improvement in the shot-to-shot reproducibility and some control of the electron beam charge and spectrum. It is shown that an increase in the dopant concentration of the gas also affects the acceleration process, as it increases the contribution to the electron energy from direct laser acceleration (DLA), where the overlap of the laser fields with the charge trapped in the plasma wave led to higher transverse and longitudinal electron momenta. By the intersection of two laser pulses in the plasma, the merging of two laser wakefields is experimentally observed, producing the emission of one single electron beam and X-rays in the forward direction. Due to their effect on the electron transverse momentum, DLA and wakefield merging

are expected to increase the total emission of X-rays produced by LWFA.

Regarding potential uses of the X-ray source, several experiments presented here demonstrated the applicability of betatron X-rays for scientific studies in different disciplines. Phase-contrast imaging of an insect and an alloy demonstrated the resolution of a few micrometres that is possible with betatron radiation. The source was also used to test an X-ray absorption spectrometer designed for a femtosecond time-resolved study of hot plasmas with a LWFA-based X-ray source.

Populärvetenskaplig sammanfattning

Det finns mer än 30 000 partikelacceleratorer runt om i världen. De används black annat för forskning på materiens minsta beståndsdelar, men har också andra viktiga användningsområden såsom att undersöka materialegenskaper, producera högupplösta bilder av biologiska och kemiska prov samt att diagnosticera och behandla cancer och andra sjukdomar.

Höga partikelenergier behövs för att föra forskningen framåt. Idag erhålls högst energi hos elektroner i radiofrekvensacceleratorer. Dessa acceleratorer är uppbyggda av metallkammare över vilka man lägger ett elektriskt fält som styr och accelererar elektronerna. Dock begränsas radiofrekvensacceleratorer av att metallväggarna inte tål hur starka elektriska fält som helst. För att nå högre energier, som närmar sig ljushastigheten, behöver man därför bygga större acceleratorer som accelererar partiklarna över längre sträckor.

Laserdrivna acceleratorer har inte samma begränsningar. Accelerationen sker i ett plasma som tål elektriska fält tusen gånger starkare än de som används i konventionella acceleratorer, vilket innebär att partiklarna kan nå samma energier på en tusendel av sträckan. På högeffektsfaciliteten vid Laser Center i Lund utförs experiment på laser wakefield-acceleration (LWFA). Elektronerna når energier på 300 miljoner elektronvolt, motsvarande 99.999861% av ljushastigheten, på några få millimeter. På MAX IV i Lund accelereras elektroner till energier som är tio gånger högre, 3 miljarder elektronvolt, men dessa måste accelereras över 300 meter.

Hur kan då en laserpuls användas för att accelerera elektroner? Ett plasma kan liknas vid en flytande "soppa" av negativt laddade elektroner och positivt laddade joner. När en högintensiv laserpuls fokuseras i plasmat utsätts laddningarna för en kraft, den ponderomotiva kraften. Eftersom elektronerna har mycket mindre massa än jonerna knuffas de undan av kraften och lämnar kvar ett område med enbart joner. Detta liknar hur det bildas en sänka i kölvattnet efter en båt som rör sig över en stilla sjö. För en roddbåt är effekten inte så stor, men den starka kraften av en motorbåt lämnar

en djup sänka efter sig. På liknande sätt kommer en högintensiv laserpuls att trycka under elektroner med stor kraft, vilket gör att ett område av positivt laddade joner följer efter laserpulsen så länge den är tillräckligt stark för att driva bort elektronerna.

Omfördelningen av elektroner i plasmat ger upphov till en vågrörelse, så att olika områden i plasmat är omväxlande positivt eller negativt laddade. Detta bildar mycket starka elektriska fält. Om en elektron fastnar i det positivt laddade området bakom laserpulsen, som en surfare bakom en motorbåt, kommer den att accelereras och följa efter laserpulsen.

Samtidigt som elektronerna rör sig i laserns riktning med en hastighet nära ljushastigheten kommer de att röra sig i sicksack från sida till sida. En accelererande laddning ger alltid ifrån sig strålning. Elektronens svängningar producerar röntgenstrålning som kallas betatron-röntgenstrålning. Denna strålning produceras på synkrotron-anläggningar när elektroner tvingas att vrida sig genom en bana med omväxlande positiva och negativa magnetiska fält. Detta moment är inte nödvändigt när elektroner accelereras med hjälp av en plasmavåg - LWFA producerar både en elektronstråle och röntgenstrålning på samma gång.

Laserpulserna som skapas i högeffektsfaciliteten vid Lunds lasercentrum har elektromagnetiska fält som är tiotusen gånger starkare än de fält som binder elektronen till kärnan i en väteatom. När laserpulsen fokuseras i vätgas omvandlas gasen till ett plasma som kan användas för LWFA.

Under experimenten som beskrivs i denna avhandling justerades laserpulsen och gasen för att få bättre kontroll över elektronstrålen och röntgenstrålningen, och för att bättre kunna undersöka mekanismerna som styr processen. Dessutom utfördes flera experiment för att undersöka eventuella tillämpningar av röntgenstrålningen - en röntgentomografi av en liten insekt, en avbildning av mikrometerstrukturen hos en aluminium-kisellegering, samt ett test av en röntgenspektrometer utformad för att mäta egenskaperna hos ett material när det övergår till ett plasma.

Även om elektronenergierna som erhålls vid laser-plasma nu är jämförbara med energier som kan erhållas med konventionella acceleratorer är LWFA ännu inte en fullt utvecklad teknik. Det krävs ytterligare landvinningar för att kunna åstadkomma stabilitet, kvalitet och praktisk styrning av laser wakefield-acceleration. Nya milstolpar nås dock hela tiden, och LWFA är på god väg att bli ett etablerat forskningsområde och en potentiell kandidat till nästa generations partikelaccelerator.

Popular scientific summary

There are more than 30,000 particle accelerators around the world. They are used to investigate the composition of matter on the most fundamental level, but they also play an important role in the characterization of materials, in the imaging of biological and chemical samples, and in the diagnosis and treatment of cancer and other diseases.

Higher particle energies are required to explore new materials and in novel chemical and medical applications. So far, the highest particle energies have been achieved by accelerating electrons in radio-frequency cavities. These are metallic chambers in which an electromagnetic field is applied to steer and accelerate electrons. However, the metallic walls of the radio-frequency cavities can be destroyed if the applied electromagnetic field is too high, limiting the accelerating force. As a result, the closer the particle velocity is to the speed of light, the longer the acceleration cavity must be.

This limit can be overcome using laser-driven particle acceleration. The plasma produced can support accelerating fields over one thousand times stronger than those in conventional particle accelerators, allowing the same energy to be transferred to the particles in a distance less than one thousand shorter. For example, in the experiments on laser-wakefield acceleration (LWFA) performed in the Lund high-power laser facility (Sweden), electrons are accelerated to energies of 300 million electronvolts, which corresponds to an electron travelling at 99.999861% of the speed of light, in a distance of a few millimetres. The electrons accelerated at the MAX-IV synchrotron facility, also in Lund, can reach energies ten times higher, 3 billion electronvolts, but they have to be accelerated over a distance of 300 metres.

The question is, how a laser pulse can be used to accelerate electrons. A plasma can be regarded of a fluid consisting of electrons and ions, or a "soup" of charges. When a high-intensity laser pulse is focused in a plasma, the variations in laser intensity generate a force on the charges called the ponderomotive force. The electrons, which are much lighter than the ions, are expelled by the force of the laser leaving a track behind the pulse called the wake, just like an aeroplane travelling through a cloud, or a boat on a lake.

A rowing boat leaves a weak wake, while the stronger force of a motorboat creates a deeper wave. In a similar way, a high-intensity laser pulse will expel the electrons along its direction of propagation leaving an electron-free region behind. The plasma wave propagates with the laser as long as the pulse is strong enough to drive the wake. The modulation of the electron distribution in the plasma, where the ions remain stationary, creates alternating negatively and positively charged regions, which produces very high accelerating fields. If an electron is trapped in the plasma wake, like a surfer in the wake of a motorboat, it will be accelerated and follow the laser pulse.

Furthermore, while the electrons follow the laser pulse at almost the speed of light, they also zigzag from side to side. An accelerated charge always emits radiation, so the electron oscillations produce X-ray pulses, known as betatron X-rays. This kind of radiation is produced at synchrotron facilities by forcing the electrons to "wiggle" when propagating through a series of magnetic dipoles where positive and negative magnetic fields are alternated. However, this is not necessary for electrons accelerated in the plasma wave. LWFA generates an electron beam and an X-ray pulse simultaneously.

At the Lund high-power laser facility, the electromagnetic field of the laser pulse can be ten thousand times higher than the Coulomb field that bind an electron to the hydrogen atom. When the laser pulse is focused in hydrogen gas, the gas becomes a plasma and LWFA takes place.

During the work described in this thesis, the laser pulse and the gas were manipulated in order to obtain better control of the electron beam and the X-ray radiation, and to provide a better understanding of the physical mechanisms involved. Moreover, several experiments were carried out to investigate the possibility of applying the X-ray pulses, for X-ray tomography of a small insect, imaging of an aluminium-silicon alloy to resolve micrometre structures, and test an X-ray spectrometer designed to measure the properties of matter during the transition to a plasma.

Although the electron energies obtained in the laser–plasma interaction are now comparable to the energies achieved with conventional accelerators, LWFA is not yet a mature technology. Improvements are required to obtain better stability, quality and more practical operation of laser wakefield accelerators. However, new milestones are being reached, and LWFA is becoming established on the roadmap for particle accelerator research and development.

Resumen divulgativo

Existen más de 30 000 aceleradores de partículas en el mundo, los cuales permiten investigar la constitución de la materia en el nivel más fundamental, y que además juegan un importante papel en la caracterización de materiales, en la imagen de muestras biológicas y químicas, y en el diagnóstico y tratamiento de cáncer y otras enfermedades.

Para explorar nuevos materiales o nuevas aplicaciones en química o medicina son necesarias partículas de energías cada vez más elevadas. Hasta ahora los electrones acelerados en cavidades de radiofrecuencia consiguen las energías más altas jamás alcanzadas. Dichas cavidades consisten en cámaras metálicas en donde se aplica un campo electromagnético que empuja a los electrones y los acelera. Sin embargo las paredes metálicas de la cavidad de radiofrecuencia pueden dañarse o destruirse si el campo electromagnético aplicado es demasiado alto, lo que limita la fuerza de aceleración que afecta al electrón. Por ello, cuando más cercana a la velocidad de la luz sea la velocidad de la partícula requerida, más larga deberá ser la cavidad aceleradora.

Los aceleradores de partículas inducidos por láser superan dicho límite. El plasma puede soportar campos de aceleración más de mil veces más altos que en un acelerador de partículas convencional, transfiriendo la misma energía a las partículas en una distancia varios miles de veces más corta. Por ejemplo, en los experimentos de aceleración en la estela láser (LWFA) que se llevan a cabo en Lund (Suecia), los electrones son acelerados a energías de 300 millones de electrónvoltios, lo que equivale a un electrón viajando a 99.999861 % la velocidad de la luz, en unos pocos milímetros. Los electrones que se aceleran en el sincrotrón MAX-IV, también en Lund, pueden alcanzar diez veces más energía, 3 000 millones de electrónvoltios, pero necesitan acelerarse a lo largo de 300 metros.

Pero, ¿cómo puede un pulso láser acelerar electrones? El plasma no es más que un fluido de electrones e iones, como una "sopa"de cargas eléctricas. Cuando un pulso láser ultra intenso se focaliza en un plasma, las variaciones en la intensidad del láser generan una fuerza que empuja a las cargas, llamada fuerza ponderomotriz. Los electrones, que son mucho más ligeros que los iones, salen despedidos

debido a la fuerza del pulso láser, dejando tras de sí una estela, tal y como un avión al cruzar una nube, o un barco en la superficie de un lago.

Un barco de remo produce una estela muy débil, pero la fuerza de un barco a motor contra el agua crea una ola profunda. Del mismo modo, un pulso láser ultra intenso expulsa los electrones a medida que se propaga en el plasma, dejando tras de sí una región libre de electrones. La onda de plasma se propagará siguiendo al láser siempre y cuando el pulso láser sea lo suficientemente intenso como seguir produciendo la estela. En esta modulación del plasma, las cargas eléctricas crean campos de aceleración extremadamente altos. Si un electrón es atrapado dentro de la estela en el plasma, como un surfista en la estela de un barco a motor, será acelerado y se propagará detrás del pulso láser.

Pero esto no es todo. Mientras los electrones siguen al pulso láser con una velocidad cercana a la velocidad de la luz, también zigzaguean de un lado a otro. La aceleración de una carga eléctrica siempre emite radiación, de forma que las oscilaciones de los electrones producen un pulso de rayos X, conocido como rayos X de betatrón. En sincrotrones, este tipo de radiación se produce forzando a los electrones a serpentear mientras se propagan a través de un conjunto de dipolos magnéticos, en los que los polos norte y sur se alternan. Pero esto no es necesario cuando los electrones se aceleran en la onda de plasma. LWFA genera, simultáneamente, un pulso de electrones y un pulso de rayos X.

En la universidad de Lund, el campo eléctrico de un pulso láser puede ser más de diez mil veces mayor que el campo eléctrico de Coulomb que liga a un electrón al átomo de hidrógeno. Por tanto, cuando el láser se enfoca en hidrógeno gaseoso, el gas se convierte en plasma y se produce LWFA.

Durante el trabajo presentado en esta tesis, el pulso láser y el gas se manipulan para obtener un mejor control del haz de electrones y de la radiación de rayos X, y para comprender mejor los fenómenos físicos que conllevan. Además, se han llevado a cabo varios experimentos para demonstrar posibles aplicaciones de los pulsos de rayos X, incluyendo tomografía de rayos X de un pequeño insecto, imagen de una aleación de aluminio y silicio con resolución micrométrica, y estudio de un espectrómetro de rayos X capaz de medir propiedades de la materia en su transición a plasma.

Aunque las energías de los electrones que se obtienen en interacciones láser–plasma son cada vez más comparables a las disponibles en aceleradores convencionales, LWFA no puede considerarse todavía una tecnología madura. Los investigadores deben aún mejorar cuestiones relacionadas con una mejor estabilidad y calidad del haz de electrones, y un desempeño de la técnica de aceleración más práctico. Sin embargo, nuevos logros se alcanzan cada año, lo que sitúa a LWFA en la hoja de ruta de la investigación y el desarrollo de aceleradores de partículas.

List of Publications

This thesis is based on the following publications, which are referred to by their Roman numerals:

I **Electron injector for compact staged high energy accelerator**
T. L. Audet, F. G. Desforges, A. Maitrallain, S. Dobosz Dufrénoy, M. Bougeard, G. Maynard, P. Lee, M. Hansson, B. Aurand, A. Persson, I. Gallardo González, P. Monot, C.-G. Wahlström, O. Lundh and B. Cros.
Nucl. Instrum. Methods Phys. Res. A **829**, 304-308 (2016).

II **Investigation of ionization-induced electron injection in a wakefield driven by laser inside a gas cell**
T. L. Audet, M. Hansson, P. Lee, F. G. Desforges, G. Maynard, S. Dobosz Dufrénoy, R. Lehe, J.-L. Vay, B. Aurand, A. Persson, I. Gallardo González, A. Maitrallain, P. Monot, C.-G. Wahlström, O. Lundh and B. Cros.
Phys. Plasmas **23**, 023110 (2016).

III **Localization of ionization-induced trapping in a laser wakefield accelerator using a density down-ramp**
M. Hansson, T. L. Audet, H. Ekerfelt, B. Aurand, I. Gallardo González, F. G. Desforges, X. Davoine, A. Maitrallain, S. Reymond, P. Monot, A. Persson, S. Dobosz Dufrénoy, C.-G. Wahlström, B. Cros and O. Lundh.
Plasma Phys. Control. Fusion **58**, 055009 (2016).

IV **A tunable electron beam source using trapping of electrons in a density down-ramp in laser wakefield acceleration**
H. Ekerfelt, M. Hansson, I. Gallardo González, X. Davoine and O. Lundh.
Sci. Rep. **7**, 12229 (2017).

V **Effects of the dopant concentration in laser wakefield and direct laser acceleration of electrons**
I. Gallardo González, H. Ekerfelt, M. Hansson, T. L. Audet, B. Aurand, F. G. Desforges, S. Dobosz Dufrénoy, A. Persson, X. Davoine, C.-G. Wahlström, B. Cros and O. Lundh.
New J. Phys. **20**, 053011 (2018).

VI **Electron acceleration and X-ray emission from interacting wakefields**
I. Gallardo González, H. Ekerfelt, J. Björklund Svensson, G. Gatti, A. Gonoskov, D. Guénot, M. Hansson, M. Marklund, J. A. Pérez-Hernández, C. Salgado, E. Wallin, G. Zeraouli and O. Lundh.
(2019) *Submitted to Phys. Rev. Lett.*.

VII **Analysis of electron injection in laser wakefield acceleration using betatron emission in capillary tubes**
F. G. Desforges, B. S. Paradkar, M. Hansson, T. L. Audet, J. Ju, I. Gallardo González, B. Aurand, P. Lee, L. Senje, A. Persson, S. Dobosz Dufrénoy, O. Lundh, G. Maynard, P. Monot, J.-L. Vay, C.-G. Wahlström and B. Cros.
Proc. of SPIE **9514**, 95140Z-1 (2015).

VIII **Optimization of soft X-ray phase-contrast tomography using a laser wakefield accelerator**
K. Svendsen, I. Gallardo González, M. Hansson, J. Björklund Svensson, H. Ekerfelt, A. Persson and O. Lundh.
Opt. Express, **26**, 33930 (2018).

IX **Laser-wakefield accelerators for high-resolution X-ray imaging of complex microstructures**
A. E. Hussein, N. Senabulya, Y. Ma, M. J. V. Streeter, B. Kettle, S. J. D. Dann, F. Albert, N. Bourgeois, S. Cipiccia, J. M. Cole, O. Finlay, E. Gerstmayr, I. Gallardo González, A. Higginbotham, D. A. Jaroszynski, K. Falk, K. Krushelnick, N. Lemos, N. C. Lopes, C. Lumsdon, O. Lundh, S. P. D. Mangles, Z. Najmudin, P. P. Rajeev, C. M. Schlepütz, M. Shahzad, M. Šmíd, R. Spesyvtsev, D. R. Symes, G. Vieux, L. Willingale, J. C. Wood, A. J. Shahani and A. G. R. Thomas.
Sci. Rep. **9**, 3249 (2018).

X **Highly efficient angularly resolving X-ray spectrometer optimized for absorption measurements with collimated sources**
M. Šmíd, I. Gallardo González, H. Ekerfelt, J. Björklund Svensson, M. Hansson, J. C. Wood, A. Persson, S. P. D. Mangles, O. Lundh and K. Falk.
Rev. Sci. Instrum. **88**, 063102 (2017).

All papers are reproduced with permission of their respective publishers.

Other publications by the author not included in this thesis:

Nano and micro structured targets to modulate the spatial profile of laser driven proton beams
L. Giuffrida, K. Svensson, J. Psikal, D. Margarone, P. Lutoslawski, V. Scuderi, G. Milluzzo, J. Kaufman, T. Wiste, M. Dalui, H. Ekerfelt, I. Gallardo González, O. Lundh, A. Persson, A. Picciotto, M. Crivellari, A. Bagolini, P. Bellutti, J. Magnusson, A. Gonoskov, L. Klimsa, J. Kopecek, T. Lastovicka, G.A.P. Cirrone, C.-G. Wahlström and G. Korn.
J. Instrum. **12**, C03040 (2017).

Manipulation of laser-accelerated proton beam profiles by nanostructured and microstructured targets

L. Giuffrida, K. Svensson, J. Psikal, M. Dalui, H. Ekerfelt, I. Gallardo González, O. Lundh, A. Persson, P. Lutoslawski, V. Scuderi, J. Kaufman, T. Wiste, T. Lastovicka, A. Picciotto, A. Bagolini, M. Crivellari, P. Bellutti, G. Milluzzo, G. A. P. Cirrone, J. Magnusson, A. Gonoskov, G. Korn, C.-G. Wahlström and D. Margarone.

Phys. Rev. Accel. Beams **20**, 081301 (2017).

Abbreviations

ASE	amplified spontaneous emission
CPA	chirped pulse amplification
DLA	direct laser acceleration
DM	deformable mirror
FTL	Fourier transform limited
FWHM	full width at half maximum
HOPG	highly oriented pyrolytic graphite
LWFA	laser-wakefield acceleration
μCT	microcomputed tomography
OTBI	over-the-barrier ionization
OAP	off-axis parabola
PCI	phase-contrast imaging
PIC	particle-in-cell
SPC	single-photon counting
XAS	X-ray absorption spectroscopy
XANES	X-ray absorption near edge structure
WDM	warm dense matter

Contents

Papers

Chapter 1

Introduction

The physical phenomenon studied in this thesis is produced by the interaction of a high-intensity laser with matter. High intensity in this context means laser intensities orders of magnitude above the ionization threshold of matter. This extreme radiation, often in the form of a femtosecond laser pulse, ionizes matter almost instantaneously, so the interaction is often considered as being between a high-intensity laser and a plasma.

Laser–plasma interactions can lead to scenarios where particles are accelerated by the electromagnetic fields induced in the plasma by the laser. Although particle accelerators are often thought of as huge facilities producing particles with extremely high energies for the study of the fundamentals of physics, particles accelerated to lower energies are also used in many other applications. Protons and ions are often employed in particle therapy and ion implantation; electron beams have applications in medical and materials science. In synchrotron facilities and free-electron lasers, accelerated electrons are forced to "wiggle" in an alternating dipole array to produce pulsed X-ray radiation. These X-rays are a very useful diagnostic tool in many scientific disciplines such as biology, chemistry, nanoscience, medicine and materials science.

In laser-wakefield acceleration (LWFA), the interaction of a high-intensity laser pulse with a plasma causes the acceleration of electrons to velocities close to the speed of light. During this process, electrons perform transverse oscillations that generate an X-ray pulse. Hence, LWFA provides a source of electrons and X-rays whose potential uses are being investigated today.

The aim of the work presented in this thesis was to study and optimize LWFA, to allow the use of the X-ray pulses in both established and new applications.

1.1 History of laser-wakefield acceleration

The theoretical basis of LWFA was conceived in 1979 by Tajima and Dawson [1]. The proposed mechanism was based on the use of the unprecedentedly high-intensity electromagnetic radiation made possible by the invention of the laser two decades previously [2], to accelerate electrons to very high energies in a very short length. The idea they conceived was that an intense and very short electromagnetic pulse, tightly focused in an underdense plasma, would excite a plasma wave, i.e. it would produce oscillations in the electron density distribution inside the plasma. The electrons, which are much lighter than ions, are accelerated by the radiation pressure, and acquire very high velocities, causing a void of negative charge behind the laser pulse. The void produces a restoring force that attracts the expelled electrons, which start oscillating producing a plasma wave travelling behind the laser pulse.

This charge modulation induces extremely high accelerating fields in each plasma period, of the order of hundreds of GV/m. This is more than three orders of magnitude higher than the maximum electric field that can be sustained in the metallic resonant cavities of conventional electron accelerators. As a result, an electron reaches velocities comparable to the speed of light in vacuum in less than 0.5 mm. For this reason, laser-wakefield accelerators are often referred to as "compact" electron accelerators.

Already in their first publication, Tajima and Dawson suggested a number of conditions that the laser pulse would have to satisfy in order to efficiently excite the plasma wave and accelerate the electrons. They stated that to accelerate electrons in the relativistic regime, the laser intensity must be at least 10^{18} W/cm^2, and that the laser pulse duration should be approximately half the plasma wave oscillation period. For a plasma electron density of 10^{18} cm^{-3}, which was typical in the experiments described in this thesis, this is of the order of a few tens of fs. It will later be shown that the plasma wave is highly excited if the laser spot size is also of the order of the plasma wavelength, corresponding in the example above to a few tens of μm. However, the laser technology available in 1979 was not capable of producing laser pulses that could be focused to such high intensities. The main reason was that as femtosecond pulses were amplified to gain energy, the peak intensity of the pulse became so high that it damaged the optics used for amplification, requiring either extremely large optics or limiting the maximum energy per pulse produced.

During the following years, alternative methods of exciting highly relativistic plasma waves for electron acceleration were explored, such as the interaction of two laser pulses with different wavelengths in the plasma (plasma-beat wave acceleration [3–5]), self-modulation of a longer laser pulse in the plasma (self-modulated laser-wakefield acceleration [6–8]) and excitation of the plasma wave

by a particle beam (plasma-wakefield acceleration [9–12]). Developments in laser technology, in particular, the invention of chirped pulse amplification (CPA) [13], for which Strickland and Mourou were recently awarded the Nobel Prize in Physics, paved the way for high-intensity femtosecond pulses. This made it possible to produce laser pulses with a short enough duration, and with sufficient energy and focusing capabilities to efficiently excite the plasma wave.

In 1985, Strickland and Mourou proposed the application of a technique initially developed for radar transmission to femtosecond laser pulses [14]. The idea was to temporally stretch the laser pulse before the amplification stages, and then compress it to a short pulse afterwards. As will be discussed in Section 2.1.1, short pulses are produced by the coherent superposition of light with a broad range of frequencies. The pulse can be stretched if each frequency is slightly delayed with respect the other, so the longer wavelengths travel in front of the pulse and shorter wavelengths travel at the end. This can be accomplished by means of dispersive and/or diffractive optics. With this technique, the duration of the laser pulse can be increased by a factor between 10^3 and 10^4, so the intensity of the pulse during amplification is reduced by several orders of magnitude, allowing the extraction of more energy without damaging the amplification material or producing other nonlinear effects. A CPA laser thus consists of four main parts, as illustrated in Figure 1.1: an oscillator where the femtosecond pulse is generated with a bandwidth broad enough to support very short pulses; a stretcher, where the pulse is temporally stretched by delaying each laser frequency by a different amount; one or several amplification stages, where the energy per pulse is increased; and finally a compressor, where the dispersion is compensated for and the pulse is shortened again.

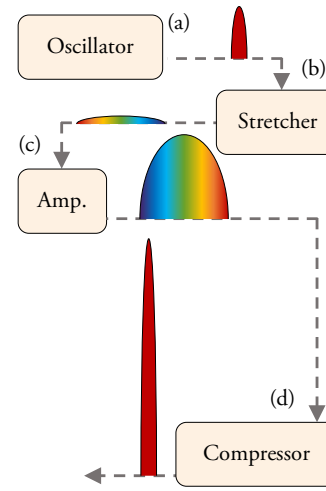

Figure 1.1. *Illustration of the CPA technique. (a) The laser pulses are produced with a duration of a few fs and an energy of a few nJ in the oscillator; (b) the pulse is elongated in a stretcher, so the lower frequencies travel in front of the pulse and the higher frequencies behind; (c) the laser pulse energy is amplified in one or several stages; and (d) another set of optics produces the opposite dispersion of the frequencies so the laser pulse is shortened in the compressor.*

Soon after the invention of CPA, femtosecond lasers with peak powers in the terawatt and multi-terawatt regime became possible. However, almost twenty years' development in laser technology was required to obtain the laser parameters required for efficient laser–plasma acceleration. Several experimental studies were performed in an attempt to focus the new generation of lasers to efficiently excite a wave in a plasma. Such efforts also allowed exploration of the capability of the accelerated electrons to perform transverse oscillations and emit radiation [15, 16], referred to in the LWFA community as betatron X-rays. Finally, high-quality laser-wakefield-accelerated electron beams were generated in 2004, when high-charge, quasi-monochromatic electron beams were achieved independently at three laser laboratories [17–19].

LWFA has enabled the introduction of a new generation of tabletop accelerators in many laboratories all over the world. While the plasma accelerating structure allows higher accelerating fields to be sustained, making the technique more compact, it also complicates the control of the process, as the physics involved in the laser and

plasma evolution is highly nonlinear. Today, efforts in the field of LWFA are being directed towards the optimization and control of the electron beam parameters, to achieve some degree of tunability and reproducibility of the electron beams, and towards higher electron energies. Researches are thus dealing with multiple scientific and technical challenges in an attempt to understand and control all the complex processes involved in LWFA. Furthermore, the betatron X-rays produced in the plasma wave have a particularly useful small source size and short pulse duration, and have become a very promising source with potential applications in many different scientific disciplines which are currently being explored.

1.2 Outline of this thesis

The structure of this thesis is as follows. Chapter 2 presents the theoretical formalism necessary to describe the laser–plasma interaction, the excitation of the plasma wave, the electron acceleration process and the emission of betatron X-rays. In Chapter 3, the methods used to experimentally produce and characterize the LWFA interaction are explained, including the laser pulse, the plasma, the electron beam and the X-rays. The work carried out on improving the control of the electron parameters and the study of physical processes during electron acceleration is summarized in Chapter 4, and refers to Papers I to VI. The experiments conducted to investigate and demonstrate the relevance of betatron X-rays in different applications, which resulted in Papers VII to X, are described in Chapter 5. Chapter 6 summarizes the findings of this work and the future challenges associated LWFA electrons and betatron X-rays are discussed.

Chapter 2

Principles of laser-wakefield acceleration and betatron radiation

A laser-wakefield accelerator requires an intense laser pulse and a plasma. As will be explained in this chapter, the quality of the resulting beam of accelerated electrons depends strongly on finding the appropriate values of the parameters for both the laser pulse and the plasma so the process is optimized.

When an ultrashort laser pulse with a duration on the femtosecond scale is focused in a plasma, such that its peak intensity exceeds 10^{18} W/cm^2, the variation in the laser intensity in the focus results in a force on the free charges in the plasma called the ponderomotive force. The electrons, which are much lighter than the ions, are pushed away, leaving a track behind the pulse known as a "wake". This modulation of the plasma creates very high electric fields. Electrons from the plasma background with velocities high enough to follow the plasma wave can "surf" on the wake, acquiring relativistic energies, and being accelerated behind the laser pulse by LWFA.

Section 2.1 presents the basic concepts of laser electromagnetic waves and plasmas, and the motion of an electron under the influence of an electromagnetic wave. Section 2.2 describes the ponderomotive force that excites the plasma wave, where electron acceleration takes place. The transverse oscillations performed by the accelerated electrons, as well as the X-ray emission produced by them, are described in Section 2.3.

2.1 Laser pulses and plasmas

Any kind of electromagnetic radiation can be described by two vector fields in space–time $(\mathbf{r}, t)$: the electric $\mathbf{E}(\mathbf{r}, t)$ field and the magnetic $\mathbf{B}(\mathbf{r}, t)$ field. The fields obey Maxwell's equations, which in free space are given by:

$$\begin{cases} \boldsymbol{\nabla} \cdot \mathbf{E}(\mathbf{r}, t) &= \dfrac{\rho(\mathbf{r}, t)}{\epsilon_0}, \\ \boldsymbol{\nabla} \cdot \mathbf{B}(\mathbf{r}, t) &= 0, \\ \boldsymbol{\nabla} \times \mathbf{E}(\mathbf{r}, t) &= -\dfrac{\partial \mathbf{B}(\mathbf{r}, t)}{\partial t}, \\ \boldsymbol{\nabla} \times \mathbf{B}(\mathbf{r}, t) &= \mu_0 \left(\mathbf{J}(\mathbf{r}, t) + \epsilon_0 \dfrac{\partial \mathbf{E}(\mathbf{r}, t)}{\partial t} \right), \end{cases} \tag{2.1}$$

with the constants ϵ_0, the vacuum electric permittivity, μ_0, the vacuum magnetic permeability, and c, the velocity of light in vacuum, such that $\epsilon_0 \mu_0 = 1/c^2$. The scalar field $\rho(\mathbf{r}, t)$ represents the total electric charge density, while the vector field $\mathbf{J}(\mathbf{r}, t)$ corresponds to the current density.

Fourier optics is a description based on harmonic analysis of Equations (2.1) in linear systems, where any electromagnetic function can be expanded by harmonic functions. The harmonic functions have the shape of monochromatic plane waves with wavelength λ, angular frequency $\omega = 2\pi c/\lambda$ and wavenumber $k = 2\pi/\lambda$, and are useful when studying the propagation of electromagnetic fields. A monochromatic plane wave in a linear, homogeneous, nondispersive and isotropic medium has the form:

$$\begin{aligned} \mathbf{E}(\mathbf{r}, t) &= \mathbf{E_0} \cos(\mathbf{k}\cdot\mathbf{r} - \omega t), \\ \mathbf{B}(\mathbf{r}, t) &= \mathbf{B_0} \cos(\mathbf{k}\cdot\mathbf{r} - \omega t). \end{aligned}$$

The wave vector $|\mathbf{k}| = k$ has the same direction as wave propagation. In order to satisfy Equations (2.1), the electric field $\mathbf{E}$, the wavevector $\mathbf{k}$ and the magnetic field $\mathbf{B}$ are mutually orthogonal. These periodic fields have maximum amplitudes given by E_0 and B_0 which, in vacuum, satisfy the relation $B_0 = E_0/c$.

The intensity of the electromagnetic wave is given by the time-averaged energy flux of the electromagnetic field, which is represented by the Poynting vector $\mathbf{S}(\mathbf{r}, t) = (\mathbf{E}(\mathbf{r}, t) \times \mathbf{B}(\mathbf{r}, t))/\mu_0$. In the case of a plane wave propagating in vacuum, the intensity is given by:

$$I(\mathbf{r}) = \langle S(\mathbf{r}, t) \rangle = \frac{c\epsilon_0}{2} |E_0|^2. \tag{2.2}$$

2.1.1 The laser pulse

Laser light is usually generated and amplified inside a medium confined in a resonator. Many laser cavities are geometrically designed so that the output electromagnetic wave contains only the fundamental transverse mode, described by the Gaussian function in the

space domain. In the paraxial approximation, when the divergence is rather small, a Gaussian beam propagating in the x direction $\mathbf{k} = k\mathbf{e_x}$, and linearly polarized along y, $\mathbf{E_l} = E_l\mathbf{e_y}$, is expressed as:

$$\mathbf{E_l}(\mathbf{r}) = E_0\mathbf{e_y}\frac{w_0}{w(x)}\exp\left\{-\frac{(y^2+z^2)}{w(x)^2}\right\} \exp\left\{-i\left[kx + \frac{k(y^2+z^2)}{2R(x)} - \varphi(x)\right]\right\},$$

where $w(x) = w_0(1 + (x/x_R)^2)^{1/2}$ is the beam waist, which has a minimum value at the focus, w_0, $R(x) = x(1 + (x_R/x)^2)$ is the curvature of the phase front, $x_R = \pi w_0^2/\lambda$ is the Rayleigh length, and $\varphi(x) = \arctan(x/x_R)$ is the Gouy phase term.

Gaussian beams have interesting properties [20]. They maintain a scaled Gaussian transverse distribution after propagating in vacuum, homogeneous materials and simple aberrant-free optical elements (Figure 2.1(a)). In comparison with other transverse modes of a laser cavity, the intensity distribution of the focused beam achieves maximum photon density, to the diffraction limit. Moreover, the beam is reasonably collimated within a range given by the Rayleigh length, x_R, from the focal plane. The beam waist $w(x)$ is defined as the radius at which the electric field has decreased by a factor $1/e$ with respect to the maximum, or equivalently, the radius at which the intensity has fallen by a factor $1/e^2$ with respect the maximum. The beam waist is related to the full width at half maximum (FWHM) of the intensity, $d(x)$, by $2w(x) = \sqrt{2}d(x)/\sqrt{\ln 2}$ (Figure 2.1(b)). In particular, a Gaussian beam with waist w_1 impinging on a thin lens of focal length f focuses to a spot with a waist $w_0 = \lambda f/\pi w_1$.

The laser beams used in the experiments described in this work were, in general, approximated to Gaussian beams. The error introduced by this approximation was studied by comparing the actual peak intensity of the focused laser pulse with the value predicted for a focused Gaussian beam.

Regarding the temporal domain, a laser pulse is often described as the product of a term oscillating with the central angular frequency $\omega_0 = 2\pi c/\lambda_0$, where λ_0 is the central wavelength, and a slowly varying envelope that accounts for the temporal shape of the pulse. This envelope can also often be described by a Gaussian function:

$$E_l(t) = E_0\exp\left\{-\frac{2\ln(2)t^2}{\tau_p^2}\right\}\exp\{-i\omega_0 t\},$$

where τ_p is the FWHM duration of the pulse intensity.

In practice, such a pulsed electromagnetic field is the result of the superposition of several electromagnetic waves within a broad optical FWHM bandwidth centred at the angular frequency ω_0.

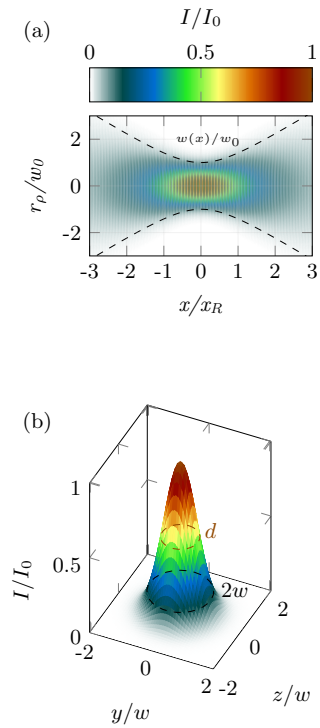

Figure 2.1. *Intensity distribution of a Gaussian beam (a) along its direction of propagation and (b) in the transverse plane.*

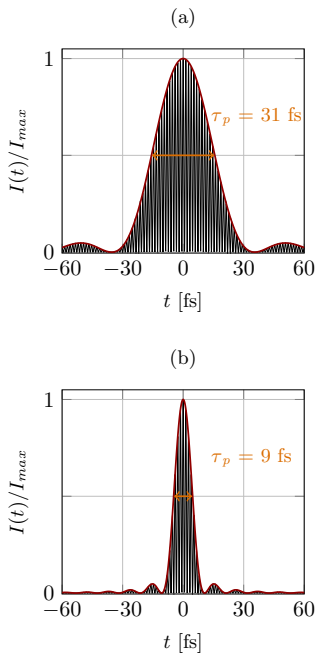

Figure 2.2. *Intensity of a laser pulse, which envelope is indicated by the red thick line, resulting from the interfere of plane waves within a wavelength bandwidth of: (a) $\Delta\lambda = 30$ nm, and (b) $\Delta\lambda = 100$ nm. The pulse duration is $\tau_p = 31$ fs and $\tau_p = 9$ fs, respectively.*

Table 2.1. *Ionization potential ϵ_{ion} and corresponding appearance intensity I_{app} of some of the ions present in the gas mixtures used in this work.*

Ion	ε_{ion} [eV]	I_{app} [W/cm^2]
H^+	13.6	1.4×10^{14}
He^+	24.6	1.5×10^{15}
He^{2+}	54.4	8.8×10^{15}
N^{5+}	97.9	1.5×10^{16}
N^{6+}	552.1	1.0×10^{19}
N^{7+}	667.0	1.6×10^{19}
Ar^{16+}	918.0	1.1×10^{19}
Ar^{17+}	4121.0	4.0×10^{21}
Ar^{18+}	4426.0	4.7×10^{21}

The pulse with the shortest achievable duration for a given optical bandwidth, $\Delta\nu$, is described as being Fourier transform limited (FTL), and is achieved when the waves of different frequencies have a relative phase such that they interfere constructively at the peak amplitude. For a Gaussian temporal envelope, the Fourier transform limit obeys the expression:

$$\Delta\nu = \frac{\Delta\omega}{2\pi} = \frac{c\Delta\lambda}{\lambda_0^2} \simeq \frac{0.44}{\tau_p}. \tag{2.3}$$

Femtosecond pulses are often generated in mode-locked Ti:sapphire lasers, in which the gain medium can produce a bandwidth up to 140 THz, corresponding to a spectral range of 300 nm centred around 800 nm. In a mode-locked laser, the different longitudinal modes coexisting in the resonant cavity, are coupled and locked in phase and interfere so as to generate an FTL pulse. A 100 fs FTL pulse generated in a Ti:sapphire laser requires a spectral bandwidth of about 10 nm, while a 30 fs pulse requires a bandwidth of roughly 30 nm. Figure 2.2 shows the pulses resulting from the coherence interference of plane waves, with wavelength bandwidths of 30 nm (a), and 100 nm (b). The wider the wavelength bandwidth of the waves that interfere, the shorter the pulse become.

The shorter and more tightly focused the laser pulse is, the higher its peak intensity will be. The peak intensity, I_0, of a temporal and spatial Gaussian laser pulse, of energy ε_p, obtained from Equation (2.2), is given by:

$$I_0 = \frac{2\varepsilon_p}{\pi w_0^2 \tau_p}.$$

In this thesis, high-intensity femtosecond laser pulses refers to laser pulse durations of $\tau_p < 1$ ps $= 10^{-12}$ s, and peak intensities of $I_0 > 10^{18}$ W/cm^2.

2.1.2 Ionization of a medium

A plasma is a state of matter in which the medium is ionized, i.e., electrons are released from ions which become positively charged. While the net charge of a plasma is zero, in a collision-less plasma the motion of its charged particles is governed by the electromagnetic forces produced by the local distribution of charges.

As already mentioned, an atom or molecule is ionized when it releases an electron and, consequently, acquires a positive charge. Several types of light–matter interactions can cause the ionization of an atom or molecule. In the simplest case, a photon with a total energy $h\nu_{XUV}$ equal to, or greater than, the binding energy of the electron, ε_{ion}, is absorbed, and the atom will release the electron through the photoelectric effect, as shown in Figure 2.3(a). Photons with sufficient energy to ionize an atom or a molecule are

typically in the extrema ultra-violet regime. However, at intensities above 10^{10} W/cm^2 multiphoton ionization may take place, in which several photons are absorbed by the atom or molecule, by means of intermediate virtual states, resulting in release of the electron, as shown in Figure 2.3(b).

Developments in laser technology have allowed the exploration of other types of ionization processes. As the intensity of the laser increases, the laser electric field can perturb the binding potential of the electron and modify its shape. The atom or molecule is said to be perturbed by a strong field. The potential experienced by the electron is bent twice at each laser pulse cycle following the amplitude of the laser electric field. This can reduce the effective potential barrier of the electron, producing a finite probability of the electron tunnelling through the barrier and escaping from the nuclear potential. This is called tunnelling ionization, and is illustrated in Figure 2.3(c).

Finally, the external laser electric field can be strong enough to bend the electron potential below the binding potential, so that the electron is free to escape. This is known as over-the-barrier ionization (OTBI) and is illustrated in Figure 2.3(d). The laser intensity defining the threshold of this regime can be estimated [21]. OTBI requires the total potential to bend under the ionization energy, which requires a laser intensity that corresponds to the appearance intensity of the ion:

$$I_{app} = \frac{\pi^2 c \epsilon_0^3 \varepsilon_{ion}^4}{2Z^2 e^6}, \tag{2.4}$$

where Z is the charge on the ion created. For a hydrogen atom, this corresponds to an intensity of 1.4×10^{14} W/cm^2, and for a helium ion, He^{2+}, it corresponds to 8.8×10^{15} W/cm^2.

In the experiments presented in this thesis, the focused laser pulse reached intensities above 10^{18} W/cm^2 in vacuum. The leading part of the laser pulse, already three orders of magnitude below the peak intensity, is thus capable of generating OTBI in light gases such as hydrogen or helium (see Table 2.1). In these cases, it is possible to assume that most of the laser pulse encounters an already fully ionized medium. In such a case, LWFA will be described by the interaction of the laser pulse with a preformed plasma, and the effects of the ionization of the medium by the leading part of the pulse can therefore be neglected.

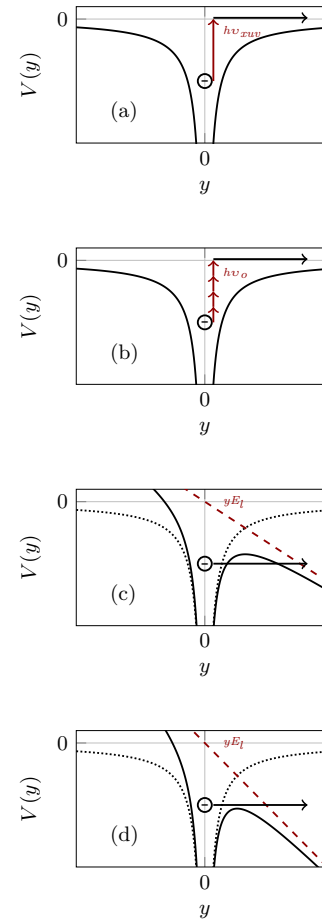

Figure 2.3. *Illustrations of the ionization processes of an electron in a hydrogen potential: (a) single-photon ionization, (b) multiphoton ionization, (c) tunnelling ionization and (d) over-the-barrier ionization.*

2.1.3 Electrons in a laser field

In order to study the interaction of a laser pulse with a plasma, it is useful to first describe the motion of a single free electron in the

laser fields, which is governed by the equations:

$$\text{Lorentz equation:} \quad \frac{\mathrm{d}\mathbf{p_e}}{\mathrm{d}t} = -e\left(\mathbf{E_l} + \mathbf{v} \times \mathbf{B_l}\right), \tag{2.5}$$

$$\text{Energy equation:} \quad \frac{\mathrm{d}}{\mathrm{d}t}\left(\gamma m_e c^2\right) = -e\left(\mathbf{v}\mathbf{E_l}\right), \tag{2.6}$$

where $\mathbf{p_e} = \gamma m_e \mathbf{v}$ is the electron momentum, $\mathbf{v}$ is the electron velocity, m_e is the electron rest mass and $\gamma = [1-(v/c)^2]^{-1/2}$ is the electron relativistic factor.

From Equation (2.5), in the non-relativistic limit when the electron velocity is much lower than the velocity of light in vacuum ($v \ll c$ and $\gamma \simeq 1$), the magnetic part of the Lorentz force is negligible, and the electron moves with the "quiver velocity", $\mathbf{v_q}$, which obeys:

$$m_e \frac{\mathrm{d}\mathbf{v_q}}{\mathrm{d}t} = -e\mathbf{E_l}. \tag{2.7}$$

It is often useful to express the electromagnetic wave in terms of the vector potential $\mathbf{A}$, which in vacuum is given by:

$$\begin{aligned} \mathbf{E_l} &= -\frac{\partial \mathbf{A}}{\partial t}, \\ \mathbf{B_l} &= \boldsymbol{\nabla} \times \mathbf{A}. \end{aligned} \tag{2.8}$$

Introducing the vector potential in Equation (2.5), and assuming that it describes a linearly polarized field, $\mathbf{A} = A\mathbf{e_y}$, it is possible to decompose the Lorentz equation in the longitudinal (x) and perpendicular (y) directions to the direction of propagation of the laser:

$$\begin{cases} \dfrac{\mathrm{d}p_{e,x}}{\mathrm{d}t} &= -ev_y \dfrac{\partial A}{\partial x}, \\ \dfrac{\mathrm{d}p_{e,y}}{\mathrm{d}t} &= e\dfrac{\partial A}{\partial t} + ev_x \dfrac{\partial A}{\partial x}. \end{cases} \tag{2.9}$$

An observer in the laboratory frame sees the electron at rest until the laser pulse arrives. Considering a plane-wave $\mathbf{A} = A_0 \cos(k\xi)\mathbf{e_y}$, with the copropagating coordinate $\xi = x - \omega_0 t/k$, the solution of Equations (2.9) for the electron trajectory gives [21]:

$$\begin{aligned} x &= \frac{a_0^2 c}{4\omega_0}\left[k\xi + \frac{1}{2}\sin\left(2k\xi\right)\right], \\ y &= \frac{a_0 c}{\omega_0}\sin\left(k\xi\right). \end{aligned} \tag{2.10}$$

The normalized vector potential, $\mathbf{a} = e\mathbf{A}/m_e c$, has also been introduced here, the peak value of which, a_0, is given, in terms of the laser electric field and intensity by:

$$a_0 = \frac{eA_0}{m_e c} = \frac{eE_l}{m_e c \omega_0} = \sqrt{\frac{e^2}{2\pi^2 \epsilon_0 m_e^2 c^5}\lambda_0^2 I_0}. \tag{2.11}$$

There are some differences between the motion in the longitudinal and transverse directions given by Equations (2.10). While the electron oscillates with the laser frequency in the transverse direction, it also has a positive net drift in the direction of propagation of the laser, together with an oscillating term at twice the laser frequency. Figure 2.4(a) shows the trajectories described in Equations (2.10) for values of $a_0 = 0.3$, 1 and 3.5, which for $\lambda = 800$ nm, correspond to laser intensities of 2.0×10^{17}, 2.2×10^{18} and 2.6×10^{19} W/cm^2, respectively. While the amplitude of the motion depends linearly on a_0 in the transverse direction, it increases as a_0^2 in the longitudinal direction. As soon as the laser intensity is such that $a_0 > 1$, the longitudinal motion quickly becomes dominant over the transverse motion.

In a frame copropagating with the averaged velocity of the electron, Equations (2.9) give the solution

$$x = \left(\frac{a_0}{2\gamma}\right)^2 \frac{c}{2\omega_0} \sin(2k\xi),$$
$$y = \frac{a_0}{\gamma} \frac{c}{\omega_0} \sin(k\xi).$$

As shown in Figure 2.4(b), when the intensity increases, the amplitude of the longitudinal oscillation increases and the figure-of-eight shape widens.

The normalized peak vector potential is then an important reference which defines the threshold between non-relativistic ($a_0 \ll 1$) and relativistic ($a_0 \geq 1$) electron motion. This is easily seen in the non-relativistic case described by the quiver velocity in Equation (2.7), since the electron velocity becomes comparable to the speed of light, $v_q \to c$, as $a_0 \to 1$.

Relativistic laser pulses, i.e. with a peak normalized vector potential $a_0 \geq 1$, are then necessary to obtain significant motion of the electron. This makes it necessary to focus the laser pulse tightly. However, with the homogeneous field considered here, there is no energy transfer from the electromagnetic fields to the electron, and the electron will move only under the influence of the laser pulse, remaining at rest once it passes.

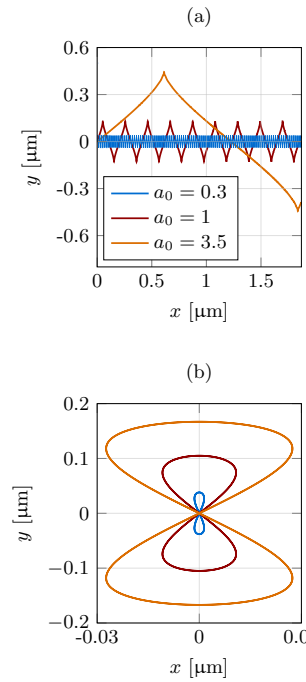

Figure 2.4. *Solution of the trajectories of a free electron under a laser field in (a) the laboratory frame, and (b) the averaged rest frame.*

2.1.4 The underdense plasma

When an electron moves under the presence of an electromagnetic field inside a plasma, it produces a change in the local charge density that induces electrostatic restoring forces. These forces tend to pull the electron back and induce an oscillation, while the positive ions in the plasma are considered to be stationary due to their much higher mass. The electron oscillations can be described collectively by Maxwell's equations (2.1) by considering the Fourier decomposition of the electromagnetic waves into plane waves, $\mathbf{E} = \int \mathbf{E}_\mathbf{k} e^{i(\mathbf{kr}-\omega t)} \mathrm{d}\mathbf{k}$

and $\mathbf{B} = \int \mathbf{B_k} e^{i(\mathbf{kr}-\omega t)} \mathrm{d}\mathbf{k}$. Disregarding the relativistic term of the Lorentz equation, the electron current density, $\mathbf{J} = -en_e\mathbf{v}$, can be expressed in terms of the electric field as $-e\mathbf{E} = m_e\dot{\mathbf{v}}$. Using $\mathbf{J} = (in_e e^2)/(\omega m_e) \int \mathbf{E_k} e^{i(\mathbf{kr}-\omega t)} \mathrm{d}\mathbf{k}$, Maxwell's equations become:

$$\begin{aligned} \mathbf{k} \times \mathbf{E_k} &= \omega \mathbf{B_k}, \\ \mathbf{k} \times \mathbf{B_k} &= \frac{\mu_0 n_e e^2}{\omega m_e} \mathbf{E_k} - \mu_0 \epsilon_0 \omega \mathbf{E_k}. \end{aligned} \tag{2.12}$$

The solutions of this system of equations depend on the direction of propagation of the wave vector $\mathbf{k}$. If $\mathbf{k} \| \mathbf{E_k}$, then $\mathbf{B_k} = 0$ and there are solutions only for

$$\omega \equiv \omega_p = \sqrt{\frac{n_e e^2}{m_e \epsilon_0}}. \tag{2.13}$$

This non-relativistic plasma angular frequency ω_p describes the oscillation in the electron number density in the longitudinal direction, forming a plasma wave known as a Langmuir wave. In the relativistic case, the plasma angular frequency is modified by the relativistic increase of the mass of the electron, which in terms of the peak normalized vector potential becomes $\omega_{pN} = \omega_p/\sqrt{a_0}$ [22]. Henceforth, the subscript N denotes "nonlinear". As the electrostatic field induced by this plasma wave is parallel to the laser's direction of propagation, it plays a major role in the electron acceleration described in Section 2.2.

Considering $\mathbf{k} \perp \mathbf{E_k}$ and a non-magnetized plasma, the solutions of Equations (2.12) describe the propagation of an electromagnetic field with angular frequency ω_0 in the plasma, and leads to the dispersion relation:

$$\omega_0^2 = \omega_p^2 + c^2 k^2. \tag{2.14}$$

Two regimes can be distinguished from this relation. If the laser frequency is lower than the plasma frequency, the wave vector k is imaginary, and describes an evanescent wave, the amplitude of which decays inside the plasma. In this case, the plasma is called "overdense", and most of the laser energy will be reflected. However, if the laser frequency is higher than the plasma frequency, the wave vector is real, and the laser pulse can propagate inside the "underdense" plasma. The limit between these two cases is given by the critical electron number density, which gives $\omega_0 = \omega_p$:

$$n_c = \frac{\omega_0^2 m_e \epsilon_0}{e^2}. \tag{2.15}$$

The phase and group velocities of an electromagnetic wave propagating in an underdense plasma can be calculated from Equa-

tion (2.14):

$$v_{ph} = \frac{\omega_0}{k} = \sqrt{c^2 + \frac{\omega_p^2}{k^2}},$$
$$v_g = \frac{\mathrm{d}\omega_0}{\mathrm{d}k} = \frac{c^2}{v_{ph}} = c\sqrt{1 - \omega_p^2/\omega_0^2}. \tag{2.16}$$

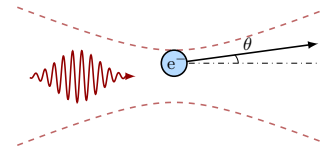

Figure 2.5. *The electron experiences a "kick" from the ponderomotive force produced by the intensity gradient of the laser pulse. The closer the electron is to the axis of laser propagation, the stronger the ponderomotive force becomes. In the relativistic regime, the electron emission angle θ becomes smaller towards this axis.*

As long as the laser does not evolve through the plasma, the phase velocity of the plasma wave is equal to the group velocity of the laser, $v_p \simeq v_g$ [23]. This means that the plasma wave closely follows the laser pulse as it propagates through the plasma, as a "plasma wake". As will be discussed in Section 2.2.3, the phase velocity of the plasma wave is an important factor, as influences the energy gain of the electrons during the acceleration process.

The laser sources used in the experiments described in Chapters 4 and 5 emitted pulses with a central wavelength around $\lambda_0 = 800$ nm, corresponding to a critical density n_c of 1.74×10^{21} cm^{-3}. LWFA requires the interaction of a high-intensity laser pulse with an underdense plasma. The typical plasma density in these experiments ranged between 10^{18} and 10^{19} cm^{-3}.

2.2 Laser-wakefield acceleration

In the description of LWFA we will assume the interaction of a high-intensity femtosecond laser pulse with a preformed underdense plasma.

2.2.1 The ponderomotive force

As discussed in Section 2.1.1, the laser fields used for LWFA are not plane waves but ultra-short, tightly focused laser pulses that are often approximated by Gaussian functions in the space and time domains. This non-homogeneous Gaussian spatial distribution of the laser intensity is necessary not only to increase the peak intensity to which the laser can be focused, but more importantly, to transfer energy from the laser pulse to the plasma electrons by means of the ponderomotive force [24].

Equation (2.7) already showed that, in the linear non-relativistic regime, an electron in an electromagnetic field moves with the quiver velocity $\mathbf{v_q}$. Note that the temporal evolution of the fields can still be considered as an harmonic oscillation $\mathbf{a}(\mathbf{r}, t) = \mathbf{a}(\mathbf{r}) \cos(kx - \omega_0 t)$. Assuming a small perturbation of the quiver velocity by the second-order motion of the electron, the ponderomotive force can be derived from the Lorentz equation in terms of the normalized vector potential. The laser fields, expressed in terms of the normalized vector potential (Equations (2.8)), and the electron momentum, expressed as the quiver momentum ($\mathbf{p_q} = m_e \mathbf{v_q}$)

and a small perturbation so that $\mathbf{p} = \mathbf{p_q} + \delta\mathbf{p}$, are substituted in Equation (2.5) [25]:

$$\begin{aligned}\frac{\mathrm{d}\delta\mathbf{p}}{\mathrm{d}t} =& - m_e\frac{\mathrm{d}\mathbf{v_q}}{\mathrm{d}t} - e\mathbf{E_l} - e\mathbf{v_q}\times\mathbf{B_l} = \\ & - m_e\mathbf{v_q}\nabla\mathbf{v_q} - m_ec\mathbf{v_q}\times(\nabla\times\mathbf{a}(\mathbf{r},t)) = \\ & = -m_ec^2\nabla\left(a^2(\mathbf{r},t)\right),\end{aligned}$$

where the identity $\mathrm{d}/\mathrm{d}t = \partial/\partial t + \mathbf{v}\nabla$ has been used. The ponderomotive force in the linear regime is given by this perturbation averaged over the laser field rapid oscillations, which in terms of the intensity of a laser pulse, becomes:

$$\mathbf{F_p} = -m_ec^2\nabla\left(\frac{a^2(\mathbf{r})}{2}\right) = -\frac{e^2}{2\epsilon_0 m_e c\omega^2}\nabla I(\mathbf{r}). \tag{2.17}$$

In the nonlinear relativistic regime, it can be shown that the effective nonlinear ponderomotive force corresponds to [26, 27]:

$$\mathbf{F_{pN}} = -m_ec^2\nabla\overline{\gamma}, \tag{2.18}$$

where $\overline{\gamma}$ corresponds to the slow component of the relativistic factor, averaged over the fast laser period.

The origin of the ponderomotive force is thus the gradient of the laser intensity. As a result, it is independent of the laser polarization and the sign of the plasma particle charge it acts upon, and depends only on the particle mass and laser pulse intensity gradient. The ponderomotive force applies to both electrons and ions in the plasma, pushing them in the same direction, but is much smaller for the heavier ions. Consequently, only its effect on the electron charges is considered, while the ions are assumed to remain stationary. For both linear and nonlinear regimes (Equations (2.17) and (2.18)), the electrons experience a stronger force in regions with locally higher intensity and, as a consequence, are pushed away from the centre of the laser pulse. The linear ponderomotive force is directed perpendicularly to the direction of the laser intensity gradient, while relativistic effects also produce a forward push causing the electrons to be ejected at an angle, $\tan\theta = p_\perp/p_\parallel = \sqrt{2/(\gamma-1)}$ [21].

2.2.2 Plasma waves

The ponderomotive force produced by a laser pulse focused in an underdense plasma expels the plasma electrons from the centre of the laser beam. The space–charge perturbation induced by the focused laser will produce restoring forces that generate a plasma wave.

In this section, the excitation of the plasma by a linearly polarized Gaussian laser pulse, as described in Section 2.1.1, is discussed. An underdense, cold plasma (such that the motion induced by the electron temperature is smaller than the laser-induced

oscillations), that is fully-ionized before the interaction with the laser pulse is also assumed [25]. A more detailed analysis of the excitation of the plasma waves can be found in the literature [21, 23].

Linear regime

The analytical solution of the excited plasma wave can be obtained in the linear regime, where $a_0 < 1$ [23]. As the amplitude of the driven laser field is not very high, a small perturbation in the electron number density is assumed, $\delta n_e = n_e - n_{e0}$, where n_{e0} is the background electron density. The continuity equation $\partial n_e/\partial t + \nabla n_e \mathbf{v} = 0$ can be approximated to

$$\frac{1}{n_{e0}}\frac{\partial \delta n_e}{\partial t} + \nabla \mathbf{v} = 0.$$

Applying the time derivative, and using the Lorentz equation (Equation (2.5)) and Gauss's law (Equations (2.1)) to express $\partial \mathbf{v}/\partial t$, gives an expression for the density perturbation [28]:

$$\left(\frac{\partial^2}{\partial t^2} + \omega_p^2\right)\frac{\delta n_e}{n_{e0}} = c^2\nabla^2\left(\frac{a^2}{2}\right).$$

The perturbation of the electron number density corresponds to a forced oscillator, where the external force is given by the laser ponderomotive force. Figure 2.6(a) shows the density perturbation induced behind a Gaussian pulse with a peak ponderomotive force of $a_0 = 0.3$ and a background electron number density of $n_{e0} = 10^{19}$ cm^{-3}. The plasma wave formed has a wavelength of $\lambda_p = 2\pi/k_p = 2\pi c/\omega_p$.

The electric field associated with the plasma wave can be calculated from Poisson's equation for the normalized electrostatic potential:

$$\nabla^2\phi = \left(\frac{\omega_p^2}{c^2}\right)\frac{\delta n_e}{n_{e0}},$$

where $\mathbf{E} = -(m_e c^2/e)\nabla\phi$. For a Gaussian laser pulse, the general solution of the fields induced in the plasma wave after the laser has passed can be written [25, 28, 29]:

$$E_x(x, r_\rho, t) = \Upsilon a_0^2 E_{wb} \exp\left\{-\frac{2r_\rho^2}{w_0^2}\right\}\cos\left(k_p x - \omega_0 t\right),$$

$$E_r(x, r_\rho, t) = -4\Upsilon a_0^2 E_{wb}\frac{c r_\rho}{\omega_p w_0^2}\exp\left\{-\frac{2r_\rho^2}{w_0^2}\right\}\sin\left(k_p x - \omega_0 t\right),$$

where $\Upsilon = \omega_p\tau_p\sqrt{\pi}/(8\sqrt{\ln 2})\exp\{-\omega_p^2\tau_p^2/(16\ln 2)\}$, and

$$E_{wb} = \frac{m_e c\omega_p}{e} \tag{2.19}$$

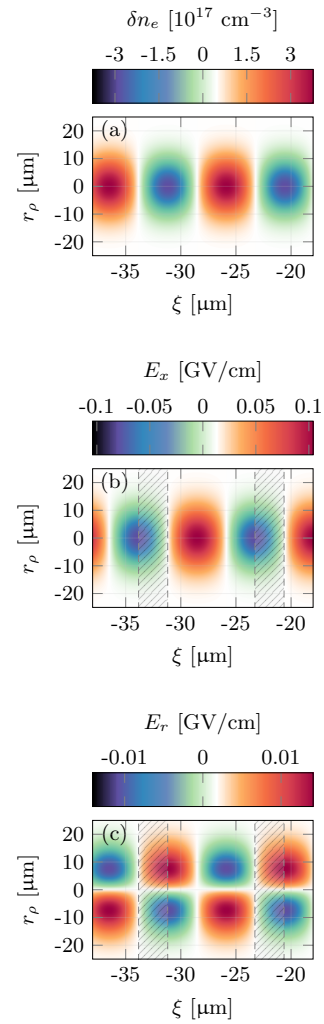

Figure 2.6. *(a) Density perturbation, (b) longitudinal electric field and (c) transverse electric field, induced by a Gaussian pulse with parameters $\lambda_0 = 800$ nm, $\tau_p = 13.2$ fs, $w_0 = 15$ µm, and an intensity corresponding to $a_0 = 0.3$, focused on an underdense plasma $n_{e0} = 10^{19}$ cm^{-3} in the linear regime.*

corresponds to the nonrelativistic wave-breaking field. These fields are illustrated for the studied case in Figure 2.6(b) and (c). Their strength is proportional to the square of the normalized vector potential of the laser a_0^2, but depends also on the laser pulse duration τ_p, as $\Upsilon \propto \tau_p \mathrm{e}^{-\omega_p^2\tau_p^2/(16\ln 2)}$. For a given laser intensity and electron number density, the pulse duration that maximizes the plasma fields is:

$$c\tau_{p,opt} = \frac{\sqrt{2\ln 2}}{\pi}\lambda_p \simeq 0.37\lambda_p. \tag{2.20}$$

This resonance condition optimizes the excitation of the plasma, as in this case the electrons experience two "kicks" from the ponderomotive force at the front and back of the laser pulse. The first kick is along the positive intensity gradient, and the second along the negative intensity gradient, while the electron is already pulled back by the restoring force. On the small scale of the plasma wavelength for the underdense plasmas used in the experiments described in this thesis, for example, $\lambda_p(n_e = 10^{18}\ \mathrm{cm}^{-3}) \simeq 30\ \mu\mathrm{m}$, the resonance condition is fulfilled only by ultra-short laser pulses $\tau_{p,opt}(n_e = 10^{18}\ \mathrm{cm}^{-3}) \simeq 40$ fs.

The longitudinal field is a maximum along the laser propagation axis, while the radial field is zero. The longitudinal field exhibits regions of electron acceleration (blue in Figure 2.6(b)) and deceleration (red), while the transverse field exhibits regions where the electrons are focused (red for $r_\rho > 0$ and blue for $r_\rho < 0$ in Figure 2.6(c)) and defocused (red for $r_\rho < 0$ and blue for $r_\rho > 0$). The longitudinal and transverse fields are dephased with respect to each other by $\pi/2$, which defines a periodical region of axial length $\lambda_p/4$, indicated by the hatched area, where an off-axis electron is simultaneously accelerated in the laser propagation direction and radially focused. It is in this region that the plasma wave supports collimated accelerated electrons.

Nonlinear regime

When the laser pulse induces a plasma wave such that the plasma electric field approaches the linear wave-breaking limit, E_{wb}, the electron number density perturbation can no longer be considered small. A complete description of the 3D nonlinear regime requires in most cases heavy numerical calculations. However, the analytical solution of a 1D approximation illustrates much of the relevant physics in nonlinear plasma excitation. For the analytical study, a nonevolving laser pulse is considered, which can be expressed by the laser co-propagating coordinate, $\xi = x - v_p t \simeq x - v_g t$, and a large enough laser spot size, $k_p w_0 \gg 1$. In the quasi-static approximation $\partial/\partial t \simeq -c\partial/\partial\xi$, Poisson's equation

$$k_p^{-2}\frac{\partial^2\phi}{\partial\xi^2} = \left(\frac{n_e}{n_{e0}} - 1\right) \tag{2.21}$$

can be written as the differential equation [30, 31]:

$$k_p^{-2}\frac{\partial^2\phi}{\partial\xi^2} = \gamma_p^2\left[\beta_p\left(1-\frac{\left(1+a^2\right)}{\gamma_p^2\left(1+\phi\right)^2}\right)^{-1/2}-1\right],$$

where $\beta_p = v_p/c$ and $\gamma_p = 1/\sqrt{1-\beta_p^2}$. Solving this second order differential equation allows the longitudinal electric field to be obtained from $E_x = -E_{wb}\partial\phi/\partial\xi$, while the density perturbation can be calculated from Equation (2.21).

Figure 2.7 shows the longitudinal electric field and modulation of the electron number density excited by a temporal and spatial Gaussian pulse in a plasma with $n_{e0} = 10^{19}$ cm^{-3} for the 1D nonlinear approximation, for (a) $a_0 = 1$ and (b) $a_0 = 3$. In both cases the pulse satisfies the matching condition with the plasma wavelength, $\tau_{p,opt} \simeq 13$ fs. Some important observations can be made in this figure. As the intensity of the laser increases, the electron charge collects in a narrower region of space, and the peak electron number density increases. Between these peaks, the electron number density is almost zero, so the induced longitudinal electric field no longer has a sinusoidal shape, but a sawtooth shape instead, the slope of which steepens with the increasing laser intensity. The maximum electric field also increases noticeably with the laser normalized vector potential, being almost five times higher for $a_0 = 3$ than for $a_0 = 1$. As an effect of the relativistic mass acquired by the electrons excited by such an intense field, the electron number density peaks become more separated as a_0 increases, effectively increasing the plasma wavelength.

The resonant condition described in Equation (2.20) still applies in the nonlinear regime. To illustrate the effect of the pulse length, Figure 2.7(c) presents the same case as in (b), but for a longer pulse duration, $\tau_p = 35$ fs. Despite the fact that the laser intensity is the same as in (b), and thus the pulse carries more energy, the density perturbation and maximum longitudinal electric field decrease as the energy transfer from the ponderomotive force is less efficient.

In order to obtain a 3D description of the nonlinear regime, numerical models are required. The transverse distribution of the electron perturbation has other effects. The nonlinear interaction of the laser pulse and the plasma, which depends strongly on the laser intensity, leads, for example, to focusing and dispersion of the laser pulse, as will be discussed in Section 2.2.5. Due to such nonlinear effects in the propagation of the laser in the plasma, a laser pulse with a duration that does not satisfy Equation (2.20) can be temporally compressed and transversally focused to a quasi-matched condition. For this reason, the resonant condition is less critical in practice than in the linear case, and the acceleration is found to be optimum as long as the laser pulse duration satisfies $c\tau_p \lesssim \lambda_p$. It is clear from the nonlinear 1D model that the transverse intensity

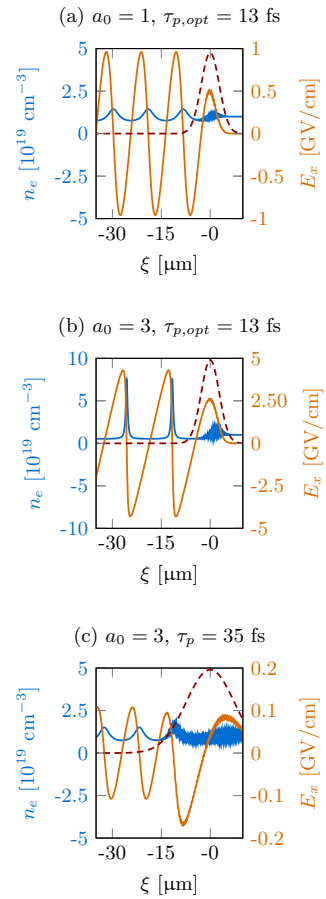

Figure 2.7. *Electron number density perturbation (blue) and longitudinal electric field (orange) under the 1D nonlinear regime approximation, induced in an underdense plasma with $n_{e0} = 10^{19}$ cm^{-3}, by a Gaussian pulse with $\lambda_0 = 800$ nm, for different laser pulse intensities and durations. The red dashed line represents the intensity envelope of the driving laser pulse.*

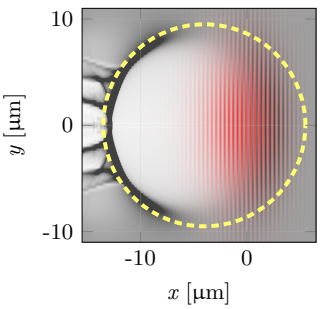

Figure 2.8. *Snapshot of a PIC simulation of a nonlinear plasma wake in the bubble regime. The black shading represents the electron number density, and the red shading the laser pulse intensity. A Gaussian pulse with* $\lambda_0 = 800$ *nm and* $a_0 = 4$ *induces the plasma wave in an underdense plasma with* $n_{e0} = 5 \times 10^{18}$ cm^{-3}. *The laser parameters satisfy the matched condition, with a beam waist of* $w_{opt} = 9.5$ μm *and a pulse duration of* $\tau_{opt} = 18.7$ *fs. The radius of the bubble satisfies* $r_b = w_{opt}$, *and is indicated by the yellow dashed line. Courtesy of H. Ekerfelt.*

distribution of the laser beam leads to a transverse variation in the nonlinear plasma wavelength, $\lambda_{pN}(r_\rho)$, creating a curved phase front of the plasma wave.

Bubble or blowout nonlinear regime

As the laser intensity increases and the peak normalized vector potential reaches $a_0 > 4$, the profile of the electron number density perturbation becomes steeper and steeper, to the point where the electrons are totally removed behind the laser pulse. This process is enhanced when the transverse and longitudinal dimensions of the laser agree with the plasma wavelength, Equation (2.20) and [32]:

$$k_p w_{opt} \equiv k_p r_b \simeq 2\sqrt{a_0}. \tag{2.22}$$

As the nonlinear plasma wavelength increases with the laser peak intensity, $\lambda_{pN} \simeq \lambda_p \sqrt{a_0}$, a higher laser intensity requires a larger laser spot size and duration to satisfy Equations (2.20) and (2.22).

Under this matching condition, and for very high peak normalized vector potentials, $a_0 > 4$, the electron void forms a spherical cavity behind the laser pulse with radius $r_b = w_{opt} = 2\sqrt{a_0}/k_p$, which can be considered as a plasma "bubble" in the background ions, where the electrons form a thin high-density sheath around the cavity [32–34]. For this reason, this regime of LWFA is known as the "bubble" or "blowout" regime. In fact, the electrons are blown out after the laser pulse even for $2 < a_0 \leq 4$, although the cavity does not attain a perfect spherical shape.

The fields induced in the bubble have ideal focusing and accelerating properties [33, 35, 36]. The longitudinal accelerating field is independent of the transverse position, r_ρ, which leads to uniform acceleration. The transverse fields pull the electrons towards the propagation axis, collimating the electron beam. The electrons accelerated in this regime have good properties, such as high energy, low energy spread and low divergence. Figure 2.8 shows a snapshot of a particle-in-cell (PIC) numerical simulation, performed with the code CALDER-Circ [37] (see Section 3.4), of a plasma wave in the bubble regime, with a peak normalized vector potential of $a_0 = 4$, a plasma density of 5×10^{18} cm^{-3}, and satisfying the matched conditions. The bubble has an spherical shape with a radius of $r_b = w_{opt} = 9.5$ μm, highlighted by the yellow dashed line.

2.2.3 Electron acceleration in a plasma wave

When a plasma electron acquires sufficient velocity to escape the plasma fluid oscillations that form the wave, and copropagate with the plasma wake, it is said to be "trapped". The electron can be trapped by different mechanisms, which will be discussed in Section 2.2.4. Here, the acceleration experienced by the electron once it is trapped in the bubble is considered.

As an illustration of the acceleration process of an electron in a laser-wakefield accelerator, the motion of a test electron in the nonlinear 1D plasma wake model introduced in Section 2.2.2 can be studied using Hamiltonian dynamics. The position and longitudinal momentum of the electron in the wake evolve as described by the following set of equations [38]:

$$\frac{\mathrm{d}\xi}{\mathrm{d}x} = 1 - \frac{\beta_p}{u_x},$$
$$\frac{\mathrm{d}\gamma}{\mathrm{d}x} = \frac{\partial\phi(\xi)}{\partial\xi},$$

where $u_x = p_x/m_e c = \gamma v/c = \gamma\beta$ is the normalized electron longitudinal momentum, $\beta_p = v_p/c$ is the normalized plasma wave phase velocity, and $\gamma = (1-u_x^2)^{-1/2}$. The set of equations can be expressed as a derivative of time $\mathrm{d}\xi/\mathrm{d}x = (1/v)\mathrm{d}\xi/\mathrm{d}t$ and $\mathrm{d}\gamma/\mathrm{d}x = \partial\gamma/\partial\xi + (1/c)\mathrm{d}u_x/\mathrm{d}t$, and the Hamiltonian $\mathcal{H}$ is constructed as a constant of motion:

$$\frac{\mathrm{d}\xi}{\mathrm{d}t} = c\frac{u_x - \beta_p}{\sqrt{1-u_x^2}} = \frac{\partial\mathcal{H}}{\partial u_x},$$
$$\frac{\mathrm{d}u_x}{\mathrm{d}t} = c\left[\frac{\partial\phi(\xi)}{\partial\xi} - \frac{\partial\gamma}{\partial\xi}\right] = -\frac{\partial\mathcal{H}}{\partial\xi},$$

with the form

$$\mathcal{H}(\xi, u_x) = c\left[\sqrt{1+u_x^2} - \beta_p u_x - \phi(\xi)\right] \equiv c\mathcal{H}_c.$$

The trajectories of the electron in the phase space $(\xi, u_x(\xi))$ can be calculated for each orbit defined for the constant of motion $\mathcal{H}_c$. The electron momentum in the electrostatic potential of the plasma wave is calculated from [38]:

$$u_x(\xi) = \beta_p\gamma_p^2(\mathcal{H}_c + \phi(\xi)) \pm \gamma_p\sqrt{\gamma_p^2\left(\mathcal{H}_c + \phi(\xi)\right)^2 - 1}. \qquad (2.23)$$

Figure 2.9(b) shows the electron phase space trajectories defined by Equation (2.23) for different values of $\mathcal{H}_c$, in the electrostatic potential excited by a laser pulse, with the parameters of the wakefield shown in Figure 2.7(b). Electrons initially at rest and in front of the laser pulse perform the plasma fluid oscillations, u_{fluid}, that form the wave (black line at the bottom) and are not trapped in the plasma wave. Electrons without sufficient initial momentum or with too high velocity are not trapped either.

Trapped electrons perform closed orbits inside the wake, represented by the orange lines in Figure 2.9. The electrons periodically gain and lose momentum from the plasma wave, moving forwards and backwards with respect to the copropagating frame of the laser pulse. The total energy gained by a single electron is given by the difference in longitudinal momentum at the moment the electron

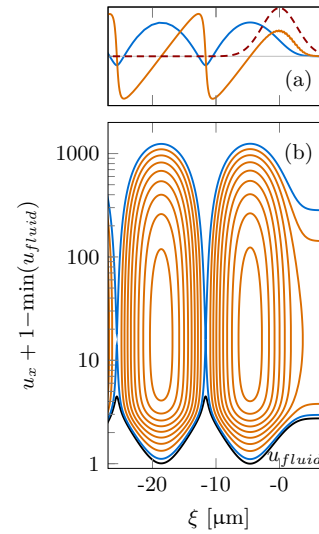

Figure 2.9. *(a) Electrostatic potential (blue) and longitudinal electric field (orange) under the 1D nonlinear regime approximation, induced in an underdense plasma with $n_{e0} = 10^{19}$ cm^{-3} by a Gaussian pulse with $\lambda_0 = 800$ nm, $a_0 = 3$ and $\tau_{p,opt} = 13$. The red dashed line represents the intensity envelope of the laser pulse. (b) Phase-space electron trajectories in the plasma wake illustrated in (a) for different initial conditions.*

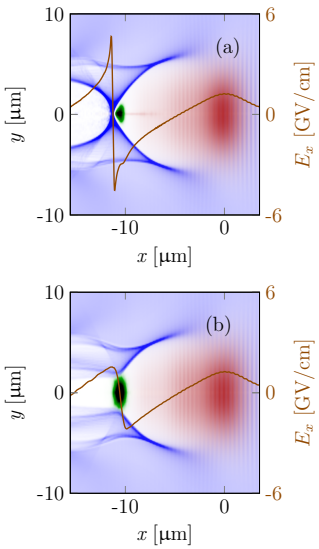

Figure 2.10. *Snapshots of a CALDER-Circ PIC simulation illustrating the effect of beam loading. The blue shading indicates the background electron number density, the red the laser pulse intensity, and the green the density of electrons trapped in the plasma wave. The brown line corresponds to the induced longitudinal field. Simulations were performed to study the experimental results presented in Paper V.*

exits the plasma wave with respect to the moment it is injected. For a given orbit, the gain is a maximum if the electron is injected at the lowest point of the orbit and extracted at the highest point. After reaching the highest point, the velocity of the electron exceeds the plasma wave velocity, and reaches the decelerating region of the bubble, i.e. it dephases, reducing its energy and velocity until it falls once more into the accelerating region.

The so-called separatrix, represented by the blue line in Figure 2.9, corresponds to the boundary that divides the orbits of the trapped and untrapped electrons. This orbit can be calculated by considering the radicand in Equation (2.23) equals zero, or $\gamma_p^2(\mathcal{H}_{c,sep} + \phi_{min}(\xi))^2 = 1$. Electrons trapped in this orbit can achieve the maximum energy gain from the wake. The distance the electrons are accelerated to gain the maximum energy is known as the dephasing length. In the linear case, this distance depends on the plasma wavelength, but not on the laser intensity, $L_d = (n_c/n_e)\lambda_p$, while in the 3D bubble regime it increases with the laser peak intensity and is given by [32]:

$$L_{dN} = \frac{4c\sqrt{a_0}}{3}\frac{\omega_0^2}{\omega_p^3}.$$

The maximum energy gain that can be extracted from the plasma wave, $\Delta\varepsilon_N$, is limited by this distance, and in the bubble regime it is approximately [32]:

$$\Delta\varepsilon_N = \frac{2}{3}m_e c^2 \frac{\omega_0^2}{\omega_p^2} a_0.$$

For a given laser-wakefield accelerator, the maximum dephasing length and energy limit benefit from a higher laser intensity, but much more from a lower plasma density. This is because the plasma wave velocity, given by the laser group velocity in Equation (2.16), increases as n_e decreases. A faster plasma wave allows the electron to be accelerated to a higher energy, over a longer distance, before experiencing dephasing.

The excitation of the plasma wave requires energy transfer from the laser pulse. As a result of the work exerted by the ponderomotive force, the laser pulse continuously loses energy, or depletes, on its leading edge, up to the point where it can no longer excite a plasma wave. This limit defines a pump depletion length, which in the 3D model can be estimated as [32]:

$$L_{pdN} \simeq c\tau_p \frac{\omega_0^2}{\omega_p^2}.$$

The electric fields induced by the charge trapped in the plasma wake will also affect the acceleration of the electrons [39]. The trapped electrons can drive their own plasma wake, which perturbs

the wake driven by the laser. This effect is known as beam loading, and has a strong impact on the quality of high-charge accelerated electrons. Snapshots of PIC simulations of loaded plasma waves, as part of the study presented in Paper V, are shown in Figure 2.10. They illustrate the effect that the amount of trapped charge can have on the accelerating field. When a noticeable electric charge is locally trapped in the plasma wake, the longitudinal electric field (brown line) is perturbed. Depending on the amount of charge, this can lead to a flattened longitudinal field, see Figure 2.10 (a), or to a change in the sign of the slope of the electric field which, in its limit, can ultimately cancel out the laser wakefield and drive its own wake, see Figure 2.10 (b). Note that in the latter case, electrons in the back of the electron bunch are decelerated by the electric field. Flattened accelerating fields as in (a) might be desirable to reduce the energy spread of the accelerated electrons, as the accelerating field becomes constant along the whole longitudinal length of the electron beam, producing quasi-monoenergetic electrons [39]. However, beam loading leads to a limit on the current of the accelerated electrons [40].

2.2.4 Electron trapping in a plasma wave

As discussed in the previous section, only electrons with enough initial energy will leave the fluid oscillations that form the plasma wave and become trapped in the plasma wave potential. Moreover, electrons must be trapped in the appropriate region of the plasma wave in order to gain the maximum energy from it while remaining collimated. Electron trapping can be triggered by several mechanisms that influence the final charge, duration, energy spread and divergence of the electron beam.

As discussed in Section 2.2.2, under matched conditions the plasma waves are highly nonlinear and the induced electric field reaches a very high amplitude. In the wave-breaking limit, the induced electron density modulation is such that electrons following the fluid oscillations become faster than the plasma wave. They can then no longer form background electrons, but can be trapped in the plasma wave, a process known as self-trapping. In the nonlinear regime, the wave-breaking limit, given in Equation (2.19), is corrected by the plasma relativistic factor, $\gamma_p = \left(1 - v_p^2/c^2\right)^{-1/2}$ [38]:

$$E_{wbN} = \sqrt{2(\gamma_p - 1)} E_{wb}.$$

As it is induced by the highly nonlinear instabilities of the plasma wave, self-trapping leads to low reproducibility and poor control of the electron parameters. However, other trapping mechanisms can be employed, leading to a degree of control of the features of the electron beam. Some of the controlled trapping mechanisms related to the studies presented in this thesis will be briefly described

here, although they represent only a few of the alternatives that are currently being explored [41].

The reproducibility of the electron beam parameters can be improved by a more stable trapping mechanism, such as ionization-induced trapping. In ionization-induced trapping, the plasma is produced in a mixture of a low-Z gas with a small percentage of a high-Z gas dopant [42, 43]. The high-Z gas is chosen such that one or more of its ions has an appearance intensity equal to, or greater than, the peak intensity of the laser pulse in vacuum. Due to the nonlinear processes of self-focusing and self-compression, described in Section 2.2.5, the peak intensity of the laser pulse can increase along its propagation in the plasma. As a result, electrons are released from the dopant molecules at the peak of the laser pulse, once the plasma wave is fully formed, and become more easily trapped in the first plasma bubble. Ionization-induced trapping is characterized by high-charge electron beams and, typically, a continuous spectrum, due to the continuous trapping of electrons during laser propagation.

Low-Z gases typically used for ionization-induced trapping are hydrogen and helium, due to their low appearance intensity, and they are often mixed with dopants such as nitrogen, argon or oxygen. Nitrogen was the dopant used for ionization-induced trapping described in Papers I-III, V-VIII and X, and a comparison with argon as dopant is included in Paper VII. Considering a typical peak intensity in the focus of around 3×10^{18} W/cm^2 in the experiments performed during those studies, the leading part of the laser pulse is not able to release the inner K shell electrons of nitrogen by OTBI, because the appearance intensity for those ions is of the order of, or above, the peak intensity of the driven laser pulse, as can be seen from Table 2.1. These electrons are released at the peak of the laser pulse and become trapped in the plasma wave.

It is noteworthy that very tight focusing of the laser beam can localize ionization-induced trapping in the plasma wave along a short pulse propagation. This mechanism is known as self-truncated ionization-induced trapping, and can produce electron beams with a low energy spread [44].

Some applications for relativistic electron beams might demand a narrow energy spread, which can be achieved by localizing the trapping of electrons in the plasma wave. A density transition in the plasma can be used to confine the electron trapping [45, 46]. As the plasma wavelength is inversely proportional to the square root of the electron number density, the bubble will expand when the laser propagates through a density down-ramp. The local phase velocity of the plasma wave at the back of the bubble can also be slowed down, so electrons may break away from the plasma wave and become trapped. Paper IV presents a numerical study of the tunability of the accelerated electron parameters by modifying the length and slope of an electron density down-ramp. Down-ramp

trapping was also experimentally studied with a 3D-printed two-stage gas cell [47] (see Paper IX). Trapping in a density down-ramp can also be combined with ionization-induced trapping, an effect that was observed, and is described in Paper III.

Once the electrons are trapped in the plasma wave, the dephasing and depletion lengths limit the maximum energy that the electrons can gain. To overcome this problem, multi-stage wakefield accelerators have been proposed [48–52]. For multi-staging to work, the external electron beam must be located at the correct position in the plasma wave. External injection thus requires very short electron bunch duration, much shorter than the plasma period, and precise transverse localization of the electrons in the plasma wave. LWFA produces very short electron bunches that are suitable for multi-staging acceleration. The mechanism also facilitates the synchronization of the electron beam and the driving laser of the plasma wave. This motivated the study on the stability of the pointing of the electron beam presented in Paper I.

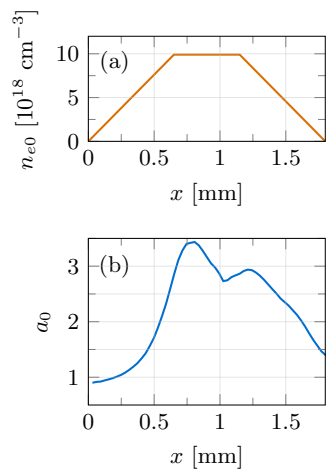

Figure 2.11. *Evolution of the normalized vector potential obtained from a PIC simulation with the code CALDER-Circ. (a) Background electron number density, with two 650 µm density ramps and a 500 µm plateau with density 10^{19} cm^{-3}. (b) Evolution of the normalized vector potential along the direction of plasma wave propagation due to the nonlinear propagation of the laser pulse with initial $a_0 = 0.9$. The normalized vector potential reaches a maximum after approximately 800 µm of propagation, with a value of 3.45.*

2.2.5 Nonlinear laser propagation in a plasma

In the quasi-static approximation, the laser pulse does not evolve while propagating in the plasma. However, even within the Rayleigh range of the focused laser, nonlinear effects will disturb the evolution of the high-intensity pulse.

The ponderomotive force that expels electrons in front of the laser pulse, and the relativistic mass increase in the electrons due to their quiver velocity, produce variations in the electron density and energy that lead to a non-uniform radial profile of the refractive index $\eta_r(r_\rho)$. From Equation (2.16), the refractive index is simply $\eta_r(r_\rho) \simeq c/v_{ph} = (1 - \omega_p^2/\omega_0^2)^{1/2}$. However, as the plasma wave becomes relativistic, the plasma frequency is influenced by the relativistic factor and becomes $\omega_p^2 \to \omega_p^2/\gamma$. In a weakly relativistic regime, $a^2 \ll 1$, and for no preformed density channel, the nonlinear refractive index can be approximated to [53]:

$$\begin{aligned}\eta_r(x, r_\rho) &= 1 - \frac{\omega_p^2}{2\omega_0^2}\frac{n_e(x, r_\rho)}{n_{e0}\gamma(x, r_\rho)} \\ &\simeq 1 - \frac{\omega_p^2}{2\omega_0^2}\left[1 - \frac{a^2(x, r_\rho)}{2} + \frac{\delta n_e(x, r_\rho)}{n_{e0}}\right].\end{aligned} \tag{2.24}$$

The term $-a^2(x, r_\rho)/2$ represents the relativistic optical guiding, or self-focusing, of the laser pulse [54, 55]. It can be seen from Equation (2.24) that the refractive index of the plasma is higher in the regions of higher intensity, or towards the axis for a Gaussian intensity distribution. The modulation of η_r hence focuses the beam towards the propagation axis. This effect can exceed the intrinsic diffraction of the laser or compensate for it, allowing stable propagation along several Rayleigh lengths. Self-focusing will occur

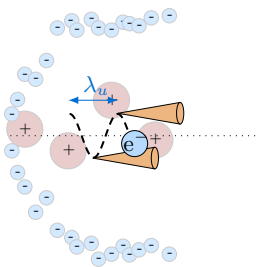

Figure 2.12. *Illustration of the betatron radiation produced in a laser-wakefield accelerator. The electron inside the ion channel in the bubble performs transverse betatron oscillations, represented by the dashed black line, leading to the forward emission of betatron X-rays (orange cones).*

when the laser power exceeds a critical limit, known as the critical power for relativistic self-focusing, and given by [56, 57]:

$$P_c = \frac{8\pi\epsilon_0 m_e^2 c^5}{e^2}\frac{\omega_0^2}{\omega_p^2}. \tag{2.25}$$

For example, the critical power for relativistic self-focusing of a 800 nm laser, for an electron number density of 10^{19} cm^{-3}, is $P_c = 3$ TW.

Equation (2.24) also accounts for the longitudinal variations in the plasma density and laser intensity. As $v_g \simeq c\eta_r$, different parts of the laser pulse might experience different group velocities along the propagation axis. The front of the pulse, where electrons accumulate due to the forward push of the ponderomotive force, travels slower than the tail of the pulse, where there is a lack of electrons. While this variation in the group velocity compresses the pulse, variations in the phase velocity lead to local longitudinal frequency shifts that broaden the laser spectrum. The laser pulse is shortened longitudinally, or self-compressed [58].

A weakly relativistic laser pulse, with $a \simeq 1$, such that its peak power is above the limit for relativistic self-focusing, will eventually shrink transversally and longitudinally due to self-focusing and self-compression in the plasma. If the energy in the pulse is sufficient and propagation in the underdense plasma long enough, a non-matched laser pulse can evolve to the matched condition, producing a plasma wave in the bubble regime.

Many other nonlinear effects take place during the complex propagation of an intense laser pulse in a plasma. The ponderomotive force produces a higher electron density in front of the pulse, which defocuses the front of the laser. In contrast, the back of the pulse encounters a lack of electrons, which guides the laser pulse and can help to self-focus pulses below the critical power limit [59]. The pump depletion mentioned in Section 2.2.3 eventually lowers the local intensity of the pulse, which affects all the above-mentioned effects. Finally, as the refractive index depends directly on the plasma density, the leading part of the laser pulse can experience ionization defocusing during the ionization of the medium.

2.3 Betatron X-ray generation

The plasma channel generated in a laser-wakefield accelerator produces focusing forces that induce transverse oscillations in the accelerated electrons in a way similar to that of an undulator in a synchrotron facility. The electron undulations represented in Figure 2.12 generate X-ray photons in the keV regime with a characteristic broad spectral shape and small divergence, known as synchrotron radiation. The synchrotron radiation emitted by electrons in a laser-wakefield accelerator was proposed [15] and demonstrated [16]

simultaneously, shortly before the first high-quality electron beams were produced by LWFA. While an array of magnets produces the electron oscillation in an undulator, transverse electric fields produce the forces that induce electron oscillations during LWFA in a plasma. The wavelength of the electron oscillations induced in the plasma channel can be thousand times shorter than the oscillations that electrons perform in manufactured undulators, of a few hundred µm instead of tens of mm. This significantly increases the efficiency of the X-ray emission, as will be discussed below. As already mentioned, the radiation emitted by the electrons oscillating in a plasma channel is known as betatron X-rays.

The principle of betatron oscillations and the main features of the emitted X-rays are described in this section.

2.3.1 Betatron oscillations in an ion channel

The electron orbits in the plasma channel can be approximated by the phenomenological description used in Section 2.2 [32]. In the bubble regime, a spherical void of electrons, or an ion cavity, with radius r_b is considered behind the laser pulse. The transverse force affecting the electrons is mainly due to the electrostatic transverse field produced by the ion cavity, as space charge effects within the electron bunch are negligible in the relativistic regime [15].

Considering the cylindrical radial coordinate r_ρ, for $r_\rho < r_b$, the transverse field can be approximated, using Gauss's law, to:

$$E_r = \frac{en_e}{\epsilon_0}\frac{r_\rho}{2}.$$

If the transverse momentum can be considered to be small in comparison to the longitudinal momentum, such that $\gamma \simeq \gamma_x \gg \gamma_y, \gamma_z$, the transverse motion of a test electron in this field can be expressed using Equation (2.5), and has the form:

$$\frac{\mathrm{d}^2 r_\rho}{\mathrm{d}t^2} = -\frac{e^2 n_e}{2m_e\gamma\epsilon_0} r_\rho = -\frac{\omega_p^2}{2\gamma} r_\rho \equiv -\omega_\beta^2 r_\rho. \tag{2.26}$$

The electron moves in the transverse plane as in a harmonic oscillator, with a betatron frequency, ω_β that corresponds to the plasma frequency corrected by the electron relativistic factor $\omega_\beta = \omega_p/\sqrt{2\gamma}$. Trajectories calculated from Equation (2.26) for different initial conditions (y_0, p_{y0}), (z_0, p_{z0}) are shown in Figure 2.13.

It is common to characterize the oscillations by the undulator period, λ_u, and the strength parameter, K_β, given by:

$$\lambda_u = \frac{2\pi}{k_u} \equiv \sqrt{2\gamma}\lambda_p,$$
$$K_\beta = \frac{\omega_\beta r_\beta \gamma}{c}.$$

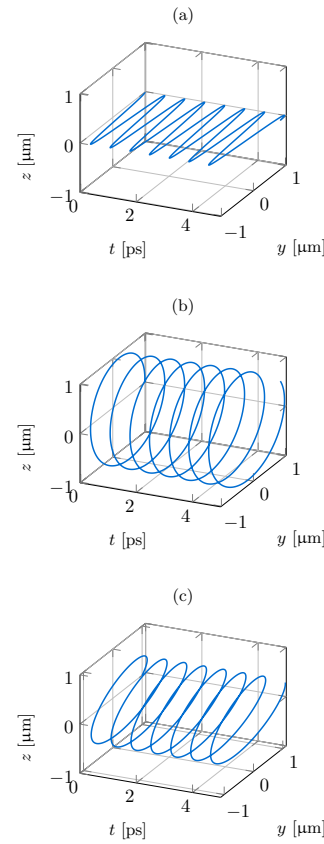

Figure 2.13. *Trajectories derived from Equation (2.26) for a $\gamma = 200$, $y_0 = 1$ µm test electron at different initial conditions: (a) $p_y = p_z = 0$, (b) $p_y = 0$, $p_z = 6m_e c$, and (c) $p_y = p_z = 3m_e c$.*

In the examples shown in Figure 2.13, these quantities correspond to $\lambda_u = 211$ µm and $K_\beta \simeq 6$. The trajectory in the longitudinal direction can be obtained by integrating the normalized velocity, β_x, obtained from $\beta_x^2 = \beta^2 - \beta_y^2 - \beta_z^2$.

2.3.2 Spectral emission of a betatron electron

The radiation spectrum can be qualitatively analysed by considering an electron oscillating only in the xy plane, $y(x) = K_\beta/k_u\gamma \sin(k_u x)$.

The averaged longitudinal normalized velocity can be approximated to [60]:

$$\langle\beta_x\rangle = \left\langle \beta\sqrt{1-\beta_y^2/\beta^2} \right\rangle \simeq \left\langle \beta\left[1 - \frac{K_\beta^2}{2\gamma^2}\cos^2(k_u x)\right]\right\rangle$$
$$\simeq 1 - \frac{1}{2\gamma^2}\left(1 + \frac{K_\beta^2}{2}\right).$$

As the electron oscillates, it emits identical radiation in each period of oscillation, λ_u. An observer located at an angle θ from the propagation direction will perceive the radiation to have a fundamental frequency of $\omega_f = 2\pi c/\lambda_f$ given by:

$$\lambda_f = \frac{\lambda_u}{\langle\beta_x\rangle} - \lambda_u\cos(\theta) \simeq \frac{\lambda_u}{2\gamma^2}\left(1 + \frac{K_\beta^2}{2} + \gamma^2\theta\right).$$

Two regimes are distinguishable from the strength parameter K_β. If the amplitude of the oscillations is small, such that $K_\beta \ll 1$, known as the undulator limit, the transverse motion will not affect the longitudinal velocity $\langle\beta_x\rangle \simeq \beta$ to any high degree, and the radiation will be peaked at the fundamental frequency $\omega_f(\theta)$ with a narrow bandwidth. Due to the relativistic motion of the accelerated charge, the emission is strongly directed in a narrow cone towards the electron propagation direction, with an opening angle $\Delta\theta = 1/\gamma$.

However, if $K_\beta \geq 1$, known as the wiggler limit, the decrease in the longitudinal velocity is no longer negligible. The observer then perceives a burst of short pulses, producing the emission of harmonics of the fundamental frequency. For $K_\beta \gg 1$, known as the asymptotic limit, the spectral emission is broad with many closely spaced frequency peaks, corresponding to the fundamental and the harmonics. The generated radiation extends out to approximately a critical frequency, ω_c, beyond which the radiation intensity decreases, given by [60, 61]:

$$E_c = \hbar\omega_c = \frac{3}{2}\frac{\omega_p^2 r_\beta \gamma^2 \hbar}{2c}. \tag{2.27}$$

The angular emission of the radiation widens to $\Delta\theta = K_\beta/\gamma$.

The radiation emitted by a relativistic electron within a spectral bandwidth $\mathrm{d}\omega$ and a solid angle $\mathrm{d}\Omega$, in the direction of observation $\mathbf{n}$, is obtained from the Liénard–Wiechert potential [62]

$$\frac{\mathrm{d}^2 I}{\mathrm{d}\omega \mathrm{d}\Omega} = \frac{e^2}{16\pi^3 \epsilon_0 c} \left| \int_{-\infty}^{+\infty} e^{i\omega[t - \mathbf{n}\mathbf{r}(t)/c]} \frac{\mathbf{n} \times [(\mathbf{n} - \boldsymbol{\beta}) \times \dot{\boldsymbol{\beta}}]}{(1 - \boldsymbol{\beta}\mathbf{n})^2} \mathrm{d}t \right|^2 . \tag{2.28}$$

In the asymptotic limit, the emitted radiation can be approximated to [61]:

$$\frac{\mathrm{d}^2 I}{\mathrm{d}\omega \mathrm{d}\Omega} = N_\beta \frac{6e^2}{\pi^2 c} \frac{\gamma_{x0}^2 \zeta^2}{(1 + \gamma_{x0}^2 \theta^2)} \left(\frac{\gamma_{x0}^2 \theta^2}{(1 + \gamma_{x0}^2 \theta^2)} \kappa_{1/3}^2(\zeta) + \kappa_{2/3}^2(\zeta) \right),$$

where $\zeta = (E/2E_c)(1 + \gamma_{x0}^2 \theta^2)$, γ_{x0}^2 is the electron relativistic factor in the longitudinal direction, $N_\beta = L/\lambda_u$ is the number of betatron periods along the acceleration length L, and $\kappa_{1/3}$ and $\kappa_{2/3}$ are the modified Bessel functions of the second kind. The spectral distribution is shown in Figure 2.14(a) for a critical energy of $E_c = 2$ keV. In the direction of electron propagation, $\theta = 0$, the radiation in the asymptotic limit becomes:

$$\left. \frac{\mathrm{d}^2 I}{\mathrm{d}\omega \mathrm{d}\Omega} \right|_{\theta=0} = N_\beta \frac{3e^2}{2\pi^2 c} \gamma_{x0}^2 \left(\frac{E}{E_c} \right)^2 \kappa_{2/3}^2 \left(\frac{E}{2E_c} \right), \tag{2.29}$$

The on-axis emitted spectrum follows the distribution $\gamma_{x0}^2 (E/E_c)^2 \kappa_{2/3}^2 (E/2E_c)$ defined only by the critical energy, shown in Figure 2.14(b) by the black line. Note that the photon energy scale is logarithmic. The value of the critical energy is indicated by the vertical dash-dotted line, which is close to the radiation peak. It can be observed that the radiation is quite well-collimated, as the radiation is practically zero for angles above $\theta = K_\beta/\gamma_{x,0} \simeq 30$ mrad. As the radiation becomes off-axis, the high-energy part of the spectrum is reduced, although the spectral distribution remains broad. This is not the case for the undulator limit, as the spectrum is narrow around the fundamental frequency, and the radiation spectrum depends strongly on the observation angle, $\omega_f(\theta)$. However, for most cases of LWFA, the strength parameter is $K_\beta \gg 1$, due to the high electron energy and typical betatron amplitudes of a few μm, and the emission typically corresponds to the wiggler regime.

The power radiated by a single oscillating electron can be calculated by including the electron orbits described above, using the relativistic Larmor formula $P_s = (2e^2/3c)\gamma^2[(\mathrm{d}\mathbf{u}/\mathrm{d}t)^2 - (\mathrm{d}\gamma/\mathrm{d}t)^2]$ [62]. For relativistic electrons with $\gamma_{x,0} \gg 1$, the power averaged over one betatron period gives [61]

$$\bar{P}_s \simeq \frac{r_e m_e}{3c} \gamma_{x,0}^2 \omega_\beta^4 r_\beta^2, \tag{2.30}$$

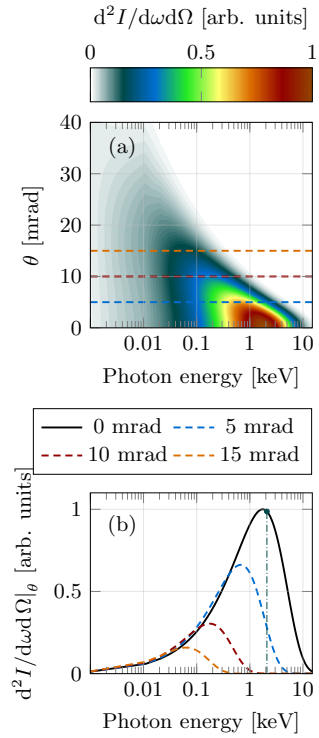

Figure 2.14. *Normalized radiation from an electron with relativistic factor of $\gamma = 200$ in the asymptotic limit: (a) as a function of the photon energy and the observation angle, and (b) at different angles with respect to the direction of electron propagation θ. The critical energy, $E_c = 2$ keV, is indicated by the vertical dash-dotted line.*

where $r_e = (1/4\pi\epsilon_0)(e^2/m_e c)$ is the classical electron radius. The total energy the electron radiates W_s is then the product of the average period power times the time the electron oscillates, $t_{osc} = N_\beta \lambda_\beta / c$, so

$$W_s = \frac{2\pi r_e m_e}{3c} N_\beta \gamma_{x,0}^4 \omega_\beta^3 r_\beta^2. \tag{2.31}$$

2.3.3 Betatron X-rays properties

As a second-order differential equation, the electron motion described in Equation (2.26) depends on the initial position and transverse momentum of the electron in the ion channel. Hence, in a laser-wakefield accelerator, each electron may oscillate with different betatron amplitudes, strength parameters and resonant frequencies.

The transverse size of the electron beam in the plasma thus modifies the spectral distribution. The radiation spectrum from the electron beam can be approximated by integrating the single-electron spectrum over an electron distribution over the beam radius. As a result, the transverse distribution of electrons smooths the single-electron spectrum, so the radiation spectrum is in general broad, even in the undulator regime.

Furthermore, if an electron gains energy in the plasma channel, for example by LWFA, the betatron parameters change $\omega_\beta(t) = \omega_p/\sqrt{2\gamma(t)}$, and the first-order solution of the electron trajectories can be written as [60]:

$$\begin{aligned} y(t) &= y_\beta(t)\cos\left(\int_0^{t'} \omega_\beta(t')\mathrm{d}t' + \phi_y\right), \\ z(t) &= z_\beta(t)\cos\left(\int_0^{t'} \omega_\beta(t')\mathrm{d}t' + \phi_z\right), \end{aligned} \tag{2.32}$$

where $y_\beta(t) = A_y/\gamma^{1/4}(t)$, $z_\beta(t) = A_z/\gamma^{1/4}(t)$ are the betatron amplitude of the oscillations, so $r_\beta(t) = \sqrt{y_\beta^2(t) + z_\beta^2(t)}$, and (A_y, ϕ_y), (A_z, ϕ_z) are constants derived from the initial conditions (y_0, p_{y0}), (z_0, p_{z0}). The transverse motion still follows sinusoidal oscillations, but with an amplitude and frequency that are now time-dependent through $\gamma(t)$.

The amplitude of the betatron oscillations, r_β, is gradually attenuated, while the betatron period, $2\pi/\omega_\beta$, increases as an effect of the electron's relativistic mass. The explicit shape of the radiation from electrons that are accelerated becomes more complex and, in general, will not correspond to a synchrotron-like spectrum. It can still be calculated from Equation (2.28) for any electron trajectories β, $\dot{\beta}$. However, the main contribution to the number of emitted photons comes from the most accelerated electrons [60].

The temporal distribution of the emitted radiation corresponds to the convolution between the temporal profiles of the electron

beam and the radiation of a single electron. As the wavelength of the electron radiation is typically in the X-ray range, i.e. much shorter than the μm length of the electron bunch, the pulse duration of the radiation can be approximated to the electron bunch duration. Despite the challenge of measuring the X-ray pulse duration, measurements of the electron bunch in a laser-wakefield accelerator [63] suggest that the X-ray pulses can be as short as a few fs. As will be discussed in Chapter 5, this makes betatron radiation very interesting for temporally-resolved X-ray studies of ultra-fast phenomena.

In the present chapter, the electrons have been considered to interact only with the field of the plasma wave. However, if the electrons are accelerated beyond the dephasing length, or if the laser pulse duration exceeds half the plasma wave period, the electron can also interact directly with the electromagnetic fields of the laser. If the electron's transverse motion is in resonance with the laser fields, the betatron oscillations can be enhanced, and the electron may be accelerated in the longitudinal direction. This effect of direct laser acceleration (DLA) will be discussed in Chapter 4 (see also Paper V).

Chapter 3

Experimental methods

As discussed in Chapter 1, LWFA requires state-of-the-art laser systems. The number of laboratories with high-intensity femtosecond lasers has continuously increased in the last two decades, and today LWFA is studied in a few tens of laboratories around the world. Such an advanced technology demands close control and monitoring of the system, since the laser performance has a considerable impact on the quality of LWFA research.

Diagnostics of the physics governing LWFA are very challenging, due to the short time scale of the process (the ps regime) and the small spatial scale (a few tens of μm in the transverse plane). As a result, precise analysis of the electron beam and betatron radiation parameters is required to retrieve information on the electron acceleration and X-ray emission processes. Computational tools are also necessary for the study of the laser–plasma interaction, to provide a better understanding of the experimental observations.

This chapter introduces the tools and methods used to perform the studies presented in this thesis. Section 3.1 describes all the experimental tools required for electron acceleration, including the laser system, the focusing optics and the gas target. Methods that allow studies of the properties of the electrons and betatron X-rays generated by the interaction of such laser pulses with a gas are explained in Sections 3.2 and 3.3, respectively. Section 3.4 introduces PIC simulations, and describes the code used for some of the simulations presented in this thesis.

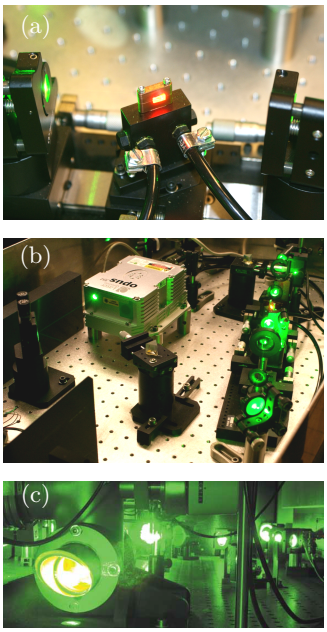

Figure 3.1. *Photographs showing different parts of the multi-terawatt laser system at the Lund high-power laser facility. (a) Ti:sapphire crystal in the oscillator. (b) View of the optical cavity that forms the oscillator. (c) View of the final amplifier.*

3.1 The laser and gas system

Electron acceleration by LWFA requires a high-intensity femtosecond laser pulse to be focused in a gas target. The tools and diagnostics used for producing the laser–plasma interaction are described in this section.

3.1.1 The Lund multi-terawatt laser system

The multi-terawatt laser system at the Lund high-power laser facility was established in 1992 [64]. Today, and after several upgrades, the laser is able to deliver an energy of more than 1 J in pulses as short as 35 fs on target, corresponding to a peak power above 30 TW. All the experimental studies described in this thesis, apart from those in Papers VI and IX, were conducted with the Lund multi-terawatt laser which is described below.

A scheme of the Lund multi-terawatt laser after its latest update is shown in Figure 3.2. It is based on CPA technology, and comprises an oscillator, a stretcher, several amplification stages and a compressor (see Section 1.1). The oscillator (a) consists of a Ti:sapphire crystal enclosed in an optical cavity based on Kerr lens mode locking [65], which has an average power output of about 320 mW. It lases at a high repetition rate, 80 MHz, with an energy of about 4 nJ per pulse, and has a bandwidth greater than 50 nm FWHM centred at 800 nm. The light is linearly polarized. Prisms in the oscillator compensate the group velocity dispersion in the cavity, so the output pulse duration is close to the FTL of 20 fs. The pulse repetition rate is decreased to 10 Hz by a pulse picker, consisting of a Pockels cell (an electro-optic crystal) and a pair of polarizers. The pulse picker sends one pulse every 100 ms to the following laser stages by modifying the polarization of the laser pulses. In order to improve the contrast of the system, i.e. the intensity ratio between the pedestal and the peak of the laser pulse, a 6-pass pre-amplifier (b), pumped by a frequency-doubled Nd:YAG laser, increases the energy per pulse from a few nJ to the μJ regime [66]. This pre-amplification of the pulse means that less gain is required in the following regenerative amplification stage, described below, which results in less background amplified spontaneous emission (ASE).

A grating stretcher (c) elongates the pulse duration to 9 ps/nm bandwidth after two passes, decreasing the pulse peak intensity by more than a factor of 22500. After the stretcher, the pulse duration decreases from 450 to about 300 ps, due to gain narrowing in the different amplification stages.

As the energy per pulse increases, the beam is expanded to larger diameters in order to ensure that the peak intensity is below the damage threshold of the optical elements in the laser. All the amplifiers in the system use Ti:sapphire crystals of different sizes, pumped by frequency-doubled Nd:YAG lasers at 532 nm. A pair of

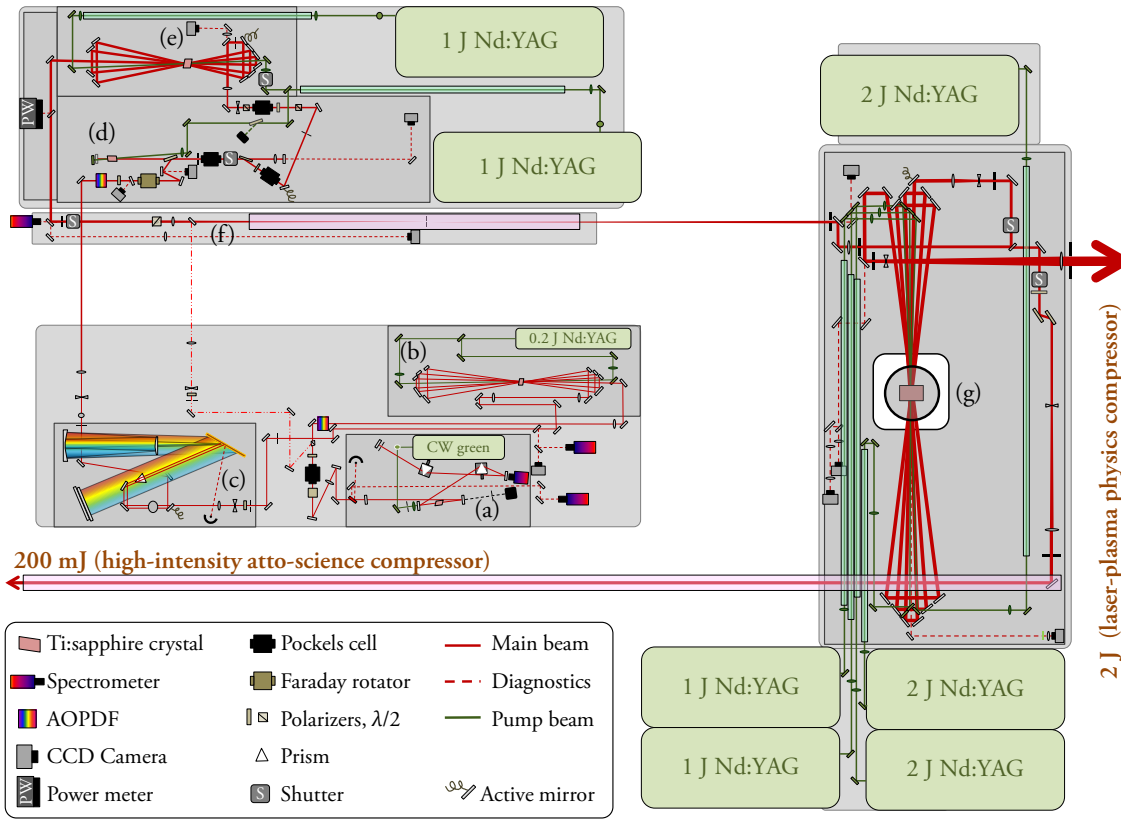

Figure 3.2. *Schematic of the Lund multi-terawatt Ti:sapphire laser based on CPA. The 2 J output is first sent to the optical compressor and then to the experiment.*

relay lenses image the output of each pump laser onto the amplification crystals, in order to maintain a homogeneity in the distribution of the pump intensity. The pulses are constantly monitored using various diagnostic tools such as spectrometers, CCD cameras and power meters. Furthermore, several active-feedback stabilization mirrors maintain the alignment of the laser chain.

Once stretched, the pulses are captured by a Pockels cell and two polarizers inside the cavity of a regenerative amplifier (d). After approximately 15 round-trips, and an increase in pulse energy from a few μJ to about 5 mJ, the pulses are released from the cavity. Two Pockels cells are used to clean up the pulses. These act as a polarization gate which is opened for only a few ns, to minimize the ASE or pre-pulses that can be produced in the regenerative cavity. A 5-pass amplifier (e) then increases the laser energy to more than

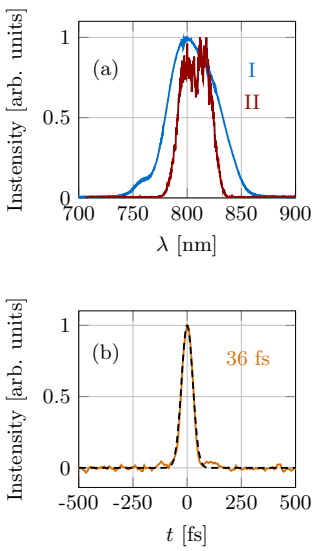

Figure 3.3. *(a) Spectra of the laser at different locations in the system: (I) oscillator output and (II) regenerative amplifier output. (b) Intensity autocorrelator signal (orange), and a fit (dashed black line) corresponding to a pulse duration of 36 fs.*

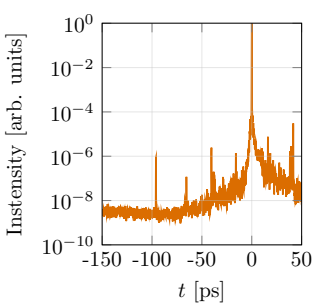

Figure 3.4. *Signal from the third-order autocorrelator, when measuring a temporal contrast below 5×10^{-9} at 100 ps before the main pulse. Some of the observed peaks are artefacts generated in the autocorrelator.*

400 mJ per pulse.

The laser pulse is then spatially filtered by focusing the beam and allowing it to pass through a 450 µm pinhole (f) in the focal plane. The spatial distribution becomes almost Gaussian by means of losing about 25% of the energy in the spatial filter. 200 mJ are split from the main beam (which is sent to another experiment), while the remaining beam with an energy of 100 mJ is sent to the final amplifier (g). The crystal in the final amplifier is cooled down to -180℃ in a cryostat in order to minimize thermal lensing effects in the crystal volume. During 6 passes, the energy of the pulses can be amplified to more than 2 J, although the experiments presented in this work were usually performed with a pre-compressor energy between 1.5 and 1.7 J.

Gain narrowing is partially compensated for by two acousto-optic programmable dispersive filters (AOPDF) that shape the spectral phase and amplitude of the pulses [67]. One is located directly after the oscillator, to homogenize the spectrum before the pre-amplifier. The second is located at the entrance of the regenerative amplifier to pre-compensate for gain narrowing. However, the output bandwidth unavoidably decreases to about 35 nm, as shown in Figure 3.3(a). The pulses, expanded to final diameters between 50 and 60 mm, are directed to a grating compressor, set to achieve pulses close to the FTL, between 35 and 40 fs. The pulse duration is measured by sending a low-power, compressed beam to a second-order intensity autocorrelator, where the signal is fitted and the FWHM determined, as shown in Figure 3.3(b).

The temporal contrast of the pulse is characterized by sending low-power pulses to a third-order autocorrelator [68]. It is necessary for the pulse pre-pedestal to have a low-intensity, and for the peak intensity to have a steep ramp, to guarantee a "clean" interaction between the target and the laser pulse, which is of great importance specially in the case of solid targets. A measurement of the temporal contrast is shown in Figure 3.4.

3.1.2 Laser focusing

When the pulses are fully compressed, their peak intensity is too high for propagation in air without causing nonlinear effects. For this reason, the compressor, the experimental chamber and beam transport between them are kept under vacuum, below 10^{-4} mbar.

In order to improve the focusing of the laser beam, a 32-actuator deformable mirror (DM) is placed at the output of the optical compressor. The pulses are then transported to the experimental chamber where a f/7.5 off-axis parabola (OAP) with a 775 mm focal length, focuses the beam to a FWHM spot size between 13 and 17 µm, depending on the beam size at the OAP. After the OAP, the focus of the laser pulse, when fully amplified, but attenuated before compression, can be sent to a wavefront sensor (Phasics SID4) loc-

ated outside the experimental chamber. The sensor software feedbacks to control the DM actuators during measurements of the laser pulse wavefront, in a loop that optimizes the laser beam focus.

The spare pulses from the laser system pulse picker, i.e. nJ pulses with MHz repetition rate, can be sent collinearly with the high-energy pulse and used to improve the pointing stability of the system. A leak of these pulses before the OAP is focused and imaged onto a CCD camera between each full-power pulse. The transverse position of the focused leak is used to control the response of a piezo-actuated mirror before the compressor. This method was used in the studies described in Papers I-III, V and VII.

The peak intensity and beam size of the focus are estimated by measuring the transmission from the entrance of the compressor to the OAP output with the laser attenuated, together with an image of the beam at the focal plane. Figure 3.6 shows the 13.2 μm FWHM focus registered during the experiment described in Paper X, where the FWHM diameter is indicated by the black dashed line. In this example, the peak intensity of the pulse was estimated to be 3.6×10^{18} W/cm^2, which corresponds to a normalized vector potential of $a_0 = 1.3$. Despite the beam aberrations producing wings around the focus, which could not be completely corrected with the DM, 75% of the beam energy is confined within the corresponding beam waist, $2w = 22.4$ μm (orange dashed line). This can be compared with approximately 86.5% in the case of a perfect Gaussian beam.

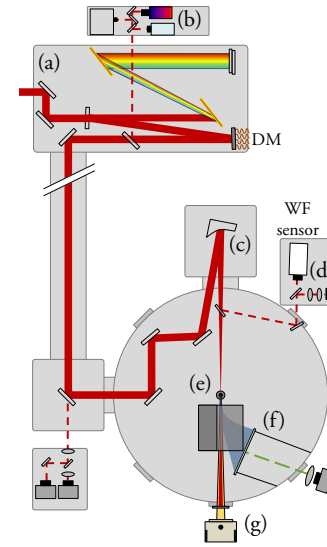

Figure 3.5. *Schematic of the Lund multi-terawatt compression, transport and focusing systems used in the LWFA experiments: (a) optical compressor, including the DM; (b) pulse duration, contrast, and spectrum characterization; (c) OAP; (d) focus diagnostics for the transverse profile and wavefront sensor; (e) gas target; (f) electron spectrometer (see Section 3.2); and (g) X-ray detector (see Section 3.3). The red, blue and yellow beams represent the laser, electrons and X-rays respectively. The rainbow gradient represents the infra-red laser pulse dispersed by the compressor gratings.*

3.1.3 Gas sources

Various structures can be used to contain the gas in laser–plasma interactions. Figure 3.7 shows some of the types used in the present work: (a) a supersonic gas nozzle, (b) a fixed-length gas cell, (c) a variable-length gas cell, and (d) a capillary.

The open geometry of gas nozzles makes alignment of characterization easier. In LWFA, gas nozzles are preferably designed to release supersonic jets, so the density profile is abrupt and the laser–gas interaction is confined [69]. This was the target option used in the study presented in Paper VI.

Another alternative is to confine the gas in a cell (see Papers I-III, V, and VIII-X). It is necessary to include entrance and exit holes in the cell for the laser beam to propagate through it, which causes gas leaks, and consequently density gradients at both ends of the cell. The holes can be pre-manufactured, or can be ablated directly with the laser beam at low power before pumping in the gas to facilitate the alignment. Too large holes can lead to a long longitudinal electron density ramp at the input and output of the cell, while too narrow holes can complicate laser alignment or result in "clipping" of the incoming laser beam.

Dielectric capillaries, with inner diameters ranging from a few tens to several hundred μm, and lengths up to a few cm, were used

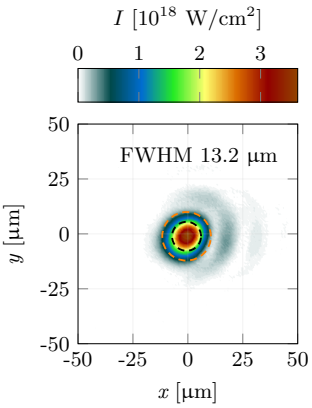

Figure 3.6. *Image of the optimized focus for the experiment described in Paper X. The FWHM diameter and waist of the Gaussian fit are marked by the black and orange dashed lines, respectively.*

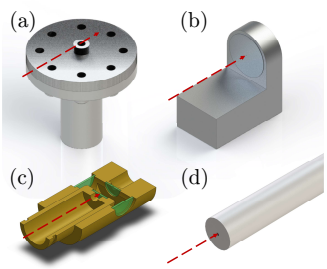

Figure 3.7. *Some of the geometries used for confining the gas sources in LWFA in the present work: (a) a gas nozzle, (b) a fixed-length gas cell, (c) a cross-section of variable-length gas cell, and (d) a gas capillary. The red dashed arrow indicates the direction of propagation of the laser beam.*

for gas confinement in the study presented in Paper VII. Dielectric capillaries can confine the laser propagation more than the natural diffraction of the beam, or act as a waveguide. However, they are very sensitive to laser alignment and focusing. Poor alignment and focusing can lead to ablation of the entrance and output of the capillary, causing deterioration in the quality of the capillary, sometimes after only a few shots.

Optically accessible targets, such as a nozzle or the variable length gas cell shown in Figure 3.7(c), can be characterized on-line or off-line using interferometric or wavefront diagnostics. The variation in the refractive index produced by the molecular density of the gas can be retrieved from the phase front variations of a probe laser beam. The molecular density produced in the target depends on the target geometry, the backing pressure and on the type of gas utilized [70]. In the case of gas nozzles, the molecular density is also sensitive to the vertical and horizontal position of the nozzle. Structures that are not accessible, such as capillaries or enclosed gas cells, can be modelled using fluid dynamics simulation software. A model can also provide information on the up-ramp and down-ramp plasma density profile at the entrance and exit, respectively, of the target.

3.2 Electron diagnostics

The electrons are accelerated within a few mm in the direction of laser propagation. The main parameters governing the electrons, energy spectrum, charge and divergence, can be obtained from the diagnostics described below.

3.2.1 Electron spectral distribution and charge

The spectral distribution of electron beams with a significant energy spread, such as those generated by LWFA, can be studied by sending the electron beam through the magnetic field of a dipole magnet and imaging the dispersed electrons using a scintillation screen, as shown in Figure 3.8. The magnetic field inside the dipole steers the electron beam by the Lorentz force (Equation (2.5)). Since the magnetic force is perpendicular to the trajectory of the electrons $\mathbf{F_B} = -e(\mathbf{v}\times\mathbf{B}) \perp \mathbf{v}$, the work performed by the magnet is zero $W = \oint \mathbf{F_B}\cdot \mathrm{d}\mathbf{s} = 0$, and the electron relativistic factor, γ, is conserved. Considering a constant magnetic field perpendicular to the electron motion, the electron trajectory in the field can be approximated by an arc of radius:

$$R = \frac{m_e c\gamma}{eB}. \tag{3.1}$$

Once the electrons exit the dipole field, they continue along a straight line. Equation (3.1) allows the calculation of the relation

between the signal position on the scintillating screen and the electron energy, for a given magnetic field distribution and screen position. As the relation is not linear, the spectral distribution of the electrons will in general vary from the spatial distribution observed directly on the scintillation screen. The higher the magnetic field, the smaller the radius of curvature of the electron trajectories; and the longer the dipole, the longer the arc travelled by the electrons. Table 3.1 summarizes the parameters of the dipoles used for electron characterization in the present work.

The non-homogeneous transverse and longitudinal distribution of the magnetic field of a real dipole magnet can be mapped using a Hall probe. The spatial characterization of the magnetic field is then used to track the trajectories followed by electrons with different energies when propagating through the dipole magnet. This allows dispersion relation to be obtained on the scintillating screen with respect to the electron energy. It is often also possible to approximate the dipole dispersion to an effective dipole length and constant magnetic field [71]. The magnetic field strength and the dipole length, together with the size and position of the detection screen, define the resolution of the electron spectrometer. These values, together with the input position of the electrons and the dipole gap size, also determine the spectral range detectable by the spectrometer. Finally, the non-zero divergence of the accelerated electrons introduces an uncertainty into the electron energy, as electrons with different combinations of energy and emission angles may hit the screen at the same position.

The electron dispersion was measured by imaging the fluorescence from a Kodak Lanex Regular scintillation screen. Studies of the photon emission from this type of screens have shown that as long as the electron energy exceeds a few MeV, the energy deposition per electron is almost constant, and the number of fluorescence photons emitted depends only on the number of electrons hitting the screen, i.e. the electron beam charge [72]. As the spectral range for electrons in set-ups such as that shown in Figure 3.8 often does not cover such low electron energies, the electron spectral distribution and the collected charge are usually obtained from the signal from the Lanex screen. After integrating the signal along the transverse direction perpendicular to the direction of dispersion, the spectral distribution of the electrons, $\mathrm{d}Q/\mathrm{d}E$, can be estimated from the number of counts at dispersion position $C(z)$ as [73]:

$$\frac{\mathrm{d}Q}{\mathrm{d}E} = \frac{1}{g_{Lx} g_{CCD}} \frac{\mathrm{d}z}{\mathrm{d}E} \frac{C(z)}{s_{px}}. \tag{3.2}$$

The scintillation screen gain, $g_{Lx} = \eta_{Lx} \exp\{-\tau_d/\tau_{Lx}\}$, includes the acquisition delay, τ_d, with respect to characteristic decay time of the Lanex screen, $\tau_{Lx} \simeq 660$ µs [74], and the calibration of the screen, $\eta_{Lx} = (6.95 \pm 0.6) \times 10^9$ photons/sr/pC [75]. The CCD

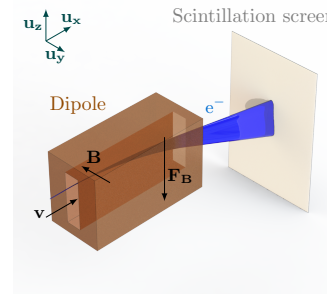

Figure 3.8. *Schematic of the electron spectrometer used to characterize the properties of the accelerated electrons. A magnet disperses the electrons perpendicularly to their direction of propagation and to the magnetic field. The spatio-spectral distribution produces fluorescence in a scintillation screen located after the dipole, the signal from which is recorded in a CCD camera.*

Table 3.1. *Characteristics of the dipoles used in the present experiments.*

Papers	B_{peak}	L_{dipole}
I-III,**V**,**VII**	0.7 T	100 mm
VI	1.2 T	100 mm
VIII,**X**	0.8 T	200 mm

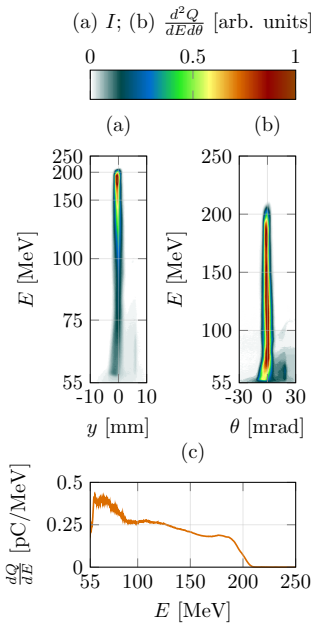

Figure 3.9. *Comparison between (a) the raw signal from the scintillation screen produced by electrons accelerated in a single laser shot, and (b) the corresponding electron spatio-spectral distribution. The retrieved electron spectrum is shown in (c). The geometry of the spectrometer set a cut-off at 55 MeV. For this shot, the collected charge was 19 pC, with a maximum energy of 210 MeV.*

camera response, $g_{CCD} = T_t Q_{CCD} \Omega \cos(\theta_{CCD}) / \cos(\theta_0)$, takes into account the transmission of the fluorescence signal to the camera, T_t, the solid angle of collection, Ω, the viewing angle, θ_{CCD}, the effective thickness of the Lanex screen from the observation point, $\cos(\theta_0)$, and the camera efficiency, or counts per impinging photon, Q_{CCD}, for the fluorescence emission, which peaks at a wavelength of 546 nm. It is important to protect the screen from laser radiation, usually by blocking the surface with a thin sheet of aluminium, and to prevent ambient light from entering the CCD camera, by enclosing the light path between the screen and the detector. The factor $(1/s_{px})(\mathrm{d}z/\mathrm{d}E)$, where s_{px} is the transverse size of the screen corresponding to a camera pixel, gives the relation between the dispersion axis, z, and the energy axis, E.

Figure 3.9(a) shows the raw scintillation signal recorded with a 16-bit CCD camera in the experiment described in Paper VI. The vertical axis corresponds to the linear distance from the electron propagation axis, where some positions are indicated by the corresponding electron energies calculated from Equation (3.1). The spectral distribution was calculated from Equation (3.2), and is shown in Figure 3.9(b). As the dispersion is greater for low-energy electrons, the charge is integrated over a longer distance in the low-electron-energy range, and the spectral distribution becomes flatter than suggested by the raw signal. The angular emission of the electrons is calculated simply taking into account the distance between the electron source and the screen. The reconstructed electron spectrum, $\mathrm{d}Q/\mathrm{d}E$, is shown in (c). This electron spectrometer thus allow the spectral shape and charge of the accelerated electrons above the cut-off energy of the spectrometer to be recovered from a single shot.

Electrons accelerated with the Lund multi-terawatt laser typically have energies up to 300 MeV, with a charge per electron pulse between 15 and 50 pC, corresponding to 9 to 31×10^7 electrons, depending on the plasma parameters and trapping mechanism. Measurements of the bunch duration have shown that the electron bunch is only a few fs long [63]. Electron pulses are thus produced with a peak current in the kA regime, which is above the peak current of most conventional accelerators.

3.2.2 Electron spatial profile and stability

As the electron spectrometer described in Section 3.2.1 disperses the electrons in one direction, the signal recorded in the scintillating screen can be used to measure the divergence of the electron beam along the direction perpendicular to the electron dispersion direction. By removing the dipole from the path of the electron beam, it is possible to use the scintillation screen to study the full spatial profile and divergence. Figure 3.10 shows an electron beam accelerated with the Lund multi-terawatt laser. The spatial dis-

tribution in this example is asymmetric, and the emission is fairly well-collimated with a FWHM divergence of 3mrad×6mrad in the horizontal and vertical directions, respectively. The centre of the electron beam can also be measured from the non-dispersed charge distribution, which allows measurements on beam pointing with a standard deviation as low as 3.4 mrad, as discussed in Paper I.

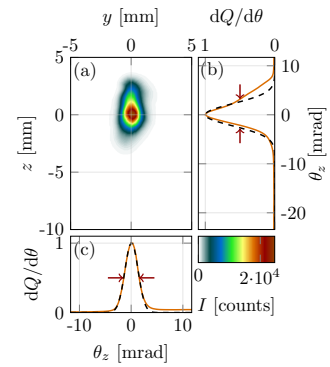

Figure 3.10. *(a) Scintillation screen signal resulting from an electron beam without dispersion, at approximately 43 cm from the source. (b) and (c) show the corresponding integrated angular emission along the vertical and horizontal directions, respectively, using the same scale as in (a). The FWHM divergence of the electron beam in each direction is indicated by the red arrows, and the corresponding Gaussian fit by the dashed black line.*

3.3 X-ray diagnostics

Initially, studies on betatron radiation were often focused on the retrieval of information on the properties and dynamics of the electron bunch. However, the betatron radiation from laser–plasma interactions is now attracting greater attention as an advanced source of X-ray radiation [76]. This section reviews the most important X-ray diagnostics used in the present work for characterization of this emission, and also in applications of the betatron source.

3.3.1 X-ray detectors

CCD X-ray sensitive cameras were used for the detection of betatron radiation and the analysis of its transmission through different materials. The Andor iKon-L SO CCD camera (referred to below as the Andor device) was used to detect the spatial profile of the X-rays in the studies presented in Papers VI, VIII and IX, while the MTE 2048B camera from Princeton Instruments (referred to below as the PI device) was used for in an X-ray spectrometer set-up described in Paper X (see Figures 3.11(a) and (b), respectively).

These cameras both work by direct X-ray detection. The X-rays impinging on the photosensitive silicon sensor are absorbed, leading to the release of electrons, and the current is recorded in each pixel. The two X-ray detection devices have the same type of chip and, therefore, share many features. Both sensors are back-illuminated, i.e. the gate electrode structures are placed after the photosensitive silicon to maximize the absorption of radiation and increase their sensitivity to low-energy X-ray photons. The sensors are also deep-depleted. The depletion zone is extended to increase the well depth of the pixels and thus, the dynamic range of the sensor. Due to their high sensitivity, both devices are also very sensitive to dark current, and can be cooled down below -50℃ to minimize thermal noise. In order to protect the chip surface from the condensation of water at such low temperatures, the chip must be under vacuum before it is cooled. The chip is composed of 2048 × 2048 13.5µm×13.5µm pixels, providing a large detection area of 27.6mm×27.6mm. The signal is digitalized, in both cases, up to 16 bits.

The PI sensor is vacuum compatible and can be placed inside the experimental chamber, while the Andor device can be connected to the vacuum chamber or, as in the experiments described here,

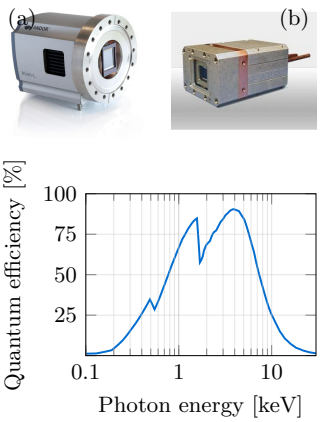

Figure 3.11. *(a) The X-ray Andor iKon-L camera and (b) the Princeton Instruments MTE 2048 B device, and (c) their quantum efficiency response.*

Table 3.2. *Parameters for the X-ray cameras.*

	Andor iKon-L SO	**PI MTE 2048B**
Set-up	Standalone	Vacuum
Pixels	2048x2048	2048x2048
s_{px}	13.5 μm	13.5 μm
Cooling	Air	Water
T_{min}	−70°C	−50°C
Well depth	150 000 e^-	100 000 e^-
Read noise	$\geq$ 4.3 e^-	$\geq$ 3 e^-
Dark current @T_{min}	0.066 $e^-/px/s$	0.02 $e^-/px/s$
Linearity	> 99%	> 98%
Digit.	16 bits	16 bits

it can be placed outside the experimental chamber as a standalone device. A 250 µm thick, ⌀60 mm beryllium filter, chosen for its high transmission of photons above 3 keV, was used to create a vacuum-compatible compartment in front of the Andor sensor, which can be pumped separately or through to the vacuum of the experimental chamber. As the PI device can be placed directly in vacuum, it is cooled by an internal coolant circuit, while the Andor device is air-cooled. Table 3.2 summarizes the main parameters for the two devices.

The conversion efficiency of the incoming photons into electrons, creating the electronic signal, depends strongly on the photon energy. The quantum efficiency measures the probability of the incoming photon to excite electrons in the epitaxial silicon crystal. The Andor and PI devices are sensitive to photons in the energy range 100 eV to 20 keV, as shown in Figure 3.11(c), both having a peak quantum efficiency around 90% at 4 keV.

3.3.2 X-ray spectral distribution and number of photons

There are several methods of studying the spectral distribution of the betatron X-rays. If the spectral emission is considered as a synchrotron-like spectrum, the critical energy that characterizes the spectral shape can be obtained using the Ross filter method [77, 78]. A Ross filter is a combination of thin metallic foils with absorption edges at energies around the expected critical energy of the betatron radiation being studied. The thicknesses of the foils are adjusted so the spectral transmission through each foil is similar for all wavelengths except for the range between two absorption edges. It is then possible to evaluate the photon flux within a particular spectral range by comparing the transmission through the different filters.

Figure 3.12(a) shows a photograph of the Ross filters used in some of the experiments described here, while the corresponding recorded X-ray transmission is shown in (b). The different materials and thicknesses are indicated, and the absorption curves of the filters are shown in (c). The materials were chosen so as to have a peak absorption at a certain photon energy, known as the K-edge (or L_I-edge in the case of the zirconium and tin), within the range of the expected critical energy of the radiation. The peaks correspond to a photon energy equal to the binding energy of an electron in a K shell (or L shell), and are characteristic of each material. The transmission of the betatron X-rays through the filters is compared to the transmission of synchrotron-like spectra, as described in Equation (2.29), and the critical energy, E_c, is obtained by least-squares fitting.

As the Ross filter measurements were performed with the Andor device in the standalone mode, the X-rays propagated through two

250 µm thick beryllium filters (one in front of the CCD chip to create a vacuum, and the other at the exit of the experimental chamber facing the camera), plus a few cm of air between the windows, $T_t = 2T_{Be,250\mu m} \cdot T_{Air}$. The filter array was placed in air, between the two beryllium windows, as close to the camera as possible. The windows, the air and the camera quantum efficiency reduced the X-ray intensity and spectral bandwidth noticeably, as can be seen from the black dashed line in Figure 3.12(c).

The transmission behind a particular filter, F, is measured after background subtraction, as the mean number of counts, N, divided by the total transmission in the areas where there are no filters, $T_{CCD}(F) = N(F)/N_0$. For a set of test critical energies, the theoretical transmission through that particular filter is calculated by integrating a spectral distribution of shape $(E/E_c)^2\kappa^2_{2/3}(E/2E_c)$ multiplied by the total transmission, $T_t(E)$, the transmission of the Ross filter, $T(F,E)$, and the energy deposition in the detector, $E{\cdot}Q_e(E)$. The integral is normalized by the integrated signal when there is no filter:

$$T_{th}(F,E_c) = \frac{\int_0^\infty \left(\frac{E}{E_c}\right)^2 \kappa^2_{2/3}\left(\frac{E}{2E_c}\right) T_t(E)T(F,E)EQ_e(E)\mathrm{d}E}{\int_0^\infty \left(\frac{E}{E_c}\right)^2 \kappa^2_{2/3}\left(\frac{E}{2E_c}\right) T_t(E)EQ_e(E)\mathrm{d}E}.$$

The estimated critical energy is that for which the sum of the squared residuals between the measured and calculated values of transmission for each filter is a minimum.

$$\Lambda^2(E_c) = \sum_i \Lambda_i^2(E_c,F_i) = \sum_i \left(T_{th}(F_i,E_c) - T_{CCD}(F_i)\right)^2$$

The filters can be cut in stripes and arranged forming a mesh where the metallic foils locally overlap, as in Figure 3.12. This allows the study of the critical energy as well as the homogeneity and intensity distribution of the incoming X-rays. This design increases the number of different transmission windows, from seven types of metals to 19 effective filters, due to the overlap of the metallic foils. The larger the number of filters, the more accurate the critical energy estimation. Furthermore, the gaps between the metal foils enable more accurate evaluation of the filter transmission. Figure 3.13(a) shows the X-ray signal through the filters. The background region at the bottom, enclosed by the blue square, was analysed and the background subtracted from the total signal.

The filter area is separated into nine by seven sections, indicated by the dashed squares. Transmission through the areas without filters (orange dashed), is averaged in each section. In Figure 3.13(b), the transmission measured through those areas is interpolated on the grid, giving the spatial distribution of the incoming X-ray beam through the filters. The distribution is then used to normalize the transmission through the sections in (a), including the single (red

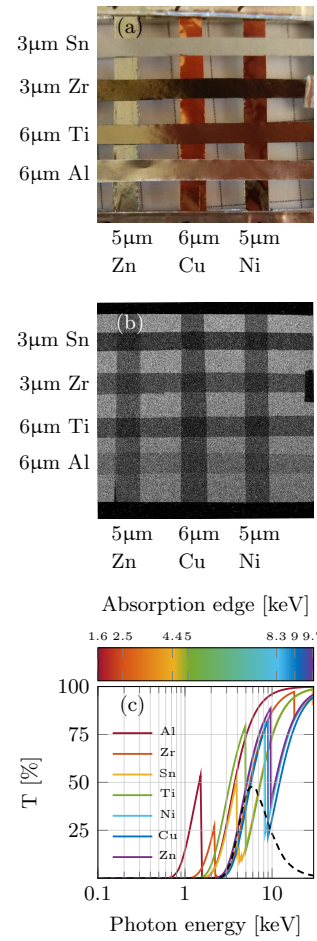

Figure 3.12. *(a) Photograph of the metallic filters used for spectral analysis. (b) Measured X-ray transmission. (c) Spectral transmission of the filters in (a), where the colour coding indicates the absorption edge energy. The black dashed line corresponds to the camera response without filters, including two 250 µm Be windows, 60 mm propagation in air and the sensor quantum efficiency.*

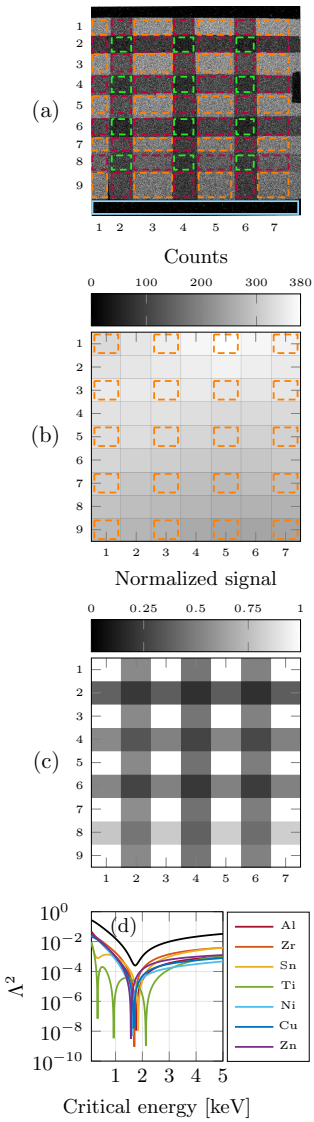

Figure 3.13. *(a) X-ray image of the Ross filters divided into sections. (b) Matrix generated from the mean values of the non-filtered regions interpolated through all the sections. (c) Transmission normalized by (b). (d) Squared residuals for each filter (colours), and sum of the squared residuals (black).*

dashed) and double (green dashed) filters, which gives the matrix shown in (c). It is important to note this, as in other Ross filter designs the filters occupy most of the sensor area, and a homogeneous distribution of the reference beam is assumed, which can lead to misinterpretation of the actual transmission through the filter. The sum of the squares of the residuals, Λ^2, is shown in black, in Figure 3.13(d). Its minimum value gives the critical energy of the betatron pulse, of 1.75 keV in the current example. The squared residuals for the separate filters Λ_i^2 are also included in (d) for comparison, showing a good agreement with the value obtained. The deviation observed for the titanium filter is believed to be due to oxidation of the foil.

Spectral characterization using Ross filters is a fairly robust method for the estimation of the critical energy of a single X-ray pulse, as the background signal is easily subtracted and the spatial distribution of the beam can be retrieved simultaneously. However, the spectral resolution is low, and despite experimental agreement with Equation (2.29) [79], a specific spectral distribution is assumed, which makes the method insensitive to spectral deviations.

If the whole X-ray beam is imaged on the camera, it is possible to obtain the total number of photons emitted, provided the spectral distribution is known. Otherwise, it is still possible to estimate the number of photons emitted per pixel, or per steradian, within the sensor. The relation between the number of photons emitted, N_{ph}, and the number of CCD counts behind a certain filter, $N_{c,F}$, $\Pi_{ph/c} = N_{ph}/N_{c,F}$, can be calculated from the retrieved critical energy and the X-ray camera response in counts per photon energy, g_X, as follows [73]:

$$\Pi_{ph/c} = \frac{\int_0^\infty \left(\frac{E}{E_c}\right)^2 \kappa_{2/3}^2\left(\frac{E}{2E_c}\right) \mathrm{d}E}{\int_0^\infty \left(\frac{E}{E_c}\right)^2 \kappa_{2/3}^2\left(\frac{E}{2E_c}\right) T_t(E) T(F,E) Q_e(E) E g_X \mathrm{d}E}.$$

Thus, the number of photons per pixel is simply given by $N_{ph} = \Pi_{ph/c} N_{c,F}$. In the example shown in Figure 3.13, this leads to a maximum of 6 emitted photons per pixel, corresponding to a peak flux of approximately 10^{11} photons/sr.

A more accurate reconstruction of the spectral distribution of the betatron radiation can be achieved by single-photon counting (SPC) [80, 81]. In this approach, the flux of the X-ray source is reduced by the use of filters or by positioning the sensor far away from the source, such that the number of photons on the chip is reduced to, at most, one photon per 100 pixels [80]. Algorithms are normally used to identify and isolate single-photon events from multi-photon ones in the image. If the camera response is known, the total number of counts produced by a single photon event gives the energy of the interacting photon. A histogram of the single-photon energies, considering the transmission of the X-rays before

reaching the sensor, provides an accurate spectral distribution of the betatron X-rays, within the spectral detection range of the sensor, without having to assume any initial spectral shape. The resolution is higher than with Ross filters, down to a few hundred eV [79]. In contrast, limited information is provided on the intensity or spatial distribution of the incoming X-ray beam.

SPC can be used to calibrate the response of an X-ray detector, by measuring the X-ray transmission through a metallic foil with a known absorption edge. The histogram of the single events recorded will show a fall in transmission corresponding to the absorption edge of the metal. The number of counts produced by the single events in the edge is then used to estimate the camera response. In the case of the Andor device, calibration gave a value of 11.9 counts/eV.

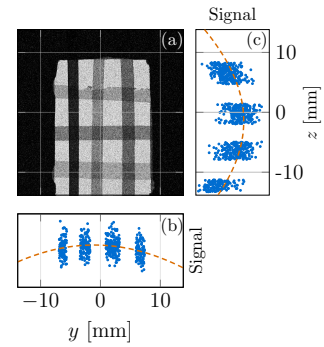

Figure 3.14. *(a) X-ray image of a Ross filter. The integrals of the non-filtered signal along the horizontal (b) and vertical (c) directions are represented by the blue dots. The Gaussian fit is shown by the dashed orange line. The X-ray divergence (FWHM) was estimated to be 63 mrad in the horizontal direction, and 49 mrad in the vertical direction.*

3.3.3 X-ray spatial profile and source size

The X-ray beam intensity distribution and divergence can be measured directly in the X-ray camera if the source is close enough for the full transverse profile of the X-ray beam to be accommodated in the sensor. However, the registered intensity can be used to estimate the source divergence even if the whole beam is not detected by the sensor area. The blue dots in Figure 3.14(b) and (c) show the integrated intensity in the non-filtered areas behind the Ross filters shown in (a), along the horizontal and vertical directions. The data were fitted to a Gaussian function, indicated by the dashed orange curve, from which the FWHM diameter was obtained. If the geometry of the set-up is known, it is possible to estimate the FWHM divergence of the X-ray beam. In the example shown in Figure 3.14, the X-ray divergence was estimated to be 63mrad×49mrad.

In order to also characterize the spatial coherence and brightness of the X-ray radiation, it is necessary to determine the size of the source [82–84]. This can be estimated by imaging an opaque object or obstacle backlit with the betatron X-rays. Figure 3.15(a) shows the image of an array of crosses consisting of 50 µm diameter tungsten wires, with a transmission of less than 0.05 for photon energies below 25 keV, used for source size characterization. As the object is practically opaque to the X-ray beam, it produces a shadow on the detector. Figure 3.15(b) shows the X-ray image produced by one of the tungsten crosses shown in (a), placed $x_1 = 44$ mm away from the source, and registered in the Andor device placed $x_2 = 1.8$ m after the wires. As a first approximation, for the shadow to be sharp, the X-ray source size is necessarily smaller than the object.

A more accurate estimate of the size can be made by considering the diffraction features at the edges of the shadow, which can be compared to the diffraction produced by an X-ray source calculated for different sizes. Assuming monochromatic X-rays with a low divergence, and considering that the longitudinal distances are much greater than the transverse ones, the normalized X-ray

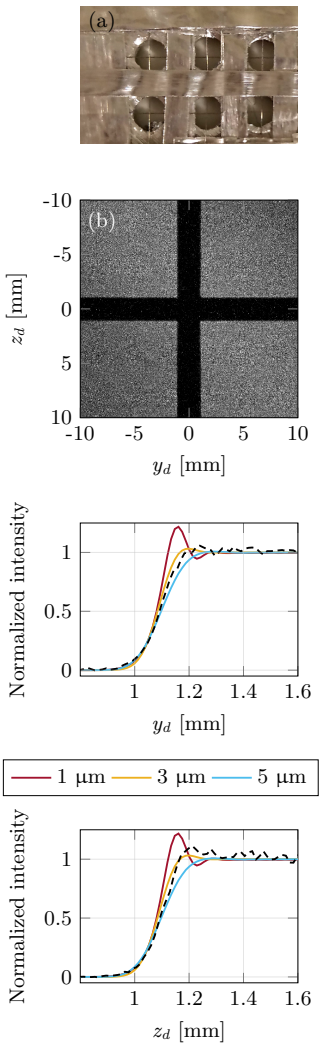

Figure 3.15. *(a) Tungsten crosses used for source size estimation. (b) Betatron X-ray image of one of the crosses after approximately 42 times magnification. (c-d) The integrated signal along the horizontal and vertical directions, respectively, (black dashed lines), and diffraction patterns calculated for different source sizes, D (colours).*

intensity after an obstacle along the y axis, for a point source, can be written [85]:

$$I(y_d) = \left| \sqrt{\frac{x_t}{i\lambda x_1 x_2}} \int \exp\left\{ \frac{-i\pi}{\lambda x_2} \left[2yy_d - \frac{x_t}{x_1} y^2 - \frac{x_1}{x} y_d^2 \right] \right\} q(y) dy \right|^2$$

where $\lambda = hc/E_{ph}$ is the wavelength of the monochromatic source, $x_t = x_1 + x_2$ is the source–detector distance, $q(y)$ is a function describing the obstacle, and y and y_d are the coordinates of the obstacle and detector planes, respectively. To consider the synchrotron-like spectral distribution of the betatron radiation, the intensity must be averaged as $I_w(y_d) = \int \mathrm{d}\lambda A_\lambda I(y_d)$, where A_λ is the normalized weight coefficient, which can be obtained from Equation (2.29). Finally, a finite transverse size is considered as a distribution of point sources, assuming a Gaussian shape $B(y_s) = \exp\{-4\ln(2) y_s^2/D^2\}$, where y_s is the coordinate in the source plane, and D is the FWHM of the source. The intensity distribution accounting for both source size and spectrum, is then given by:

$$I_{s,\lambda}(y_d) = \int \mathrm{d}y_s B(y_s) \int \mathrm{d}\lambda (A_\lambda) I\left(y_d + y_s \frac{x_2}{x_1} \right).$$

The dashed black curve in Figure 3.15(c) and (d) shows the integrated signal produced by the tungsten cross in (b) along the horizontal and vertical directions, respectively. This is compared with the values calculated for a synchrotron-like spectrum with E_c = 2 keV. The different colours represent different FWHM of the X-ray source, D. Diffraction produces one or several oscillations at the edge of the wire shadow. The best fit in this example corresponded to a source size of approximately 3 µm in the horizontal and vertical directions. These methods were employed in the study described in Paper VIII for the characterization of the X-ray source size and divergence, which will be discussed in Section 5.2.1.

3.3.4 X-ray crystals

X-ray crystals allow studies of the spectral distribution of X-rays with high resolution. The molecular structure of the crystal, where atoms are separated by distances on the sub-nm scale, can be used to diffract the sub-nm wavelength photons of an X-ray beam. X-ray crystals can be used as a diagnostic tool to obtain information on the spectral distribution of the radiation [76], or in X-ray absorption spectroscopy (XAS) diagnostics [86], as in the case described in Paper X.

The first order diffraction angle of photons of wavelength λ_{ph}, in a crystal with a lattice interplanar distance d_l, is given by the Bragg angle, θ_B, such that $2d_l \sin(\theta_B) = \lambda_{ph}$. The crystal can be rotated to modify the angle of incidence of the radiation, in

order to detect different parts of the X-ray spectrum. In a real X-ray crystal, the spectral resolution is limited by dislocations in the crystal lattice, which can locally modify the interplanar distance and lead to diffraction at different angles. The resolution is also affected by the penetration depth, i.e. the length of the path travelled by the X-ray inside the crystal before being diffracted, as this will change the position of the diffracted photon on the detector.

In the study presented in Paper X, the X-ray crystal was chosen so as to achieve a high spectral resolution, of a few eV, a high diffraction efficiency, and a spectral range of a few hundred eV. A special type of graphite crystal known as highly oriented pyrolytic graphite (HOPG) was used. HOPGs are mosaic crystals, i.e. crystals where the crystallites inside the material are randomly orientated within a small angular spread with respect to the crystal surface [87]. The mosaic spread of the crystal is defined as the FWHM of the angular distribution of the crystallites. A photon with an angle of incidence slightly different from the Bragg angle has a certain probability of finding a randomly orientated crystallite to be diffracted from. This increases the efficiency of the crystal considerably and reduces its sensitivity to alignment. However, due to the mosaic spread of the crystal, X-ray photons with slightly different wavelengths can be diffracted by the same angle by different crystallites, which degrades the spectral resolution [87]. The spectral range of the detector is limited either by the mosaic spread of the crystal, or by the finite size of the crystal and the detector.

The spectrometer efficiency can also be increased by using the von Hamos geometry [88], as described in Paper X. In this approach, the X-ray crystal is cylindrically bent in the sagittal direction, i.e. the direction perpendicular to the direction of propagation of the X-rays (see Figure 3.16). While the beam is diffracted in the propagation plane as in a flat crystal, it is also focused in the perpendicular plane, increasing the photon intensity at the detector. The radiation can be focused in the detector by choosing the appropriate source–crystal and crystal–detector distances, F, such that for a crystal of curvature R_x they are equal and obey $F = R_x / \sin(\theta_B)$.

As a result, different geometries are required to study the spectral absorption-edges of different materials in the von Hamos geometry. Figure 3.17 shows configurations designed for a crystal with a radius of curvature of $R_x = 115$ mm, for the observation of the absorption edges of various targets. The closer to the source the crystal is placed, the higher the photon collection. However, it is important to shield the detector from gamma rays and noise produced by electron collisions in the chamber. A larger source–crystal distance can then improve the signal-to-noise ratio at the detector.

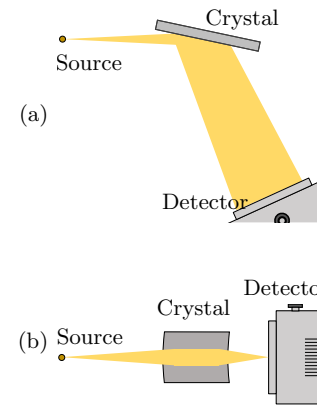

Figure 3.16. *Schematic of a spectrometer with von Hamos geometry: (a) top view, and (b) side view. The X-rays are diffracted in the propagation plane, but focused in the direction perpendicular to propagation.*

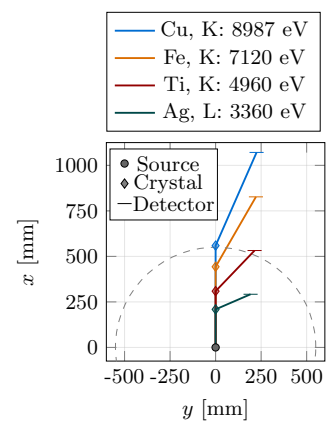

Figure 3.17. *Geometrical configurations for a focusing von Hamos spectrometer used to observe different absorption edges, for a crystal curvature of $R_x = 115$ mm. The size of the Lund experimental chamber is indicated by the dashed line.*

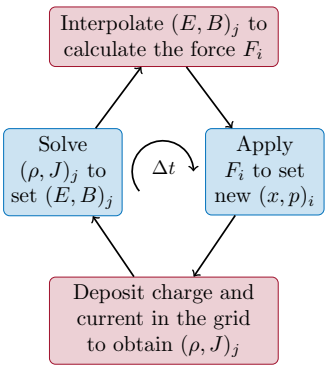

Figure 3.18. *Diagram of the PIC iterative method.*

3.4 Particle-in-cell simulations

Particle-in-cell simulations have become a useful tool for the study of laser–plasma interactions, and are today an essential part in the study of LWFA. The results of most of the experiments presented in this thesis are compared with numerical simulations carried out with PIC codes. This not only allows confirmation of the findings, but also provides a deeper and broader understanding of the physics and laser–plasma dynamics that cannot be resolved by experimental diagnostics.

In a PIC simulation, particles (ions and electrons) are represented by weighted clusters of particles with the same position and momentum, known as macro-particles. They are freely distributed over a mesh representing the spatial and momentum coordinates, or phase space $(x, p)_i$. Since the macro-particles are not restricted to the mesh geometry, the resolution in phase space is given by the number of macro-particles. The macro-particle distribution creates a charge density and current $(\rho, J)_j$ that is deposited in the grid of the phase-space mesh. Applying Maxwell's equations (Equation (2.1)), the electromagnetic fields $(E, B)_j$ induced by the charge and current distribution $(\rho, J)_j$ are calculated using a finite differential method. The forces exerted by the fields on the macro-particles in each mesh cell, F_i, are found using the electromagnetic fields in the Lorentz equation (Equation (2.5)). The forces push the macro-particles along a discrete time step Δt, which rearranges the charge distribution. This process is repeated iteratively as shown in Figure 3.18 [89]. At the end of the simulation, it is possible to obtain the phase-space distribution of the macro-particles and the plasma fields at each time step. It is, however, important to avoid numerical artefacts or errors when performing and interpreting the results of PIC simulations.

The LWFA PIC simulations described here were carried out on resources provided by the Swedish National Infrastructure for Computing (SNIC) at Lunarc (the center for scientific and technical computing at Lund University). The simulations were performed with the quasi-cylindrical code CALDER-Circ [37], which uses cylindrical coordinates but decomposes the fields into azimuthal Fourier modes. Non-cylindrical features of LWFA, such as linearly polarized laser pulses, can be described by a small number of modes, in such a way that the Fourier expansion can be truncated and still reproduce the nonlinear laser–plasma interaction. As a result, the computational load requirements are lower than in fully 3D codes, while still describing 3D features.

Chapter 4

Studies of laser-wakefield acceleration

It is necessary to understand the physics and mechanisms involved in the trapping, acceleration and oscillation of the electrons in a plasma wave. This makes possible to develop techniques that can localize or restrict electron trapping, that can induce a higher X-ray photon flux, or that can improve the shot-to-shot reproducibility of the accelerated electrons and X-rays generated. In other words, studies on process of LWFA will allow optimization of this electron and X-ray source, so that it can become a viable alternative for various applications.

In this chapter, the studies on electron trapping, electron acceleration and wakefield interaction phenomena, reported in Papers I to VI, are summarized. Section 4.1 describes different experimental and numerical studies, the aim of which was to improve the control of electron trapping in the plasma wave, and which resulted in Papers I to IV. In Section 4.2, the most relevant findings reported in Paper V are explained, where a complementary electron acceleration mechanism, known as DLA, was studied in a laser-wakefield accelerator employing ionization-induced trapping. The last part of the chapter, Section 4.3, discusses the effect on the accelerated electrons and X-rays of the interaction of two intersecting wakefields produced by a laser pulse split into two halves and focused in a gas with a narrow angle between them, the results of which are presented in Paper VI.

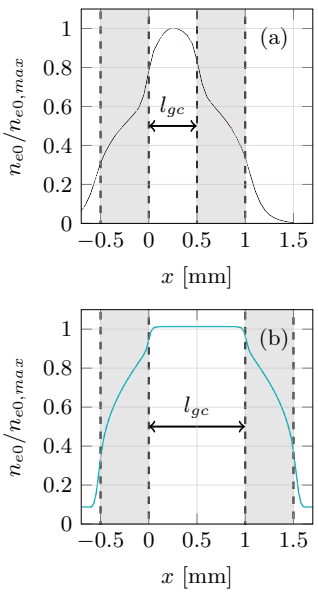

Figure 4.1. *Normalized density profiles at steady state in the gas cells used in the studies presented in Papers I and II (a), and Papers III and V (b). (Adapted from Papers II and III).*

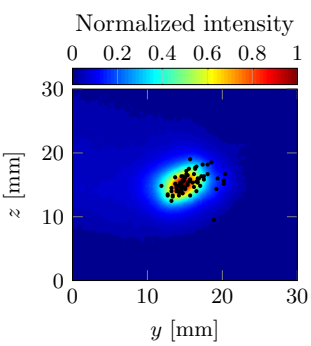

Figure 4.2. *Averaged transverse profile of 70 consecutive electron beams, where the centre of each beam is indicated by a black dot. (Adapted from Paper I.)*

4.1 Control of electron trapping and acceleration in a plasma wave

The properties of laser-wakefield-accelerated electrons are entangled with position and momentum of the the electrons at the moment they are trapped, and with the evolution of the plasma wave while the electrons are accelerated. The control of the electron properties accomplished in the studies described in this section requires very specific values of the parameters for the driving laser pulse and the plasma density at which the LWFA takes place. However, in order to understand how and why these values result in certain electron features, it is necessary to interpret how they affect the electron trapping and acceleration mechanisms in each experimental case. This will allow the manipulation of the electron beam properties to some extent, and pave the way for the development of new or complementary methods of electron trapping control in the plasma wave.

4.1.1 Ionization-induced trapping in a variable-length gas cell

Papers I, II, III and V present the results of experiments carried out with the same laser parameters in two similar variable-length gas cells, specifically designed for LWFA. The plasma density profile was characterized for each gas cell by means of interferometry techniques and fluid simulations. Figures 4.1(a) and (b) show the resulting longitudinal density profiles for the two gas cells from such simulations, where the inner length of the gas cell is set to (a) $l_{gc} = 0.5$ mm, and (b) $l_{gc} = 1$ mm. These profiles are measured in the steady state, a few ms after opening the electrovalve that releases the gas, when the plasma density becomes stable. The 500 μm thick sapphire plates at the entrance and exit of the gas cells, represented by the shaded areas in Figure 4.1, have a hole at the centre with a diameter of either 100 or 200 μm. These cause a density gradient at both ends of the cell, and a flat, almost uniform, profile inside, the length of which depends on the value of l_{gc}.

In all these experiments, the linearly polarized laser beam was focused to an almost circular spot, with a FWHM of approximately 17 μm. The pulse duration after compression was about 37 fs. The peak intensity of the laser pulse focused in vacuum was estimated to be 3×10^{18} W/cm^2, which corresponds to a normalized vector potential of $a_0 = 1.2$. A piezo-electrically actuated mirror was used to correct the long-term drift of the laser pointing, as described in Section 3.1.2. The pointing stability was estimated to be of the order of 1 μrad from measurements of the standard deviation of the laser beam centre for more than 300 laser shots. The electron beam features were analysed with an electron spectrometer that dispersed the electrons in the direction perpendicular to the laser polarization,

and which geometry limited the spectral range to electron energies above approximately 50 MeV (as described in Section 3.2.1).

To increase the reproducibility of the accelerated electron spectrum, the trapping position, the electron-accelerating field and the acceleration length must be well defined. This is mandatory for the development of an electron injector for LWFA staging, which is the main goal of the design of the variable-length gas cell described in Papers I and II. The transport and efficient acceleration of a laser-wakefield-accelerated electron bunch to a second plasma wave demands very specific electron beam parameters, such as short duration, low divergence and a finite energy spread [90].

In particular, the electron beam pointing must be as stable as possible to control the transverse positioning in the second plasma wakefield, and to avoid transverse field effects. The electron beam pointing stability was characterized in the study presented in Paper I, by recording each of the non-dispersed transverse profiles of electrons accelerated by 70 consecutive laser pulses. The inner length of the gas cell was set to 1.8 mm, and it was filled with a gas mixture of 99% hydrogen and 1% nitrogen, corresponding to a plasma density in the plateau of 1.2×10^{19} cm^{-3}. The black dots in Figure 4.2 indicate the central position of the electron beam profiles, where the sum of the intensity distributions in the Lanex screen is represented by the colourscale. The accelerated electrons had a mean divergence of 9 mrad, and a pointing fluctuation of 3.4 mrad in the vertical direction and 4.5 mrad in the horizontal direction, i.e., three orders of magnitude greater than the laser beam pointing fluctuations. The fact that the electron pointing stability is not uniquely related to the laser pointing stability, emphasizes the need to stabilize as many of the plasma and laser parameters as possible in order to obtain reproducible electron acceleration.

A comparison of electrons accelerated in pure hydrogen and in the mixture of 99% hydrogen and 1% nitrogen was performed for a inner length of the gas cell set to $l_{gc} = 2.0$ mm. While only self-trapping takes place in pure hydrogen, the mixture containing 1% nitrogen allows ionization-induced trapping in the plasma wave. Figure 4.3(a) shows the total charge detected by the scintillation screen for electrons accelerated at different plateau plasma densities in the gas cell, presented in Paper III. Ionization-induced trapping does not require a nonlinear wakefield above the wave-breaking limit to trap and accelerate electrons, so electrons are accelerated at lower plasma densities even in the self-compression and self-focusing effects are weaker. While the increase in trapped charge with increasing plasma density is practically linear for densities between 4 and 7×10^{18} cm^{-3}, the threshold for self-trapping is more abrupt and is above plasma densities of 10^{19} cm^{-3}.

The electron spectra obtained using the two trapping mechanisms are different. Figure 4.3(b) shows two typical scintillation screen images of dispersed electrons accelerated in pure hydrogen

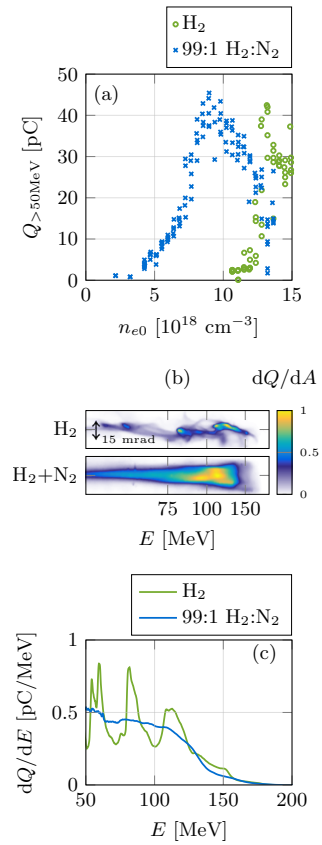

Figure 4.3. *(a) Measured electron charge at different plasma densities for a 2.0 mm long gas cell filled with pure hydrogen (green circles), and a mixture of hydrogen and nitrogen (blue crosses). (b) Examples of typical electron beams with a charge of 40 pC recorded on the scintillation screen after dispersion in the magnet, for both types of gas target. (c) Reconstructed electron spectrum for pure hydrogen (green) and the hydrogen/nitrogen gas mixture from (blue) (b).*

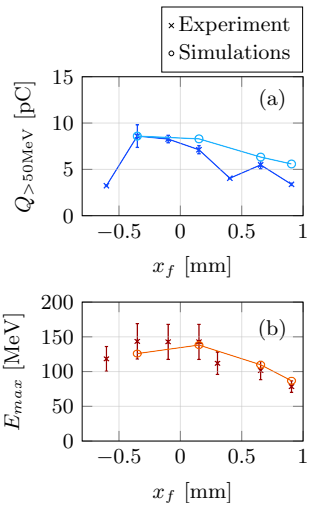

Figure 4.4. *(a) Experimental (dark blue) and simulated (light blue) collected charge and (b) experimental (red) and simulated (orange) maximum energy of the electrons accelerated in a 0.5 mm long gas cell, for different longitudinal positions of the laser pulse focus in vacuum x_f. (Adapted from Paper II.)*

(above) and in the hydrogen/nitrogen mixture (below). The measured charge was 40 pC in both cases, but the plasma density was 7×10^{18} cm^{-3} for the hydrogen/nitrogen mixture and 13×10^{18} cm^{-3} in the case of pure hydrogen. The reconstructed spectra are shown in Figure 4.3(c). Electrons accelerated by the interaction of the laser with the gas mixture show a broad, continuous spectrum. As the laser beam is self-focused and self-compressed in the plasma, inner-shell electrons are released continuously by ionization of the nitrogen ions and trapped in the plasma wave along the gas cell density plateau, producing a continuous spectrum. In contrast, electrons trapped by self-trapping exhibit several localized spectral peaks, corresponding to several wavebreaking events of the plasma wave. As a consequence, the spectra of self-trapped electrons in pure hydrogen vary from shot to shot, while the spectral distribution of electrons accelerated in the gas mixture is highly reproducible.

Given that the peak intensity of the laser beam in vacuum is lower than the threshold for ionization-induced trapping [91], but above the critical power for self-focusing (see Equation (2.25)), electron acceleration relies on the self-compression and self-focusing of the laser beam in the plasma. This nonlinear effect is affected by the location of the focal plane of the laser beam in vacuum with respect to the inner part of the entrance plate of the gas cell, set at $x = 0$.

In the study described in Paper II, electrons were accelerated while scanning different positions of the laser beam focal plane in vacuum x_f, for an inner length of the gas cell of approximately 0.5 mm and a maximum plasma density of $n_{e0} = 8 \times 10^{18}$ cm^{-3}. The crosses in Figures 4.4(a) and (b) indicate the experimentally measured electron charge and maximum energy. The results show that both the accelerated charge and the maximum electron energy decrease when the laser focus is before the entrance of the gas cell, $x_f = -0.6$ mm. It is expected that, in this case, the laser will diverge before entering the gas cell, leading to weaker self-focusing of the laser beam and, consequently, a lower maximum laser intensity in the plasma. The measured electron charge and maximum energy are reasonably constant when the laser focus in vacuum is set between $x_f = -0.35$ mm and $x_f = 0.15$ mm. Both quantities decrease as the focal position is moved to higher values, suggesting that the acceleration length and/or the maximum acceleration field become smaller as x_f increases.

The above results are compared with results from PIC simulations performed with the code WARP [92] for some of the focal positions, and are shown by the circles in Figures 4.4(a) and (b). This code uses Fourier decomposition of the azimuthal modes of the electromagnetic fields, as does the CALDER-Circ code described in Section 3.4. Simulations were carried out at a similar maximum plasma density and with the shape of the density gradients shown in Figure 4.1(a). The charge of the simulated electron beams was nor-

malized to the charge measured experimentally for $x_f = -0.35$ mm. The trend observed in the experimental results agreed qualitatively with the simulations.

Figure 4.5 shows the evolution of the peak normalized vector potential, a_0, along the direction of laser propagation in the plasma for the four simulated focal positions. Self-focusing and self-compression occur along the up-ramp in the density profile, which leads to a rapid increase in a_0 at the entrance of the gas cell in all cases. However, changing the focal position, x_f, changes the maximum value of a_0 obtained and its longitudinal position. This maximum value starts decreasing when $x_f > 0.15$ mm.

The vertical dashed lines in Figure 4.5 represent the longitudinal positions where electrons start becoming trapped in the simulated plasma waves. This limit is reached earlier when $x_f \leq 0.15$ mm, but a longer propagation distance is required for $x_f > 0.15$ mm. As a consequence, not only is less charge trapped in the plasma wave, but it is also accelerated along a shorter distance, reaching a lower maximum energy. The position of the focal plane of the laser pulse in vacuum thus influences the trapping of the electrons in the plasma wave, affecting the final accelerated charge and the electron spectrum.

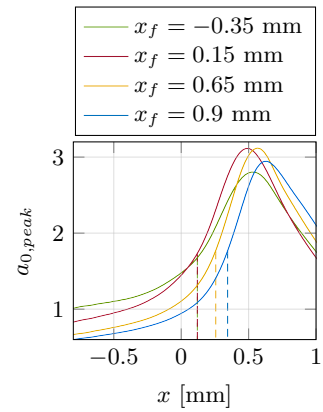

Figure 4.5. *Evolution of the peak normalized vector potential a_0, obtained in the simulations for different focal positions, x_f. (Adapted from Paper II.)*

4.1.2 Trapping in a plasma density down-ramp

Some applications of relativistic electrons require a narrow energy spread and low beam emittance, for example free-electron lasers. Ionization-induced trapping increases the reproducibility and charge of the beams in comparison to self-trapped electrons, but it generally entails a large energy spread, often 100%. If the electron trapping is very localized in phase space, instead of continuous, the energy spread can be reduced as all the charge will experience the same accelerating field.

The propagation of the plasma wave through a drop, or down-ramp, of the plasma density can cause trapping of electrons from the back of the plasma wave bubble. The phase velocity of the plasma wave decreases in the down-ramp, locally reducing the limit for wavebreaking, and triggering the trapping of electrons. If the trapping is localized only in the density down-ramp, some of the electron properties, such as the trapped charge, the electron bunch length and the electron emittance, are directly entangled with the longitudinal plasma profile. Paper IV presents a numerical study performed using PIC simulations with the code CALDER-Circ, where the effect of the density down-ramp parameters on the accelerated electron properties was studied.

The structure of the plasma density interacting with the pulse is described in Figure 4.6. The longitudinal profile of the up-ramp and background plasma density in the first density plateau $n_1 = 6 \times 10^{18}$ cm^{-3}, region (I), were the same in all simulations in

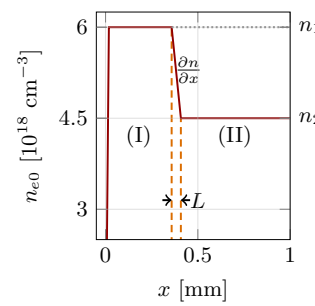

Figure 4.6. *Geometry of the longitudinal profile of plasma density used in the numerical study described in Paper IV. The transition between the two density plateaus, (I) at n_1 and (II) at n_2, is tailored by modifying the length, L, and the height, n_2. The laser propagates from left to right.*

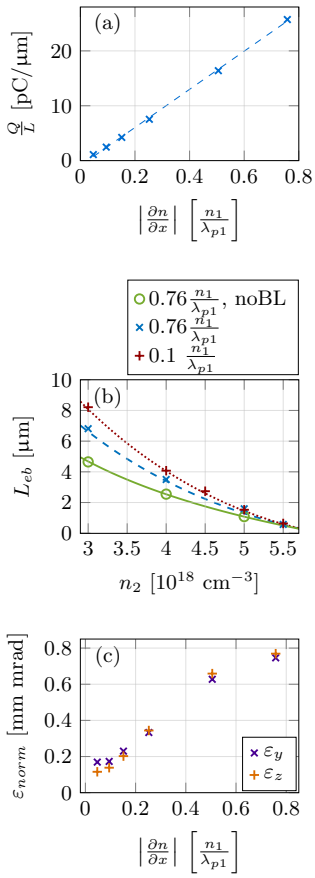

Figure 4.7. *(a) Trapped charge per unit length of the down-ramp as a function of the down-ramp gradient. (b) Longitudinal length of the electron bunch as a function of the plasma density at the plateau (II) for different gradients, $\partial n/\partial x$, given in the legend. The green circles represent the case where beam loading in the electron bunch is neglected. (c) Normalized emittance in the transverse plane as a function of the down-ramp gradient. The laser pulse is linearly polarized along the y axis.*

order to maintain the same initial conditions for laser pulse evolution and formation of the plasma bubble before the density down-ramp. The down-ramp is set by defining a lower plasma density, n_2, with a transition length, L, which leads to the density gradient $(\partial n/\partial x) = (n_2 - n_1)/L$. The pulse driving the plasma wave is defined as a 30 fs FWHM laser pulse focused to a 18 μm FWHM diameter, described by a Gaussian function in the temporal and spatial coordinates, and with a normalized vector potential in vacuum of $a_0 = 1.8$. The simulations showed that while the bubble is highly excited in region (I), there is no electron trapping until the beginning of the density down-ramp. Electron trapping occurs along the density down-ramp, and stops when the plasma wave reaches the second density plateau (II). The trapped electrons are then accelerated in the density plateau defined by n_2. (Further details on the simulation parameters can be found in Paper IV.)

It was observed that for a given density gradient, $\partial n/\partial x$, the number of electrons trapped in the plasma wave decreases as the plasma density n_2 approaches n_1. However, the decrease in the density difference in a constant gradient $\partial n/\partial x$ effectively decreases the down-ramp length L. It is thus interesting to analyse the accelerated charge per unit length of the down-ramp, for a fixed $n_2 = n_1/2$, which is shown in Figure 4.7(a). The trapped charge per unit length increases as the density gradient becomes steeper. It was found that the dependence is roughly linear, so the trapped charge, Q, can be expressed in terms of two constants, $k_1 > 0$ and $k_2 < 0$, such that $Q = k_1(\partial n/\partial x)L + k_2 L$, where k_1 is independent of the density gradient. The dashed line in Figure 4.7(a) corresponds to this expression, where k_1 and k_2 have been chosen to give the best fit to the simulations.

Since the electrons are trapped only in the density down-ramp, the bunch length is expected to depend on the bubble expansion between density regions (I) and (II). This bubble expansion is difficult to predict as it is affected by the laser evolution in the two different density regions and by the perturbation in the plasma wave caused by the charge trapped in the down-ramp. The results of the simulations presented in Paper IV suggest that it is possible to express the full pulse length, L_{eb}, as:

$$L_{eb} = C_1 \Delta\lambda_p + C_2 Q^2, \tag{4.1}$$

where $\Delta\lambda_p$ is the difference in the plasma wavelength between regions (I) and (II). While the bubble elongation is accounted by C_1, the factor C_2 accounts for the plasma wave perturbation produced by beam loading. Hence, C_1 can be calculated by measuring the bubble expansion in a simulation where the beam loading is "turned off", i.e., removing macro-particles representing accelerated electrons as soon as their forward momentum becomes significant. The electron bunch length obtained in the simulations is shown in

Figure 4.7(b), where the lines correspond to Equation (4.1) with the constants that give the best fit to the simulation results.

The emittance of a particle beam is an important parameter in accelerator physics, and is a measure of the area the particles occupy in the phase space. As this is a conserved quantity, a low emittance is desired to efficiently transport and focus an electron beam. The simulations reported in Paper IV showed that the gradient of the density down-ramp influences the normalized emittance of the electron beam for the two axes of the transverse plane (see Figure 4.7(c)). The bubble expansion is so abrupt in a steep down-ramp that the trapped electrons usually follow complex trajectories in the plasma wave structure and, in general, acquire a higher transverse momentum. In contrast, in a gentle density transition, the electrons are trapped consecutively from the back of the bubble with a much smaller transverse momentum, reducing the transverse emittance of the beam. To conclude, these results show that the shape of the density down-ramp can be designed to optimize the parameters of the electron beam, e.g. the charge, the bunch length and the emittance, for use in different applications.

4.1.3 Localization of ionization-induced trapping in a density down-ramp

In the experimental set-up described in Section 4.1.1, ionization-induced trapping of electrons released from nitrogen ions can be localized in the density down-ramp if the parameters of the laser pulse and gas cell are chosen appropriately. As reported in Paper III, it was found that at $l_{gc} = 0.7$ mm, and after optimizing the position of the laser focal plane, the gas cell backing pressure and the compression of the laser pulse, electrons accelerated in a gas mixture of 99% hydrogen and 1% nitrogen present two localized spectral peaks, one at about 150 MeV and another one at aboutd 90 MeV. When using pure hydrogen, with the same plasma density, $n_{e0} = 9.6 \times 10^{18}$ cm^{-3} below the self-trapping threshold, only the higher energy spectral peak remained, although the measured charge decreased from 9 pC for the gas mixture to roughly 1 pC. The electron beam features are reproducible in both cases, as can be seen in Figure 4.8(a), where the scintillation signals from five consecutive electron beams are shown. The corresponding spectra are shown in Figure 4.8(b).

CALDER-Circ PIC simulations were performed to study the origin of the two spectral peaks observed for electrons accelerated in the gas mixture. A 34 fs (FWHM) laser pulse focused at the beginning of the density plateau inside the gas cell to a 17 µm (FWHM) spot was considered, with a peak normalized vector potential in vacuum of $a_0 = 1.25$. The plasma density distribution was defined similarly to that shown in Figure 4.1(b), with $l_{gc} = 0.8$ mm and

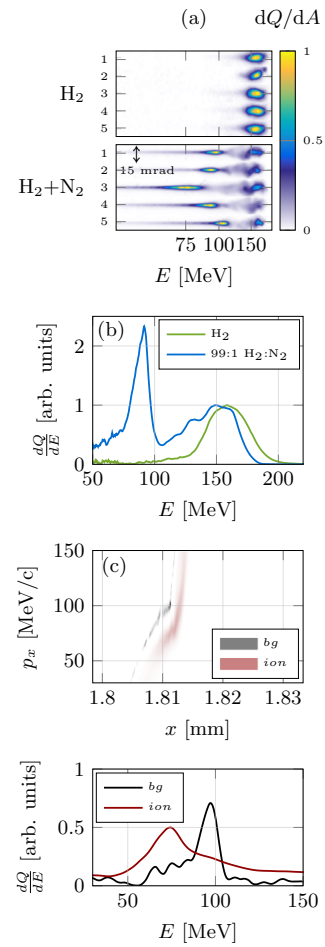

Figure 4.8. *(a) Scintillation signals from five consecutive electron beams accelerated in pure hydrogen and in a hydrogen/nitrogen mixture. (b) Measured spectra for typical electron beams in both cases. (c) Longitudinal phase space at the exit of the simulated gas cell for electrons from the background plasma density (black) and electrons released by field ionization of nitrogen ions (red). (d) Spectra of the corresponding phase space in (c).*

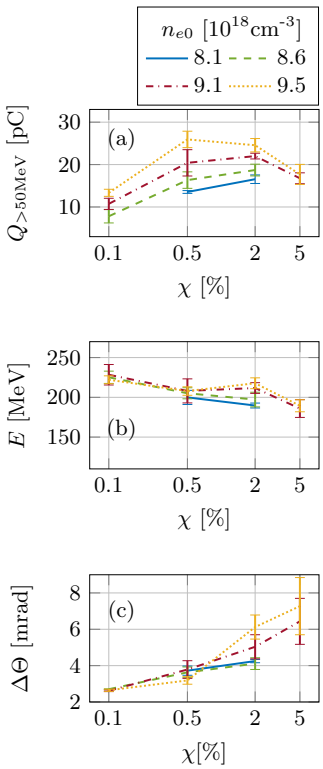

Figure 4.9. *(a) Measured charge, (b) maximum electron energy and (c) FWHM divergence as a function of the nitrogen concentration χ for different plasma densities in the gas cell density plateau.*

$n_{e0,max} = 9.1 \times 10^{18}$ cm^{-3}. (Futher details concerning the simulation parameters can be found in Paper III.)

The simulations showed that, although electrons are slowly and continuously trapped by ionization-induced trapping in the density plateau, most of the charge is trapped and accelerated during the density down-ramp. The nonlinear laser propagation in the plasma and the inner length of the gas cell are such that the plasma wake is highly excited at the down-ramp. In fact, both electrons forming the background plasma density at the back of the bubble and electrons released from the nitrogen ions closer to the peak of the laser pulse, become trapped in the density down-ramp. However, electrons released from the nitrogen K shell are trapped longitudinally closer to the laser pulse, as shown in the longitudinal phase space in Figure 4.8(c). The accelerating field there is smaller than at the back of the bubble, where the background electrons become trapped. As a result, each group of electrons exhibits a spectral peak at a different energy, the background electrons being more energetic than those released around the peak of the laser pulse, in qualitative agreement with the two-peak structure that was observed experimentally.

This localization of the electron trapping depends strongly on the laser and plasma parameters. The laser pulse duration and focal plane position must be chosen so that nonlinear propagation in the plasma leads to a sufficient peak intensity at the density down-ramp to produce ionization-induced trapping. Once the conditions for the localization of the electron trapping have been optimized, the accelerated beams are highly reproducible. This is an example of the control of LWFA that can be achieved by the manipulation of the laser and plasma parameters.

4.2 Effect of the dopant concentration on ionization-induced trapped electrons

The experimental set-up described in Section 4.1.1 was used to study the acceleration of electrons in gas mixtures of hydrogen doped with nitrogen in a variable-length gas cell with $l_{gc} = 0.8$ mm (Paper V). If the gas cell backing pressure is adjusted so that the background plasma density resulting from the hydrogen electrons and the nitrogen L shell electrons is the same for different nitrogen concentrations, it is possible to compare the electrons accelerated with the same laser pulse and background plasma density parameters, but different numbers of electrons released from the inner shell of the nitrogen ions at the peak of the laser pulse.

Figure 4.9 summarizes the experimentally measured changes in charge, maximum electron energy and divergence of the electron beams, as a function of the nitrogen concentration in the gas mixture (0.1%, 0.5%, 2% and 5%), and for different background plasma densities in the gas cell density plateau. For each gas mixture, the

detected charge tends to increase with the plasma density. However, the experimental results show that for a given plasma density, when more nitrogen is added to the gas mixture, the charge increases up to a maximum and then decreases. For a higher plasma density, this maximum is found at a lower nitrogen concentration. The maximum energy is similar for the different plasma densities, but decreases as the nitrogen concentration increases. The maximum energy decreased from 250 MeV for $\chi = 0.1\%$, to about 188 MeV for $\chi = 5\%$, as can be seen in Figure 4.9(b). The divergence of the electron beams is measured as the FWHM of the scintillation screen signal integrated along the direction of electron dispersion. As the spectrometer dipole disperses the electrons in the direction perpendicular to laser polarization, the divergence of the electron beam is measured in the direction of laser polarization. Figure 4.9(c) clearly shows that the divergence increases with the dopant concentration.

Figure 4.10(a) shows the electron spectra averaged over five consecutive electron beams for each nitrogen concentration at a background plasma density of $n_{e0} = 9.5 \times 10^{18}$ cm^{-3}. While the increase in the beam divergence is evident, as χ is increased, it can also be seen that electrons at energies above 140 MeV are emitted at a preferential angles for $\chi = 2\%$ and $\chi = 5\%$. To emphasize this feature, the integrated charge in the electron energy range between 140 MeV and 250 MeV, indicated by the dashed lines, is shown in the upper plots. The electron charge shows local peaks for an angle of emission of approximately 6 mrad, while the on-axis charge decreases. The preferential angular emission of the high energy electrons is also seen for $\chi = 2\%$ and $\chi = 5\%$ when the plasma density is increased, as can be seen in Figures 4.10(b) and (c).

The increase in the divergence and the formation of such preferential angular emission of the high-energy electrons were observed in the direction of laser polarization, which indicates that it could be caused by the interaction between the laser fields and the electrons. During the analysis of the data, this preferential angular emission of the high-energy electrons, or "fork" structure, was identified as an imprint of DLA [93]. DLA occurs when the transverse betatron oscillations of relativistic electrons, such as those during LWFA, are in resonance with an overlapping electric field. When this happens, electrons gain transverse momentum in the direction of laser polarization direction, which is transferred to longitudinal momentum via the magnetic part of the Lorentz force (see Equation (2.5)) [94, 95].

Since DLA is only observed when nitrogen is added to the gas mixture (see Figure 4.3(b)), it is expected that the mechanism is somehow enhanced by ionization-induced trapping in the plasma wave. Furthermore, since the increase in plasma density leads to a decrease in the plasma wavelength (see Equation (2.13)), and thus in a decrease in the bubble radius, the trapped charge is closer to the peak of the laser pulse. This explains why the forked structure sharpens as the plasma density increases.

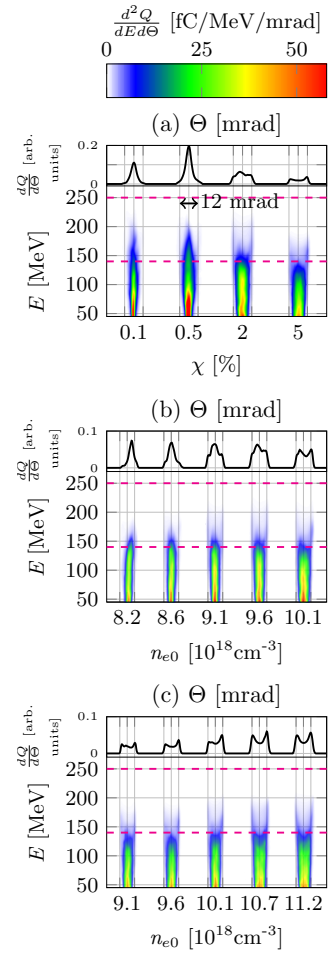

Figure 4.10. *(a) Averaged spectra for electrons accelerated at a plasma density of* 9.5×10^{18} cm^{-3} *as a function of the nitrogen concentration,* χ*. Note that the colourscale saturates for* $\chi = 0.1\%$ *and* $\chi = 0.5\%$*. (b-c) Averaged spectra as a function of the plasma density for (b)* $\chi = 2\%$ *and (c)* $\chi = 5\%$*. The upper plots represent the charge integrated between 140 MeV and 250 MeV, indicated by the dashed lines.*

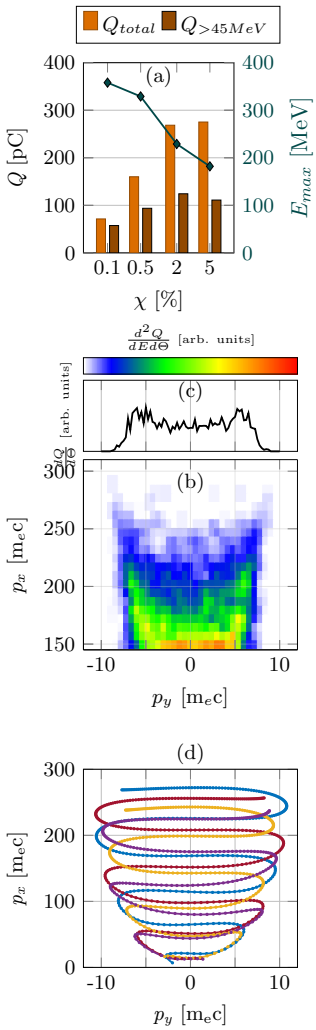

Figure 4.11. *Results from PIC simulations. (a) Accelerated charge and maximum energy for a 37 fs, $a_0 = 1.08$ laser pulse for different concentrations of nitrogen. (b) Histogram of the phase space at the end of the simulation with a 45 fs, $a_0 = 0.9$ laser pulse. (c) Integrated charge along the transverse momentum, p_y. (d) Trajectories in phase-space of four high energy electrons.*

The interaction between a laser pulse and a plasma, with parameters similar to the experimental ones, was simulated with the code CALDER-Circ. (The simulation parameters can be found in Paper V.) The plasma density in the density plateau was set to 10^{19} cm^{-3}, and the same gas mixtures as in the experiment were considered. Figure 4.11(a) shows the accelerated charge and maximum electron energy obtained at the end of such simulations. A higher nitrogen concentration leads to a higher trapping by ionization of the nitrogen in the plasma density plateau. These electrons are trapped from the beginning of the density plateau and closer to the peak of the laser pulse, in comparison to those trapped by self-trapping or in the density down-ramp. As a result, more charge is trapped and more quickly when the nitrogen concentration is increased. In addition, the simulations show that the charge trapped in the density plateau perturbs the wakefield, lowering the accelerating field. Thus, as nitrogen is added to the gas mixture, the electrons are accelerated to lower energies. In fact, the number of electrons accelerated above 45 MeV, which is approximately the energy threshold of the experimental spectrometer, reaches a maximum for $\chi = 2\%$, and then decreases, in a similar way to that observed experimentally. Consequently, when the nitrogen concentration is increased, more charge is trapped in the first bubble; charge that can interact with the laser pulse and experience DLA. At the same time, the wakefield becomes weaker due to beam loading, and the electrons that do not experience DLA are accelerated to lower energies, making the fork structure more prominent.

The effect of DLA on electron acceleration was found to be appreciable by tracking electrons in a new simulation in which the laser pulse duration was increased to 45 fs, and the nitrogen concentration was set to $\chi = 5\%$. The energy per pulse was conserved by reducing the normalized vector potential. The phase space of the electrons before exiting the density down-ramp shows that, while the high-energy electrons are distributed in a ring in the direction of laser polarization, as in a driven harmonic oscillator potential, the transverse momentum perpendicular to the direction of polarization is almost zero. As a consequence, the high-energy electrons are emitted with significant transverse momenta in the laser polarization direction, i.e. at a non-zero angle, producing the fork structure seen in Figures 4.11(b) and (c). By following the phase-space trajectories of some of the highest-energy electrons (Figure 4.11(d)), it can be seen that the electrons progressively gain a net transverse momentum and, when this transverse momentum reaches a maximum, they experience a "kick" in longitudinal momentum due to DLA.

The results of Paper V thus show how the dopant concentration can be used as another parameter to control the properties of the accelerated electrons. The addition of nitrogen to hydrogen gas does not only enables ionization-induced trapping, but it can also stimu-

late DLA of the electrons trapped in the plasma wave, affecting the electron beam energy, spectrum and divergence. Future research is planned to study the effect of the enhancement in electron transverse momentum by DLA on the properties of betatron X-rays.

4.3 Interaction of intersecting wakefields

The studies described in Section 4.1 present techniques for the control of trapping and acceleration of electrons in the laser wakefield, which rely mainly on variations in the laser and plasma parameters. These techniques can help to improve the quality of some electron beam features, such as the beam charge, the energy spread or the emittance, but often compromise the quality of the others. For example, beam loading of the plasma wave limits the amount of charge that can be accelerated with a relatively low energy spread. Techniques that can increase the charge trapped in the plasma wave often induce a larger divergence and transverse size of the electron beam, and a lower electron energy.

Alternative schemes based on LWFA have been suggested to overcome some of these limitations. In particular, numerical studies have been carried out to investigate the use of multiple laser beams to produce high-charge monoenergetic electron beams [96]. In this approach, two (or more) high-intensity laser pulses propagate in an underdense plasma so that each of them produce a plasma wake. If the pulses are sufficiently separated, the laser wakefields can attract and spiral around each other, forming a braided pattern [97]. The plasma waves can also collide and merge into a single wakefield [98]. Results from PIC simulations have shown that the merging of two laser wakefields forming a small angle, $\theta < 15°$, can produce a single electron beam with parameters comparable to those produced in the laser wakefields independently [98]. The effects of merging and braiding of plasma waves on the betatron X-ray emission have also been studied [99], showing an increase in the X-ray energy radiated when the angle of interaction of the laser pulses is less than 10° (see Figure 4.12). In these numerical studies [98, 99], it was noticed that the merging or braiding of the wakefields benefited from a smaller angle of interaction.

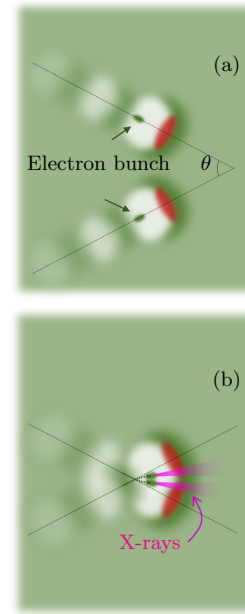

Figure 4.12. *Illustration of the braiding of two laser wakefields. (a) Two laser pulses, at an angle θ between them, are focused in a plasma. Each of the laser-driven plasma waves traps and accelerates electrons in the first bubble, before the intersection point. (b) The interaction of the laser pulses and wakefields perturbs the electron density and forms a single bubble. Electrons can perform higher oscillations, which can increase the betatron X-ray emission. (Adapted from [99])*

Paper VI describes the experimental results obtained from the study of the intersection of two laser wakefields forming a small angle, $\theta \approx 2.6°$. The experiment was performed at the Spanish Center for Pulsed Lasers (CLPU). The VEGA-2 laser system delivers about 4 J, 27 fs FWHM, linearly polarized laser pulses on target, with a central wavelength at 800 nm. The experimental set-up is illustrated in Figure 4.13(a). The two laser pulses were produced using two pairs of split mirrors, as shown in Figure 4.13(b). In the first pair (referred to as A), the 100 mm diameter laser beam was divided into two halves by introducing a small angle along the hori-

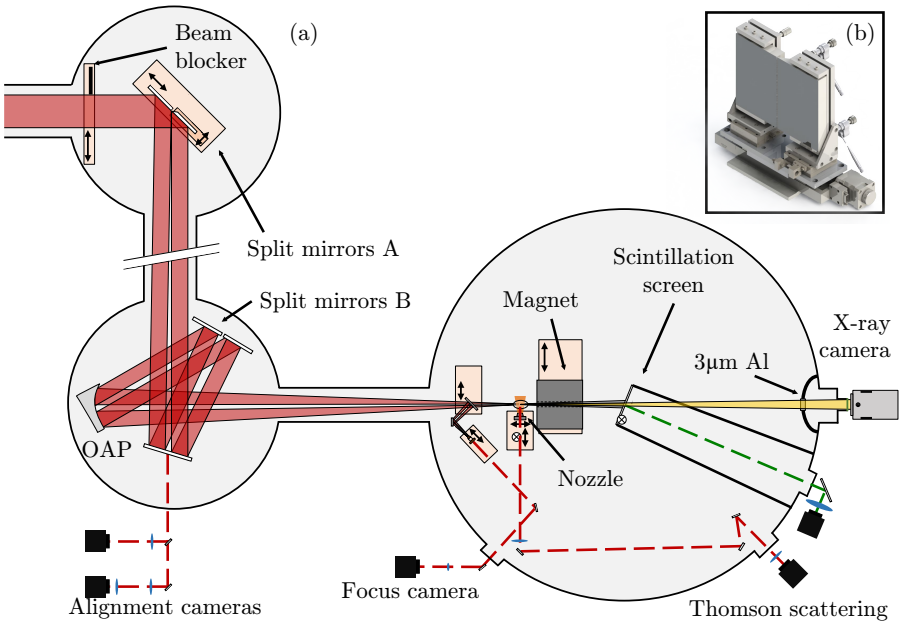

Figure 4.13. *(a) Illustration of the experimental set-up used for the intersecting wakefield experiment. (b) 3D model of the split mirrors used for the division and collimation of each individual laser beam.*

zontal direction y. The second pair (referred to as B) compensated for the angle introduced, so that the two laser pulses were reflected parallel to each other with a transverse separation between the centres of the beam of approximately 63 mm. The two laser pulses were then focused in a 1.3 m focal length OAP, propagating with a relative angle of about 2.6°. The foci were imaged at low power onto a CCD camera outside the experimental chamber, showing two elliptical foci with a FWHM of 43μm×30μm in the horizontal and the vertical directions, respectively, from which peak intensities of 2.5×10^{18} W/cm^2 ($a_0 \approx 1$) were estimated. The observation of interference fringes in the overlapping foci was used for synchronization of the laser pulses. A 5 mm supersonic gas jet of a mixture of 99.5% helium and 0.5% nitrogen formed a background plasma density estimated to be 4.5×10^{18} cm^{-3}, so ionization-induced trapping ensured the interaction of loaded laser wakefields. The plasma density profile, which was characterized off-line, consisted of a 3 mm long plasma density plateau with a 1.15 mm density up-ramp and down-ramp at the beginning and end of the gas jet, respectively.

An electron spectrometer dispersed the electrons in the direction perpendicular to the interacting plane of the laser pulses, where energies above approximately 60 MeV could be detected. A motorized beam blocker allowed the study of the electron acceleration

produced by one laser pulse in the plasma. The results are shown in Figure 4.14(a) and (b). The black arrow in the figure indicates an opening angle corresponding to 40 mrad. The electron beams exhibit a continuous energy spread, typical in ionization-induced trapping, a maximum energy of about 245 MeV, between 60 and 90 pC per pulse, a divergence between 6 and 9 mrad and good reproducibility. Since the laser pulses were focused at an angle, the electrons propagated to different horizontal positions on the scintillation screen (see Figure 4.14(a-b)).

The beam blocker was removed, and a motorized translation stage was used to move one of the mirrors in (A) in the direction parallel to the reflecting surface, so that a relative delay between the laser pulses of $\tau = 5.2$ ps was introduced. The electron beams accelerated by each laser pulse were still distinguishable at different horizontal positions on the screen, as can be seen in Figure 4.14(c), although the signal from electrons accelerated by the laser arriving later became weaker. This could be a consequence of variations in the plasma density after the propagation of the first plasma wave.

When both pulses were synchronized and sent to the gas jet, $\tau = 0$, a single electron beam located around the central axis was observed. The emission was reproducible, and Figure 4.14(d) shows five of eight consecutive measurements, when one single electron beam was observed. The black arrow also indicates an opening angle of 40 mrad here. The averaged spectra, reconstructed from the signals in Figures 4.14(a), (b) and (d), are shown in Figure 4.14(e), where the shaded area represents the shot-to-shot standard deviation. The intersection of the wakefields produced an increase in the measured charge, the average value of which was about 160 pC, i.e. approximately the sum of the charge measured from the electron beam accelerated by one laser pulse only. The maximum electron energy was, however, similar in beams produced with the synchronized pulses, and was found to be 285 MeV on average. Figure 4.14(f) shows the angular distribution of the charge along the intersection plane for individual and synchronized laser pulses, where the shot-to-shot standard deviation is again represented by the shaded area. It can be seen that the electron beam produced with the synchronized laser pulses was emitted in between the electron beams generated by the single laser pulses. The central emission shows a larger divergence, with a FWHM of 12 mrad, on average. The generation of a single electron beam, emitted at the central axis formed by the two intersecting laser pulses, and with a charge about twice that measured for a single laser pulse, is an indication of merging of the two laser wakefields.

The horizontal tilt of one mirror in (B) could be changed using a motorized actuator to achieve small variations in the incident angle of one of the laser pulses. This changes the longitudinal position at which the laser pulses intersect, and was observed to affect the merging of the wakefields. Figure 4.15 shows the signals recorded

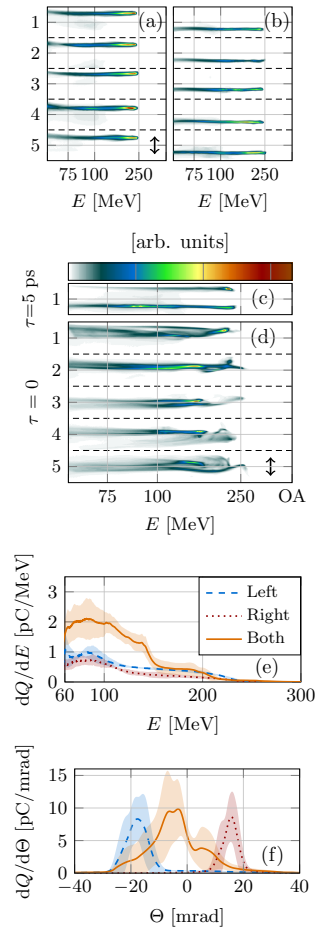

Figure 4.14. *Signal from the scintillation screen resulting from electron beams accelerated using the right (a) and left laser pulse (b), (c) the two laser pulses with a long delay of $\tau \approx 5$ ps; and (d) the two synchronized pulses. Averaged spectrum (e) and angular distribution of the charge (f), measured on electron beams accelerated by the left (dashed blue line), the right (dotted red line) and both synchronized laser pulses (orange line).*

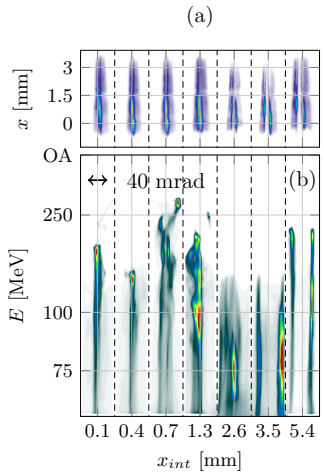

Figure 4.15. *Thomson scattering (a) and electron dispersion in the scintillation screen (b), as a function of the longitudinal position of intersection of the laser beams with respect to the beginning of the plasma density plateau, $x_{\int}$.*

from the Thomson scattered light (a) and scintillation screen (b) while changing the position of x_{int}, where $x_{int} = 0$ is defined at the beginning of the plasma density plateau. Each electron beam signal represents one of a sequence of five to ten measurements, and represents merging of the laser wakefields at those positions for which it was observed. For x_{int} between 0 and 0.7 mm, electron merging was observed in 16 out of 23 laser shots, producing a single electron beam along the central axis. Although merging was still observable for $0.7 \leq x_{int} \leq 2.9$ mm, two electron beams could be distinguished in most of the charge distributions registered on the scintillation screen; both beams being located closer to the central axis that the electron beams produced by a single laser pulse. However, no merging was observed for x_{int} above 2.9 mm. It is expected that in this case the laser pulses intersect at the end of the density plateau and beginning of the density down-ramp. Hence, the laser pulses and plasma waves did not interact during propagation in the density plateau, and propagated independently to the scintillation screen.

Since the two intersecting laser pulses are identical, interference of the laser fields is expected when interacting in the plasma. This interference can cause multifilamentation at the intersection point, depending on the number of intensity maxima formed across the laser foci. If one of these filaments is located on the central axis, it can produce a central plasma wave and a bubble that induces merging of the wakefield [99]. However, this effect is sensitive to the relative phase of the laser pulses. The variations in phase would be less noticeable if the self-compression of the laser optimized the spot size of the pulse with respect to the interference pattern produced. The change in the intersecting point of the laser pulses in the plasma can thus be used to optimize the laser nonlinear propagation, in order to minimize the phase sensitivity of wakefield merging.

The Andor sensor described in Section 3.3.1 was placed 1.1 m from the gas nozzle along the central axis, in order to study the effect of wakefield merging on the X-ray emission in the forward direction. X-rays propagated outside the experimental chamber through a 125 μm Kapton window, and through 250 μm of beryllium in front of the X-ray camera chip (see Figure 4.13). The area covered by the chip corresponded to an opening angle of approximately ±12.5 mrad in the horizontal and vertical directions. The mean number of counts after background subtraction measured in the X-ray camera as a function of the temporal delay between the laser pulses is shown in Figure 4.16(a). Practically no X-rays were detected when the laser pulses were delayed. The on-axis emission significantly increased when the pulses were synchronized or delayed by a short time $|\tau| < 9$ fs. This emission could be related to the propagation of accelerated electrons along the central axis. At long delays, the accelerated electron beams were localized on one side of the scintillation screen, around the horizontal position where the first laser pulse arriving in the plasma produced the electron beams

shown in Figures 4.14(a) and (b). As the delay decreased, the electron beam gradually shifted towards the central axis, so the charge collected at the opposite side started to increase. However, the electrons were emitted in the forward direction, towards the X-ray detector, when the delay between the pulses was below $|\tau| < 9$ fs. Although it was not possible to quantify the effect on the overall X-ray emission, wakefield merging increased the X-ray emission along the bisector of the angle formed by the two intersecting laser pulses.

These results demonstrate the first experimental observation of the merging of laser wakefields, producing electron beams with twice charge but similar maximum energy, and slightly larger divergence than those produced by single laser pulses. Merging is sensitive to the position of intersection of the laser beams in the plasma, and produces betatron X-rays along the central axis of the laser pulse intersection. It is still necessary to analyse the effect on the total emission of X-rays, since merging is expected to significantly increase the transverse momentum of the electrons in the plasma wave.

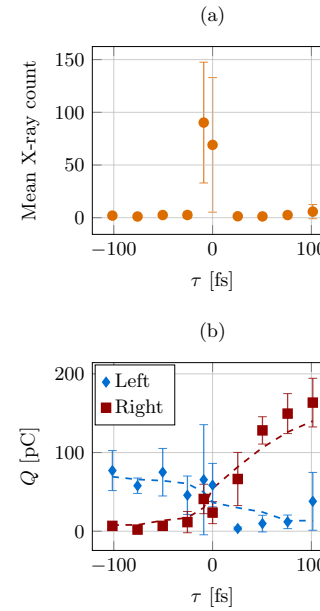

Figure 4.16. *Average number of X-rays detected in the Andor sensor (a), and average electron beam charge collected on the left (blue diamonds) and right (red squares) of the central axis (b), as a function of the delay between the laser pulses τ. The error bars indicate the standard deviation over five laser shots. The dashed lines in (b) are to guide the eye.*

Chapter 5

Characterization and applications of betatron X-rays

The betatron X-rays produced in a laser-wakefield accelerator are generated directly by the electron oscillations in the plasma wave, with no requirement for electron transportation or insertion devices to produce the radiation, and with an intrinsic small source size and short pulse duration. Although such X-rays were not expected when LWFA was first proposed, the use of this source of radiation in biomedicine, materials science or plasma physics, is becoming of considerable interest in the LWFA community [100].

This chapter presents a selection of results from the experiments conducted regarding the application of betatron X-rays. The experiments were performed at the Lund high-power laser facility and at the Central Laser Facility (CLF) at the Rutherford-Appleton Laboratory, UK, and resulted in Papers VII to X. In Section 5.1, the use of betatron X-rays to characterize the electrons accelerated by the laser-wakefield is described. The small size of the betatron source allows a high spatial resolution to be achieved when used for X-ray imaging. Examples of its application to phase-contrast imaging of biological samples and complex materials are presented in Section 5.2. The X-ray pulse is estimated to be only a few fs long [101]. This makes betatron radiation a good candidate for the study of fast dynamic processes in plasmas physics, which typically take place on the fs and ps time scale. This potential is discussed in Section 5.3.

Table 5.1. *Mean parameters of the accelerated electrons (Paper VII).*

Mixture	$Q_{>40MeV}$	$\langle\theta_e^{FWHM}\rangle$
H_2	55 pC	6 mrad
99:1 H_2:N_2	100 pC	23 mrad
99:1 H_2:Ar	130 pC	24 mrad

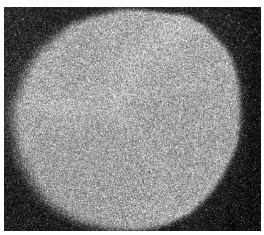

Figure 5.1. *Example of the recorded signal for X-rays, generated in a 20 mm long capillary filled with a mixture of hydrogen and nitrogen.*

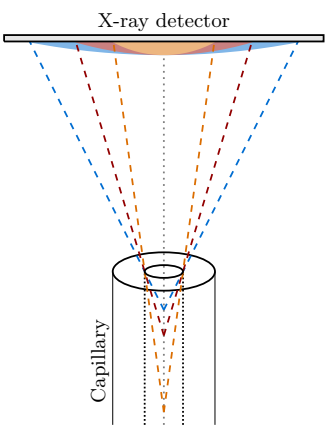

Figure 5.2. *Relation between the radial distribution of the X-rays on the X-ray detector and the emission at different longitudinal positions in the capillary.*

5.1 The use of betatron X-rays for the characterization of LWFA-electrons

Betatron radiation can be used as a diagnostic of the accelerated electrons. As discussed in Section 2.3, the features of X-ray radiation are directly entangled with the electron parameters. Since the X-rays are generated by electron oscillations, measurements of the X-ray source size provide an indication of the maximum oscillation amplitude of the accelerated electrons [82]. The transverse profile of the X-rays depends on the electron trajectories, which also depends on the initial position and momentum of the electrons. Studying the X-ray beam profile in the far field thus allows mapping of the transverse momenta, p_y and p_z, of the electrons, which can be used to determine the electrons trajectories in the plasma channel [102]. Furthermore, the spectral distribution of the X-ray, together with the electron beam spectrum, can be used to estimate the electron amplitude oscillation in the plasma wave by numerical analysis [103].

Paper VII described how analysis of the X-ray flux and spatial distribution was used to obtain information on the dynamics of the trapping and acceleration of electrons inside a glass capillary. Electron acceleration using pure hydrogen was compared with that in a mixture of 99% hydrogen and 1% nitrogen, and a mixture of 99% hydrogen and 1% argon, as an extension of a previous study [104].

The electrons were accelerated by focusing the laser at the entrance of a gas-filled dielectric capillary with a length of 20 mm and a inner diameter of about 156 µm. The peak laser intensity in vacuum was estimated to be 3.8×10^{18} W/cm^2, and the capillary backing pressure corresponded to a background electron plasma density of approximately 12×10^{18} cm^{-3} for pure hydrogen and the mixtures with nitrogen and argon. The accelerated electrons were analysed using a spectrometer, as described in Section 3.2. Table 5.1 summarizes the main parameters measured for the electron beams. The electron spectrum was continuous in all three cases, which can be a feature of continuous trapping during plasma wave propagation in the capillary. The average electron energy measured in the three gas targets corresponds to 70 MeV. The mean electron divergence was measured in the direction of laser polarization and increases in all gas mixtures, as discussed in Section 4.2. (Further details about the electron beams can be found in Paper VII.)

Figure 5.1 shows a typical X-ray image from the capillary for the mixture of hydrogen and nitrogen. The X-ray beam shows the circular geometry of the capillary at the exit, as its angular emission is greater than the aperture of the capillary exit. While a point X-ray source would produce a sharp shadow of the capillary exit, the intensity transition at the edge of the shadow depends on the dimensions of the source, and can be used to estimate the transverse and longitudinal size of the X-ray source, as discussed in Section 3.3.3.

The critical energy of the X-rays, estimated with a set of Ross filters placed in front of the detector, was found to be 2.6 keV (as defined in Equation (2.27)) for pure hydrogen and for the mixture of hydrogen and nitrogen.

The capillary structure not only guides the laser, but also affects the X-ray propagation along its length. As shown in Figure 5.2, emission at different longitudinal positions in the capillary leads to a limited radial extension of the X-ray signal in the detector [105]. This limit for an X-ray beam generated at the longitudinal position x measured from the capillary entrance, is expressed in the radial coordinate r as $r(x) \simeq r_{cap}D/(L_{cap}-x)$, where L_{cap} and r_{cap} denote to the length and inner radius, respectively, of the capillary, and D is the capillary–detector distance. The longitudinal distribution of the X-ray emission along x can be retrieved by studying the radial X-ray signal distribution in the detector $S(r)$, as [106]

$$\frac{\mathrm{d}I(x)}{\mathrm{d}x} = -\frac{\partial S(r)}{\partial r}\frac{r^2}{r_{cap}D}.$$

Analysis of the radial intensity distribution of the X-ray images gives the averaged azimuthal distribution, as shown in Figure 5.3(a). Doping hydrogen with nitrogen or argon led to a higher photon flux in the detector. The peak flux was similar in both cases, and was estimated to be 10^5 photon/mrad^2. As the electron number density, average electron energy and critical energy were found to be similar for all three gas mixtures, the poweraveraged over an electron betatron period would be expected to be similar in all cases (see Equation (2.30)). Thus, the increase in the flux observed in doped hydrogen may be a consequence of the higher number of accelerated electrons or a longer distance along which electrons oscillate (see Equation (2.31)).

The longitudinal X-ray emission in the capillary is calculated from the radial distribution of the X-ray, and shown in Figure 5.3(b). Analysis showed that X-ray emission starts sooner in the capillary when the hydrogen gas is doped. The length along the capillary over which X-ray emission takes place exceeds 5 mm for both the nitrogen- and argon-doped gas mixtures. In the case of pure hydrogen, X-ray emission starts a few mm further along the capillary, and the total emission length is not longer than 3 mm. The earlier X-ray emission may indicate earlier electron trapping or greater acceleration when the plasma wave is produced in the gas mixture.

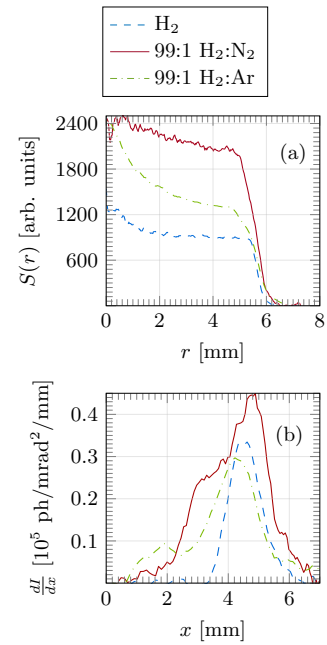

Figure 5.3. *(a) X-ray yield radial distribution measured on the detector for different gas mixtures at a background electron number density $n_{e0} = 11 \times 10^{18}$ cm^{-3}. (b) Reconstructed longitudinal profile of the electron emission in the capillary. Adapted from Paper VII.*

5.2 Phase-contrast imaging with betatron X-rays

The purpose of medical radiology is often to reveal small internal structures in soft tissue composed of several elements with similar low degrees of absorption. The high contrast and high spatial

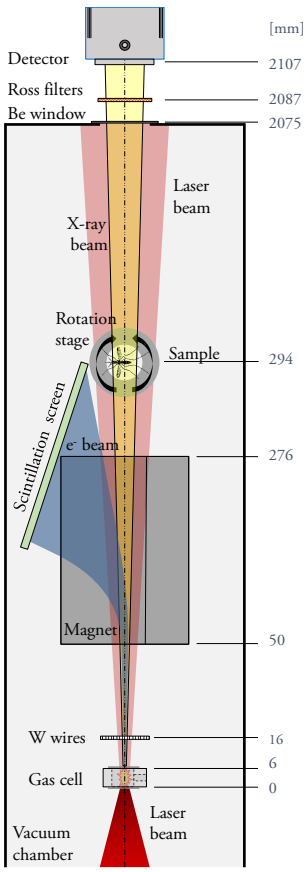

Figure 5.4. *Schematic of the experimental set-up for the characterization and application of X-ray emission for PCI μCT. The longitudinal positions of various elements of the set-up are given on the right-hand side (not to scale). The laser beam propagates upwards in the figure.*

resolution of X-ray phase-contrast imaging (PCI) provide an imaging alternative with a lower dose to the patient than traditional absorption-based X-rays [107]. In PCI, information is provided by the intensity modulation produced by the phase shift experienced by the X-rays when propagating through different parts of the sample. The image contrast arises from changes in the refractive index in the sample, instead of from changes in the absorption, as in the case of conventional radiography. The cross section for elastic scattering causing the phase shift of the X-rays is usually greater than for absorption when propagating inside low-density materials [108]. Therefore, PCI can be used to image samples with very low absorption, and to improve contrast for materials with very similar degrees of absorption, which is often the case in biological samples.

Different methods for the measurement of the phase variations of the X-rays include the use of phase gratings to diffract the X-ray beam [109, 110], a perfect silicon crystal to produce a flat X-ray wavefront before the sample [111], or an X-ray interferometer [112]. Propagation-based phase contrast is the method used in the experiments described in Papers VIII and IX [113]. This technique only requires spatial coherence, which is achievable with a small source size and sufficient propagation of the X-ray beam after the sample. The X-ray source should also provide an appropriate photon energy, collimation and flux, such that a sufficient number of photons is collected in the detector. The particularly small source size of betatron X-rays of a few μm (Section 3.3.3), together with good collimation, high energy and some degree of tunability, make betatron X-rays a suitable source [100, 111, 114–117].

5.2.1 Phase-contrast imaging of low-absorbing samples

X-rays produced by LWFA were fully characterized for different plasma densities, by means of the methods described in Section 3.3, in order to find the most favourable conditions for PCI (Paper VIII). The source, once optimized and tested by performing PCI of different low-absorption samples [118], is used for the microcomputed tomography (μCT) of an insect.

Figure 5.4 shows the set-up used for the realization of PCI and μCT. The elements placed inside the vacuum chamber, including a set of tungsten wires for source size characterization, the sample rotation stage, and the gas cell, are motorized so that they can be moved in the transverse and/or longitudinal directions for positioning and alignment. A 6 mm long gas cell, such as that shown in Figure 3.7(b), was used in the experiment. The cell was filled with a gas mixture consisting of 99% helium and 1% nitrogen, to cause ionization-induced trapping in the plasma wave. This leads to early and continuous trapping of electrons during laser propagation in the plasma, which in general means more trapped charge, oscil-

lating over a longer distance, hence producing more X-ray photons than in other trapping mechanisms (as discussed in Section 5.1).

The X-ray source was first completely characterized to determine the best conditions for μCT. Ten laser shots were used at each plasma density in the gas cell to produce X-rays, and their transmission through Ross filters was measured. The critical energy was estimated from each X-ray image, and used to calculate the number of photons registered in the sensor. The results were averaged over the ten shots, and the critical energy and peak photon flux are shown in Figures 5.5(a) and (b), respectively. The shot-to-shot standard deviation is indicated by the error bars. The transverse profile of X-ray beam through the non-filtered parts of the Ross filters were integrated along the transverse axes y and z, as described in Section 3.3.3. The curves obtained were fitted to Gaussian functions, from which the X-ray beam centre and FWHM divergence were obtained, as shown in Figure 5.5(c) and (d), respectively. In most cases, the integral of the X-ray signal along the direction parallel to the laser polarization, y, did not exhibit a local maximum, but a monotonic gradient instead. The fit to a Gaussian function is less precise in such cases, which were omitted from Figures 5.5(c) and (d). The beam divergence and the instability in X-ray beam pointing increase as the electron number density increases, which could be an effect of the stronger nonlinear laser propagation and higher load of the plasma wave.

It is possible to identify the conditions under which the emission is more stable and the number of photons is higher. A plasma density of 10.2×10^{18} cm^{-3} was chosen for the tomography. The FWHM divergence of the X-ray beam was estimated to be 40×29 mrad×mrad. The diffraction after a 25 μm tungsten wire cross was used to estimate the X-rays source size, the results of which are shown in Figure 5.5(e). The size was estimated to be 3.6 μm in the horizontal direction, and 2.6 μm in the vertical direction. Both source size and divergence are greater in the direction of laser polarization. As this is a similar regime to that discussed in Section 4.2, this may be caused by laser-induced ionization of nitrogen and the overlap of the trapped electrons with the laser fields. The radiation has a critical energy of 2.4 keV under these conditions. The soft X-ray regime (below 5 keV) can be beneficial for PCI of low absorbing samples. As the phase shift of the X-rays is proportional to the photon wavelength, the contrast of PCI is increased at low X-ray energies without a significant degradation of the signal-to-noise ratio.

An important parameter in characterizing an X-ray source is its brightness, defined as the number of photons per unit time, angular divergence, cross section and spectral bandwidth. While the total average flux of betatron X-rays is not yet comparable to those of other X-ray sources, the small source size, good collimation and especially the extremely short duration, make betatron X-rays par-

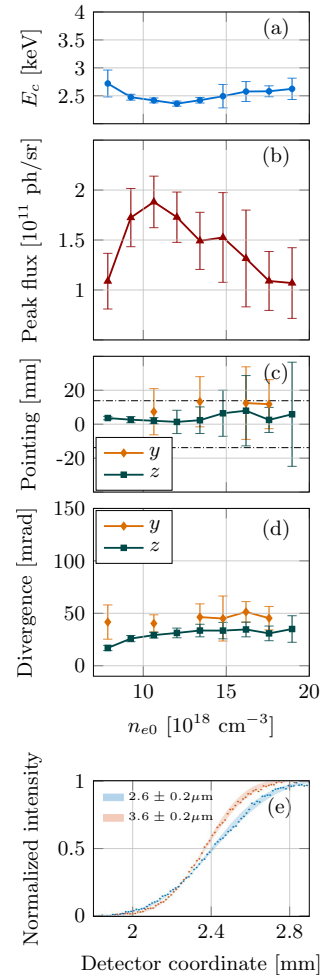

Figure 5.5. *Averaged results and standard deviation from ten laser shots at each electron number density: (a) critical energy, (b) peak photon flux, (c) pointing position in the sensor, and (d) FWHM divergence. The limits of the detector chip are marked by the dash-dotted black lines in (c). (e) (Dots) measurement of the X-ray diffraction and (shadow) theoretical fitting for a given source size, in (blue) the horizontal and (red) vertical direction.*

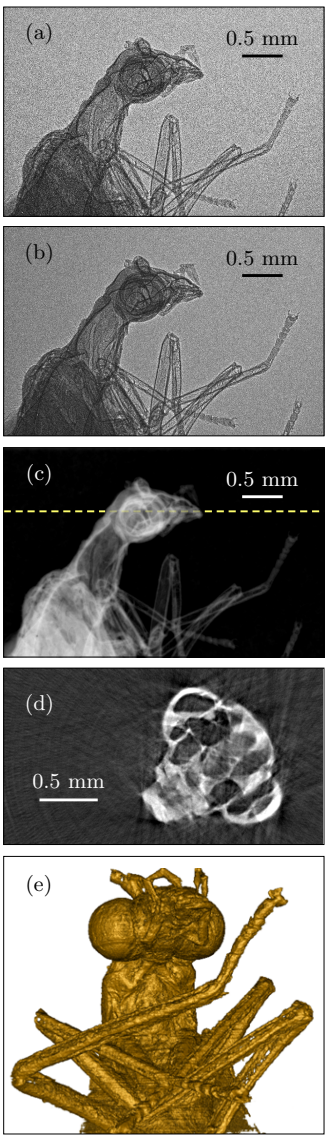

Figure 5.6. *(a) Raw and (b) averaged images, and (c) the projected thickness obtained by PCI. (d) A tomographic slice of the insect head, the position of which is indicated by the dashed line in (c). (e) Volume rendering obtained from the tomography slices.*

ticularly bright. Assuming an X-ray pulse duration of 10 fs [101], the peak brightness of the source at $n_e = 10.6 \times 10^{18}$ cm^{-3} was estimated to be 1.5×10^{21} photons/s/mm^2/mrad^2/0.1%BW, which is comparable to the X-ray brilliance available in the latest generation of synchrotrons [119].

Figure 5.6(a) shows a single-shot raw image of the insect studied by μCT. Five images were taken at each angle of rotation of the sample to increase the signal-to-noise ratio. The resolution of the images was noticeable increased, as ca be seen in Figure 5.6(b). Refraction of the X-rays at the volume boundaries produces edge enhancement, seen as a "glow" around the edges of the specimen. Details such as the hairs on the surface of the insect are distinguishable in these images, and features as small as 4 μm can be resolved, in accordance with the resolution limit given by the detector pixel size and source size. The phase shift was obtained using Paganin's algorithm [120], which assumes a single material in the sample, and from which the projected thickness was obtained (Figure 5.6(c)). Since this algorithm also acts as a low-pass filter, some of the details visible in Figure 5.6(b) are lost when retrieving the thickness.

PCI tomography was performed by rotating the object by 180°, in steps of 1°. Five data acquisitions were performed at each angle, making a total of 900 acquisitions. (Details on the in-line phase contrast method, geometry optimization, and tomography reconstruction can be found in Paper VIII.) The μCT image is retrieved applying the filtered back projection to the sinograms obtained from the projected thickness at different angular rotations, which allows the visualization of sections through the object, such as that shown in Figure 5.6(d). Volume-rendering software was used to create a 3D model of the sample, shown in Figure 5.6(e). The μCT allows details of the object as small as 13 μm to be visualized.

Although LWFA betatron X-rays have been shown to be a suitable and optimizable source of radiation for X-ray PCI and μCT, some limitations must be overcome before they can be used as an alternative to other sources [121]. In particular, a higher number of photons per X-ray pulse and a higher acquisition rate would be necessary to reduce the μCT acquisition time and to perform *in vivo* imaging [122]. Extension on the photon energy towards the 15-75 keV range is also necessary if the goal is medical applications, such as mammographies, angiography or tomography [107]. Such applications also require an increase in the field of view to a few tens of cm, which requires a substantial increase in the number of photons emitted. In any case, the spatial resolution provided by betatron X-rays today is already comparable to that provided by alternative sources, and the lower average photon flux of the betatron source also provides a better control of the dose on the object, which is of great importance for *in vivo* diagnostics.

5.2.2 Phase-contrast imaging of complex microstructures

As already discussed, PCI increases the contrast between different components with similar atomic number, in comparison to conventional X-ray absorption. For this reason PCI can also be applied to the study of microstructures in composite materials. This can be particularly useful in heterogeneous alloys, such as eutectic aluminium-silicon (Al-Si). The high corrosion resistance and low density of aluminium benefits from the addition of silicon as this improves the ductility and impact resistance of the alloy. This makes Al-Si widely used in industrial casting [123]. Eutectic Al-Si has non-periodic lamellae caused by the interfacial dynamics of the alloy during the solidification process, and the inter-lamellar spacing between the aluminium and silicon phases can be as fine as 1 µm. Paper IX describes the investigation of the potential of betatron X-ray imaging of alloy microstructures, by comparing eutectic Al-Si samples imaged with a LWFA-based X-ray source at CLF, with images obtained at a synchrotron beamline of the Swiss Light Source (SLS) at the Paul Scherrer Institute in Switzerland.

The geometry of the set-up used for PCI acquisition at the CLF is illustrated in Figure 5.7. The Astra-Gemini laser system delivers about 12 J, 40 fs FWHM, linearly polarized laser pulses on target, with a central wavelength at 800 nm. The laser pulses were focused to a 36.3 µm $1/e^2$ diameter spot at the entrance of a two-stage variable-length gas cell, reaching an estimated peak normalized vector potential of $a_0 \simeq 2.2$. Characterization of the gas cell showed that, at a plasma density of 4.1×10^{18} cm^{-3} in the 3 mm long first gas cell stage (filled with a gas mixture of 2% nitrogen and 98% helium) and 3.7×10^{18} cm^{-3} in the 15.5 mm long second stage (filled with pure helium), electrons were trapped in the density down-ramp between the two stages and accelerated in the second stage, reaching energies of around 1 GeV. The X-ray pulses generated were characterized with an array of Ross filters, providing an estimated critical energy of approximately 10 keV, with about 2×10^8 photons above 1 keV. The source size was estimated to be below 3 µm, with a divergence of a few mrad. The X-rays propagated through the Al-Si sample placed 193 mm away from the source and, after passing through Kapton and beryllium windows, were recorded with the Andor device, 4 m downstream.

The Al-Si samples were machined into a cylinder with a diameter of 1 mm and a thickness of 1 mm. Figure 5.8(a) shows a microscope image of one sample, and the corresponding betatron X-ray transmission is shown in (b). Details of the lamellar structures can already be discerned in the image, where the region indicated by the white square is enlarged in Figure 5.8(c). The line-out indicated by the black line in (c) is shown in (d). The lamellar structure can be clearly seen, and was fitted to a Gaussian function, giving a

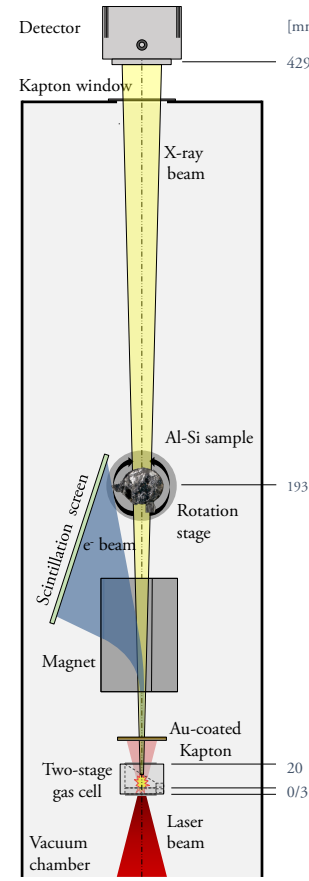

Figure 5.7. *Schematic of the experimental set-up for PCI of microstructures in a eutectic Al-Si alloy. The Au-coated Kapton blocks the laser light, and the accelerated electrons are dispersed away from the direction of X-ray beam propagation with a magnet dipole with a peak magnetic field of 1 T. The X-rays transmitted through the Al-Si sample are sent over 4 m to the X-ray detector. The longitudinal positions of the different elements of the set-up are given on the right-hand side (not to scale). The laser beam propagates upwards in the figure.*

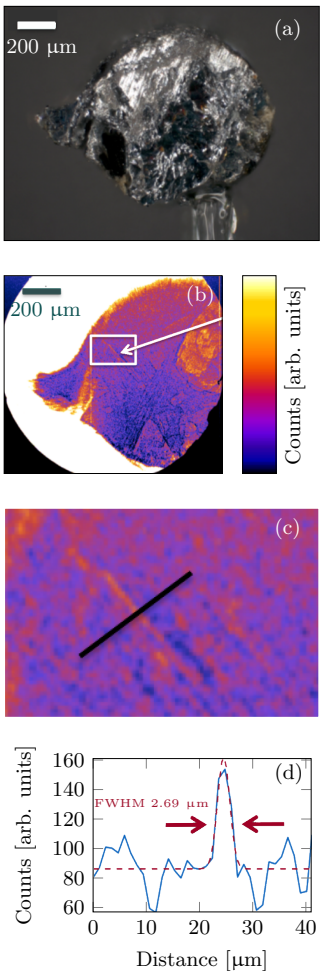

Figure 5.8. *(a) Microscope image and (b) betatron X-ray image of one of the eutectic Al-Si sample. (c) Enlargement of the region of interest indicated by the white square in (b), where lamellar structures can be seen. (d) Line-out of the black line in (c), showing a lamellar size smaller than 3 µm. (Adapted from Paper IX.)*

lamellar FWHM of 2.7 µm, demonstrating the < 3 µm resolution of the LWFA-based X-ray source.

A second eutectic Al-Si sample with 20% less silicon dopant, but manufactured using a similar casting process and having similar eutectic microstructures, was analysed at the tomographic microscopy and coherent radiology experiments (TOMCAT) beamline of the SLS. The X-rays source, with a source size of 127µm×38µm (FWHM), was sent to a monochromator set at 28 keV. The X-ray beam propagated in air to the Al-Si cylinder, placed 20 m away from the source, and to a 100 µm thick X-ray scintillation screen, placed 110 mm behind the sample, which fluorescence was 10× magnified and imaged in a 7.5 µm pixel size detector.

The performance of the two X-ray imaging sources was compared by evaluating the normalized sharpness and the spatial resolution obtained in each case. The overall sharpness was calculated with the algorithm proposed by Shaked and Tastl [124], while a Fourier-based criterion was used to define the spatial resolution [125]. (Further details on both methods can be found in Paper IX.) Comparison showed that the images obtained with the betatron source at the CLF are comparable in both sharpness and spatial resolution with respect to the images obtained at the SLS. The fact that the LWFA-based X-ray images can resolve high-frequency variations in the intensity, observed by comparison of the power spectral density function of the images, minimizes the artefacts that arise from the phase-retrieval algorithms required to analyse the phase-contrast images.

The average lamellar spacing measured in the Al-Si sample can be correlated to the average growth rate, which is of the order of a few µm/s, and to the undercooling of the material [126]. Real-time monitoring is necessary for the development and improvement of additive manufacturing but is not currently available [127], although some attempts have recently been made with synchrotron-based PCI [128–130]. The results reported in Paper IX thus suggest that betatron X-rays are a suitable source for such an application, with sufficient spatial and temporal resolution for time-resolved PCI of microstructured alloys.

5.3 Towards time-resolved spectroscopy of warm dense matter

The feature that currently offers the best potential in laser-wakefield X-ray sources is probably the femtosecond scale duration, comparable only to that in the scarcely available X-ray free-electron lasers. The short duration of the X-rays generated in a laser-wakefield accelerator can be exploited, for example, in temporally resolved X-ray absorption spectroscopy (XAS). The collimation of the source, typically below 100 mrad, is beneficial as it increases the photon col-

lection in the spectrometer. The X-ray source can also be used in a broad spectral range due to the broadband nature of the radiation. In addition, if part of the laser energy is split off before betatron generation, it can be used as a synchronized pump for pump–probe spectroscopy.

In particular, betatron radiation has attracted great interest regarding its applicability in XAS of phase transitions in mid-Z elements, whose absorption edges are in the keV range. In fact, the measurement of the X-ray transmission just above the absorption edge, known as X-ray absorption near edge structure (XANES), allows information to be recovered on the electronic density of states and atomic structure. An illustration of an XAS signal, the transmission of the K-edge of iron oxide Fe_2O_3 at 7.112 keV, is shown in Figure 5.9 [131]. The position, slope and structures of the edge and near edge depend on the valence, phase, oxidation and temperature of the matter, and evolve during the transition from one state to another. The very rapidly evolving transitions of warm dense matter (WDM) can be studied by analysing temporally resolved XANES.

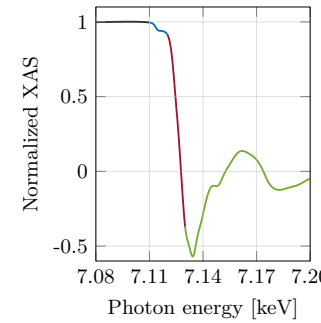

Figure 5.9. *Example of XAS transmission of the K-edge of iron oxide, where the pre-edge (blue), rising edge (red) and near edge (green) are differentiated [131].*

WDM refers to the transition state where matter is too hot to be considered a solid, but too dense to be considered as a plasma. This is a very interesting state of matter that plays an important role in the study of stars and inertial confinement fusion. However, it is a regime in which to numerical prediction is difficult. Calculations are often developed by *ab initio* methods, and although a few theoretical models have been proposed, they have yet to be compared with experimental measurements. Picosecond resolution of WDM has been achieved with X-rays produced with short laser pulses [132, 133] and in synchrotrons [134]. Femtosecond resolution requires shorter X-ray pulses, such as those generated in a laser-wakefield accelerator [135]. Betatron X-ray pulses are intrinsically short, being only a few fs long.

The goal of the study presented inPaper X was to design a crystal spectrometer for the optimization of XANES, with the aim of studying WDM with betatron X-rays produced in a laser-wakefield accelerator. A curved 20 mm × 20 mm HOPG crystal in the von Hamos configuration was used in the spectrometer, as described in Section 3.3.4. The mosaic spread of the HOPG crystal partially focuses the X-rays along the dispersion direction [87]. Furthermore, the crystal is placed such that its axis of curvature, indicated by the dotted line in Figure 5.10, does not coincide with the position of the source and the detector. The X-ray beam is then defocused on the detector. As shown in Figure 5.10(b), this allows angular resolution of the X-ray radiation in the direction perpendicular to the direction of X-ray diffraction. If the sample blocks only one half of the X-ray beam vertically, it is possible to identify two areas on the detector, one where the X-rays have propagated through the sample (red beam) and another where they have not, i.e. reference area (blue

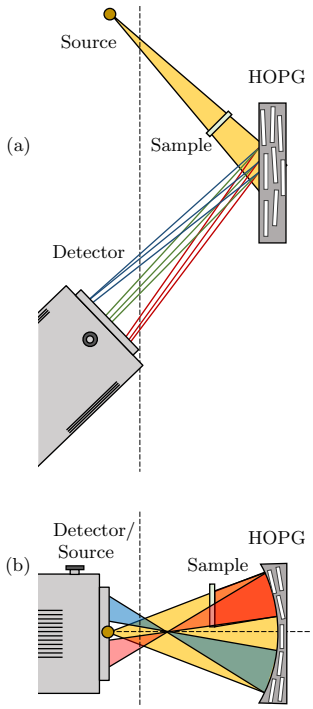

Figure 5.10. *Schematic of the spectrometer set-up: (a) top view and (b) side view. The axis of the X-ray crystal curvature is indicated by the dashed lines. (a) In the direction of propagation, the X-rays are diffracted at different wavelengths, while the mosaic spread partially focuses the beam. (b) In the direction perpendicular to propagation, the sample blocks half of the X-ray beam vertically, allowing both the spectral absorption (red) and a free-propagation reference (blue) to be recorded in a single shot.*

beam). In this way, XANES measurements can be self-referenced, overcoming problems associated with the limited shot-to-shot spectral stability the betatron X-rays. Ray-tracing modelling was performed to characterize the spectrometer, which is described in more detail in Paper X.

Several geometries were considered to study the absorption edges of iron, titanium, silver and copper, as shown in Figure 3.17. Finally, the configuration for the K-edge of copper was chosen, centred around 8.99 keV and corresponding to a Bragg angle of approximately $\theta_B = 11.9°$. As the edge absorption of copper is at a relatively high energy, a larger source–crystal distance is required that with the other materials considered. This increases the horizontal spread and improves the energy resolution, while facilitating the shielding of the detector from spurious radiation. Given the crystal curvature, $R_x = 115$ mm, the source–crystal distance was increased by 25% with respect to the focused position and set to $F' = 700$ mm, providing a compromise between the increase in angular resolution and the decrease in crystal efficiency. With this configuration, a spectrometer energy detection range of about 600 eV centred at 8.99 keV, and an energy resolution of approximately 6 eV were estimated with the ray-tracing model. The defocusing caused by the crystal was estimated to result in an angular resolution of about 10 mrad, and a horizontal spread of approximately 7 mm.

The spectrometer design was tested with betatron X-rays generated with the Lund multi-terawatt laser. An extension chamber was docked to the experimental chamber to accommodate the X-ray crystal and the detector in the desired geometry. LWFA was achieved by focusing the laser pulse to a FWHM spot size of 14 μm, reaching a peak intensity in vacuum estimated to be 3.6×10^{18} W/cm^2, at the entrance of a 6 mm fixed-length gas cell filled with a 99:1 mixture of helium and nitrogen. The electrons were dispersed away from the direction of X-ray propagation by a 200 mm long dipole magnet with a peak magnetic field of 0.8 T. Using a background plasma density set at about 10^{19} cm^{-3}, betatron X-rays with properties as described in Section 5.2.1 were generated, with a critical energy of approximately 2.5 keV. The sample used for the XANES was a 3 μm thick copper foil placed 30 mm behind the betatron source, blocking only of the X-ray beam in the direction perpendicular to the dispersion axis of the crysta. The crystal and detector were placed at the positions calculated above.

Figure 5.11(a) shows the angular spectral signal accumulated digitally for 315 shots. Due to the low flux of the signal in the detector, each measurement could be analysed by SPC. Events with photon energy outside the spectral range of the spectrometer were dismissed, significantly reducing the noise in the signal. The left side of the figure corresponds angularly to the reference beam, while the right side corresponds to the X-ray transmission through the copper foil. A sharp fall in transmission, corresponding to the K-edge,

can be seen above 8.99 keV for the X-rays transmitted through the 3 µm copper foil. The normalized XANES spectrum reconstructed from this signal is shown by the red line in Figure 5.11(b). The grey line corresponds to a reference spectrum obtained from cold copper [131, 136]. This reference was convoluted with a different instrument spectral broadening, to account for the penetration depth of the X-rays in the crystal. The best fit was observed for a FWHM broadening of 5.5 eV, close to the value of 5.9 eV estimated by comparing the result from ray-tracing model to the spectrometer response (see Paper X), and corresponding to a penetration depth in the HOPG crystal of approximately 700 µm.

A 40 mJ heating beam was extracted from the main laser beam and focused to a top-hat spot of 500 µm diameter onto the copper sample, reaching an estimate peak intensity of 5×10^{14} W/cm^2, and sent 2 ps before the X-rays arrived at the foil, in order to explore the time resolved XANES of heated copper. It was found that while the reduction in the laser energy decreased the flux of the generated betatron X-rays to less than half, most probably due to deterioration of the laser pulse wave front and focusing capability, the extracted energy was not sufficient to properly heat a volume of a 0.5 mm diameter, 1.5 µm thick copper foil. As a result, the XANES spectrum obtained from 700 measurements of heated copper was not conclusive. However, this experiment provided some very useful findings. It demonstrated the feasibility of angularly resolved XANES at 9 keV with LWFA betatron X-rays, as well as the ability of the ray-tracing model to estimate the response of the spectrometer with different geometries. Despite the mosaic spread of the crystal, the FWHM resolution of the spectrometer was found to be approximately 5.5 eV, allowing resolution of the XANES signal. It is expected that single-shot XANES could be achieved using this set-up with a more powerful laser system, for example, one that is ten times more energetic (10 J per pulse).

Very recently, after the publication of Paper X, the capability of a LWFA betatron source to perform XANES in the femtosecond regime of warm dense aluminium [137], and warm dense copper [101] has been demonstrated. Using a 2×50 TW laser system, sufficient signal and temporal resolution were obtained in the latter experiment to measure a rise time of 75 fs to an electron temperature above 10 000 K from the pre-edge of the L_2 and L_3 edges of copper. These two experiments on temporally resolved WDM represent a considerable step towards the application of betatron X-rays, especially considering the compactness of the X-ray generation and the feasibility of providing a synchronized heating pump.

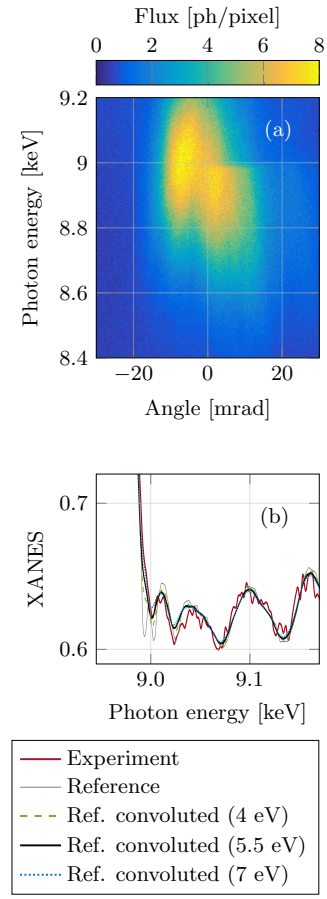

Figure 5.11. *(a) Experimental X-ray normalized transmission averaged over 315 shots and where single events outside the energy range of the spectrometer, 8.6-9.2 keV, have been removed. (b) Measured cold copper XANES spectra (red) compared to a reference spectrum (gray) [131], and to the convoluted reference with the modelled point spread function horizontally stretched to different FWHM. Adapted from Paper X.*

Chapter 6

Summary and outlook

During the work presented in this thesis, several experimental studies have demonstrated the utility of betatron X-rays as diagnostic tool for biology, materials science and warm dense matter. Characterization of the X-ray source produced during LWFA showed a very small source size, down to less than 3 μm, and a small divergence, between 20 and 50 mrad. The compactness of the radiation generation process made it particularly flexible and versatile for the implementation of set-ups for a wide range of applications and investigations. In addition, the very short pulse duration, of a few fs, is of great benefit, as betatron radiation can be used to resolve faster temporal events.

However, a number of limitations must be overcome before betatron X-rays can become an alternative to other X-ray sources [100, 121, 138]. The average flux of betatron X-rays is much lower than those provided by alternative sources, due to the limited number of photons emitted per X-ray pulse and the low repetition rate of TW lasers, usually 10 Hz, which limits the applicability of the source. Furthermore, betatron X-rays have poor shot-to-shot reproducibility, and it is difficult to tune the source parameters. Investigations of the trapping and acceleration processes of electrons in LWFA, the development of new accelerating plasma structures, studies of new regimes of X-ray generation, and progress towards more stable and higher repetition rate laser sources are necessary to overcome these restrictions. Some of these aspects were investigated in this work and were presented in Chapter 4.

The results described in the Chapter 5 of this thesis constitute some of the most recent successes in the application of betatron X-rays to high-spatial-resolution imaging of biological samples and complex materials, and to the time-resolved XAS of very hot plasmas. The results presented here demonstrate that betatron X-rays are becoming a real alternative to other X-ray sources. However, the studies described in Papers IX and X were made possible by collab-

oration with experts in materials science and in warm dense matter, respectively. They exemplify that the application of betatron X-rays will benefit from research carried out by a multidisciplinary scientific team. In order to transform this radiation into a useful source for other scientific disciplines, researchers in LWFA and betatron X-rays will need to work together with specialists in, for example, biology, medicine, materials science and high-energy-density science.

The author's contributions

I **Electron injector for compact staged high energy accelerator**
This paper describes the characterization and performance of a variable-length gas cell designed for the acceleration of electrons by LWFA, and carried out in two different laser facilities. The goal was to produce electron beams with high pointing stability and narrow energy spread for the development of an electron injector for multi-staging LWFA.
I took an active part in the performance of the experiment and acquisition of the data taken with the Lund multi-terawatt laser, and I provided feedback during preparation of the manuscript.

II **Investigation of ionization-induced electron injection in a wakefield driven by laser inside a gas cell**
In this study, a variable-length gas cell filled with a mixture of hydrogen and nitrogen was used for the acceleration of electrons that are trapped in the plasma wave by ionization-induced trapping. The electron beam charge, spectra, and maximum energy were analysed for different positions of the laser focal plane along the direction of propagation of the laser. Comparison of the experimental data with simulations showed that the position of the focal plane affects the nonlinear evolution of the laser beam in the plasma, having an effect on the trapping and acceleration of the electrons.
I took an active part in the performance of the experiment and data acquisition, and I provided feedback during preparation of the manuscript.

III **Localization of ionization-induced trapping in a laser wakefield accelerator using a density down-ramp**
The features of electrons trapped in a variable-length gas cell were compared for regimes of self-trapping and ionization-induced trapping. It was found that under certain conditions, ionization-induced trapping was localized in the density down-ramp at the exit of the gas cell, producing two peaks in the electron spectrum.
I took an active part in the performance of the experiment and data acquisition; I participated in the scientific discussions on the results from the experiment and simulations, and I provided feedback during preparation of the manuscript.

IV **A tunable electron beam source using trapping of electrons in a density down-ramp in laser wakefield acceleration**
This paper describes a numerical study with PIC simulations on the effect of the plasma density down-ramp parameters on the electron beam charge, energy spread, longitudinal length and emittance.
The PIC simulations were performed by the first author of the paper. I participated in discussions of the numerical results, and I provided feedback during preparation of the manuscript.

V **Effects of the dopant concentration in laser wakefield and direct laser acceleration of electrons**
This experiment was carried out to study the properties of electrons accelerated in a gas cell filled with a mixture of hydrogen and different concentrations of nitrogen. It was found that the charge trapped by ionization-induced trapping, which increased with increasing nitrogen concentration, was subjected to direct laser acceleration, producing a forked shape in the signal detected after electron dispersion in a magnetic field.
I took an active part in the performance of the experiment and data acquisition. The PIC simulations were performed by the second author of the paper. I analysed the experimental data, discussed the results from the experiment and simulations, and I wrote the manuscript.

VI **Electron acceleration and X-ray emission from interacting wakefields**

In this study, two laser pulses were focused in a gas at a small relative angle to study the interaction of laser wakefields produced by two laser pulses, by analysing the effects of the longitudinal position of the interaction and the temporal delay between the two laser pulses on the electron beam and X-ray pulse parameters.

I was co-applicant for laser beam-time to perform the experiment at CLPU, in Spain. I was main responsible for the design of the experiment, I took an active part in the building of the experimental set-up and data acquisition, I analysed the experimental data, and I wrote the manuscript.

VII **Analysis of electron injection in laser wakefield acceleration using betatron emission in capillary tubes**

The transverse intensity distribution of the betatron X-ray beam from electrons accelerated in a capillary was used to study the longitudinal emission of the X-rays generated. The results were compared for capillaries filled with pure hydrogen, a mixture of hydrogen and nitrogen, or a mixture of hydrogen and argon.

I took an active part in the acquisition of the argon mixture data and I provided feedback during preparation of the manuscript.

VIII **Optimization of soft X-ray phase-contrast tomography using a laser wakefield accelerator**

In this study, betatron X-rays produced in a gas cell by LWFA were optimized and used for phase-contrast tomography of an insect.

I was jointly responsible for the design and set-up of the experiment, and I was main responsible of the data acquisition. I also analysed the X-ray source characterization data and provided feedback during preparation of the manuscript.

IX **Laser-wakefield accelerators for high-resolution X-ray imaging of complex microstructures**
Betatron X-rays were used to resolve microstructures in an eutectic aluminium-silicon sample. The image quality was compared to that in images obtained using a synchrotron X-ray source.
I took part in the data acquisition for the X-ray source characterization, and I provided feedback during preparation of the manuscript.

X **Highly efficient angularly resolving X-ray spectrometer optimized for absorption measurements with collimated sources**
This paper presents an X-ray spectrometer designed to study the temporally resolved X-ray absorption of warm dense matter. The set-up was found to have a high efficiency and angular resolution, allowing the acquisition of self-referenced data with a LWFA-based X-ray source.
I took an active part in the design and building of the experimental set-up, and had main responsibility for the betatron X-ray generation and data acquisition. I provided feedback during preparation of the manuscript.

I have also contributed to the upgrade and maintenance of the Lund multi-terawatt laser system, and its operation during the studies described in Papers I-III, V, VII, VIII and X, as well as other experiments not included here.

Acknowledgements

What I enjoy most about science is how it brings people together. There would be no advanced technology today if the development science were confined to individuals. These lines are for those whose help, talent and support made the work I have described here possible.

I would like to thank Prof. Dr. Claes-Göran Wahlström and Dr. Olle Lundh for their enthusiastic invitation to come to Lund more than four years ago, and for giving me the opportunity to become involved in this adventure. Olle, thank you for your supervision and support during these years. When things were delayed, did not work, or were just incomprehensible, you always had a calm and optimistic attitude. Thank you also for never letting me underestimate any of my own work. Claes-Göran, thank you for having your door always open for any "stupid questions" or concerns, and for your effort to make everyone feel notable, both in the group, and the whole division.

I am extremely grateful to have met and worked with Dr. Anders Persson. Thank you for everything you have taught me, for all your support in the lab, and my special thanks for all your help outside the lab.

I have had some great colleagues in our research group, and I would like to thank them all for the time we have spent together. Henrik, discussing anything with you, physics or life, always provides me with some priceless learning. Infinite thanks for your PIC simulations, lab work, discussions, support and, overall, friendship. Thanks to Martin for being such a mentor to me when I was new in the group, for your capacity to easily explain complicated physics, and for being such a nice office-mate and friend. I would also like to thank Jonas, for your enthusiasm whether talking on accelerating schemes or food; Diego, for your active approach to work, and for your esteem for Bolita; Kristoffer, for your always positive attitude; and Bastian, for boosting my knowledge on the laser during the short time we shared in the lab. It has been a pleasure to work with all of you. Thanks also to the "proton people": Lovisa, Kristoffer, Malay, Alexander and Giada. You have been great company and colleagues. Thank you Ellen for the translation

of the popular summary. I would also like to express my thanks to my former colleagues in Salamanca, and in particular to Cruz, for sowing the seed that developed into this thesis.

I have participated in many international collaborations, learning new ways of working and thinking. I would like to extend my gratitude to all the people I met during these projects: Xavier; Brigitte, Thomas, Frédéric and Sandrine; Lorenzo, Piotr and Valentina; Kateřina, Michal and the PALS team; Brendan, Matthew, Stuart, Jason, Jonathan, Elias, Nuno, Amina and the Astra-Gemini team; and Giancarlo, Jose Antonio, Carlos, Ghassan, and the VEGA team. Thanks also to those participating in the PLIONA project for such interesting discussions.

I would also like to thank to everyone at the Atomic Physics Division, including professors and lectures, researchers, students and former members, for contributing to such a stimulating atmosphere. Special thanks to Anne and Jakob for keeping everything outside the labs working, and infinite thanks to Åke for recovering the files of this thesis when they got lost!

I have met and worked with many people through various networks I became involved in the Department of Physics. Karolina, Yupan, Christoffer, and Damiano, thanks for the incredible journey involved in organizing the IONS. Elin, Kajsa, Dina and Egle, working with you in the Female Research Network has been one of my most inspiring experiences.

My friends have always been the best of me. In the past thirty years, I have met some of the best people in the world at school, camps, volunteering, university, Erasmus, public libraries, hikes, apartments, festivals and workplaces. Thanks for always having me with you, in your mind, or as a life-size printed cardboard version of me, while work on this thesis kept us apart. And thanks also to the very random and loving "host family" that I found in Lund, you made me feel here at home.

I cannot express in words what my family means to me. They have constantly and unconditionally believed in me in everything I have undertaken. Barri, Mam, Juanete, Alvi, Poulo. Thank you for never, not even for one second, thinking I would not succeed in my undertakings, including this thesis.

The last mention is to the person who has probably been affected most by my work on this thesis. Thank you Constantin, for always trying to bring sunshine into my cloudy thoughts, and for giving me the best sound in the world, your laughter.

Bibliography

1. T. Tajima and J. M. Dawson. *Laser electron accelerator.* Phys. Rev. Lett. **43**, 267 (1979).

2. T. H. Maiman. *Stimulated optical radiation in ruby.* Nature **187**, 493–494 (1960).

3. C. E. Clayton, C. Joshi, C. Darrow and D. Umstadter. *Relativistic plasma-wave excitation by collinear optical mixing.* Phys. Rev. Lett. **54**, 2343 (1985).

4. F. Amiranoff, M. Laberge, J. R. Marquès, F. Moulin, E. Fabre, B. Cros, G. Matthieussent, P. Benkheiri, F. Jacquet, J. Meyer, Ph. Miné, C. Stenz and P. Mora. *Observation of modulational instability in Nd-laser beat-wave experiments.* Phys. Rev. Lett. **68**, 3710 (1992).

5. Y. Kitagawa, T. Matsumoto, T. Minamihata, K. Sawai, K. Matsuo, K. Mima, K. Nishihara, H. Azechi, K. A. Tanaka, H. Takabe and S. Nakai. *Beat-wave excitation of plasma wave and observation of accelerated electrons.* Phys. Rev. Lett. **68**, 48 (1992).

6. A. Modena, Z. Najmudin, A. E. Dangor, C. E. Clayton, K. A. Marsh, C. Joshi, V. Malka, C. B. Darrow, C. Danson, D. Neely and F. N. Walsh. *Electron acceleration from the breaking of relativistic plasma waves.* Nature **337**, 606–608 (1995).

7. R. Wagner, S.-Y. Chen, A. Maksimchuk and D. Umstadter. *Electron acceleration by a laser wakefield in a relativistically self-guided channel.* Phys. Rev. Lett. **78**, 3125 (1997).

8. D. Gordon, K. C. Tzeng, C. E. Clayton, A. E. Dangor, V. Malka, K. A. Marsh, A. Modena, W. B. Mori, P. Muggli, Z. Najmudin, D. Neely, C. Danson and C. Joshi. *Observation of electron energies beyond the linear dephasing limit from a laser-excited relativistic plasma wave.* Phys. Rev. Lett. **80**, 2133 (1998).

9. C. E. Clayton, K. A. Marsh, A. Dyson, M. Everett, A. Lal, W. P. Leemans, R. Williams and C. Joshi. *Ultrahigh-gradient*

acceleration of injected electrons by laser-excited relativistic electron plasma waves. Phys. Rev. Lett. **70**, 37 (1993).

10. K. Nakajima, D. Fisher, T. Kawakubo, H. Nakanishi, A. Ogata, Y. Kato, Y. Kitagawa, R. Kodama, K. Mima, H. Shiraga, K. Suzuki, K. Yamakawa, T. Zhang, Y. Sakawa, T. Shoji, Y. Nishida, N. Yugami, M. Downer and T. Tajima. *Observation of ultrahigh gradient electron acceleration by a self-modulated intense short laser pulse.* Phys. Rev. Lett. **74**, 4428 (1995).

11. F. Amiranoff, S. Baton, D. Bernard, B. Cros, D. Descamps, F. Dorchies, F. Jacquet, V. Malka, J. R. Marquès, G. Matthieussent, P. Miné, A. Modena, P. Mora, J. Morillo and Z. Najmudin. *Observation of laser wakefield acceleration of electrons.* Phys. Rev. Lett. **81**, 995 (1998).

12. E. Adli, A. Ahuja, O. Apsimon, R. Apsimon, A.-M. Bachmann, D. Barrientos, F. Batsch, J. Bauche, V. K. Berglyd Olsen, M. Bernardini, T. Bohl, C. Bracco, F. Braunmüller, G. Burt, B. Buttenschön, A. Caldwell, M. Cascella, J. Chappell, E. Chevallay, M. Chung, D. Cooke, H. Damerau, L. Deacon, L. H. Deubner, A. Dexter, S. Doebert, J. Farmer, V. N. Fedosseev, R. Fiorito, R. A. Fonseca, F. Friebel, L. Garolfi, S. Gessner, I. Gorgisyan, A. A. Gorn, E. Granados, O. Grulke, E. Gschwendtner, J. Hansen, A. Helm, J. R. Henderson, M. Hüther, M. Ibison, L. Jensen, S. Jolly, F. Keeble, S.-Y. Kim, F. Kraus, Y. Li, S. Liu, N. Lopes, K. V. Lotov, L. Maricalva Brun, M. Martyanov, S. Mazzoni, D. Medina Godoy, V. A. Minakov, J. Mitchell, J. C. Molendijk, J. T. Moody, M. Moreira, P. Muggli, E. Öz, C. Pasquino, A. Pardons, F. Peña Asmus, K. Pepitone, A. Perera, A. Petrenko, S. Pitman, A. Pukhov, S. Rey, K. Rieger, H. Ruhl, J. S. Schmidt, I. A. Shalimova, P. Sherwood, L. O. Silva, L. Soby, A. P. Sosedkin, R. Speroni, R. I. Spitsyn, P. V. Tuev, M. Turner, F. Velotti, L. Verra, V. A. Verzilov, J. Vieira, C. P. Welsch, B. Williamson, M. Wing, B. Woolley and G. Xia. *Acceleration of electrons in the plasma wakefield of a proton bunch.* Nature **561**, 363–367 (2018).

13. D. Strickland and G. Mourou. *Compression of amplified chirped optical pulses.* Opt. Commun. **56**, 219–221 (1985).

14. G. E. Cook. *Pulse compression-key to more efficient radar transmission.* IEEE Proc. IRE **48**, 310–316 (1960).

15. S. Kiselev, A. Pukhov and I. Kostyukov. *X-ray generation in strongly nonlinear plasma waves.* Phys. Rev. Lett. **93**, 135004 (2004).

16. A. Rousse, K. Ta Phuoc, R. Shah, A. Pukhov, E. Lefebvre, V. Malka, S. Kiselev, F. Burgy, J.-P. Rousseau, D. Umstadter and D. Hulin. *Production of a keV X-ray beam from synchro-*

tron radiation in relativistic laser-plasma interaction. Phys. Rev. Lett. **93**, 135005 (2004).

17. S. P. D. Mangles, C. D. Murphy, Z. Najmudin, A. G. R. Thomas, J. L. Collier, A. E. Dangor, E. J. Divall, P. S. Foster, J. G. Gallacher, C. J. Hooker, D. A. Jaroszynski, A. J. Langley, W. B. Mori, P. A. Norreys, F. S. Tsung, R. Viskup, B. R. Walton and K. Krushelnick. *Monoenergetic beams of relativistic electrons from intense laser-plasma interactions.* Nature **431**, 535–538 (2004).

18. C. G. R. Geddes, Cs. Toth, J. van Tillborg, E. Esarey, C. B. Schroeder, D. Cruhwiler, C. Nieter, J. Cary and W. P. Leemans. *High-quality electron beams from a laser wakefield accelerator using plasma-channel guiding.* Nature **431**, 538–541 (2004).

19. J. Faure, Y. Glinec, A. Pukhov, S. Kiselev, S. Gordienko, E. Lefebvre, J.-P. Rousseau, F. Burgy and V. Malka. *A laser-plasma accelerator producing monoenergetic electron beams.* Nature **431**, 541–544 (2004).

20. A. E. Siegman. *Lasers.* Univ Science Books (1986). ISBN 0-93570-211-3.

21. P. Gibbon. *Short Pulse Laser Interactions with Matter.* Imperial College Press (2005). ISBN 1-86094-135-4.

22. G. Genoud. *Laser-driven plasma waves for particle acceleration and X-ray production.* PhD thesis Lund University, LRAP-443 (2011).

23. E. Esarey, P. Sprangle, J. Krall and A. Ting. *Overview of plasma-based accelerator concepts.* IEEE Trans. Plasma Sci. **24**, 252–288 (1996).

24. W. L. Kruer. *The physics of laser plasma interactions.* Westview Press (1988). ISBN 9780813340838.

25. E. Esarey, C. B. Schroeder and W. P. Leemans. *Physics of laser-driven plasma-based electron accelerators.* Rev. Mod. Phys. **81**, 1229 (2009).

26. P. Sprangle, E. Esarey, J. Krall and G. Joyce. *Propagation and guiding of intense laser pulses in plasmas.* Phys. Rev. Lett. **69**, 2200 (1992).

27. E. Esarey, P. Sprangle, J. Krall, A. Ting and G. Joyce. *Optically guided laser wake-field acceleration.* Phys. Fluids B Plasma Phys. **5**, 2690 (1993).

28. L. M. Gorbunov and V. I. Kirsanov. *Excitation of plasma waves by an electromagnetic wave packet.* Sov. Phys. JETP **66**, (2) (1987).

29. E. Guillaume. *Control of electron injection and acceleration in laser-wakefield accelerators.* PhD thesis Écoles Polytechnique (2015).

30. D. Teychenne, G. Bonnaud and J.-L. Bobin. *Wave-breaking limit to the wake-field effect in an underdense plasma.* Phys. Rev. E **48**, R3248(R) (1993).

31. E. Esarey, A. Ting, P. Sprangle, D. Umstadter and X. Liu. *Nonlinear analysis of relativistic harmonic generation by intense lasers in plasmas.* IEEE Trans. Plasma Sci. **21**, 95–104 (1993).

32. W. Lu, M. Tzoufras, C. Joshi, F. S. Tsung, W. B. Mori, J. Vieira, R. A. Fonseca and L. O. Silva. *Generating multi-GeV electron bunches using single stage laser wakefield acceleration in a 3D nonlinear regime.* Phys. Rev. ST Accel. Beams **10**, 061301 (2007).

33. A. Pukhov and J. Meyer-ter-vehn. *Laser wake field acceleration: the highly non-linear broken-wave regime.* App. Phys. B **74**, 355–361 (2002).

34. W. Lu, C. Huang, M. Zhou, W. B. Mori and T. Katsouleas. *Nonlinear theory for relativistic plasma wakefields in the blowout regime.* Phys. Rev. Lett. **96**, 165002 (2006).

35. J. B. Rosenzweig, B. Breizman, T. Katsouleas and J. J. Su. *Acceleration and focusing of electrons in two-dimensional nonlinear plasma wake fields.* Phys. Rev. A **44**, R6189(R) (1991).

36. W. Lu, C. Huang, M. Zhou and M. Tzoufras. *A nonlinear theory for multidimensional relativistic plasma wave wakefields.* Phys. Plasmas **13**, 056709 (2006).

37. A. F. Lifschitz, X. Davoine, E. Lefebvre, J. Faure, C. Rechatin and V. Malka. *Particle-in-cell modelling of laser-plasma interaction using Fourier decomposition.* J. Comput. Phys. **228**, 1803–1814 (2009).

38. E. Esarey and M. Pilloff. *Trapping and acceleration in nonlinear plasma waves.* Phys. Plasmas **2**, 1432 (1995).

39. C. Rechatin, X. Davoine, A. Lifschitz, A. Ben Ismail, J. Lim, E. Lefebvre, J. Faure and V. Malka. *Observation of beam loading in a laser-plasma accelerator.* Phys. Rev. Lett. **103**, 194804 (2009).

40. M. Tzoufras, W. Lu, F. S. Tsung, C. Huang, W. B. Mori, T. Katsouleas, J. Vieira, R. A. Fonseca and L. O. Silva. *Beam loading in the nonlinear regime of plasma-based acceleration.* Phys. Rev. Lett. **101**, 145002 (2008).

41. M. Hansson. *Controlled trapping in laser wakefield accelerators.* PhD thesis Lund University, LRAP-516 (2016).

42. A. Pak, K. A. Marsh, S. F. Martins, W. Lu, W. B. Mori and C. Joshi. *Injection and trapping of tunnel-ionized electrons into laser-produced wakes.* Phys. Rev. Lett. **104**, 025003 (2010).

43. C. McGuffey, A. G. R. Thomas, W. Schumaker, T. Matsuoka, V. Chvykov, F. J. Dollar, G. Kalintchenko, V. Yanovsky, A. Maksimchuk and K. Krushelnick. *Ionization induced trapping in a laser wakfield accelerator.* Phys. Rev. Lett. **104**, 025004 (2010).

44. M. Mirzaie, S. Li, M. Zeng, N. A. M. Hafz, M. Chen, G. Y. Li, Q. J. Zhu, H. Liao, T. Sokollik, F. Liu, Y. Ma, L. M. Chen, Z. M. Sheng and J. Zhang. *Demonstration of self-truncated ionization injection for GeV electron beams.* Sci. Rep. **5**, 14659 (2015).

45. S. Bulanov, N. Naumova, F. Pegoraro and J. Sakai. *Particle injection into the wave acceleration phase due to nonlinear wake wave breaking.* Phys. Rev. E **58**, R5257(R) (1998).

46. H. Suk, N. Barov, J. B. Rosenzweig and E. Esarey. *Plasma electron trapping and acceleration in a plasma wake field using a density transition.* Phys. Rev. Lett. **86**, 1011 (2001).

47. M. Vargas, W. Schumaker, Z.-H. He, Z. Zhao, K. Behm, V. Chvykov, B. Hou, K. Krushelnick, A. Maksimchuk, V. Yanovsky and A. G. R. Thomas. *Improvements to laser wakefield accelerated electron beam stability, divergence, and energy spread using three-dimensional printed two-stage gas cell targets.* Appl. Phys. Lett. **104**, 174103 (2014).

48. J. S. Liu, C. Q. Xia, W. T. Wang, H. Y. Lu, C. Wang, A. H. Deng, W. T. Li, H. Zhang, X. Y. Liang, Y. X. Leng, X. M. Lu, C. Wang, J. Z. Wang, K. Nakajima, R. X. Li and Z. Z. Xu. *All-optical cascaded laser wakefield accelerator using ionization-induced injection.* Phys. Rev. Lett. **107**, 035001 (2011).

49. B. B. Pollock, C. E. Clayton, J. E. Ralph, F. Albert, A. Davidson, L. Divol, C. Filip, S. H. Glenzer, K. Herpoldt, W. Lu, K. A. Marsh, J. Meinecke, W. B. Mori, A. Pak, T. C. Rensink, J. S. Ross, J. Shaw, G. R. Tynan, C. Joshi and D. H. Froula. *Demonstration of a narrow energy spread,* ~ 0.5 GeV *electron beam from a two-stage laser wakefield accelerator.* Phys. Rev. Lett. **107**, 045001 (2011).

50. H. T. Kim, K. H. Pae, H. J. Cha, I. J. Kim, T. J. Yu, J. H. Sung, S. K. Lee, T. M. Jeong and J. Lee. *Enhancement of electron energy to the multi-GeV regime by a dual-stage laser-wakefield accelerator pumped by petawatt laser pulses.* Phys. Rev. Lett. **111**, 165002 (2013).

51. G. Golovin, S. Chen, N. Powers, C. Liu, S. Banerjee, J. Zhang, M. Zeng, Z. Sheng and D. Umstadter. *Tunable monoenergetic*

electron beams from independently controllable laser-wakefield acceleration and injection. Phys. Rev. ST Accel. Beams **18**, 011301 (2015).

52. S. Steinke, J. van Tilborg, C. Benedetti, C. G. R. Geddes, C. B. Schroeder, J. Daniels, K. K. Swanson, A. J. Gonsalves, K. Nakamura, N. H. Matlis, B. H. Shaw, E. Esarey and W. P. Leemans. *Multistage coupling of independent laser-plasma accelerators.* Nature **530**, 190–193 (2016).

53. E. Esarey, P. Sprangle, J. Krall and A. Ting. *Self-focusing and guiding of short laser pulses in ionizing gases and plasmas.* IEEE J. Quantum Electron. **33**, 1879–1914 (1997).

54. A. G. Litvak. *Finite-amplitude wave beams in a magnetoactive plasma.* Sov. Phys. JETP **30**, 344–347 (1970).

55. C. E. Max, J. Arons and A. B. Langdon. *Self-modulation and self-focusing of electromagnetic waves in plasmas.* Phys. Rev. Lett. **33**, 209 (1974).

56. P. Sprangle, C.-M. Tang and E. Esarey. *Relativistic self-focusing of short-pulse radiation beams in plasmas.* IEEE Trans. Plasma Sci. **15**, 145–153 (1987).

57. G.-Z. Sun, E. Ott, Y. C. Lee and P. Guzdar. *Self-focusing of short intense pulses in plasmas.* Phys. Fluids **30**, 526 (1987).

58. W. B. Mori. *The physics of the nonlinear optics of plasmas at relativistic intensities for short-pulse lasers.* IEEE J. Quantum Electron. **33**, 1942–1953 (1997).

59. J. Faure, V. Malka, J.-R. Marquès, P.-G. David and F. Amiranoff. *Effects of pulse duration on self-focusing of ultra-short lasers in underdense plasmas.* Phys. Plasmas **9**, 756 (2002).

60. S. Corde, K. Ta Phuoc, G. Lambert, R. Fitour, V. Malka, A. Rousse, A. Beck and E. Lefebvre. *Femtosecond X rays from laser-plasma accelerators.* Rev. Mod. Phys. **85**, 1 (2013).

61. E. Esarey, B. A. Shadwick, P. Catravas and W. P. Leemans. *Synchrotron radiation from electron beams in plasma-focusing channels.* Phys. Rev. E **65**, 056505 (2002).

62. J. D. Jackson. *Classical electrodynamics.* Wiley, New York (1975).

63. O. Lundh, J. Lim, C. Rechatin, L. Ammoura, A. Ben-Ismail, X. Davoine, G. Gallot, J.-P. Goddet, E. Lefebvre, V. Malka and J. Faure. *Few femtosecond, few kiloampere electron bunch produced by a laser–plasma accelerator.* Nat. Phys. **7**, 219–222 (2011).

64. S. Svanberg, J. Larsson, A. Persson and C.-G. Wahlström. *Lund high-power laser facility - systems and first results.* Phys.

Scr. **49**, 187 (1994).

65. D. E. Spence, P. N. Kean and W. Sibbett. *60-fsec pulse generation from a self-mode-locked Ti:sapphire laser.* Opt. Lett. **16**, 42–44 (1991).

66. M. Glimtoft. *Contrast enhancement of femtosecond terawatt laser pulses by preamplification and temporal pulse cleaning.* Master's thesis Lund University, LRAP-352 (2006).

67. P. Tournois. *Acousto-optic programmable dispersive filter for adaptive compensation of group delay time dispersion in laser systems.* Opt. Commun. **140**, 245–249 (1997).

68. S. Fourmaux, S. Payeur, S. Buffechoux, P. Lassonde, C. St-Pierre, F. Martin and J. C. Kieffer. *Pedestal cleaning for high laser pulse contrast ratio with a 100 TW class laser system.* Opt. Express **19**, 8486–8497 (2011).

69. K. Schmid and L. Veisz. *Supersonic gas jets for laser-plasma experiments.* Rev. Sci. Instrum. **83**, 053304 (2012).

70. K. Svensson, M. Hansson, F. Wojda, L. Senje, M. Burza, B. Aurand, G. Genoud, A. Persson, C.-G. Wahlström and O. Lundh. *Supersonic jets of hydrogen and helium for laser wakefield acceleration.* Phys. Rev. Accel. Beams **19**, 051301 (2016).

71. K. Svensson. *Experiments on laser-based particle acceleration.* PhD thesis Lund University, LRAP-527 (2016).

72. Y. Glinec, J. Faure, A. Guemmnie-Tafo, V. Malka, H. Monard, J. P. Larbre, V. De Waele, J. L. Marignier and M. Mostafavi. *Absolute calibration for a broad range single shot electron spectrometer.* Rev. Sci. Instrum. **77**, 103301 (2006).

73. J. Ju. *Electron acceleration and betatron radiation driven by laser wakefield inside dielectric capillary tubes.* PhD thesis Université Paris Sud (2013).

74. R. Nowotny and A. Taubeck. *A method for the production of composite scintillators for dosimetry in diagnostics radiology.* Phys. Med. Biol. **54**, 1457 (2009).

75. A. Buck, K. Zeil, A. Popp, K. Schmid, A. Jochmann, S. D. Kraft, B. Hidding, T. Kudyakov, C. M. S. Sears, L. Veisz, S. Karsch, J. Pawelke, R. Sauerbrey, T. Cowan, F. Krausz and U. Schramm. *Absolute charge calibration of scintillating screens for relativistic electron detection.* Rev. Sci. Instrum. **81**, 033301 (2010).

76. F. Albert, K. Ta Phuoc, R. Shah, S. Corde, R. Fitour, A. Tafzi, F. Burgy, D. Douillet, T. Lefrou and A. Rousse. *Full characterization of laser-produced keV X-ray betatron source.* Plasma Phys. Control. Fusion **50**, 124008 (2008).

77. P. Kirkpatrick. *On the theory and use of Ross filters.* Rev. Sci. Instrum. **10**, 186 (1939).

78. P. Kirkpatrick. *Theory and use of Ross filters II.* Rev. Sci. Instrum. **15**, 223 (1944).

79. S. Fourmaux, S. Corde, K. Ta Phuoc, P. M. Leguay, S. Payeur, P. Lassonde, S. Gnedyuk, G. Lebrun, C. Fourment and V. Malka. *Demonstration of the synchrotron-type spectrum of laser-produced betatron radiation.* New J. Phys. **13**, 033017 (2011).

80. B. R. Maddox, H. S. Park, B. A. Remington and M. McKernan. *Calibration and characterization of single photon counting cameras for short-pulse laser experiments.* Rev. Sci. Instrum. **79**, 10E924 (2008).

81. W. Fullagar, J. Uhlig, M. Walczak, S. Canton and V. Sundström. *The use and characterization of a backilluminated charge-coupled device in investigations of pulsed X-ray and radiation sources.* Rev. Sci. Instrum. **79**, 103302 (2008).

82. R. C. Shah, F. Albert, K. Ta Phuoc, O. Shevchenko, D. Boschetto, A. Pukhov, S. Kiselev, F. Burgy, J.-P. Rousseau and A. Rousse. *Coherence-based transverse measurement of synchrotron X-ray radiation from relativistic laser-plasma interaction and laser-accelerator electrons.* Phys. Rev. E **74**, 045401(R) (2006).

83. S. Kneip, C. McGuffey, J. L. Martins, S. F. Martins, C. Bellei, V. Chvykov, F. Dollar, R. Fonseca, C. Huntington, G. Kalintchenko, A. Maksimchuk, S. P. D. Mangles, T. Matsuoka, S. R. Nagel, C. A. J. Palmer, J. Schreiber, K. T. Phuoc, A. G. R. Thomas, V. Yanovsky, L. O. Silva, K. Krushelnick and Z. Najmudin. *Bright spatially coherent synchrotron X-rays from a table-top source.* Nat. Phys. **6**, 980–983 (2010).

84. M. Schnell, A. Sävert, B. Landgraf, M. Reuter, M. Nicolai, O. Jäckel, C. Peth, T. Thiele, O. Jansen, A. Pukhov, O. Willi, M. C. Kaluza and C. Spielmann. *Deducing the electron-beam diameter in a laser-plasma accelerator using X-ray betatron radiation.* Phys. Rev. Lett. **108**, 075001 (2012).

85. I. N. Tilikin, T. A. Shelkovenko, S. A. Pikuz and D. A. Hammer. *Determination of the size of a radiation source by the method of calculation of diffraction patterns.* Optika i Spektrokopiya **115**, 147–156 (2013).

86. D. B. Thorn, C. G. R. Geddes, N. H. Matlis, G. R. Plateau, E. H. Esarey, M. Battaglia, C. B. Schroeder, S. Shiraishi, T. Stöhlker, C. Tóth and W. P. Leemans. *Spectroscopy of betatron radiation emitted from laser-produced wakefield accelerated electrons.* Rev. Sci. Instrum. **81**, 10E325 (2010).

87. H. Legall, H. Stiel, M. Schnürer, M. Pagels, B. Kanngießer, M. Müller, B. Beckhoff, I. Grigorieva, A. Antonov, V. Arkadiev and A. Bjeoumikhov. *An efficient X-ray spectrometer based on thin mosaic crystal films and its application in various fields of X-ray spectroscopy.* J. Appl. Cryst. **42**, 572–579 (2009).

88. L. von Hamos. *Röntgenspektroskopie und Abbildung mittels gekrümmter Kristallreflektoren.* Naturwissenschaften **20**, 705–706 (1932).

89. C. K. Birdsall and A. B. Langdon. *Plasma physics via computer simulation.* Adam Hilger (1991). ISBN 0-07-005371-5.

90. B. Cros, B. S. Paradkar, X. Davoine, A. Chancé, F. G. Desforges, S. Dobosz-Dufrénoy, N. Delerue, J. Ju, T. L. Audet, G. Maynard, M. Lobet, L. Gremillet, P. Mora, J. Schwindling, O. Delferriére, C. Bruni, C. Rimbault, T. Vinatier, A. D. Piazza, M. Grech, C. Riconda, J. R. Marquès, A. Beck, A. Specka, P. Martin, P. Monot, D. Normand, F. Mathieu, P. Audebert and F. Amiranoff. *Laser plasma acceleration of electron with multi-PW laser beams in the frame of CILEX.* Nucl. Instrum. Methods Phys. Res. A **740**, 27–33 (2014).

91. M. Chen, E. Esarey, C. B. Schroeder, C. G. R. Geddes and W. P. Leemans. *Theory of ionization-induced trapping in laser-plasma accelerators.* Phys. Plasmas **19**, 033101 (2012).

92. J.-L. Vay, D. P. Grote, R. H. Cohen and A. Friedman. *Novel methods in the particle-in-cell accelerator code-framework Warp.* Comput. Sci. Disc. **5**, 014019 (2012).

93. J. L. Shaw, N. Lemos, L. D. Amorim, N. Vafaei-Najafabadi, K. A. Marsch, F. S. Tsung, W. B. Mori and C. Joshi. *Role of direct laser acceleration of electrons in a laser wakefield accelerator with ionization injection.* Phys. Rev. Lett. **118**, 064801 (2017).

94. A. Pukhov, Z.-M. Sheng and J. Meyer-ter-Vehn. *Particle acceleration in relativistic laser channels.* Phys. Plasmas **6**, 2847 (1999).

95. A. Pukhov. *Strong field interaction of laser radiation.* Rep. Prog. Phys. **66**, 47 (2003).

96. M. Wen, B. Shen, X. Zhang, L. Ji, W. Wang, J. Xu and Y. Yu. *Generation of high charged energetic electrons by using multi-parallel laser pulses.* Phys. Plasmas **17**, 103113 (2010).

97. C. Ren, R. G. Hemker, R. A. Fonseca, B. J. Duda and W. B. Mori. *Mutual attraction of laser beams in plasmas: braided light.* Phys. Rev. Lett. **85**, 2124 (2000).

98. L. Yang, Z. Deng, C. T. Zhou, M. Y. Yu and X. Wang. *High-charge energetic electron bunch generated by intersecting laser*

pulses. Phys. Plasmas **20**, 033102 (2013).

99. E. Wallin, A. Gonoskov and M. Marklund. *Radiation emission from braided electrons in interacting wakefields*. Phys. Plasmas **24**, 093101 (2017).

100. F. Albert and A. G. R. Thomas. *Applications of laser wakefield accelerator-based light sources*. Plasma Phys. Control. Fusion **58**, 103001 (2016).

101. B. Mahieu, N. Jourdain, K. Ta Phuoc, F. Dorchies, J.-P. Goddet, A. Lifschitz, P. Renaudin and L. Lecherbourg. *Probing warm dense matter using femtosecond X-ray absorption spectroscopy with a laser-produced betatron source*. Nat. Commun. **9**, 3276 (2018).

102. K. Ta Phuoc, S. Corde, R. Shah, F. Albert, R. Fitour, J.-P. Rousseau, F. Burgy, B. Mercier and A. Rousse. *Imaging electron trajectories in a laser-wakefield cavity using betatron X-ray radiation*. Phys. Rev. Lett. **97**, 225002 (2006).

103. F. Albert, R. Shah, K. Ta Phuoc, R. Fitour, F. Burgy, J.-P. Rousseau, A. Tafzi, D. Douillet, T. Lefrou and A. Rousse. *Betatron oscillations of electrons accelerated in laser wakefields characterized by spectral X-ray analysis*. Phys. Rev. E **77**, 056402 (2008).

104. F. G. Desforges, B. S. Paradkar, M. Hansson, J. Ju, L. Senje, T. L. Audet, A. Persson, S. Dobosz-Dufrénoy, O. Lundh, G. Maynard, P. Monot, J.-L. Vay, C.-G. Wahlström and B. Cros. *Dynamics of ionization-induced electron injection in the high density regime of laser wakefield acceleration*. Phys. Plasmas **21**, 120703 (2014).

105. G. Genoud, K. Cassou, F. Wojda, H. E. Ferrari, C. Kamperidis, M. Burza, A. Persson, J. Uhlig, S. Kneip, S. P. D. Mangles, A. Lifschitz, B. Cros and C.-G. Wahlström. *Laser-plasma electron acceleration in dielectric capillary tubes*. Appl. Phys. B **105**, 309 (2011).

106. S. Corde, C. Thaury, K. Ta Phuoc, A. Lifschitz, G. Lambert, J. Faure, O. Lundh, E. Benveniste, A. Ben-Ismail, I. Arantchuk, A. Marciniak, A. Stordeur, P. Brijesh, A. Rousse, A. Specka and V. Malka. *Mapping the X-ray emission region in a laser-plasma accelerator*. Phys. Rev. Lett. **107**, 215004 (2011).

107. M. Hoheisel. *Review of medical imaging with emphasis on X-ray detectors*. Nucl. Instrum. Methods Phys. Res. A **563**, 215–224 (2006).

108. A. Momose and J. Fukuda. *Phase-contrast radiographs of non-stained rat cerebellar specimen*. Med. Phys. **22**, 375 (1995).

109. C. David, B. Nöhammer and H. H. Solak. *Differential X-ray phase contrast imaging using a shearing interferometer.* Appl. Phys. Lett. **81**, 3287 (2002).

110. H. Miao, A. Panna, A. A. Gomella, E. E. Bennett, S. Znati, L. Chen and H. Wen. *A universal moiré effect and application in X-ray phase-contrast imaging.* Nat. Phys. **12**, 830–834 (2016).

111. T. J. Davis, D. Gao, T. E. Gureyev, A. W. Stevenson and S. W. Wilkins. *Phase-contrast imaging of weakly absorbing materials using hard X-rays.* Nature **373**, 595–589 (1995).

112. A. Momose, T. Takeda, Y. Itai and K. Hirano. *Phase-contrast X-ray computed tomography for observing biological soft tissues.* Nat. Med. **2**, 473–475 (1996).

113. S. W. Wilkins, T. E. Gureyev, D. Gao, A. Pogany and A. W. Stevenson. *Phase-contrast imaging using polychromatic hard X-rays.* Nature **384**, 335–338 (1996).

114. S. Kneip, C. McGuffey, F. Dollar, M. S. Bloom, V. Chvykov, G. Kalintchenko, K. Krushelnick, A. Maksimchuk, S. P. D. Mangles, T. Matsuoka, Z. Najmudin, C. A. J. Palmer, J. Schreiber, W. Schumaker, A. G. R. Thomas and V. Yanovsky. *X-ray phase contrast imaging of biological specimens with femtosecond pulses of betatron radiation from a compact laser plasma wakefield accelerator.* App. Phys. Lett. **99**, 093701 (2011).

115. Z. Najmudin, S. Kneip, M. S. Bloom, S. P. D. Mangles, O. Chekhlov, A. E. Dangor, A. Döpp, K. Ertel, S. J. Hawkes, J. Holloway, C. J. Hooker, J. Jiang, N. C. Lopes, H. Nakamura, P. A. Norreys, P. P. Rajeev, C. Russo, M. J. V. Streeter, D. R. Symes and M. Wing. *Compact laser accelerators for X-ray phase-contrast imaging.* Phil. Trans. R. Soc. A **372**, 20130032 (2014).

116. J. Wenz, S. Schleede, K. Khrennikov, M. Bech, P. Thibault, M. Heigoldt, F. Pfeiffer and S. Karsch. *Quantitative X-ray phase-contrast microtomography from a compact laser-driven betatron source.* Nat. Commun. **6**, 7568 (2015).

117. J. M. Cole, D. R. Symes, N. C. Lopes, J. C. Wood, K. Poder, S. Alatabi, S. W. Botchway, P. S. Foster, S. Gratton, S. Johnson, C. Kamperidis, O. Kononenko, M. De Lazzari, C. A. J. Palmer, D. Rusby, J. Sanderson, M. Sandholzer, G. Sarri, Z. Szoke-Kovacs, L. Teboul, J. M. Thompson, J. R. Warwick, H. Westerberg, M. A. Hill, D. P. Norris, S. P. D. Mangles and Z. Najmudin. *High-resolution μCT of a mouse embryo using a compact laser-driven X-ray betatron source.* P. Natl. Acad. Sci. USA **115**, 6335–6340 (2018).

118. K. Svendsen. *In-line phase contrast imaging using betatron X-rays produced by a laser-plasma accelerator.* Master's thesis Lund University, LRAP-536 (2017).

119. A. Schöps, P. Vagin and M. Tischer. *Properties of the insertion devices for PETRA III and its extension.* AIP Conf. Proc. **1741**, 020019 (2016).

120. D. Paganin, S. C. Mayo, T. E. Gureyev, P. R. Miller and S. W. Wilkins. *Simultaneous phase and amplitude extraction from a single defocused image of a homogeneous object.* J. Microsc. **206**, 33–40 (2002).

121. F. Albert, A. G. R. Thomas, S. P. D. Mangles, S. Banerjee, S. Corde, A. Flacco, M. Litos, D. Neely, J. Vieira, Z. Najmudin, R. Bingham, C. Joshi and T. Katsouleas. *Laser wakefield accelerator based light sources: potential application and requirements.* Plasmas Phys. Control. Fusion **56**, 084015 (2014).

122. J. J. Socha, M. W. Westneat, J. F. Harrison, J. S. Waters and W.-K. Lee. *Real-time phase-contrast X-ray imaging: a new technique for the study of animal form and function.* BMC Biology **5**, 6 (2007).

123. J. R. Davis, editor. *Alloying: understanding the basics.* ASM International (2001). ISBN 978-0-87170-744-4.

124. D. Shaked and I. Tastl. *Sharpness measure: towards automatic image enhancement.* Proc. Int. Conf. on Image Process. ICIP **1** (2005).

125. P. Modregger, D. Lübbert, P. Schäfer and R. Köhler. *Spatial resolution in Bragg-magnified X-ray images as determined by Fourier analysis.* Phy. Stat. Sol. (A) **204**, 8 (2007).

126. P. Magnin and R. Trivedi. *Eutecti growth: a modification of the Jackson and Hunt theory.* Acta Metall. Matter. **39**, 453–467 (1991).

127. Energetics Incorporated, Columbia, Maryland for the National Institute of Standards and Technology, U.S. Department of Commerce. *Measurement science roadmap for metal-based additive manufacturing.* Workshop Summary Report (2013).

128. A. J. Shahani, E. B. Gulsoy, J. W. Gibbs, J. L. Fife and P. W. Voorhees. *Integrated approach to the data processing of four-dimensional datasets from phase-contrast X-ray tomography.* Opt. Express **22**, 20 (2014).

129. A. J. Shahani, E. B. Gulsoy, V. J. Roussochatzakis, J. W. Gibbs, J. L. Fife and P. W. Voorhees. *The dynamics of coarsening in highly anisotropic systems: Si particles in Al-Si liquids.* Acta Materialia **97**, 325–337 (2015).

130. A. J. Shahani, E. B. Gulsoy, S. O. Poulsen, X. Xiao and P. W. Voorhees. *Twin-mediated crystal growth: an enigma resolved.* Sci. Rep. **6**, 28651 (2016).

131. K. V. Klementiev. *XANES dactyloscope for Windows* (2013). freeware: www.cells.es/Beamlines/CLAESS/software/xanda.html.

132. F. Dorchies, A. Lévy, C. Goyon, P. Combis, D. Descamps, C. Fourment, M. Harmand, S. Hulin, P. M. Leguay, S. Petit, O. Peyrusse and J. J. Santos. *Unraveling the solid-liquid-vapor phase transition dynamics at the atomic level with ultrafast X-ray absorption near-edge spectroscopy.* Phys. Rev. Lett. **107**, 245006 (2011).

133. F. Dorchies, F. Festa, V. Recoules, O. Peyrusse, A. Benuzzi-Mounaix, E. Brambrink, A. Levy, A. Ravasio, M. Koening, T. Hall and S. Mazevet. *X-ray absorption K edge as a diagnostic of the electronic temperature in warm dense aluminum.* Phys. Rev. B **92**, 085117 (2015).

134. F. Dorchies, V. Recoules, J. Bouchet, C. Fourment, P. M. Leguay, B. I. Cho, K. Engelhorn, M. Nakatsutsumi, C. Ozkan, T. Tschentscher, M. Harmand, S. Toleikis, M. Störmer, E. Galtier, H. J. Lee, B. Nagler, P. A. Heimann and J. Gaudin. *Time evolution of electron structure in femtosecond heated warm dense molybdenum.* Phys. Rev. B **92**, 144201 (2015).

135. M. Z. Mo, Z. Chen, S. Fourmaux, A. Saraf, K. Otani, J. C. Kieffer, Y. Y. Tsui, A. Ng and R. Fedosejevs. *Laser wakefield generated X-ray probe for femtosecond time-resolved measurements of ionization states of warm dense aluminum.* Rev. Sci. Instrum. **84**, 123106 (2013).

136. *Brookhaven national lab, mail-in EXAFS service* (accessed 13-Jan-2017). https://www.bnl.gov/ps/x18b/service.asp.

137. M. Z. Mo, Z. Chen, S. Fourmaux, A. Saraf, S. Kerr, K. Otani, R. Masoud, J.-C. Kieffer, Y. Tsui, A. Ng and R. Fedosejevs. *Measurements of ionization states in warm dense aluminum with betatron radiation.* Phys. Rev. E **95**, 053208 (2017).

138. S. M. Hooker. *Developments in laser-driven plasma accelerators.* Nat. Photonics **7**, 775–782 (2013).

Papers

Paper I

Electron injector for compact staged high energy accelerator

T. L. Audet, F. G. Desforges, A. Maitrallain, S. Dobosz Dufrénoy, M. Bougeard, G. Maynard, P. Lee, M. Hansson, B. Aurand, A. Persson, I. Gallardo González, P. Monot, C.-G. Wahlström, O. Lundh and B. Cros.

Nucl. Instrum. Methods Phys. Res. A **829**, 304-308 (2016).

Nuclear Instruments and Methods in Physics Research A 829 (2016) 304–308

Contents lists available at ScienceDirect

Nuclear Instruments and Methods in Physics Research A

journal homepage: www.elsevier.com/locate/nima

Electron injector for compact staged high energy accelerator

T.L. Audet [a], F.G. Desforges [a], A. Maitrallain [b], S. Dobosz Dufrénoy [b], M. Bougeard [b], G. Maynard [a], P. Lee [a], M. Hansson [c], B. Aurand [c], A. Persson [c], I. Gallardo González [c], P. Monot [b], C.-G. Wahlström [c], O. Lundh [c], B. Cros [a,*]

[a] Laboratoire de Physique des Gaz et des Plasmas, CNRS, Univ Paris Sud, Université Paris-Saclay, 91405 Orsay, France
[b] Laboratoire Interactions, Dynamique et Lasers, CEA, Université Paris-Saclay, 91191 Gif-Sur-Yvette, France
[c] Department of Physics, Lund University, P.O. Box 118, S-22100 Lund, Sweden

ARTICLE INFO

Available online 21 January 2016

Keywords:
Laser
Wakefield
Electron
Acceleration
Plasma
Multi-stage

ABSTRACT

An electron injector for multi-stage laser wakefield experiments is presented. It consists of a variable length gas cell of small longitudinal dimension (≤10 mm). The gas filling process in this cell was characterized both experimentally and with fluid simulation. Electron acceleration experiments were performed at two different laser facilities. Results show low divergence and low pointing fluctuation electron bunches suitable for transport to a second stage, and a peaked energy distribution suitable for injection into the second stage wakefield accelerator.

1. Introduction

In laser wakefield experiments, the laser beam needs to interact with a plasma of controlled density value and distribution. The plasma can be created by discharge [1] or directly by laser ionization of gas [2] provided by a gas jet or confined in a material structure such as a capillary tube [3,4] or a gas cell [5].

The choice of confinement structure is linked to experimental requirements in terms of plasma density, length, homogeneity, stability and reproducibility. To accelerate electron bunches to the GeV level, the interaction length has to be of the order of a few cm; in that case a guiding structure, such as a dielectric capillary with or without discharge, is needed to guide the laser along the plasma and prevent laser diffraction. To achieve lower energy electron bunches, the plasma length can be reduced to mm scale, and a gas cell is an appropriate confinement structure. Indeed, the use of gas cells to confine the gas has been shown to contribute to the stability of the generated electron bunches [6–8] as the gas is relatively homogeneous in comparison with a supersonic gas jet.

In the frame of CILEX [9], multi-stage laser plasma acceleration experiments will be implemented at the APOLLON facility, and the main components are designed and tested using existing facilities. A prototype of the electron injector, called ELISA for ELectron Injector for compact Staged high energy Accelerator, has been built. Electron bunches with a divergence lower than 10 mrad are required in order to be transported to the second stage and with an energy spread of ~1% to be efficiently accelerated in the wakefield of the second stage. The energy range targeted for the injector is 50–200 MeV, as these relativistic energies can be achieved at various facilities and the transport beam line size is manageable. The stability of the electron bunch pointing is also a key parameter as the electron bunch injected into the second stage accelerator needs to be positioned precisely at the center of the focal volume, in order to avoid phase slippage or transverse fields effects. In addition, the injector has to provide electron bunches with the highest possible charge. These considerations have led to the choice of a gas cell for the stability, with short length (≤ 10 mm) for low energy. The use of ionization-induced injection [10–12] is also investigated to produce low energy spread and low divergence electron bunches with high charge.

The remaining of the paper is organized as follows: Section 2 presents the gas cell design and its characterization and Section 3 shows some examples of electron properties measured during acceleration experiments at two different laser facilities.

2. Gas cell design and characterization

2.1. Cell description

A gas cell with variable length was used to confine hydrogen gas (H_2), with the addition of a small fraction of N_2 for the ionization-induced injection scheme. The gas cell and the motorized positioning holder are shown in Fig. 1(a)and a schematic drawing of a section of the gas cell is presented in Fig. 1(b). The main part of the cell is a 20 mm diameter cylinder with a 3 mm

* Corresponding author.
E-mail address: brigitte.cros@u-psud.fr (B. Cros).

http://dx.doi.org/10.1016/j.nima.2016.01.035
0168-9002/

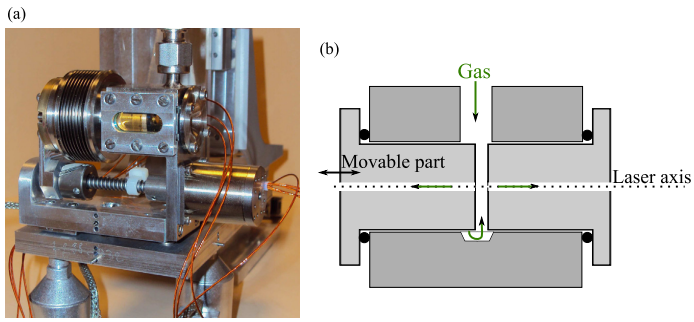

Fig. 1. (a) Picture of ELISA gas cell. (b) Schematic drawing of a section of the gas cell showing the gas inlet (top) and groove (opposite bottom).

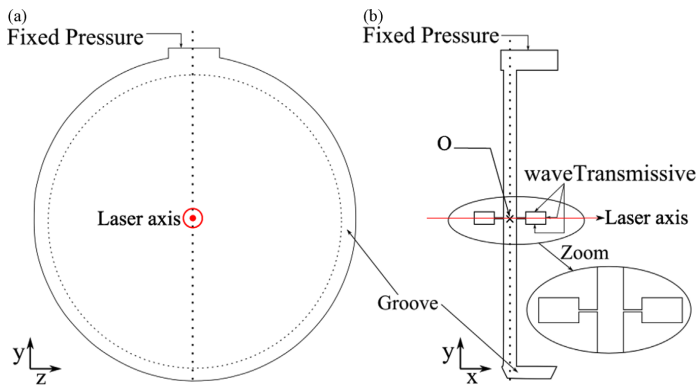

Fig. 2. Simulation geometry and boundary conditions. (a) Transverse cross section. (b) Longitudinal section with zoom on central part. Dotted lines on each figure indicate the position of the other figure plane.

diameter gas inlet at the top. Optical quality windows are present on each side for optical diagnostics transverse to the laser propagation axis. The cell inner length can be varied from 0 to 10 mm. Replaceable entrance and exit plates made of 500 μm thick steel, drilled with 200 μm diameter holes, are mounted to the cell with indium seals. The gas is injected in the cell by the opening of an electrovalve allowing the gas to flow from a reservoir into the cell volume. As the gas will then leak through the entrance and exit holes into the vacuum chamber, it is crucial to know the dynamics of the gas flow in order to control the value of the density with which the laser pulse interacts and minimize density fluctuations.

2.2. Fluid simulations

Fluid simulations are an efficient tool to determine the dynamics of the gas flow with good precision. It gives access to the gas distribution on the whole geometry which can be difficult to measure experimentally due to the low densities and short lengths, or due to the presence of walls preventing optical probing.

3D simulations were performed using openFOAM [13] and the turbulent, transient solver sonicFoam with sonic flow capabilities. SonicFoam is particularly suitable for this case because of the high initial ratio between the inlet pressure and the pressure inside the cell, and between the pressure inside the cell and the pressure in the vacuum boxes when the cell is filled. The gas used in the simulation is H_2 and the geometry is schematically presented in Fig. 2. The transverse section is represented in Fig. 2(a). The gas inlet is located at the top where the pressure is fixed at 500 mbar, representing the end of the pipe connecting the reservoir to the gas cell. The longitudinal section drawn in Fig. 2(b) shows two vacuum boxes connected to the inner part of the cell by 200 μm wide, 500 μm long pipes representing the entrance and exit plates. A groove located all around the inner part of the cell and aligned with the gas inlet is used to improve the homogeneity of the filling process (also visible in Fig. 1(b)). It allows the gas to flow around the central part of the gas cell when the cell length is smaller than the gas pipe diameter (3 mm) in a cylindrical manner. The boundary condition applied to the 3 outer boundaries of each vacuum box allows the gas to go through and exit the simulation box (labeled as waveTransmissive in Fig. 2). Thanks to this transmissive boundary condition, vacuum boxes can be reduced to a small volume to reduce computation time without over filling them and avoid modifying the flow of gas by its accumulation inside the vacuum boxes. This boundary condition is realistic, as in practice the vacuum chamber surrounding the cell is very large compared to the characteristic length of the cell (ratio of ~ 1 m/1 mm) so that the pressure inside the vacuum chamber is always low compared to the pressure inside the cell.

Electronic density at the center of the cell (point O in Fig. 2(b)), calculated from simulated gas density assuming complete ionization, is plotted as a function of time in Fig. 3(a). We can see a slow increase at the beginning and until $t_1 = 28$ μs as gas is mainly flowing along the groove surrounding the inside of cell as seen in Fig. 4(a) where the density of hydrogen ρ_{H_2} is represented on the

surfaces of the simulation domain. Between $t_1 = 28$ μs and $t_2 = 50$ μs the gas starts to reach the inner part of the cell and especially the center in an almost cylindrical manner as seen in Fig. 4(b). Due to this cylindrical filling we can observe a strong increase of the density on axis and even an overshoot because of the compressibility of the gas. At $t_3 = 103$ μs the density in the cell is almost homogeneous (see Fig. 4(c)) and leakage through the entrance and exit holes and in the vacuum boxes establish density gradients, reducing the density inside the cell until ~180 μs when a steady state is reached.

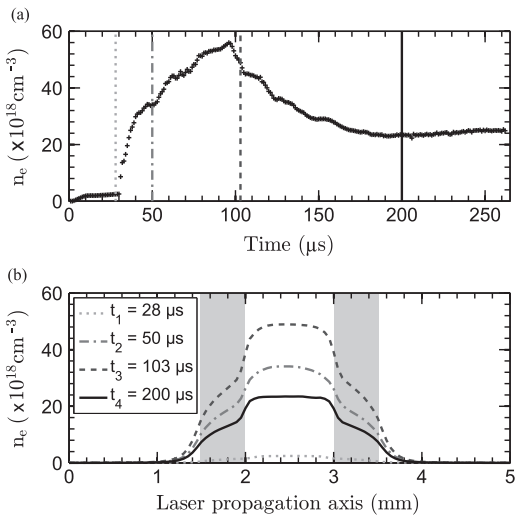

Fig. 3. Results of fluid simulations for $L_{cell} = 1$ mm and a $P_{reservoir} = 500$ mbar. (a) Density at the center of the cell (point O in Fig. 2(b)) as a function of time. Vertical lines indicate 4 times selected for tracing the longitudinal density profile in the subplot below. (b) Longitudinal density profile at 4 different times. Gray areas indicate the locations of the entrance and exit plates in which holes are drilled.

Density profiles along the propagation axis at times t_1 to t_4 are presented in Fig. 3(b). Early in the simulation (~50 μs) a stable longitudinal density profile is established. Then the maximum value of the density changes until a steady state is reached at $t_4 = 200$ μs, but the shape of the longitudinal distribution remains similar. It consists of a plateau in the inner part of the cell whose length can be changed by changing the cell length. On each side of the plateau, sharp gradients at the transition with the holes are followed with smoother gradients inside the entrance and exit plates, indicated by gray areas in Fig. 3(b), and sharper gradients outside the cell in the vacuum boxes.

2.3. Interferometric measurements of mean density

Experimental measurements were performed to validate the value of the maximum density obtained from simulation inside the cell. Off-line interferometric measurements using a set-up similar to ref. [14] were performed. The experimental setup consists of a Mach–Zehnder interferometer where a reference beam propagating in ~10^{-5} mbar vacuum interferes with a beam passing through the transverse section of the cell (equipped with windows as seen in Fig. 1). About ~1/3 of the central, brightest fringe of the interference pattern is selected with a slit and focused on a photo-diode whose signal is recorded with an oscilloscope. When gas is let in, the signal consists of oscillations corresponding to dark and bright fringes passing through the slit and imaged on the photo-diode.

The phase shift was then reconstructed using the method described in [14] and an example for an inner length of the cell of $L_{cell} = 1$ mm and a reservoir pressure of $P_{reservoir} = 500$ mbar is given in Fig. 5(a). We observe a delay of ~27 ms between the valve opening ($t_0 = 0$ ms) and the arrival of the gas inside the cell corresponding to the time needed for the gas to expand from the

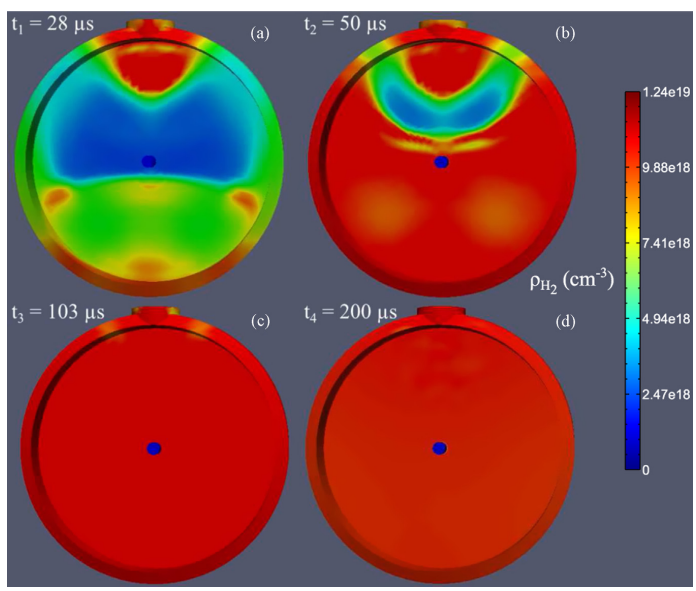

Fig. 4. Density of hydrogen ρ_{H_2} projected on the surfaces of the simulation domain for several times. The blue circle in the center on each figure is the low density surface of a vacuum box. The maximum of the color scale is the density corresponding to a pressure of 500 mbar. (For interpretation of the references to color in this figure caption, the reader is referred to the web version of this paper.)

reservoir to the cell. We assume a flat density profile in the transverse dimension which is validated in the simulation since the highest density difference in the transverse direction is $\sim 2\%$ during the steady state. Using the relation between the optical index and the density we can then reconstruct the mean density inside the cell during the steady state e.g. between 40 and 495 ms. We can also evaluate density fluctuations by calculating the standard deviation of the density during the steady state. The mean density as a function of the reservoir backing pressure for different cell lengths is displayed in Fig. 5(b). We can see that the cell length has no influence on the density inside the cell except for high backing pressure where we start to see a discrepancy between the different lengths although error bars are almost superimposed.

Experimental results are found to be in good agreement with numerical ones. Indeed, the density value during the steady state in the simulation ($t_{final} = 262$ μs) is $n_{eFinal}^{sim} = 24.9 \times 10^{18}$ cm^{-3} for a cell length of 1 mm and a fixed pressure of 500 mbar, compared to a measured value of $n_e = 23.7 \times 10^{18}$ cm^{-3} in the steady state with the same parameters. The pressure loss between the electrovalve and the gas cell is not taken into account in the simulation which explains the slightly higher value.

3. Electron acceleration using the gas cell

The gas cell described in Section 2 was used for laser driven electron acceleration experiments at two different laser facilities. At the Lund Laser Centre (LLC), the laser beam pointing stability provides controlled conditions to study the stability of accelerated electron bunches. At UHI100 laser facility at CEA Saclay, the higher energy available provides the opportunity to explore various parameter sets to tune the electron properties.

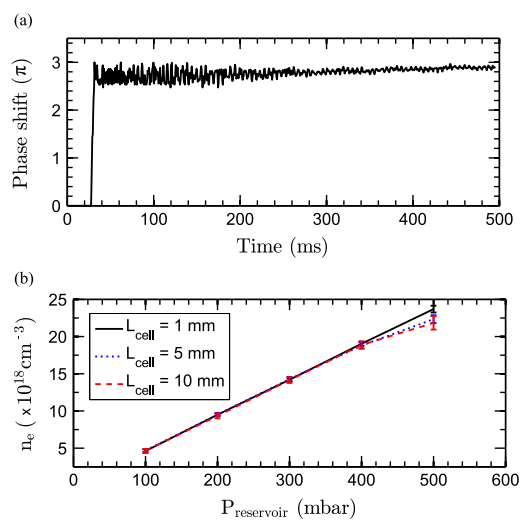

Fig. 5. Interferometric measurements results. (a) Example of phaseshift dynamics for $L_{cell} = 1$ mm and $P_{reservoir} = 500$ mbar. (b) Measured mean density inside the cell during the steady state (between 40 and 495 ms) as a function of reservoir backing pressure for different cell lengths; error bars are standard deviation of the density during the steady state.

3.1. Stability

We first show an example to illustrate the pointing stability of the electron beam measured at the LLC. In this study, the laser pulse full-width-at-half-maximum (fwhm) duration was $\tau_L = (37 \pm 3)$ fs. A closed-loop wavefront optimization using a deformable mirror and a wavefront sensor was done to achieve almost symmetrical Gaussian-like distribution of the intensity in the focal plane with a fwhm spot size of 17 μm and pointing fluctuations of the order 1 μrad (evaluated by the standard deviation of the center position on more than 300 shots). The peak intensity in the focal plane was estimated to be $I_{Lund} = (3.1 \pm 0.5) \times 10^{18}$ W/cm^2. Fig. 6 presents accumulated electron bunches footprints observed ~ 42 cm after the laser focal plane of 70 consecutive shots in a gas mixture of 99% H_2 + 1% N_2 with a cell length $L_{cell} = 1.8$ mm and $n_e = 1.2 \times 10^{19}$ cm^{-3}. The laser pulse was entering the gas cell at the beginning of the steady state, 40 ms after the valve opening time. Electron bunches have a mean charge of $Q = 160$ pC with a standard deviation of $\sigma_Q \sim 27\%$, a mean divergence of $\theta \simeq 9$ mrad and pointing fluctuations of $\phi_x = 3.4$ mrad in the vertical direction and $\phi_y = 4.5$ mrad in the horizontal direction. Electron bunches pointing fluctuations are therefore 3 orders of magnitude larger than laser pointing fluctuations which indicates other sources of pointing fluctuations or other mechanism amplifying the laser pointing fluctuations on the electron bunches fluctuations.

3.2. Peaked spectrum

This second experimental result has been achieved at the UHI100 laser facility at CEA Saclay. For this campaign the Ti:Sapphire laser system delivered $\tau_U \simeq 45$ fs fwhm laser pulses and the wavefront was optimized with a deformable mirror to achieve a laser spot size of ~ 32 μm fwhm resulting in an intensity in the focal plane estimated to be $I_{UHI} \simeq 5.2 \times 10^{18}$ W/cm^2. In Fig. 7a typical peaked spectrum obtained in this facility in pure H_2 at an electronic density of $n_e = 1.2 \times 10^{19}$ cm^{-3} and a cell length of $L_{cell} = 1.5$ mm is presented. It presents a peak at $E_{peak} \simeq 76$ MeV with a fwhm relative energy spread of $\Delta E/E_{peak} \simeq 10\%$ and ~ 0.5 pC is contained in the fwhm of the peak which corresponds to $\sim 43\%$ of the total charge.

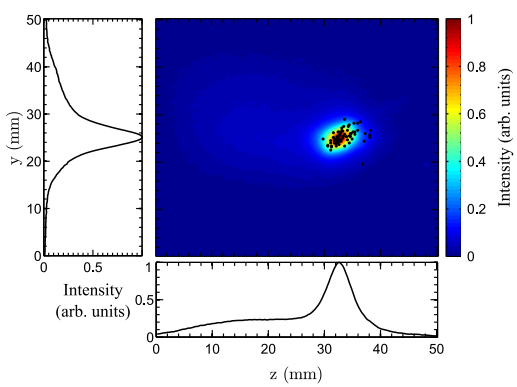

Fig. 6. Accumulated electron footprints in false colors and associated projections for 70 consecutive shots at $n_{e0} = 1.2 \times 10^{19}$ cm^{-3} and $L_{cell} = 1.8$ mm. Dots indicate each electron bunch center. (For interpretation of the references to color in this figure caption, the reader is referred to the web version of this paper.)

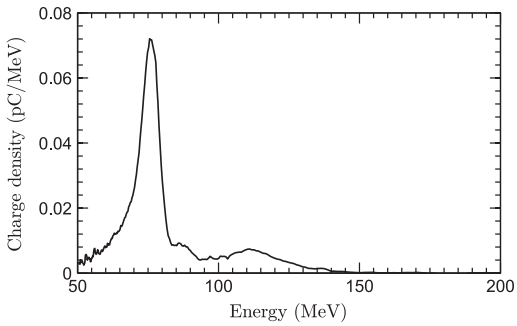

Fig. 7. Peaked electron spectrum containing ~ 1.1 pC in the 50–200 MeV energy range with a fwhm relative energy spread of $\Delta E/E_{peak} \simeq 10\%$ at $E_{peak} \simeq 76$ MeV , obtained at $n_e = 1.2 \times 10^{19}$ cm^{-3} with $L_{cell} = 1.5$ mm.

4. Conclusion

A gas cell with variable length was designed as a confinement structure to achieve a homogeneous and stable plasma target for laser wakefield acceleration experiments. It was characterized for density values and distribution appropriate for the development of an electron injector. The dynamics of its gas filling process was characterized both experimentally and using fluid simulation and was found to be linearly dependent on the backing pressure and almost independent of the length of the cell in the range of interest.

Electron acceleration experiments were conducted at two laser facilities. Using this gas cell, electron bunches can be generated at a repetition rate of $\sim$2–3 shots per minute with a pointing stability of ~ 4 mrad and a divergence of ~ 9 mrad . Electron bunches with a peaked energy distribution with $\sim$10% fwhm relative energy spread can also be generated. The properties of generated electron bunches are compatible with injection in an appropriate magnetic transport line [15].

This gas cell was easily implemented in the environment of different laser facilities and is used together with a magnetic transport line to optimize injector properties [16,17].

Acknowledgments

This work was supported by the Triangle de la Physique under Contract no. 2012-032TELISA. Authors also acknowledge the support of the Swedish Research Council, the Knut and Alice Wallenberg Foundation, the Swedish Foundation for Strategic Research, Laserlab-Europe/CHARPAC and EuCARD2/ANAC2 (Grant agreement nos. 284464 and 312453, EC's 7th Framework Programme).

References

[1] D.J. Spence, S.M. Hooker, Physical Review E 63 (2000) 015401, http://dx.doi.org/10.1103/PhysRevE.63.015401.
[2] M.V. Ammosov, N.B. Delone, V.P. Krainov, Soviet Physics JETP 64 (1986) 1191.
[3] N.E. Andreev, K. Cassou, F. Wojda, G. Genoud, M. Burza, O. Lundh, A. Persson, B. Cros, V.E. Fortov, C.-G. Wahlstrom, New Journal of Physics 12 (4) (2010) 045024.
[4] F.G. Desforges, B.S. Paradkar, M. Hansson, J. Ju, L. Senje, T.L. Audet, A. Persson, S.D. Dufrénoy, O. Lundh, G. Maynard, P. Monot, J.-L. Vay, C.-G. Wahlström, B. Cros, Physics of Plasmas 21 (2014) 120703, http://dx.doi.org/10.1063/1.4903845.
[5] C.E. Clayton, J.E. Ralph, F. Albert, R.A. Fonseca, S.H. Glenzer, C. Joshi, W. Lu, K. A. Marsh, S.F. Martins, W.B. Mori, A. Pak, F.S. Tsung, B.B. Pollock, J.S. Ross, L. O. Silva, D.H. Froula, Physical Review Letters 105 (2010) 105003, http://dx.doi.org/10.1103/PhysRevLett.105.105003.
[6] F.G. Desforges, M. Hansson, J. Ju, L. Senje, T.L. Audet, S. Dobosz-Dufrénoy, A. Persson, O. Lundh, C.-G. Wahlström, B. Cros, Nuclear Instruments and Methods in Physics Research Section A 740 (2013) 54, http://dx.doi.org/10.1016/j.nima.2013.10.062.
[7] J. Osterhoff, A. Popp, Z. Major, B. Marx, T.P. Rowlands-Rees, M. Fuchs, M. Geissler, R. Hörlein, B.H.S. Becker, E.A. Peralta, U. Schramm, F. Grüner, D. Habs, F. Krausz, S.M. Hooker, S. Karsch, Physical Review Letters 101 (2008) 085002, http://dx.doi.org/10.1103/PhysRevLett.101.085002.
[8] M. Vargas, W. Schumaker, Z.-H. He, Z. Zhao, K. Behm, V. Chvykov, B. Hou, K. Krushelnick, A. Maksimchuk, V. Yanovsky, A.G.R. Thomas, Applied Physics Letters 104 (2014) 174103, http://dx.doi.org/10.1063/1.4874981.
[9] B. Cros, B.S. Paradkar, X. Davoine, A. Chancé, F.G. Desforges, S.D. Dufrénoy, N. Delerue, J. Ju, T.L. Audet, G. Maynard, M. Lobet, L. Gremillet, P. Mora, J. Schwindling, O. Delferrière, C. Bruni, C. Rimbault, T. Vinatier, A.D. Piazza, M. Grech, C. Riconda, J.R. Marquès, A. Beck, A.E. Specka, P. Martin, P. Monot, D. Normand, F. Mathieu, P. Audebert, F. Amiranoff, Nuclear Instruments and Methods in Physics Research Section A 740 (2013) 158, http://dx.doi.org/10.1016/j.nima.2013.10.090.
[10] M. Chen, Z.-M. Sheng, Y.-Y. Ma, J. Zhang, Journal of Applied Physics 99 (2006) 056109, http://dx.doi.org/10.1063/1.2179194.
[11] A. Pak, K.A. Marsh, S.F. Martins, W. Lu, W.B. Mori, C. Joshi, Physical Review Letters 104 (2010) 025003, http://dx.doi.org/10.1103/PhysRevLett.104.025003.
[12] C. McGuffey, A.G.R. Thomas, W. Schumaker, T. Matsuoka, V. Chvykov, F. J. Dollar, G. Kalintchenko, V.Y.A. Maksimchuk, K. Krushelnick, V.Y. Bychenkov, I.V. Glazyrin, A.V. Karpeev, Physical Review Letters 104 (2010) 025004, http://dx.doi.org/10.1103/PhysRevLett.104.025004.
[13] Openfoam documentation, ⟨http://www.openfoam.com⟩, 2015.
[14] J. Ju, B. Cros, Journal of Applied Physics 112 (2012) 113102, http://dx.doi.org/10.1063/1.4768209.
[15] A. Chancé, O. Delferrière, J. Schwindling, C. Bruni, N. Delerue, A.E. Specka, B. Cros, G. Maynard, B.S. Paradkar, P. Mora, Nuclear Instruments and Methods in Physics Research Section A 740 (2013) 158, http://dx.doi.org/10.1016/j.nima.2013.10.036.
[16] T.L. Audet, M. Hansson, P. Lee, F.G. Desforges, G. Maynard, S.D. Dufrénoy, R. Lehe, J.L. Vay, B. Aurand, A. Persson, I.G. Gonzáles, A. Maitrallain, P. Monot, C.G. Wahlström, O. Lundh, B. Cros, Investigation of ionization-induced electron injection in a wakefield driven by laser inside a gas cell, 2016, submitted for publication.
[17] M. Hansson, T.L. Audet, H. Ekerfelt, B. Aurand, I.G. Gonzáles, F.G. Desforges, X. Davoine, A. Maitrallain, S. Reymond, P. Monot, A. Persson, S.D. Dufrénoy, C.G. Wahlström, B. Cros, O. Lundh, Localization of ionization-induced trapping in a laser wakefield accelerator using a density down-ramp, 2016, submitted for publication.

Paper II

Investigation of ionization-induced electron injection in a wakefield driven by laser inside a gas cell

T. L. Audet, M. Hansson, P. Lee, F. G. Desforges, G. Maynard, S. Dobosz Dufrénoy, R. Lehe, J.-L. Vay, B. Aurand, A. Persson, I. Gallardo González, A. Maitrallain, P. Monot, C.-G. Wahlström, O. Lundh and B. Cros.

Phys. Plasmas **23**, 023110 (2016).

PHYSICS OF PLASMAS 23, 023110 (2016)

Investigation of ionization-induced electron injection in a wakefield driven by laser inside a gas cell

T. L. Audet,[1,a)] M. Hansson,[2] P. Lee,[1] F. G. Desforges,[1] G. Maynard,[1] S. Dobosz Dufrénoy,[3] R. Lehe,[4] J.-L. Vay,[4] B. Aurand,[2] A. Persson,[2] I. Gallardo González,[2] A. Maitrallain,[3] P. Monot,[3] C.-G. Wahlström,[2] O. Lundh,[2] and B. Cros[1,b)]
[1]*Laboratoire de Physique des Gaz et des Plasmas, CNRS, Univ. Paris-Sud, Université Paris-Saclay, 91405 Orsay, France*
[2]*Department of Physics, Lund University, P.O. Box 118, S-22100 Lund, Sweden*
[3]*Laboratoire Interactions, Dynamique et Lasers, CEA, Université Paris-Saclay, 91191 Gif-sur-Yvette, France*
[4]*Lawrence Berkeley National Laboratory, Berkeley, California 94720, USA*

(Received 22 September 2015; accepted 3 February 2016; published online 16 February 2016)

Ionization-induced electron injection was investigated experimentally by focusing a driving laser pulse with a maximum normalized potential of 1.2 at different positions along the plasma density profile inside a gas cell, filled with a gas mixture composed of $99\%H_2 + 1\%N_2$. Changing the laser focus position relative to the gas cell entrance controls the accelerated electron bunch properties, such as the spectrum width, maximum energy, and accelerated charge. Simulations performed using the 3D particle-in-cell code WARP with a realistic density profile give results that are in good agreement with the experimental ones. The interest of this regime for optimizing the bunch charge in a selected energy window is discussed. © *2016 AIP Publishing LLC*.
[http://dx.doi.org/10.1063/1.4942033]

I. INTRODUCTION

The mechanism of laser wakefield acceleration (LWFA) in a plasma[1] can produce electric fields 3 orders of magnitude higher than in conventional RF accelerators. LWFA thus appears as a promising way to achieve compact relativistic electron sources. In this scheme, the plasma wave is excited by the ponderomotive force of a short intense laser pulse. At sufficiently high intensity gradient (typically achievable with an ultrashort laser pulse with intensity above $\sim 10^{19}$ W/cm^2), plasma electrons are blown out of the laser axis behind the laser pulse. A cavity or "bubble" where only ions remain is created behind the laser pulse leading to strong transverse and longitudinal electrostatic fields. Plasma electrons can be trapped in this field and accelerated to high energy. This mechanism can occur continuously or several times over the plasma length as long as the laser intensity is high enough, which leads to accelerated electron bunches with a wide energy spread.

Several methods to increase the number of electrons and reduce the electron bunch energy spread have been proposed and tested such as the use of colliding pulses,[2,3] density ramp injection,[4,5] density transition injection,[6,7] or ionization-induced injection.[8–10] The mechanism of ionization-induced injection can be implemented simply by adding a small proportion of high-Z gas to the low-Z gas constituting the target medium. During the interaction with the intense laser pulse, the outer shell electrons of the high-Z gas are ionized in the front of the laser pulse and mostly contribute to the plasma wave, without being trapped. Electrons from the inner-shell of the high-Z atoms, having a much higher ionization threshold, are ionized closer to the intensity peak in a region where they can be more easily trapped by the plasma wave. This mechanism has shown its ability to increase the trapped charge[11] and lower the transverse emittance of the electron bunches[12] and is thus a promising candidate as an injector for multi-stage laser plasma accelerators. Although previous studies have used it in injector-accelerator experiments,[13,14] a detailed specific study of the injection mechanism and the physics controlling the electron bunch properties in the experiments needed to be performed.

In this paper, the properties of electron bunches with energy in the range of 50–200 MeV, produced by ionization-induced injection using a single laser pulse focused in a gas cell target, are reported. The laser normalized vector potential and maximum plasma density are such that electron injection is dominated by ionization-induced injection, as shown in the previous work.[11] The focal spot position was varied along the propagation axis to explore different injection conditions along the plasma density profile.

The use of gas cells has been shown to contribute to the stability of electron production[15–18] as the gas confined in the cell is relatively homogeneous. Nevertheless, windows cannot be used to confine the gas on the intense short-pulse laser path, and density gradients are established due to gas leakage between the higher pressure volume of the gas cell and the low pressure chamber around it. Direct experimental measurement of these gradients is particularly difficult due to the small volume and large range of density to be probed. We have thus evaluated the gradients by their calculation through fluid simulations.

We performed experimental measurements of electron properties inside short gas cells, for which the focal plane position of the laser pulse was varied along the gradient. Experimental results were analyzed and compared with

a)Electronic mail: thomas.audet@u-psud.fr
b)Electronic mail: brigitte.cros@u-psud.fr

numerical modeling with the Particle-In-Cell (PIC) code WARP.[19] It shows that the density profile and the focus position play a major role in the regime of intensity studied. The remaining of the paper is organized as follows: in Section II, the experimental set-up and parameters are described; Section III presents experimental results of the cell position scan and their analysis with the help of simulations; the influence of other parameters such as the cell length and laser energy on the bunch properties is discussed in Section IV.

II. EXPERIMENTAL CONDITIONS

Experiments were performed at the Lund Laser Centre (LLC), using a Ti:sapphire multi-terawatt laser system. Linearly polarized laser pulses, with duration $\tau_L = (37 \pm 3)$ fs full-width-at-half-maximum (fwhm), were focused using a 78 cm focal length off-axis parabola to a fwhm spot size of 17 μm. The laser wavefront was corrected using a deformable mirror to achieve a symmetrical circular distribution of energy in the transverse focal plane in vacuum. The laser envelope was close to the envelope of a Gaussian pulse and the measured Rayleigh length was $z_R \simeq 1$ mm. The laser energy on target was $E_L = (585 \pm 65)$ mJ and the resulting peak intensity in the focal plane was $I_L = (3.1 \pm 0.5) \times 10^{18}\,\mathrm{W/cm^2}$, which corresponds to a normalized vector potential of $a_0 = (e/m_e c^2) \times (2I_L/\varepsilon_0 \omega_L)^{1/2} = 1.2 \pm 0.1$.

The target gas was contained in a variable length gas cell placed in the experimental vacuum chamber. The cell was made as a large diameter cylinder with replaceable entrance and exit faces, at the center of which 200 μm diameter holes were drilled to let the laser and electron bunches pass through. The thickness of the entrance and exit plates was 500 μm. A gas mixture composed of $99\%H_2 + 1\%N_2$ was let in through an electrovalve opened 40 ms before the laser pulse. The stationary state plateau gas density in the cell was characterized prior to the experiment using interferometric measurements similar to the ones described in Ref. 20. Calculation of the profile with fluid simulations was performed using a transient turbulent sonic solver in OpenFOAM (sonicFoam).[21] The normalized density profile n_e/n_{e0} obtained from simulations is plotted as a function of the position along the laser propagation axis as a solid line in Fig. 1.

The grey areas represent schematically the areas occupied by the walls of the gas cell; the laser is propagating from left to right. The density profile consists of a maximum in the inner part of the cell which length can be varied by moving the exit plate; on each side, sharp gradients at the transition with the plates are followed by smoother gradients in the vicinity of the holes, and sharp gradients outside the cell. The colored circles, labeled (a) to (d), represent the different positions of the focal plane in-vacuum relative to the gas cell, used to achieve results shown in Section III.

The focal plane is at a maximum distance of 1.4 mm from the 200 μm entry hole (in the case where it is located at 0.9 mm). In vacuum, the fwhm laser spot size at 1.4 mm from the focal plane is $\sim$41 μm; in this case, all the detected laser energy is entering the gas cell. At the LLC facility, the laser pointing is actively stabilized to cancel drift of the laser

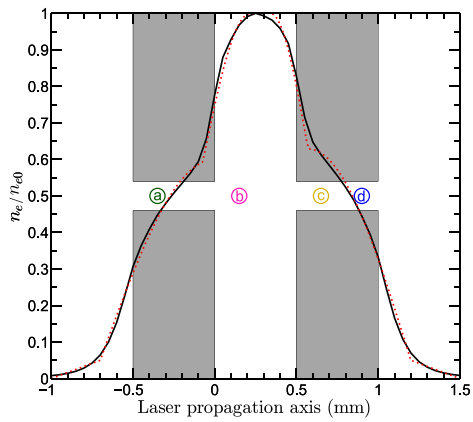

FIG. 1. Normalized density profile for an inner cell length of $L_{cell} = 0.5$ mm calculated with OpenFOAM (black solid line) and approximated density profile used in WARP simulations (red dotted line). The grey areas represent the entrance and exit plates. The colored circles are the in-vacuum focal plane positions of the laser pulse in the experimental study used for the numerical study.

spot in the focal plane, ensuring alignment of the gas cell to be optimized and stable over time of measurement duration. For the experimental results presented in this paper, the maximum electron number density in the cell was $n_{e0} = 8.3 \times 10^{18}\,\mathrm{cm^{-3}}$, and the corresponding plasma frequency is $\omega_p = 1.6 \times 10^{14}$ rad/s which leads to $\omega_p \tau_L \simeq 6$. The critical power for self-focusing associated to this density is $P_C = 3.6$ TW, which gives a ratio of laser power to critical power $P_L/P_C = (P_L[GW]/17) \times (n_e/n_c) \simeq 4.1$, where n_c is the critical density. Self-focusing is thus expected to occur mainly in the area where the density is close to its maximum.

The generated electron bunches were characterized using a 12 cm-long magnetic dipole with a maximum field strength of 0.7 T and a LANEX screen imaged by a 16 bits CCD. The charge was calculated from LANEX images using published calibration factor[22] and the lowest energy that could be measured was $\sim$50 MeV.

III. VARYING THE FOCAL PLANE POSITION

In this section, electron properties are presented for different positions of the focal plane relative to the entrance of the gas cell. Experimentally, the inner length of the cell was below 1 mm but was not known precisely. As the electron energy distribution is sensitive to the plasma length, measured electron spectra were compared with the results of simulations performed for several values of the plasma length. The best fit of experimental spectra was achieved for a cell length value of $L_{cell} = 0.5$ mm.

Experimental results at different focus positions were then analyzed by comparison to quasi-three-dimensional, electromagnetic PIC simulations with the numerical code WARP, which uses a Fourier decomposition of the electromagnetic fields in the azimuthal direction with respect to the laser-propagation direction.[23] Two Fourier modes were

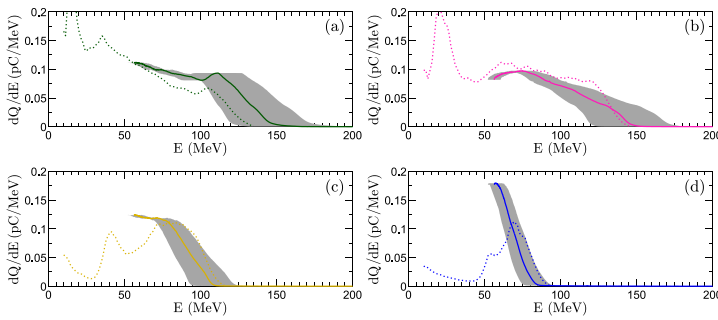

FIG. 2. Electron spectra for different positions z_f of the focal plane in vacuum (a) $z_f = -0.35$ mm, (b) $z_f = 0.15$ mm, (c) $z_f = 0.65$ mm, and (d): $z_f = 0.9$ mm. Solid lines represent the experimental spectra (averaged over 2 shots), gray areas represent the experimental energy uncertainty, and dotted lines represent WARP simulation results for a maximum density in the cell of $n_{e0} = 7.8 \times 10^{18}$ cm^{-3} and an inner cell length of $L_{cell} = 0.5$ mm. Simulation spectra are normalized to the maximum value of the experimental spectrum for the position $z_f = -0.35$ mm.

included in the simulations. A field ionization module based on the Ammosov-Delone-Krainov model was used to model ionization dynamics.[24] The longitudinal profile calculated with OpenFOAM was used in the WARP simulations, with a maximum electron density of $n_{e0} = 7.8 \times 10^{18}$ cm^{-3}, for a gas mixture of 99% of H_2 and 1% of N_2. The laser was linearly polarized. The driving laser parameters are $a_0 = 1.1$, a spot size of 17 μm fwhm, and a duration of 40 fs. All simulations were carried out with 36 macroparticles per cell with a grid resolution of $1.25 \times \lambda_L/2\pi$ and $0.05 \times \lambda_L/2\pi$ in r- and z-directions, respectively.

In Figs. 2(a)–2(d) are displayed electron spectra, obtained from experimental data and from PIC simulation results, for different positions of the in-vacuum focal plane z_f corresponding to the circles labeled (a) to (d) in Fig. 1. Only electrons with energy above ∼50 MeV could be detected experimentally and grey areas around the experimental spectra represent the uncertainty on the energy determination estimated from typical electron pointing fluctuations and divergence. We can observe for all focus positions a good agreement between experimental and simulation data. The electron spectrum shape is shown to be strongly dependent on the parameter z_f. At $z_f = -0.35$ mm, the spectra exhibit a plateau up to ∼110 MeV and then a quasi-linear decrease up to ∼150 MeV. As the value of z_f is increased, the extension of the plateau is reduced, and it vanishes at $z_f = 0.9$ mm.

Fig. 3 shows experimental and simulation results for (a) the total charge above 50 MeV, Q_{tot} and (b) the maximum energy, E_{max}, of the electron bunch; crosses indicate experimental points for gas mixture and open circles with lines simulation results; E_{max} is defined as the energy above which the charge density becomes less than 10% of the maximum. The value of the charge obtained by simulations was normalized to the average of the experimental values at $z_f \simeq -0.35$ mm. Triangles in Fig. 3(a) are experimental results for pure H_2 for similar n_e (8.5×10^{18} cm^{-3}) and L_{cell} (0.8 ± 0.5 mm, respectively). These data show that the addition of 1% N_2 increases the accelerated charge by up to a factor of 10 for the range of parameters studied here, so that the injection of most electrons can be attributed to ionization-induced injection.

Simulation results and experimental data for gas mixture exhibit the same behavior. Experimental data show that both E_{max} and Q_{tot} are increasing from $z_f \simeq -0.6$ mm to $z_f \simeq -0.35$ mm. $z_f = -0.6$ mm corresponds to a position of the focal plane in vacuum in front of the entrance of the cell, so that during the propagation, the laser diffracts significantly before the density is high enough for laser pulse self-focusing to occur; consequently, the maximum intensity is relatively low, leading to a low amplitude accelerating field. From $z_f \simeq -0.6$ mm to $z_f \simeq -0.35$ mm, the maximum energy is increasing, from $z_f = -0.35$ mm to $z_f = 0.15$ mm it is nearly constant, and it decreases for z_f larger than 0.15 mm. The reduction of the maximum energy for z_f larger than 0.15 mm indicates a reduction of the accelerating length and/or of the accelerating field.

The evolution of the normalized vector potential a_0 along the propagation axis, as given by PIC simulations, is

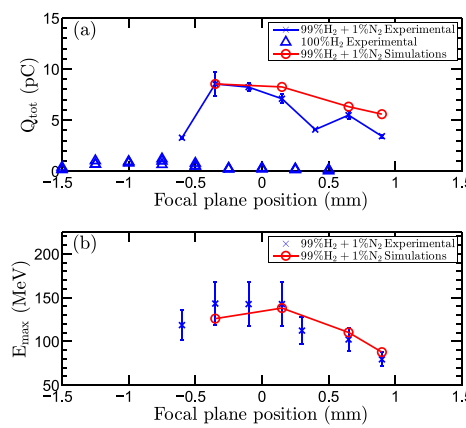

FIG. 3. Simulation and experimental results comparison for charge and energy as a function of focal plane position, blue crosses are experimental data points, and red circles with solid line are simulation results: (a) Q_{tot}: bunch charge for electrons with energy higher than 50 MeV; Blue triangles represent the experimental values of the charge obtained with pure hydrogen and (b) E_{max}: electron maximal energy.

plotted in Fig. 4 with the focal plane position as a parameter. The evolution of a_0 is similar for the four cases corresponding to the spectra of Fig. 2. It shows that laser focusing and defocusing are in these cases dominated by the density profile. Indeed, a_0 starts to increase around the same location for all cases which corresponds to the beginning of the laser self-focusing and decreases when the density is dropping. The variation of z_f changes the maximum absolute values of a_0, which are decreasing when z_f is increased above $z_f = 0.15$ mm.

The locations where electron injection begins are indicated by vertical dashed lines in Fig. 4, and they are defined as the first locations at which electrons with an energy higher than 10 MeV are present. It can be seen that the beginning of injection occurs around the same value of $a_0 \simeq 1.7 \pm 0.1$ for all cases which is consistent with the ionization-induced trapping threshold given in Ref. 10 (in our case at the injection we have $\gamma_p \simeq 15$ and $k_p L_{RMS} \simeq 2.1$, where γ_p is the Lorentz factor of the plasma wave, k_p its wave number, and L_{RMS} the longitudinal root-mean-square laser pulse length). As z_f is increased above 1.15 mm, this value of a_0 is reached after a longer propagation distance; injection then starts later and the acceleration length is reduced as the plasma length is constant.

In the simulation, we also observe that the largest maximum longitudinal electric field of the wake is obtained for $z_f = 0.15$ mm. Therefore, a shift of z_f away from $z_f = 0.15$ mm leads to a reduction of the length available to inject and accelerate electrons and of the amplitude of the electric field responsible for the trapping and acceleration processes. The consequence is that both the charge and the maximum energy of accelerated electrons are reduced when z_f is shifted away from $z_f = 0.15$ mm, as observed in Fig. 3. These results show that a change of the laser focal plane position along the density profile allows control of the position of injection, and subsequently the accelerated charge and energy distribution.

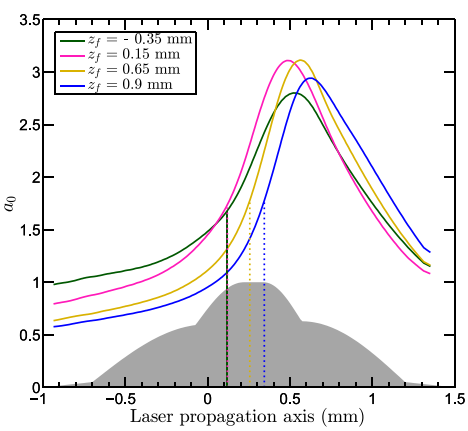

FIG. 4. Normalized vector potential obtained from WARP simulations along the propagation axis for different positions of the focal plane in vacuum. Solid lines represent the value of the normalized vector potential and vertical dashed lines indicate the start of injection in each case (for cases $z_f = -0.35$ mm and $z_f = 0.15$, vertical lines are superimposed).

TABLE I. Parameters of 4 different cases for comparison of accelerated charge in experiments; n_e is the maximum value of the plateau, and the nonlinear dephasing length L_φ is evaluated for this density.

Case No.	Case 1	Case 2	Case 3	Case 4
n_e (10^{18} cm^{-3})	8.3	9.5	8.5	9.3
L_{cell} (mm)	0.5	0.7	10	5
L_{cell} (L_φ)	0.9	1.5	18.5	10.5
L_φ (mm)	0.56	0.46	0.54	0.48
z_f (mm)	0.9	−0.25	−0.25	−0.5

IV. VARYING THE DENSITY, CELL LENGTH, AND LASER INTENSITY

In addition to the focus position, in the regime of interest for an injector, other parameters, such as the plasma density and length, and the laser strength, have a significant role in determining the accelerated charge and the energy of the electron bunch. In this section, we examine the influence of these parameters on the total charge and in a limited energy range suitable for an injector. The energy window 60–70 MeV is of interest as it contains a significant charge for all parameter sets. Table I summarizes the parameters of 4 different cases that were studied experimentally.

The laser vector potential is $a_0 = 1.2$ and the corresponding values of the total charge, Q_{tot} (blue bars), and of the charge in the [60–70 MeV] energy range, $Q_{[60-70\text{MeV}]}$ (red bars), for these 4 cases are plotted in Fig. 5(a). For all cases, the selected value of z_f corresponds to the focal position maximizing the charge in the 60–70 MeV energy range. Case 1 is extracted from the study presented in Section III (i.e., $z_f = 0.9$ mm). We then compare three other sets of parameters to case 1. We first increase the density (case 2) keeping the cell length in the same range and observe a strong increase on both Q_{tot} and $Q_{[60-70\text{MeV}]}$: Q_{tot} is increased

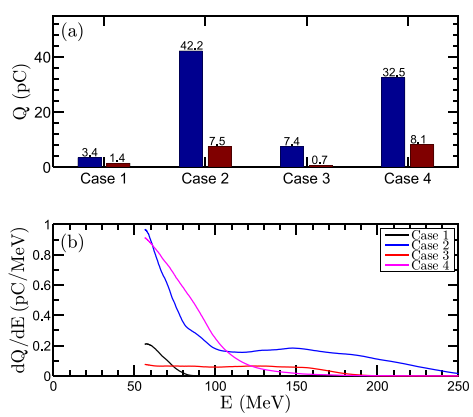

FIG. 5. Experimental cases comparison. (a) Total charge Q_{tot} (blue bars) and charge in the 60–70 MeV energy range $Q_{[60-70\text{MeV}]}$ (red bars) for parameters of cases 1 to 4 listed in Table I. (b) Corresponding energy spectra.

by a factor of ∼12 and $Q_{[60-70\mathrm{MeV}]}$ by a factor of ∼5. Then, we increase the length at a similar density (case 3), and we can observe a significant increase for Q_{tot} but a decrease for $Q_{[60-70\mathrm{MeV}]}$. Finally, we increase both the density and the cell length (case 4) and observe an increase for both Q_{tot} and $Q_{[60-70\mathrm{MeV}]}$.

To further understand this behavior, we plotted the electron spectra for cases 1–4 in Fig. 5(b). Compared with case 1 (solid black line), case 2 (solid blue line) exhibits a higher charge density over the whole spectrum and extends to higher electron energy. For case 2, as the density is higher, the laser self-focuses earlier in the profile, leading to higher charge and higher accelerating field amplitude. The length for case 3 is much longer than the dephasing length and the ionization-induced injection process is in this case continuous which explains the broad spectrum observed in Fig. 5(b) (solid red line). Both the dephasing length and the depletion length at this density ($n_{e0} \sim 8.3 \times 10^{18}\,\mathrm{cm}^{-3}$, $L_D \simeq 2.3$ mm, and $L_\varphi \simeq 0.6$ mm (Ref. 25)) are larger than the cell length of case 1; therefore, an increase in length compared with case 1 leads to an increase of E_{max} as seen in Fig. 5(b) for case 3. For case 4, density and length are both increased, leading to an increase of accelerated charge (similar to case 2) and energy spectrum broadening (similar to case 3). In comparison with case 2, case 4 presents a lower high energy charge density which is probably due to the dephasing effect. The comparison of these 4 cases shows that the charge in the range of 60–70 MeV is maximized for larger n_{e0}, although for the set of parameters studied it reaches only 25% of the total measured charge at a value around 8 pC.

The effect of a_0 variations was studied numerically using WARP simulations, as the laser energy could not be increased in the experiment. In Fig. 6 are plotted Q_{tot} and $Q_{[60-70\mathrm{MeV}]}$ and the associated spectra at $n_{e0} = 7.8 \times 10^{18}\,\mathrm{cm}^{-3}$ and $z_f = 0.65$ mm and for different values of a_0 indicated on the horizontal axis. Q_{tot} and $Q_{[60-70\mathrm{MeV}]}$ are normalized to the same value as in Fig. 3(a) to be comparable to experimental values in pC and the spectra are normalized to the same value as in Fig. 2 to be comparable to experimental spectra in pC/MeV. Fig. 6(a) shows that an increase of a_0 from 1.1 to 2 multiplies Q_{tot} by 13.7 and $Q_{[60-70\mathrm{MeV}]}$ by 8.3. In Fig. 6(b), we observe that the spectra exhibit higher charge density over all the spectrum for higher a_0 and a higher E_{max}. We also observe a peak appearing around 50 MeV for $a_0 = 2$ which can be of interest for an injector at this energy.

Fig. 7 presents the evolutions of a_0 along the propagation axis and the beginning of injection for the different cases. For all simulation results, injection is observed when $\triangle\phi = \phi_i - \phi_{min} \simeq 1$, where ϕ_i is the normalized electrostatic potential of the plasma wave ($\phi = e\Phi/m_e c^2$) at the position of creation of electrons ionized from N^{5+} and N^{6+} and ϕ_{min} its first minimum. To satisfy this condition at a density lower than n_{e0}, i.e., to drive a similar amplitude plasma wave at lower density, the laser amplitude must be higher.[26] For a value in-vacuum of $a_0 = 2$, the laser power is high enough for self-focusing to occur in the entry gradient. In this case, injection is observed at $n_e \simeq 0.4 \times n_{e0}$ when $a_0 \simeq 1.9$. It thus shows that increasing the initial value of a_0 and keeping z_f constant lead to injection earlier during the propagation.

For $a_0 = 1.5$ and 2, we observe significant injection of hydrogen electrons although their contribution to the spectrum is smaller than the contributions of electrons coming from ionized N^{5+} and N^{6+}. Indeed, electrons from hydrogen represent ∼9% and ∼17% of the total charge in case of an initial a_0 of 1.5 and 2, respectively. We also observe that the maximum longitudinal electric field is ∼1.9 and ∼2.7 times higher for $a_0 = 1.5$ and $a_0 = 2$, respectively. Both effects, earlier injection and the excitation of larger amplitude electric fields over a longer distance, contribute to produce higher charge and electron bunches with higher energy.

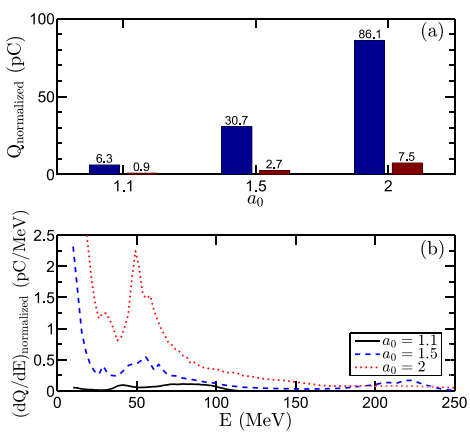

FIG. 6. (a) Simulated electron bunches total charge Q_{tot} (blue bars) and charge in the 60–70 MeV energy range $Q_{[60-70\mathrm{MeV}]}$ (red bars) and (b) associated electron energy distribution for different values of a_0. Normalization is the same as in Fig. 3.

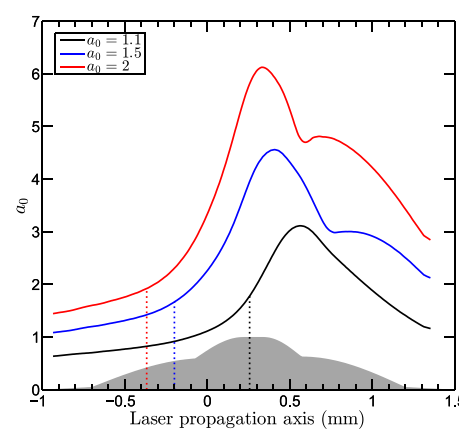

FIG. 7. Evolution of a_0 along the propagation axis for different values of a_0 in vacuum. Solid lines represent the value of the normalized vector potential and dashed lines indicate the start of injection in each case.

V. CONCLUSION

In conclusion, we showed that the position of the laser focal plane along the density profile of a gas cell plays a major role in triggering the ionization-induced injection of electrons and controlling acceleration processes, and therefore on determining the properties of generated electron bunches. Especially, we showed that the focal plane position relative to the cell entrance changes the maximum value of a_0, which has an impact on the longitudinal position of injection and electrostatic fields magnitude. By changing the focal plane position, the electron bunch charge and energy distribution can be tuned, either to optimize the electron bunch total charge or the charge in a given energy range, for example, 60–70 MeV optimized to 41% of the total measured charge for the case of Fig. 2(d) (case 1). For this case, the focal plane in vacuum is located in the exit density gradient ($z_f = 0.9$ mm) and $a_0 = 1.1$, simulation results show a distribution centered at ∼68 MeV. The charge in the 60–70 MeV range can be increased by a factor of ∼5 by increasing the density (case 2). When a_0 is increased from 1.1 to 2, simulations predict 13.6 times higher charge electron bunch exhibiting a peaked distribution at ∼50 MeV.

ACKNOWLEDGMENTS

Authors acknowledge the use of the computing facility clusters GMPCS of the LUMAT federation (FR LUMAT 2764). This work was supported by the Triangle de la Physique under Contract No 2012-032TELISA. Authors also acknowledge the support of the Swedish Research Council, the Knut and Alice Wallenberg Foundation, the Swedish Foundation for Strategic Research, Laserlab-Europe/CHARPAC, and EuCARD2/ANAC2 (Grant Agreements Nos. 284464 and 312453, EC's 7th Framework Programme). This work was supported in part by the Director, Office of Science, Office of High Energy Physics, U.S. Dept. of Energy under Contract No. DE-AC02-05CH11231.

[1]T. Tajima and J. M. Dawson, Phys. Rev. Lett. **43**, 267 (1979).
[2]E. H. Esarey, R. F. Hubbard, W. P. Leemans, A. Ting, and P. Sprangle, Phys. Rev. Lett. **79**, 2682 (1997).
[3]J. Faure, C. Rechatin, A. Norlin, A. F. Lifschitz, Y. Glinec, and V. Malka, Nature **444**, 737 (2006).
[4]S. V. Bulanov, N. Naumova, F. Pegoraro, and J. Sakai, Phys. Rev. E **58**, R5257 (1998).
[5]C. G. R. Geddes, K. Nakamura, G. R. Plateau, C. Tóth, E. Cormier-Michel, E. H. Esarey, C. B. Schroeder, J. R. Cary, and W. P. Leemans, Phys. Rev. Lett. **100**, 215004 (2008).
[6]K. Schmid, A. Buck, C. M. S. Sears, J. M. Mikhailova, R. Tautz, D. Herrmann, M. Geissler, F. Krausz, and L. Veisz, Phys. Rev. Spec. Top. - Accel. Beams **13**, 091301 (2010).
[7]M. Burza, A. Gonoskov, K. Svensson, F. Wojda, A. Persson, M. Hansson, G. Genoud, M. Marklund, C.-G. Wahlström, and O. Lundh, Phys. Rev. Spec. Top. -Accel. Beams **16**, 011301 (2013).
[8]M. Chen, Z.-M. Sheng, Y.-Y. Ma, and J. Zhang, J. Appl. Phys. **99**, 056109 (2006).
[9]A. Pak, K. A. Marsh, S. F. Martins, W. Lu, W. B. Mori, and C. Joshi, Phys. Rev. Lett. **104**, 025003 (2010).
[10]M. Chen, E. H. Esarey, C. B. Schroeder, C. G. R. Geddes, and W. P. Leemans, Phys. Plasmas **19**, 033101 (2012).
[11]F. G. Desforges, B. S. Paradkar, M. Hansson, J. Ju, L. Senje, T. L. Audet, A. Persson, S. D. Dufrénoy, O. Lundh, G. Maynard, P. Monot, J.-L. Vay, C.-G. Wahlström, and B. Cros, Phys. Plasmas **21**, 120703 (2014).
[12]C. McGuffey, A. G. R. Thomas, W. Schumaker, T. Matsuoka, V. Chvykov, F. J. Dollar, G. Kalintchenko, V. Y. A. Maksimchuk, K. Krushelnick, V. Y. Bychenkov, I. V. Glazyrin, and A. V. Karpeev, Phys. Rev. Lett. **104**, 025004 (2010).
[13]C. E. Clayton, J. E. Ralph, F. Albert, R. A. Fonseca, S. H. Glenzer, C. Joshi, W. Lu, K. A. Marsh, S. F. Martins, W. B. Mori, A. Pak, F. S. Tsung, B. B. Pollock, J. S. Ross, L. O. Silva, and D. H. Froula, Phys. Rev. Lett. **105**, 105003 (2010).
[14]B. B. Pollock, C. E. Clayton, J. E. Ralph, F. Albert, A. Davidson, L. Divol, C. Filip, S. H. Glenzer, K. Herpoldt, W. Lu, K. A. Marsh, J. Meinecke, W. B. Mori, A. Pak, T. C. Rensink, J. S. Ross, J. Shaw, G. R. Tynan, C. Joshi, and D. H. Froula, Phys. Rev. Lett. **107**, 045001 (2011).
[15]J. Osterhoff, A. Popp, Z. Major, B. Marx, T. P. Rowlands-Rees, M. Fuchs, M. Geissler, R. Hörlein, B. H. S. Becker, E. A. Peralta, U. Schramm, F. Grüner, D. Habs, F. Krausz, S. M. Hooker, and S. Karsch, Phys. Rev. Lett. **101**, 085002 (2008).
[16]M. Vargas, W. Schumaker, Z.-H. He, Z. Zhao, K. Behm, V. Chvykov, B. Hou, K. Krushelnick, A. Maksimchuk, V. Yanovsky, and A. G. R. Thomas, Appl. Phys. Lett. **104**, 174103 (2014).
[17]F. G. Desforges, M. Hansson, J. Ju, L. Senje, T. L. Audet, S. Dobosz-Dufrénoy, A. Persson, O. Lundh, C.-G. Wahlström, and B. Cros, Nucl. Instrum. Methods Phys. Res., Sect. A **740**, 54 (2014).
[18]M. Hansson, L. Senje, A. Persson, O. Lundh, C.-G. Wahlström, F. G. Desforges, J. Ju, T. L. Audet, B. Cros, S. D. Dufrénoy, and P. Monot, Phys. Rev. Spec. Top. -Accel. Beams **17**, 031303 (2014).
[19]J.-L. Vay, D. P. Grote, R. H. Cohen, and A. Friedman, Comput. Sci. Discovery **5**, 014019 (2012).
[20]J. Ju and B. Cros, J. Appl. Phys. **112**, 113102 (2012).
[21]See http://www.openfoam.com for Openfoam documentation, 2014.
[22]A. Buck, K. Zeil, A. Popp, K. Schmid, A. Jochmann, S. D. Kraft, B. Hidding, T. Kudyakov, C. M. S. Sears, L. Veisz, S. Karsch, J. Pawelke, R. Sauerbrey, T. Cowan, F. Krausz, and U. Schramm, Rev. Sci. Instrum. **81**, 033301 (2010).
[23]A. Lifschitz, X. Davoine, E. Lefebvre, J. Faure, C. Rechatin, and V. Malka, J. Comput. Phys. **228**, 1803 (2009).
[24]G. L. Yudin and M. Y. Ivanov, Phys. Rev. A **64**, 013409 (2001).
[25]W. Lu, M. Tzoufras, C. Joshi, F. S. Tsung, W. B. Mori, J. M. Vieira, R. A. Fonseca, and L. O. Silva, Phys. Rev. Spec. Top. -Accel. Beams **10**, 061301 (2007).
[26]L. M. Gorbunov and V. I. Kirsanov, Sov. Phys. - JETP **93**, 509–518 (1987).

Paper III

Localization of ionization-induced trapping in a laser wakefield accelerator using a density down-ramp

M. Hansson, T. L. Audet, H. Ekerfelt, B. Aurand,
I. Gallardo González, F. G. Desforges, X. Davoine, A. Maitrallain,
S. Reymond, P. Monot, A. Persson, S. Dobosz Dufrénoy,
C.-G. Wahlström, B. Cros and O. Lundh.

Plasma Phys. Control. Fusion **58**, 055009 (2016).

OPEN ACCESS
IOP Publishing
Plasma Physics and Controlled Fusion
Plasma Phys. Control. Fusion **58** (2016) 055009 (7pp)
doi:10.1088/0741-3335/58/5/055009

Localization of ionization-induced trapping in a laser wakefield accelerator using a density down-ramp

M Hansson[1], T L Audet[2], H Ekerfelt[1], B Aurand[1], I Gallardo González[1], F G Desforges[2], X Davoine[3], A Maitrallain[4], S Reymond[1,5], P Monot[4], A Persson[1], S Dobosz Dufrénoy[4], C-G Wahlström[1], B Cros[2] and O Lundh[1]

[1] Department of Physics, Lund University, PO Box 118, 22100 Lund, Sweden
[2] Laboratoire de Physique des Gaz et des Plasmas, CNRS, Univ. Paris-Sud, Université Paris-Saclay, 91405 Orsay, France
[3] CEA, DAM, DIF, Bruyères-le-Châtel, 91297 Arpajon, France
[4] Laboratoire Interactions, Dynamique et Lasers, CEA, Université Paris-Saclay, 91191 Gif-sur-Yvette, France
[5] ENSTA ParisTech, Université Paris-Saclay, 828 boulevard des Maréchaux, 91762 Palaiseau, France

E-mail: martin.hansson@fysik.lth.se

Received 19 February 2016
Accepted for publication 26 February 2016
Published 23 March 2016

Abstract

We report on a study on controlled trapping of electrons, by field ionization of nitrogen ions, in laser wakefield accelerators in variable length gas cells. In addition to ionization-induced trapping in the density plateau inside the cells, which results in wide, but stable, electron energy spectra, a regime of ionization-induced trapping localized in the density down-ramp at the exit of the gas cells, is found. The resulting electron energy spectra are peaked, with 10% shot-to-shot fluctuations in peak energy. Ionization-induced trapping of electrons in the density down-ramp is a way to trap and accelerate a large number of electrons, thus improving the efficiency of the laser-driven wakefield acceleration.

Keywords: laser, wakefield, trapping, down-ramp, ionization

(Some figures may appear in colour only in the online journal)

1. Introduction

With the breakthrough in 2004 [1–3], the research on laser wakefield accelerators [4] has shown the possibility of generating beams of relativistic electrons with peaked electron energy spectra. The energy of the electrons in the beams depends strongly on the laser system in use, but also on other experimental parameters, such as length and density of the interaction medium, with energies ranging from a few tens of keV [5] up to a few GeV [6]. Much effort is now focused on controlling the properties of the generated beams [7], such as the energy and number of accelerated electrons as well as the divergence and pointing, and on reducing the shot-to-shot fluctuations of these beams [8]. Several techniques to control the injection and trapping of electrons in an excited plasma wave have been demonstrated experimentally to decrease the shot-to-shot fluctuations in charge and energy of the electrons in the generated beams. These methods include trapping by colliding pulses [9], trapping in density transitions [10, 11] and down-ramps [7, 12, 13] and ionization-induced trapping [14, 15].

Trapping of electrons in a density down-ramp is similar to the mechanism of self trapping, which occurs when the electrons that constitute the plasma wave approach and exceed the phase velocity of the wave. In a density down-ramp the phase velocity of the plasma wave behind the driving laser pulse is decreased and the threshold for trapping is thereby

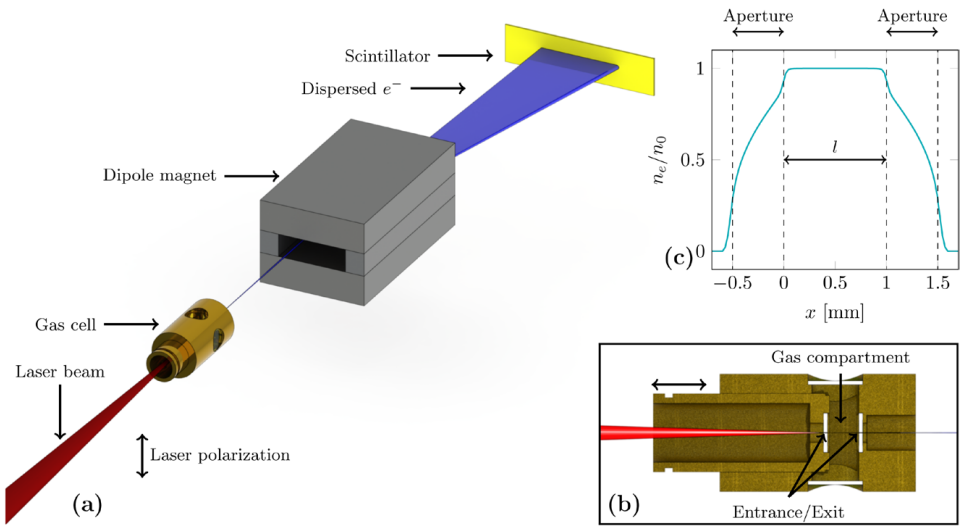

Figure 1. Schematic illustration of the experimental set-up. The laser pulses are focused, through an entrance aperture, into a cell filled with gas. The electrons, accelerated in the interaction, propagate along the optical axis and are then dispersed by a dipole magnetic field before impacting on a scintillating screen and recorded with a 16-bit CCD-camera. (b) Detailed cross section view of the gas cell. The gas cell allows the length to be varied under vacuum during the experiment. (c) Density distribution along the optical axis of the laser beam. The dashed lines marks the entrance and exit apertures through the windows confining the gas, and l is the inner length of the cell, i.e. the distance between the inner surfaces of the windows. The density gradients are characterized using computational fluid dynamics.

also decreased. A drawback of using this technique is that the amount of charge in the bunches of accelerated electrons is relatively small as compared to other mechanisms for injection.

The method of ionization-induced trapping is instead based on the release of free electrons, by field ionization of ions, close to the peak of the laser pulse inside the first period of the excited plasma wave. In contrast to trapping due to a density down-ramp, beams containing a large number of electrons are typically observed when using ionization-induced trapping. However, this type of trapping typically occurs over an extended length, and the electron energy distribution is therefore usually wide. Methods to localize ionization-induced injection and thereby generate quasi-monoenergetic electron energy spectra are certainly of interest including self-truncation of ionization-induced trapping and ionization-induced trapping in a shock [16, 17].

In this paper we present an experimental study, supported by particle-in-cell simulations, on controlled trapping of electrons using a combination of the mechanisms described above. This way, the advantage of higher charge due to ionization-induced trapping is combined with the localization of trapping in a density down-ramp, to produce peaked spectra with high charge. The accelerated beams of relativistic electrons are shown to be reproducible with respect to charge and energy.

2. Experimental setup

Experiments are conducted using the multi-terawatt laser at the Lund Laser Centre, based on chirped pulse amplification (CPA) in Ti:sapphire crystals. The duration of the laser pulses, when fully re-compressed after amplification, that are used in this experiment is (37 ± 3) fs full width at half maximum (FWHM) and each pulse contains approximately (585 ± 60) mJ of energy. The pulses are focused using an off-axis parabolic mirror with an effective focal length of 0.75 m. Furthermore, closed loop wave-front optimization is performed using a wave-front sensor (Phasics SID4) and a deformable mirror in the beam line. With this optimization the focal spot is almost circularly symmetric with a diameter of 17 μm (FWHM).

From the measured pulse duration and energy together with images of the focused laser pulse, the peak intensity is estimated to $(3.0 \pm 0.5) \times 10^{18}$ W cm^{-2} when the laser pulse is focused in vacuum, corresponding to a peak normalized vector potential $a_0 = 1.2 \pm 0.1$.

The leakage through the final dielectric folding mirror of a co-propagating reference beam is focused using a lens, and the focal plane is imaged onto a camera. The images of the focus of the reference beam is used, together with a piezo-electrically actuated mirror, to lock the position of the focused pulses and thus prevent long term drifts of the pointing.

The laser pulses are focused through an entrance aperture, with a diameter of either 100 μm or 200 μm, into a gas cell of variable length (see figures 1(a) and (b)). The gas cell is mounted using a 5-axis holder to allow accurate positioning of the cell along the optical axis, with the entrance of the cell at the beam waist. Gas is filled from a reservoir through an electronically controlled valve that is opened well before the laser pulse arrives at the target, to reach a stationary density of gas

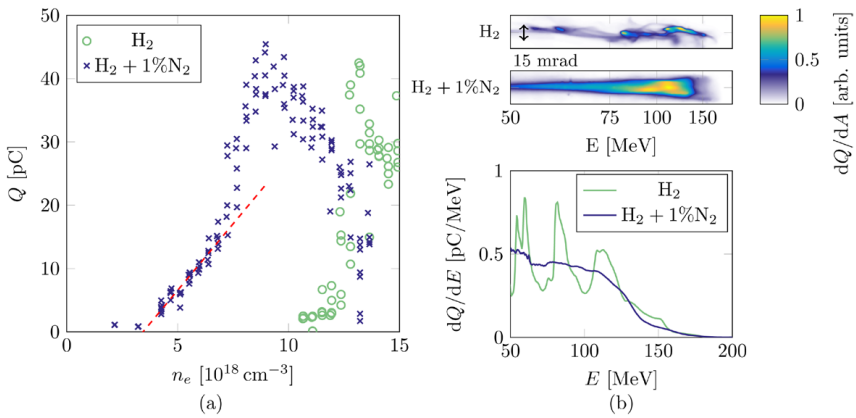

Figure 2. (a) Accelerated charge as a function of electron number density in the density plateau of the cell with the inner length set to 2 mm. The threshold in electron number density is clearly lower when 1% of nitrogen is present in the gas as compared to pure hydrogen. Furthermore the threshold for trapping is not as sharp as when pure hydrogen is used. The red dashed line is fitted to the accelerated charge using the gas mixture at electron number densities between 4×10^{18} cm^{-3} and 7×10^{18} cm^{-3}. (b) Typical shape of dispersed electron beams of electrons, and corresponding spectra, accelerated in the gas mixture and in pure hydrogen for beams containing approximately 40 pC of charge. The electron number density is set to 9×10^{18} cm^{-3} when the gas mixture is used and 13×10^{18} cm^{-3} when pure hydrogen is used. The colormap in each image is normalized to its maximum value. The beams of electrons accelerated in the gas mixture typically have a large divergence and a wide electron energy spectrum whereas the beams of electrons accelerated in pure hydrogen typically consist of multiple peaked features.

in the cell. The number density of neutral gas molecules was characterized using interferometry as a function of backing pressure off-line before the experiment started. Furthermore, the density gradients at the entrance and exit were characterized using computational fluid dynamics simulations (using both OpenFOAM SonicFOAM solver and COMSOL CFD). The length of the gradients (from 10% to 90% of the plateau density) are between 0.5 mm and 0.7 mm depending on the size of the apertures. The normalized gas density distribution along the optical axis of the laser beam is shown in figure 1(c).

To compare self-trapping with ionization-induced trapping, two types of gases are used in the experiment. Pure hydrogen gas is used to allow only self-trapping, whereas a mixture of hydrogen and 1% nitrogen is used to enable ionization-induced trapping.

The electrons accelerated in the interaction co-propagate with the laser pulse along the optical axis onto a scintillating screen (Kodak Lanex regular), covered with an aluminum foil that blocks the laser light. The light emitted from the rear side of the scintillating screen is recorded using a 16-bit CCD-camera, and the total response of the system is calibrated and used together with published calibration factors for the screen [18] to determine the amount of charge in the beams of electrons impacting on the screen. Furthermore, a dipole magnet is mounted on a manual linear translation stage and can be moved into the electron beam under vacuum to disperse the electrons depending on their energy. Numerically tracing the electrons through the dipole magnetic field allows electron energy spectra to be determined from the acquired images of the dispersed electrons impacting the scintillating screen.

Before acquiring a series of data, the longitudinal laser focus position, with respect to the gas cell is fine tuned, either by moving the cell or by changing the curvature of the deformable mirror, to yield the best quality of the beams of accelerated electrons. Similarly, the pulse compression is optimized by fine tuning the grating separation.

3. Experiments and results

3.1. Self trapping and ionization-induced trapping

The inner length of the cell, i.e. the distance between the inner surfaces of the front and back windows, is set to 2 mm and a sequence of shots is recorded while the backing pressure supplied to the gas cell is varied using either pure hydrogen or a gas mixture containing 1% of nitrogen.

As shown in figure 2(a), the electron number density threshold for trapping of electrons is significantly lower for the gas mixture than for pure hydrogen. This is expected, since the threshold for ionization-induced trapping is lower than for self-trapping [19]. Furthermore, it is observed that the threshold for trapping is much sharper in the case of self-trapping in pure hydrogen than for ionization-induced trapping in the gas mixture. Using the gas mixture at low electron number density, 4×10^{18} cm^{-3} to 7×10^{18} cm^{-3}, the amount of charge in the beams of accelerated electrons scales almost linearly with the electron number density in the plasma, indicated by the red dashed line in figure 2(a). The shot-to-shot fluctuations in charge, as deviations from a fitted linear dependence on the density, is only 1.2 pC here. At higher electron number densities the charge increases more rapidly with density but the relative shot-to-shot fluctuations in charge remains low, and is on average 14.5% at each selected value of electron number density.

A typical image of a dispersed electron beam accelerated when the cell is filled with the gas mixture to provide

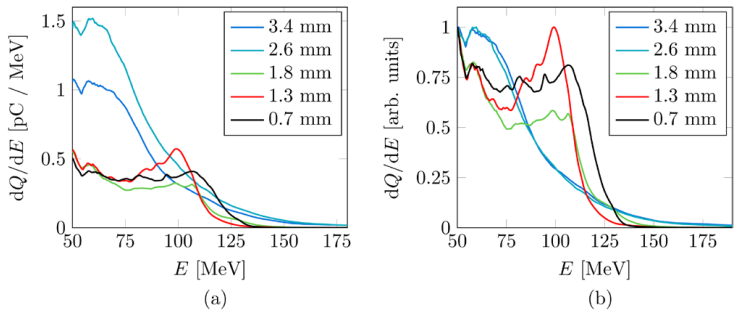

Figure 3. (a) Evolution of the electron energy spectrum for beams accelerated using the gas mixture at an electron number density of 12×10^{18} cm^{-3} as the length of the gas cell is varied. A peaked feature is observed for cell lengths between 0.7 mm and 1.8 mm. The visibility of the peaked feature is highest at a cell length of 1.3 mm as shown in (b) where the spectra are normalized at 50 MeV. For longer cells the amount of charge is larger but no peak is observed in the electron energy spectra.

an electron number density of 9×10^{18} cm^{-3} is shown in figure 2(b). This image shows the reproducible features of the beams of accelerated electrons trapped by ionization, with a large energy spread up to a cut-off energy of approximately 150 MeV and a rather large divergence that is increasing with electron energy (≈12 mrad at 100 MeV). The beam charge, of electrons with energy above 50 MeV, is in this case 38 pC.

Beams with similar amount of charge are produced using pure hydrogen at a higher electron number density, 13×10^{18} cm^{-3}. A typical image of a dispersed electron beam accelerated under these conditions is shown in figure 2(b). Due to oscillations of the peak normalized vector potential, a_0, these beams typically contain multiple, peaked, components as self trapping occurs at multiple locations along the plasma and the energy and number of peaks are fluctuating from shot to shot. Each of these components has an energy spread of about 10% and a divergence smaller than 10 mrad.

3.2. Trapping in a density down-ramp

The length of the cell is varied in a sequence of shots with the cell filled with the gas mixture of hydrogen and 1% of nitrogen and the typical spectral shapes are studied. The electron number density is set to 12×10^{18} cm^{-3} to operate the accelerator well above the threshold for ionization-induced trapping [20]. At this density, the power of the laser pulse exceeds the critical power for self-focusing, $P/P_c \approx 4$. The peak normalized vector potential is therefore expected to increase rapidly as the laser pulse enters the gas cell and reaches approximately the value for a matched pulse, for which the transverse size of the laser pulse is approximately equal to the transverse size of the electron void. For a laser pulse containing 585 mJ of energy this corresponds to $a_0 = 3.2$, according to the theory by Lu *et al* [21]. Under these conditions, the dephasing length is $L_d \approx 0.6$ mm. Thus, for regular ionization-induced trapping, broad electron energy spectra, without peaked features are expected.

In figure 3(a), spectra are shown for five shots at different inner cell lengths. For inner cell lengths of above 1.8 mm, the electron energy spectra are wide and monotonically decreasing with energy. For cell lengths of 1.8 mm and lower, the charge distribution is modified and a peak builds up at energies around 100 MeV. The visibility of the peak is largest for a cell length of 1.3 mm as made clear in figure 3(b), in which the spectra are normalized to the charge at 50 MeV.

For cell length below 1.8 mm, it is observed that the shape of the distribution is not sensitive to the cell length and with a peak in the range 100–110 MeV, which suggests that the distance from the point of trapping to the end of acceleration is unaffected by changes in the cell length. This is consistent with the assumption that these electrons are trapped in the density down-ramp at the back of the gas cell.

For a cell length of 0.7 mm, after re-optimizing both longitudinal laser focus position, using the deformable mirror, and pulse compression by adjusting the grating separation, and after decreasing the electron number density to 9.6×10^{18} cm^{-3}, the peaked features in the spectrum are even more clear (see figure 4(a)). In addition, another peaked feature at higher energy is observed. The peak at lower energy is reproducible and appeared in 73 of 100 shots in a sequence. For these shots the energy of the peak is 90 MeV ± 10% and the energy spread is 20 MeV ± 48%. For the remaining 27 shots, a component at similar energy and divergence is still observed, but is not contributing to a peak in the spectrum but rather a wide distribution of energies up to ≈ 120 MeV. In both cases the divergence was only approximately 3 mrad.

The peak at higher energy is observed on all shots in this sequence at an energy of 150 MeV ± 7%, with an energy spread of 50 MeV ± 18%. This second peaked feature has a larger divergence (≈10 mrad) than the component at lower energy. The total amount of detected charge is on average 9 pC ± 28% in this series of shots.

Under the same conditions, but switching to pure hydrogen, only the peak at 150 MeV remain, as shown in figure 4(b). In this series of shots, the amount of charge is on average 1.0 pC ± 29%, but increases to 2.0 pC when moving the cell only 0.25 mm along the optical axis.

Typical spectra from the two cases, normalized at the peak at high energy, are shown in figure 4(c). Here it can be observed that the energy spread of the component at 150 MeV

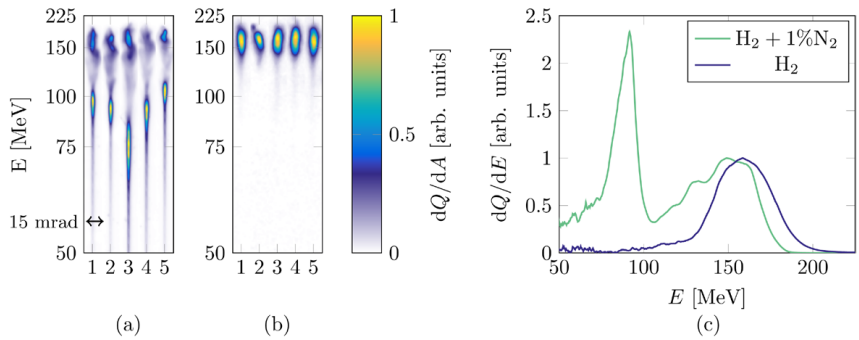

Figure 4. Typical traces of the dispersed electron beams using (a) a mixture of hydrogen and 1% nitrogen and (b) pure hydrogen, at an electron number density of 9.6×10^{18} cm^{-3} in a cell with an inner length of 0.7 mm. Each trace is normalized to its peak value. The total amount of detected charge is 9 pC $\pm$ 28% in the case of the gas mixture and 1.0 pC $\pm$ 29% in the case of the pure hydrogen. Typical energy spectra of beams of electrons accelerated in pure hydrogen and in a mixture of 1% nitrogen in hydrogen are shown in (c). The energy spectra of all beams feature a peak at approximately 150 MeV. In addition, the beams accelerated in the gas mixture typically contain another peak at a lower energy ($\approx$ 90 MeV). Each curve is normalized to its corresponding value at the peak around 150 MeV, to allow the shapes to be compared.

is approximately 50 MeV (FWHM) in both cases. The component at low energy, for this shot at 90 MeV, has a significantly smaller energy spread of only 15 MeV.

3.3. Three-dimensional particle-in-cell simulations

Simulations are performed using the fully relativistic three-dimensional particle-in-cell code CALDER-CIRC [22], which is exploiting the fact that only a low number of azimuthal Fourier components are required to model laser wakefield acceleration. In the simulations the time step is set to 52 attoseconds and a window following the laser pulse, with a size of 50 μm longitudinally and 75 μm radially, is used. The spatial grid size is set to 16 nm in the longitudinal direction and 190 nm in the radial direction, and three azimuthal Fourier modes are used.

The laser pulse is defined in the simulations to have a pulse duration of 34 fs and a transversal size of 17 μm (FWHM) when focused in vacuum, with a peak normalized vector potential of 1.25, approximately corresponding to laser parameters in the experiment. The waist of the laser beam, when not affected by the propagation in the plasma, is chosen in the simulations to be located at the beginning of the density plateau inside the cell. Furthermore, the shape of gradients of the density distribution in the entrance and exit of the cell are fitted as piece-wise linear functions, consisting of three parts, from the results from the characterization of the gradients using computational fluid dynamics. The length of the gradient is chosen to be 500 μm, in the fall from 90% to 10% of the plateau density, which corresponds to the shortest possible gradient determined using computational fluid dynamics.

First, simulations are performed at different electron number densities to determine the threshold of self trapping in the density plateau. A simulation is then performed for a cell with an inner length of 0.8 mm at an electron number density of 9.1×10^{18} cm^{-3} to avoid self-trapping in the density plateau. The results from this simulation are summarized in figure 5 (a). Here, the evolution of the electron energy spectra are shown for the electrons released by ionization from H and $N - N^{4+}$ in black (upper) and the electrons released by ionization from N^{5+} and N^{6+} green (lower). Also, the evolution of the peak normalized vector potential inside the plasma is shown in red and the electron number density is shown in blue. Each of these curves are normalized to the corresponding maximum value of the simulation. Furthermore, in figures 5(c) and (d), the electron distribution is shown, both in real space and longitudinal phase-space, close to the laser pulse before (b), in the middle (c) and in the end (d) of the density down-ramp together with the corresponding electron energy spectrum at each position.

Under these conditions, ionization-induced trapping occurs continuously in the plateau between the input and exit of the cell and provide a wide, but very weak, background in the electron energy spectrum.

An increased rate of trapping of electrons is observed in the density down-ramp, both for electrons from the background plasma and for electrons ionized from N^{5+} and N^{6+}. The electron energy spectrum at the end of the density down-ramp contains two slightly separated peaks, consistent with the experimental results. The peak at higher energy is identified to contain electrons from ionization of hydrogen and from the first ionization states of nitrogen ($N - N^{4+}$). These electrons are released into the plasma, by ionization from their corresponding atoms or ions, far from the peak of the laser pulse, and the simulation shows that these electrons are injected and trapped in the density down-ramp at the exit of the gas cell by density down-ramp injection. The spectral peak at lower energy is due entirely to electrons from ionization of N^{5+} and N^{6+}, which occur much closer to the peak of the laser pulse. The simulation shows that these electrons are also trapped in the density down-ramp at the exit from the gas cell.

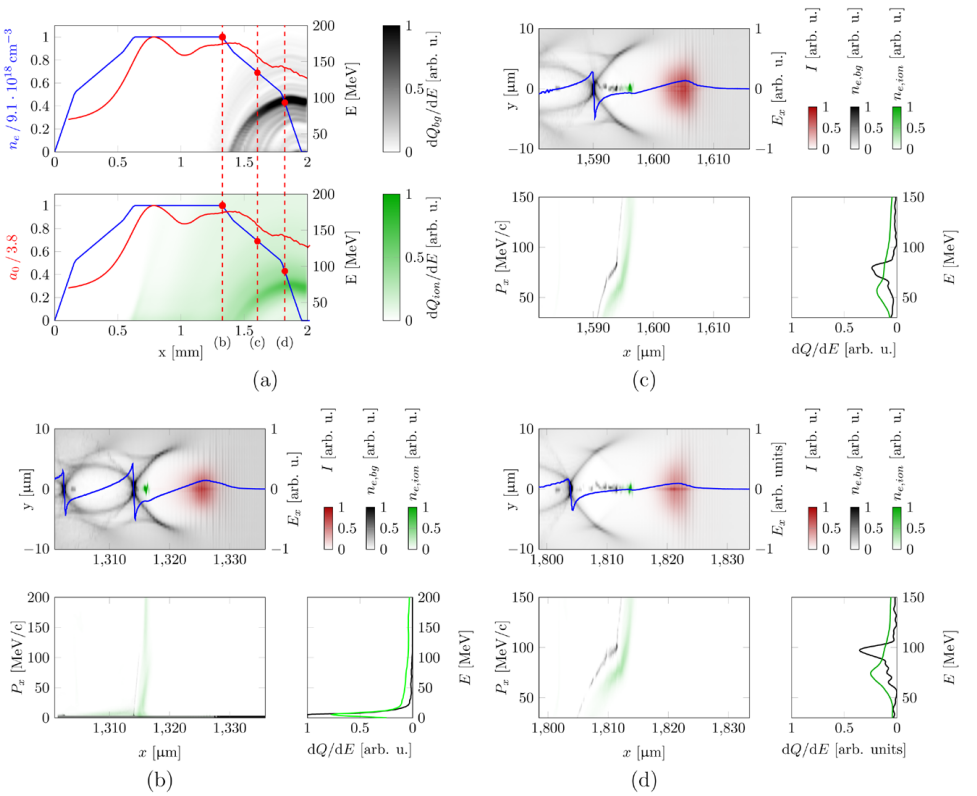

Figure 5. Summary of a particle-in-cell simulation (a) showing the evolution of the spectrum of the trapped electrons released by ionization from H and N − N^{4+} (black) and from N^{5+} and N^{6+} (green). Three snapshots ((b)–(d)) from the simulation showing trapping of electrons in the density down-ramp at the exit of the cell, with the corresponding position of each snapshot marked in the density profile in (a). For each snapshot, the density distribution of the background electrons is shown in black, and the electrons released from N^{5+} and N^{6+} in green. The intensity distribution of the laser pulse is shown in red. Before the density down-ramp (b), only a small fraction of electrons, mainly released by ionization of N^{5+} and N^{6+}, has been trapped. The electrons released from H and N − N^{4+} and trapped in the density down-ramp (c) are well separated in phase-space from the electrons released from N^{5+} and N^{6+} that are also trapped in this ramp. After further acceleration, and phase-space rotation due to the longitudinal extent of the injected electrons, these two populations form two peaks in the energy spectrum (d).

The simulation further reveals a longitudinal separation of the electrons that build up the two components after they have been trapped in the plasma wave. During the subsequent acceleration in the density down-ramp, the electrons from ionization of N^{5+} and N^{6+} are located closer to the center of the electron void, and thus experience a lower accelerating field than the trapped electrons ionized from H and N − N^{4+}, which are located further to the back of the electron void.

The reason for this separation is a fundamental difference in the injection and trapping mechanism. The electrons, already released from the atoms far from the peak of the laser pulse, are injected at the back of the electron void following the laser pulse, as the size of the bubble is growing in the density down-ramp. In contrast, ionization of N^{5+} and N^{6+} releases electrons into the plasma closer to the peak of the laser pulse and they are able to pass through the rest of the laser field into the electron void. The released electrons are then accelerated by the longitudinal electric field and catch up with and exceeds the speed of the laser pulse (corresponding to a relativistic factor $\gamma_l \approx 14$).

Overall, the final electron energy spectrum of the simulation agrees qualitatively well with the experimental findings under similar conditions. However, the energy of the two spectrally peaked features are lower than observed in the experiments. We attribute those differences to discrepancies in the parameters of the laser pulse and/or density distribution between the experiment and simulation. In particular, the effect of a longer density ramp is two-fold: (I) the effective length of acceleration becomes longer. (II) The plasma wavelength is increasing more slowly, which means that the dephasing of the electrons due to the expansion of the plasma wave is slower.

4. Discussions

Our experiment using a gas mixture shows two different regimes of laser wakefield acceleration of ionization-induced trapped electrons. For cells longer than approximately 2 mm, a large number of electrons are trapped by ionization-induced trapping, after self-focusing of the laser pulse, in the density plateau. This process occurs over an extended length, as long as the conditions for trapping are fulfilled, and the resulting electron energy spectra are therefore wide without peaked features. Under these conditions, the threshold, in electron number density, for ionization-induced trapping is lower than for self-trapping. For electron number densities in the range between 4×10^{18} cm^{-3} and 7×10^{18} cm^{-3}, the amount of charge in the bunches of accelerated electrons scales linearly with electron number density in the plateau, with only small shot-to-shot fluctuations. This regime is therefore favorable when good control over the charge is desired, but has the drawback of generating beams of electrons with wide energy spectra.

For shorter cells, only few electrons are trapped in the density plateau and provide broad and weak distributions in the energy spectra. However, the density down-ramp at the exit of the cell increases the rate of trapping by ionization, as observed in the simulations. The reason for this increased rate of trapping is the decreased phase velocity of the wake, as the wake period increases behind the laser pulse as it propagates through the density down-ramp, which facilitates trapping of electrons. The region from which electrons can be ionized to become trapped in the wake therefore locally increases in a density down-ramp. Localization of the trapping, together with phase-space rotation of the distribution of trapped electrons [7], yield a peak in the electron energy spectrum.

Similarly, the threshold for trapping of electrons from the background plasma also decreases in the density down-ramp at the exit of the cell, and these trapped electrons also contribute to a peak in the electron energy spectrum (see figures 4(b) and (c)). The electrons trapped from the background plasma are subject to a stronger accelerating field in the wake which results in a higher energy for these electrons compared to the electrons from ionization from N^{5+} and N^{6+}.

While the electron energy is higher for the electrons trapped from the background plasma in the density down-ramp, the amount of charge is significantly higher when also ionization-induced trapping occurs in the density down-ramp.

Due to pump depletion, as the length of the cell is increased, the strength of the laser pulse as it reaches the exit down-ramp is decreased. Therefore, the amount of charge injected in the down-ramp is expected to decrease, which agrees well with our observation of no peaked features for cells longer than approximately 1.8 mm.

5. Conclusions

We have shown experimentally, and supported by simulations, that the advantage of ionization-induced trapping to provide high charge in beams of accelerated electrons can be combined with a density down-ramp to localize the injection and thereby providing peaked electron energy spectra. Higher charge in the accelerated beams, as compared to pure density down-ramp injection, also implies a better efficiency of the accelerator. The peak energy of the electrons trapped by field ionization of N^{5+} and N^{6+} at the back of a gas cell shows only small shot-to-shot fluctuations and the method is therefore a suitable choice for a stable wakefield accelerator.

Acknowledgments

We acknowledge the support of the Swedish Research Council, the Knut and Alice Wallenberg Foundation, the Swedish Foundation for Strategic Research, the Triangle de la Physique (Grant Agreement No. 2012-032TELISA), Laserlab-Europe/LEPP (Grant Agreement No. 654148, EC's Horizon 2020) and EuCARD2/ANAC2 (Grant Agreement No. 312453, EC's 7th Framework Programme). The simulations were performed on resources provided by the Swedish National Infrastructure for Computing (SNIC) at Lunarc. SR acknowledges support from the ERASMUS programme.

References

[1] Faure J, Glinec Y, Pukhov A, Kiselev S, Gordienko S, Lefebvre E, Rousseau J P, Burgy F and Malka V 2004 *Nature* **431** 541–4
[2] Geddes C G R, Toth C, van Tilborg J, Esarey E, Schroeder C B, Bruhwiler D, Nieter C, Cary J and Leemans W P 2004 *Nature* **431** 538–41
[3] Mangles S P D *et al* 2004 *Nature* **431** 535–8
[4] Tajima T and Dawson J M 1979 *Phys. Rev. Lett.* **43** 267–70
[5] He Z H, Thomas A G R, Beaurepaire B, Nees J A, Hou B, Malka V, Krushelnick K and Faure J 2013 *Appl. Phys. Lett.* **102** 064104
[6] Leemans W P *et al* 2014 *Phys. Rev. Lett.* **113** 245002
[7] Hansson M, Aurand B, Davoine X, Ekerfelt H, Svensson K, Persson A, Wahlström C G and Lundh O 2015 *Phys. Rev. ST Accel. Beams* **18** 071303
[8] Hansson M *et al* 2014 *Phys. Rev. ST Accel. Beams* **17** 031303
[9] Faure J, Rechatin C, Norlin A, Lifschitz A, Glinec Y and Malka V 2006 *Nature* **444** 737–9
[10] Schmid K, Buck A, Sears C M S, Mikhailova J M, Tautz R, Herrmann D, Geissler M, Krausz F and Veisz L 2010 *Phys. Rev. ST Accel. Beams* **13** 091301
[11] Burza M, Gonoskov A, Svensson K, Wojda F, Persson A, Hansson M, Genoud G, Marklund M, Wahlström C G and Lundh O 2013 *Phys. Rev. ST Accel. Beams* **16** 011301
[12] Gonsalves A J *et al* 2011 *Nat. Phys.* **7** 862–6
[13] Golovin G, Chen S, Powers N, Liu C, Banerjee S, Zhang J, Zeng M, Sheng Z and Umstadter D 2015 *Phys. Rev. ST Accel. Beams* **18** 011301
[14] McGuffey C *et al* 2010 *Phys. Rev. Lett.* **104** 025004
[15] Desforges F G *et al* 2014 *Phys. Plasmas* **21**
[16] Mirzaie M *et al* 2015 *Sci. Rep.* **5** 14659
[17] Thaury C *et al* 2015 *Sci. Rep.* **5** 16310
[18] Buck A *et al* 2010 *Rev. Sci. Instrum.* **81** 033301
[19] Pak A, Marsh K A, Martins S F, Lu W, Mori W B and Joshi C 2010 *Phys. Rev. Lett.* **104** 025003
[20] Chen M, Esarey E, Schroeder C B, Geddes C G R and Leemans W P 2012 *Phys. Plasmas* **19** 033101
[21] Lu W, Tzoufras M, Joshi C, Tsung F S, Mori W B, Vieira J, Fonseca R A and Silva L O 2007 *Phys. Rev. ST Accel. Beams* **10** 061301
[22] Lifschitz A, Davoine X, Lefebvre E, Faure J, Rechatin C and Malka V 2009 *J. Comput. Phys.* **228** 1803–14

Paper IV

A tunable electron beam source using trapping of electrons in a density down-ramp in laser wakefield acceleration

H. Ekerfelt, M. Hansson, I. Gallardo González, X. Davoine and O. Lundh.

Sci. Rep. **7**, 12229 (2017).

www.nature.com/scientificreports

OPEN

Received: 10 July 2017
Accepted: 12 September 2017
Published online: 25 September 2017

A tunable electron beam source using trapping of electrons in a density down-ramp in laser wakefield acceleration

Henrik Ekerfelt[1], Martin Hansson[1], Isabel Gallardo González[1], Xavier Davoine[2] & Olle Lundh[1]

One challenge in the development of laser wakefield accelerators is to demonstrate sufficient control and reproducibility of the parameters of the generated bunches of accelerated electrons. Here we report on a numerical study, where we demonstrate that trapping using density down-ramps allows for tuning of several electron bunch parameters by varying the properties of the density down-ramp. We show that the electron bunch length is determined by the difference in density before and after the ramp. Furthermore, the transverse emittance of the bunch is controlled by the steepness of the ramp. Finally, the amount of trapped charge depends both on the density difference and on the steepness of the ramp. We emphasize that both parameters of the density ramp are feasible to vary experimentally. We therefore conclude that this tunable electron accelerator makes it suitable for a wide range of applications, from those requiring short pulse length and low emittance, such as the free-electron lasers, to those requiring high-charge, large-emittance bunches to maximize betatron X-ray generation.

In 1979[1], Tajima and Dawson proposed using a plasma as an accelerating structure for electrons. A focused laser pulse can excite a plasma wave due to the fact that the high intensity laser pulse acts as an electron plough, creating an ion cavity in its wake. This cavity is quickly replenished with electrons which results in a plasma wave trailing the laser pulse. The phase velocity of the plasma wave is close to the group velocity of the laser pulse. The plasma wave transforms the transverse electric fields of the laser into strong longitudinal electric fields that can reach hundreds of GV/m. These fields can in turn be used to accelerate charged particles. This concept is now referred to as laser wakefield acceleration (LWFA). In 2004, the first quasi-monoenergetic beams were produced using this technique without an external electron injection source[2–4]. When the driving laser pulse is strong enough, the ion cavity is commonly referred to as a bubble[5], which is the terminology that will be used to refer to the plasma wave behind the laser pulse in this report.

A density down-ramp is a region where the background density of the plasma is making a transition from a higher to a lower electron density in the direction of laser pulse propagation. When a laser pulse travels through a density down-ramp, the trailing bubble will elongate, since the size of the bubble scales as $n_e^{-1/2}$, where n_e is the background electron number density[6]. The elongation can, under certain conditions, trigger wave breaking at the back of the bubble; that in turn causes transverse electron injection. This scheme was first proposed by Bulanov *et al.*[7], who considered a slow density transition, and later by Suk *et al.*[8] who suggested using a sharper transition. It has since then been studied both experimentally and numerically[9–17]. The effects of changing the down-ramp length (by varying the gradient) have been studied earlier in detail by Samant *et al.*[18]. They propose to use the density down-ramp injection as an injector for a soft X-ray free-electron laser (FEL). In a recent paper, Massimo *et al.*[19] conducts a numerical study on a more shock-like profile where they also vary the peak density. Both papers find results that are in agreement with ours. In this paper, we further explain the physical processes and provide scaling laws for some of the electron bunch properties.

In previous experimental studies[10,13], it was shown that density down-ramp injection is ideal for reproducibility. It allows for control of the electron bunch charge, by tuning the density difference between the two density regions, and the bunch energy, by controlling the length of the plasma after the density down-ramp.

[1]Department of Physics, Lund University, P.O. Box 118, S-22100, Lund, Sweden. [2]CEA, DAM, DIF, Bruyères-le-Châtel, 91297, Arpajon, France. Correspondence and requests for materials should be addressed to H.E. (email: henrik.ekerfelt@fysik.lth.se)

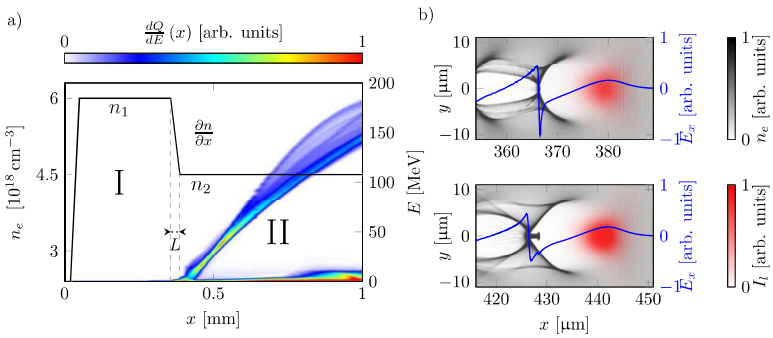

Figure 1. (**a**) A typical density profile used in the simulations. The profile is divided into a high - density region (I), characterized by the density n_1, and a low - density region (II), characterized by the density n_2. They are connected through a density down-ramp characterized by the gradient $\partial n/\partial x$ and its length L. The evolution of the energy spectrum $dQ/dE(x)$ of the electron bunch as a function of the longitudinal position x of the laser pulse's peak is shown as a density map in the background, where Q is the beam charge and E the beam energy. It can be seen that the electron bunch is trapped at the density down-ramp and then accelerated throughout the lower plasma density region. (**b**) Two snapshots from a typical simulation. A plasma wave has been excited to the bubble-regime by the laser pulse. The background electron density n_e is shown in grayscale, the laser intensity I_l is shown by the red color scale, and the longitudinal electric field E_x on the optical axis is shown as the blue curve in the graph. The upper plot is a snapshot from just before the laser pulse enters the density down-ramp. The lower plot shows a snapshot after the laser pulse has passed the down-ramp and traveled into the second region of constant density. The bubble expands in the density down-ramp and as a consequence, electrons are trapped along the optical axis from the back of the bubble, and begin to accelerate.

Today, LWFA is one of the most promising compact accelerator techniques. There are many different proposed applications of the electron beams and/or betatron X-ray beams produced during the acceleration. Each application has its preferred set of electron bunch parameters. For example, to use the produced electron bunch as an injector for a compact FEL, one would typically prefer a short electron bunch with low emittance, low energy spread and high current[20]. However, if one would like to utilize the betatron (synchrotron-like) X-rays produced during the acceleration process, other characteristics such as high charge and large emittance (larger betatron oscillations) are preferred[21].

In this report, we present a numerical study on the effect of down-ramp injection on the electron bunch parameters. The focus of the report lies on investigating the injection process and therefore the setup is kept constant until the density down-ramp. It is shown that the amount of charge in the electron bunch can be tuned by two parameters in the density profile; the density difference between two density regions where injection occurs as well as the steepness of the density down-ramp. The mean electron bunch energy and energy spread for different cases are presented and compared at a given distance. Furthermore, the trapped electrons fill up the bubble from the back along the optical axis as it expands. This allows for control of the electron bunch duration/length. Lastly, it is shown that the divergence of the trapped electron bunch depends on the steepness of the density down-ramp.

This study was performed using the quasi-cylindrical particle-in-cell code CALDER-Circ[22]. This code decreases the computational load by exploiting the cylindrical symmetry of the LWFA process. The numerical parameters for the simulations are given in the Method section.

Results

The density profile of a typical simulation is illustrated in Fig. 1a. The plasma profile is composed of an 18-μm long entrance ramp to the first plateau density (region I) characterized by the density n_1 which extends for 340 μm, followed by a density down-ramp to the second plateau (region II) characterized by the density n_2 which ends after 840 μm. The down-ramp between region I and II is characterized by its length L and its gradient $\partial n/\partial x = (n_1 - n_2)/L$. In this study we vary L, n_2, and consequently $\partial n/\partial x$. All other parameters are kept constant in order to as well as possible differentiate all the different mechanisms at play. This ensures that an identical laser pulse enters the down-ramp in each simulation. The plasma profile is 130 μm wide in both transverse directions with no density gradients. n_1 is kept constant to keep the laser parameters fixed when the laser pulse enters the down-ramp. We emphasize that alternatively, n_1 could be varied to achieve similar results for the charge, bunch length, and emittance of the electron bunch. However, this would also change the laser pulse's evolution, and it would be hard to isolate what effects comes from changing the down-ramp parameters. Varying n_2 greatly impacts the acceleration process since the accelerating fields change.

A typical simulation is illustrated with snapshots from one of the simulations in Fig. 1b. Note that the laser pulse effectively excites a bubble by the end of region I yet no injection has occurred until this point. The electrons

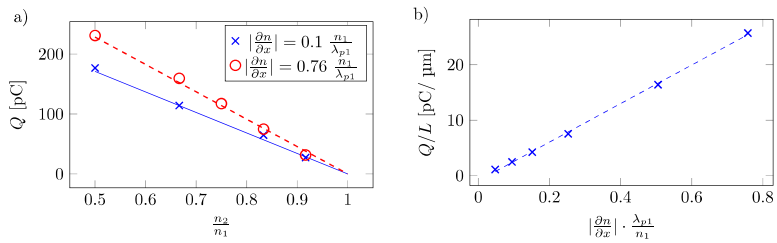

Figure 2. (**a**) Trapped charge as a function of the lower density value for two different gradient slopes. The symbols show data taken from the simulations. The corresponding lines are Eq. (2) with $k_1 = 34.761\lambda_{p1}/(n_1\mu\text{m})$ pC and $k_2 = -0.912$ pC/μm. (**b**) Trapped charge over down-ramp length as a function of different density down-ramp gradients with $n_2/n_1 = 0.5$. The amount of charge per length increases with the steepness of the gradient. The dashed blue line is Eq. (2) plotted with $k_1 = 34.76\lambda_{p1}/(n_1\mu\text{m})$ pC and $k_2 = -0.91$ pC/μm.

are injected at the back of the first bubble during the density down-ramp by so-called transverse-injection. When the back of the bubble has reached the end of the down-ramp the injection stops. In region II, the laser pulse still effectively drives a bubble with injected charge.

For the simulations the following laser parameters were used: a normalized vector potential $a_0 = 1.8$, a Gaussian laser focus with a full width at half maximum (FWHM) width of 18 μm, and a temporal Gaussian with $t_{FWHM} = 30$ fs. The focal plane of the laser beam in vacuum was located at the beginning of region I, 20 μm into the plasma.

In this section we present results that will show that modifying the properties of the density down-ramp is a promising method for controlling the electron bunch's charge, length and transverse emittance. The results presented in this report are only valid if we are in or close to the bubble regime: the laser pulse length and waist are in the same range, a_0 is higher than 2, the plasma densities are chosen so that the laser pulse length is smaller than the plasma wavelength. The densities should also be high enough to ensure self-focusing and guidance of the laser pulse over several Rayleigh lengths.

Amount of accelerated charge and bunch energy. As can be seen in Fig. 1a, a quasimonoenergetic beam without a low-energy tail is accelerated to more than 100 MeV after 0.5 mm propagation in region II. The electron bunch parameters are measured 0.9 mm into the plasma for different down-ramp lengths and density differences. The amount of trapped charge was measured for down-ramps with different density slopes $\partial n/\partial x$ and density ratios n_2/n_1. The results are plotted in Fig. 2a.

As is clear from Fig. 2a, the amount of charge have a quasi-linear dependence on the density difference. The trend shows that the amount of charge injected in a density down-ramp where the density difference is varied can be described by a very simple linear relation for the beam charge Q:

$$Q = k\left(\frac{\partial n}{\partial x}\right)(n_1 - n_2) = k\left(\frac{\partial n}{\partial x}\right)\frac{\partial n}{\partial x}L \tag{1}$$

where $k(\partial n/\partial x)$ is a function of the density slope and the laser properties. This relation agrees with previous experimental findings[13]. Since n_1 is close to the self-injection threshold, injection is reached even for small density differences, in contrast to the cases studied by Massimo *et al.*[19].

In Fig. 2b, the average amount of injected charge per μm (the total injected charge Q over the down-ramp length L) is plotted for different density slopes with a fixed density ratio of $n_2/n_1 = 0.5$. As can be seen, the beam charge over the down-ramp length scales nearly linearly with the slope. However, the higher charge per length unit with steeper gradient is compensated by the fact that injection occurs over a shorter distance, as an increase in steepness by some factor also decrease the gradient length L by the same factor for the same density difference. Note that, in Fig. 2a, as the slope steepness $\partial n/\partial x$ is increased almost one order of magnitude, the amount of charge increases by 25% in total for the density ratio of $n_2/n_1 = 0.5$. Using a linear fit, $Q/L = k_1(\partial n)/(\partial x) + k_2$, from Fig. 2b, one can describe the charge dependence for the different slopes by making it a function of the down-ramp length L and adding the linear correction term k_2

$$Q = k_1\frac{\partial n}{\partial x}L + k_2 L. \tag{2}$$

Here, k_1 is not dependent on the gradient slope and k_2 is negative. For our specific laser and plasma conditions, we have found that $k_1 = 34.76\ \lambda_{p1}/(n_1\ \mu\text{m})$ pC and $k_2 = -0.91$ pC/μm. To test the validity of the model, Eq. (2) (with different k_1 and k_2) was tested on the data presented by Samant *et al.*[18] and Massimo *et al.*[19]. It is found that the relation can be used to describe the trend of injected charge for the cases where the down-ramp steepness $\partial n/\partial x > = 2 \cdot 10^{16}\ \text{cm}^{-3}\mu\text{m}^{-1}$.

The setup of this numerical experiment, keeping n_1 fixed and varying the acceleration density n_2 impacts the acceleration process. The acceleration part is intimately linked to the injection, through the chosen value of

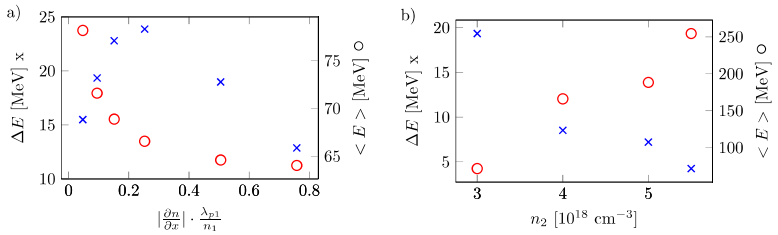

Figure 3. (**a**) In blue, energy-spread (root mean square error from mean energy) as a function of the different down-ramp steepness. In red the mean energy is plotted for a fixed lower density of $n_2 = 3 \cdot 10^{18}$ cm^{-3}. (**b**) In blue, energy spread for different lower densities n_2. In red mean energy for the same simulations with a fixed steepness of 0.1 $(n_1)/(\lambda_{p1})$. These values are measured 0.9 mm into the plasma.

n_2, which will directly affect the laser evolution, the accelerating field and the dephasing length. It will also have impact on the beamloading effects that depends on n_2 and the beam charge/current. Even though this paper is mainly focused on the beam parameters that directly results from the injection part of the process, in particular the electron bunch length, charge, and transverse emittance; for completeness, we also provide information on the electron bunch energy and energy spread for the different scenarios.

In Fig. 3a the energy spread and mean energy for different gradient slopes with $n_2 = 3 \cdot 10^{18}$ cm^{-3} is presented. The energy spread is lowest for the shortest down-ramp. The trapping of the electrons in the steepest gradient takes place over the shortest amount of time, thus the electrons are accelerated for almost the same amount of time. The mean energy increases with a decrease in the gradient slope due to the fact that the average background density including the density down-ramp is higher, and more charge in the steeper cases decreases the accelerating field due to a stronger beamloading effect.

In Fig. 3b the energy spread and mean energy for different gradient lengths with $(\partial n)/(\partial x) = 0.1\ (n_1)/(\lambda_{p1})$ is shown. Note that caution should be used before interpreting this comparison since the values are measured at the same position, and not at the dephasing length for each acceleration process.

Control of electron bunch length. In density down-ramp injection, the electron bunch length is expected to be equal to the difference between the bubble lengths in the high and low density regions given that the injection occurs throughout the down-ramp. It is therefore important to measure and estimate this bubble length and growth as precisely as possible. From Fig. 1b it is clear that the pulse length of the trapped electrons is the same as the elongation of the wakefield, indicating the possibility of predicting the length of the electron bunch. Similar effects can be seen in Massimo *et al.*[19] in which the effects of a varied peak density on the bunch length is presented. An analytical and numerical scaling law for the bubble radius r_b is given in a previous paper by Lu *et al.*[6]. In this paper[6], the relation $r_b = c_r\sqrt{a_0}\lambda_p$ is derived. Here, c_r is a constant, $\lambda_p = 2\pi v/\omega_p$ where $v \approx c$ is the group velocity of the laser pulse and $\omega_p = \sqrt{\frac{n_e q_e^2}{m_e \varepsilon_0}}$ is the non-relativistic angular plasma - frequency. n_e is the electron density, q_e is the electron charge, m_e is the rest mass of the electron and ε_0 is the vacuum permittivity.

The constant of proportionality c_r is determined from PIC-simulations for a special case when the laser beam duration, waist, amplitude, and the plasma density are all matched. These matched properties that are discussed in the same paper[6] are hereafter referred to as a matched condition. However, in experimental conditions, a matched laser pulse can be hard to achieve for different reasons, such as limited available beam power or energy in comparison to the laser pulse duration. Furthermore, a laser pulse going through a density down-ramp can not be matched in both density regions.

The size of the bubble does not only depend on the local plasma density, but also on the amount of trapped charge. The simulations conducted for this study show that it is possible to predict the full width pulse length L_{eb} of the electron bunch with the relation

$$L_{eb} = C_1 \Delta\lambda_p + C_2 Q^2. \tag{3}$$

Here, $\Delta\lambda_p$ is the difference in λ_p for the two density regions, C_1 is a unitless constant coupling the theoretical linear non-relativistic plasma wavelength λ_p to the true plasma wavelength, and C_2 is a constant with units of length/charge ^{2}. The second term C_2Q^2 is chosen to correct for the elongation of the bubble due to the beamloading effects observed in the simulation. C_1 includes the dependence of a_0 and is taken from the simulations with beamloading turned off, i.e., $C_1\Delta\lambda_p$ is the true plasma wavelength difference between the two density regions without injected charge. How beamloading is turned off in the simulations is explained in the Method section.

The relation presented in Eq. (3) is displayed in Fig. 4a together with the electron beam lengths measured in the different simulations. The linear fits displayed in Fig. 2a that model the trapped charge are used to draw the predictive lines for the red and blue data sets. For both fits, $C_1 = 0.83$ and $C_2 = 0.63 \cdot 10^{-4}$ pC^{-2}. C_2 is calculated by fitting the difference in electron bunch length between the simulation with and without beamloading to the amount of charge squared. The quadratic dependence on Q was chosen because it allows for accurately fitting both curves with the same constant C_2 while still yielding a simple predictive relation. From existing literature by

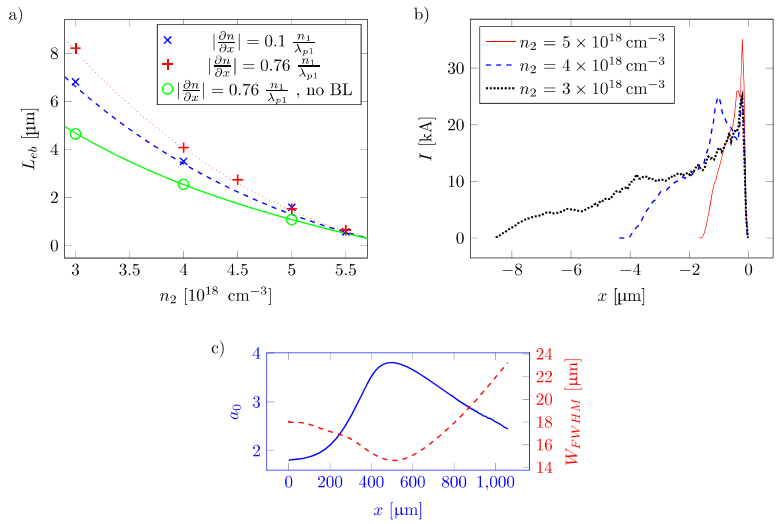

Figure 4. (**a**) The green circles correspond to the electron bunch length measurements with beamloading turned off. The green line is a fit using Eq. (3) with $C_1 = 0.83$ and $C_2 = 0$. The red plus signs are data points from the simulation of the electron bunch length, the dashed red curve represents a fit according to Eq. (3). The blue crosses and dotted line represents the same values for a gentler gradient slope. (**b**) Spatial electron density profiles of three different acceleration densities: $n_2 = 3$, 4 and $5 \cdot 10^{18}$ cm^{-3}. Here, $\partial n/\partial x = 0.76 n_1/\lambda_{p1}$ with beamloading. (**c**) The peak normalized vector potential a_0 (in blue) and FWHM width (dashed red) as function of the laser pulse's peak position during a simulation with $n_2 = 3 \cdot 10^{18}$ cm^{-3} and $\partial n/\partial x = 0.76 n_1/\lambda_{p1}$. For the different simulation, the peak value of a_0 varies between 3.8 and 4.3, but the behaviour is the same for all simulations, a_0 increases and the width of the pulse decreases.

Tzoufras *et al.*[23] one would expect a linear dependence on Q, however, a quadratic dependence fits better with the simulation parameters in this report. Observe that the parameters in this report differentiates from the paper[23] by Tzoufras *et al.* in two significant ways: The analysis by Tzoufras *et al.* is conducted for the matched regime and are making sure the beamloading is optimal. In this report, charge is injected while the background density (and thus the wakefield) changes while they are adding charge to a bubble in a constant background density. The green data set is taken from simulations where the beamloading effect is turned off, as discussed earlier. These simulations without beamloading effects almost perfectly follow the relation in Eq. (3) if $Q = 0$ and $C_1 = 0.83$. The data points are taken for $\partial n/\partial x = 0.1\, n_1 \lambda_{p1}^{-1}$ but there is no difference in bunch length for different $\partial n/\partial x$ when beamloading is turned off. Do note that the bunch length is significantly elongated by the beamloading effect on the wakefield, as can be seen in Fig. 4a.

In the theory from Lu *et al.* presented above, the bubble radius r_b scales with $a_0^{-1/2}$. The variation of a_0 due to laser self-focusing or laser beam evolution should thus play a role in the length of the electron bunch. The evolution of a_0 and the FWHM beam waist of the laser is shown in Fig. 4c. However, as previously mentioned, this relation only holds for laser wakefield accelerators in a matched regime. In the matched regime, where the equation $2\pi W_0/\lambda_p = a_0$ (W_0 is the e^{-2} laser beam waist) is fulfilled, a_0 can not be changed without changing either λ_p or W_0 accordingly. In the case presented in this report, a_0 evolves due to a temporal and spatial compression of the laser pulse (as can be seen in Fig. 4c). The ratio $W_0/(\lambda_p a_0)$ is therefore no longer constant, and the scaling laws of the matched regime are not applicable. The ponderomotive push on the electrons from the laser scales with a_0 and an increase in bubble length can be expected from this effect. However, at the same time, the laser waist decreases and the laser pulse interacts with a smaller number of electrons. Thus, the widths of the plasma column that is pushed away decreases, which reduces the bubble length. It is important to note these effects counteract each other but the sum of these effects are not generally zero. Thus the model for the bubble radius, which assumes that $r_b \propto a_0^{1/2}$, is not valid for this setup. To support this argument, a comparison between the bubble length before and after the down-ramp has been performed for different down-ramp lengths. The simulations show that for the cases with beamloading suppressed, there is no significant difference in the bubble length after the short and long gradients. At the same time, $a_0^{1/2}$ has increased by more than 10% for the longer gradient ($L = 72$ μm) due to the self-focusing effects from crossing a longer plasma region.

The longitudinal profile of three different electron bunches are shown in Fig. 4b. The charge distribution can be approximated as triangles, starting at approximately the same point in $x - dQ/dx$ space and then a straight

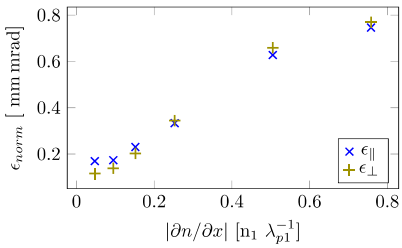

Figure 5. The normalized emittance as a function of the different density gradients. The normalized emittance scales with the sharpness of the density down-ramp. All the shown data is from simulations where $n_2 = 3 \cdot 10^{18}$ cm^{-3}. Here $\varepsilon_\parallel$ and $\varepsilon_\perp$ is the normalized transverse emittance parallel and perpendicular to the polarization of the laser pulse.

line can be drawn from this point to the end of the bunch length. This may be useful, as a triangular beam shape is required for optimal beamloading[23], and consequently preservation of energy spread. However, for the parameters used in these simulations, optimal beamloading was not obtained.

Controlling emittance. From the simulations, it is clear that the divergence of the electron bunch also depends on the density gradient. The normalized emittance[24] of electron bunches for different density gradients are shown in Fig. 5. A straight-forward relation can be seen between the steepness of the density gradient and the emittance. For a steep gradient, the back of the bubble slows down more rapidly, lowering the threshold for trapping, thus causing electrons with larger transversal momentum to be trapped.

In Fig. 6, two sequences of density down-ramp injection are portrayed in the form of density sections from the simulations as the laser pulse passes through the down-ramp. The sequences are divided into the left and right side of the figure. They are from two different down-ramps: $\partial n/\partial x = 0.76\, n_1 \lambda_{p1}^{-1}$ with $L = 9$ μm and $\partial n/\partial x = 0.1\, n_1 \lambda_{p1}^{-1}$ with $L = 72$ μm, respectively. For both simulations $n_2 = 3 \cdot 10^{18}$ cm^{-3}. Every part of the sequence is accompanied by a number of tracked macro particles with their trajectories throughout the whole simulation plotted as lines. The dot on each line mark the position of the macro particle at the time of the depicted frame. From these examples, the difference in emittance is visually obvious.

It is clear that these simulations span over different injection regimes. The steep gradient (to the left) results in an electron beam with large oscillations from a non-trivial process. Macro particles injected almost at the same time are spread out over the electron bunch. The bubble expands rapidly over the plasma wave structure, and electrons are suddenly placed within the accelerating structure. Some of the trapped particles first enters in a decelerating and defocusing region behind the bubble, providing them with a big transverse momentum. However, due to the fast bubble expansion, these particles eventually reenter through the back of the bubble and become trapped, but keep a significant amount of their transverse momentum, increasing the overall beam transverse emittance. The gentler gradient (to the right in Fig. 6) gives rise to a smoother trapping of the macro particles over the course of the gradient where they align nicely after each other. The macro particles that are injected first are at the front of the bunch, the last to be injected are placed at the end of the bunch, in contrast to the steep gradient.

Discussion

Described here is a numerical study on density down-ramps of different steepness and heights. Using only those two parameters, it is possible to tune three important parameters of the electron bunch. Given that the laser pulse is strong enough to drive a wakefield in both density regions, we should see similar effects for different densities and different density regions. It is also possible to vary the density n_1. Care should be taken to keep the accelerating density n_2 large enough to sustain a bubble and maintain a decent acceleration. In these simulations, it was clear that for densities below $3 \cdot 10^{18}$ cm^{-3} the electron bunch was driving its own significant wakefield, ruining the acceleration process.

First, we have shown numerically that the electron beam charge depends quasi- linearly on the density jump Δn in our case. However, a general expression for the injection cross section is hard to derive due to the complex nature of the wavebreaking process. As is demonstrated in this report, the injection process itself is affecting the expansion of the bubble through the beamloading effect. This makes the process rather complicated. Kostyokov *et al.*[25] derives a cross section σ for self-injection in a matched regime

$$\frac{\sigma}{\pi} \approx 8\left(R^2 - \frac{dR}{dt}^{-1}\right), \tag{4}$$

where R is the bubble radius normalized to c/ω_p. Comparing the results in this report to the model, we can not find a quantitative match. However, as the density down-ramp is getting steeper and dR/dt increases, the cross section σ increases which agrees well with the findings here.

To maximize the amount of charge in the electron bunch, a sharp density transition should be chosen. This comes at the price of a large emittance; however, if one wants a betatron source, this is ideal. From the particle

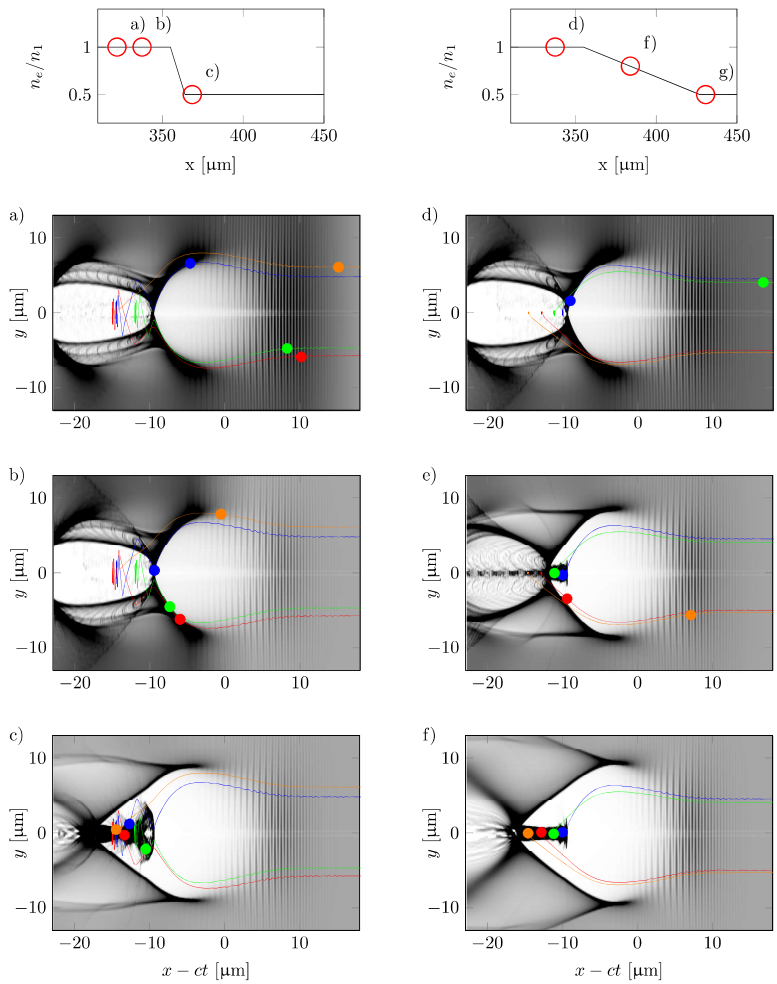

Figure 6. To the left, a series of 3 snapshots from the injection process for a steep gradient where $\partial n/\partial x = 0.76\ n_1\lambda_{p1}^{-1}$ with $L = 9$ µm. To the right, 3 snapshots from the injections process for a gentler gradient where $\partial n/\partial x = 0.1\ n_1\lambda_{p1}^{-1}$ with $L = 72$ µm. For both simulations $n_2 = 3 \cdot 10^{18}$ cm^{-3}. The trajectories are for 4 tracked macro particles from each process. The dot represent each macro particle's position in the frame at the time of the snapshot. As can be seen, for the steep gradient, injection is a complex process. Macro particles located in a defocusing and decelerating region are suddenly placed within the bubble structure as the bubble expands, and they can then be trapped. For the gentler gradient, the macro particles enters from the rear of the bubble as a continuous process throughout the gradient.

trajectories in Fig. 6 it can be seen that that the trapping mecanism is different in the two different cases. In the gentler gradient, particles travelling along the edge of the bubble are trapped. This is well described by Kalmykov *et al.*[26] where they present a model that states that the particles with the longest slippage time are the particles that are trapped. The slippage time is defined as the time that a particle interacts with the bubble. In other words, the particles that travels along the edge of the bubble until the back are the particles that get trapped first. The same paper also explains that as the change in density increases, the expansion rate of the bubble increases, and particles with shorter slippage time can be trapped. This implies that even particles that are experiencing decelerating

and defocusing fields are trapped, and as can be seen from the trajectories, some of them enter the bubble with a relatively large radial momentum, which causes a large oscillation for the particle. The larger the emittance, the more oscillations, which produces more X-rays[21].

The bunch length is an important quality of the electron bunch. For example, the produced X-ray pulse in a betatron source will not be shorter than the generating electron bunch[21]. It also affects the acceleration process in LWFA. In the blowout regime, the accelerating electric field is changing linearly with respect to the position in the bubble. This will cause an increase in energy spread for any extended electron bunch. The difference in energy gain will thus increase linearly with the electron bunch length. This might pose a problem for long electron bunches over an extended acceleration region as the energy spread will increase. Since the acceleration process starts earlier for the head of the electron bunch, those electrons will have higher energies in the beginning. Unless optimal beamloading[23] is achieved, the tail of the electron bunch will gain more energy than the head due to phase-space rotation of the bunch. At some point during the acceleration process, the tail of the electron bunch will have gained roughly the same amount of energy that as the front part. If this happens, the bunch has reached a minimum in energy spread. For the simulation summarized in Fig. 1a, this happens when the average energy is around 40 MeV.

In conclusion, we show a possibility to tailor the parameters of the electron bunch produced in LWFA by tuning the density down-ramp. We demonstrate that the amount of charge, the bunch length, and the emittance can be controlled in a simple manner. However, these parameters are not fully decoupled and can therefore not be tuned independently.

Methods

The results here are presented for a laser with a central wavelength of 800 nm. The density down-ramp is characterized by three parameters: n_1 is defined as the electron density of the high-density plateau, n_2 is the electron density of the low-density plateau where electrons are accelerated, and $|\partial n/\partial x|$ is used to characterize the steepness of the gradient of the density down-ramp. The longitudinal plasma gradient is normalized to the upper plasma density and the theoretical linear non-relativistic plasma wavelength at that density. The parameters used to characterize the longitudinal density profile of the simulation is shown in Fig. 1a along with the longitudinal energy distribution of the accelerated electron and the density profile. In order to isolate the effects of the density down-ramp, the high density part n_1 of the simulation was kept at a constant electron density of $6 \cdot 10^{18}$ cm^{-3} throughout all simulations discussed in this paper.

The moving simulation box was kept large enough to simulate at least the first full plasma wave (or "bubble") after the laser pulse in the low density region. The peak intensity of the laser pulse was kept at a distance of 23 μm behind the front boundary of the moving window. The cell-size of the simulation grid was set to be 16 nm in the longitudinal direction and 190 nm in the radial direction, with 3200 and 400 cells in the respective dimension. Each cell contained 48 macro particles. The integration timestep was set to 52 as. A third order spatial interpolation scheme was used. The macro particles were not randomly distributed but placed in a regular pattern evenly distributed in x, r, and θ. An anti-numerical Cherenkov Maxwell solver was used[27]. The fields are decomposed into three Fourier modes in the azimuthal direction. Test-particle diagnostics were used to determine the emittance of the accelerated electron bunch.

To be able to independently study the bubble expansion due to the density down-ramp and exclude the contributions invoked by beamloading, simulations were performed where macro particles with a forward momentum greater than 10 $m_e c$ were removed from the current deposition. This was done in order to get the reference values in Fig. 4.

The datasets generated during and/or analysed during this study are available from the corresponding author on reasonable request.

References

1. Tajima, T. & Dawson, J. M. Laser electron accelerator. *Phys. Rev. Lett.* **43**, 267–270, https://doi.org/10.1103/PhysRevLett.43.267 (1979).
2. Mangles, S. *et al.* Monoenergetic beams of relativistic electrons from intense laser–plasma interactions. *Nature* **431**, 535–538, https://doi.org/10.1038/nature02939 (2004).
3. Faure, J. *et al.* A laser–plasma accelerator producing monoenergetic electron beams. *Nature* **431**, 541–544, https://doi.org/10.1038/nature02963 (2004).
4. Geddes, C. G. R. *et al.* High-quality electron beams from a laser wakefield accelerator using plasma-channel guiding. *Nature* **431**, 538–541, https://doi.org/10.1038/nature02900 (2004).
5. Pukhov, A. & Meyer-ter Vehn, J. Laser wake field acceleration: the highly non-linear broken-wave regime. *Appl. Phys. B* **74**, 355–361, https://doi.org/10.1007/s003400200795 (2002).
6. Lu, W. *et al.* A nonlinear theory for multidimensional relativistic plasma wave wakefields. *Physics of Plasmas* **13**, 056709, https://doi.org/10.1063/1.2203364 (2006).
7. Bulanov, S., Naumova, N., Pegoraro, F. & Sakai, J. Particle injection into the wave acceleration phase due to nonlinear wake wave breaking. *Phys. Rev. E* **58**, R5257–R5260, https://doi.org/10.1103/PhysRevE.58.R5257 (1998).
8. Suk, H., Barov, N., Rosenzweig, J. B. & Esarey, E. Plasma electron trapping and acceleration in a plasma wake field using a density transition. *Phys. Rev. Lett.* **86**, 1011–1014, https://doi.org/10.1103/PhysRevLett.86.1011 (2001).
9. Chien, T.-Y. *et al.* Spatially localized self-injection of electrons in a self-modulated laser-wakefield accelerator by using a laser-induced transient density ramp. *Phys. Rev. Lett.* **94**, 115003, https://doi.org/10.1103/PhysRevLett.94.115003 (2005).
10. Geddes, C. G. R. *et al.* Plasma-density-gradient injection of low absolute-momentum-spread electron bunches. *Phys. Rev. Lett.* **100**, 215004, https://doi.org/10.1103/PhysRevLett.100.215004 (2008).
11. Gonsalves, A. *et al.* Tunable laser plasma accelerator based on longitudinal density tailoring. *Nature Physics* **7**, 862–866, https://doi.org/10.1038/nphys2071 (2011).
12. Burza, M. *et al.* Laser wakefield acceleration using wire produced double density ramps. *Phys. Rev. ST Accel. Beams* **16**, 011301, https://doi.org/10.1103/PhysRevSTAB.16.011301 (2013).
13. Hansson, M. *et al.* Down-ramp injection and independently controlled acceleration of electrons in a tailored laser wakefield accelerator. *Phys. Rev. ST Accel. Beams* **18**, 071303, https://doi.org/10.1103/PhysRevSTAB.18.071303 (2015).

14. Hansson, M. *et al.* Localization of ionization-induced trapping in a laser wakefield accelerator using a density down-ramp. *Plasma Physics and Controlled Fusion* **58**, 055009, https://doi.org/10.1088/0741-3335/58/5/055009 (2016).
15. Thaury, C. *et al.* Shock assisted ionization injection in laser-plasma accelerators; *Sci. Rep.* **5**; DOI: https://doi.org/10.1038/srep16310 (2015).
16. Schmid, K. *et al.* Density-transition based electron injector for laser driven wakefield accelerators. *Phys. Rev. ST Accel. Beams* **13**, 091301, https://doi.org/10.1103/PhysRevSTAB.13.091301 (2010).
17. Buck, A. *et al.* Shock-front injector for high-quality laser-plasma acceleration. *Phys. Rev. Lett.* **110**, 185006, https://doi.org/10.1103/PhysRevLett.110.185006 (2013).
18. Samant, S. A., Upadhyay, A. K. & Krishnagopal, S. High brightness electron beams from density transition laser wakefield acceleration for short-wavelength free-electron lasers. *Plasma Physics and Controlled Fusion* **56**, 095003, https://doi.org/10.1088/0741-3335/56/9/095003 (2014).
19. Massimo, F., Lifschitz, A. F., Thaury, C. & Malka, V. Numerical studies of density transition injection in laser wakefield acceleration. *Plasma Physics and Controlled Fusion* **59**, 085004, https://doi.org/10.1088/1361-6587/aa717d (2017).
20. McNeil, B. W. & Thompson, N. R. X-ray free-electron lasers. *Nat. Photon.* **4**, 814–821, https://doi.org/10.1038/nphoton.2010.239 (2010).
21. Corde, S. *et al.* Femtosecond x rays from laser-plasma accelerators. *Reviews of Modern Physics* **85**, 1, https://doi.org/10.1103/RevModPhys.85.1 (2013).
22. Lifschitz, A. *et al.* Particle-in-cell modelling of laserplasma interaction using fourier decomposition. *Journal of Computational Physics* **228**, 1803–1814, https://doi.org/10.1016/j.jcp.2008.11.017 (2009).
23. Tzoufras, M. *et al.* Beam loading by electrons in nonlinear plasma wakes. *Physics of Plasmas* **16**, 056705, https://doi.org/10.1063/1.3118628 (2009).
24. Floettmann, K. Some basic features of the beam emittance. *Phys. Rev. ST Accel. Beams* **6**, 034202, https://doi.org/10.1103/PhysRevSTAB.6.034202 (2003).
25. Kostyukov, I., Nerush, E., Pukhov, A. & Seredov, V. Electron self-injection in multidimensional relativistic-plasma wake fields. *Phys. Rev. Lett.* **103**, 175003, https://doi.org/10.1103/PhysRevLett.103.175003 (2009).
26. Kalmykov, S., Yi, S. A., Khudik, V. & Shvets, G. Electron self-injection and trapping into an evolving plasma bubble. *Phys. Rev. Lett.* **103**, 135004, https://doi.org/10.1103/PhysRevLett.103.135004 (2009).
27. Lehe, R., Lifschitz, A., Thaury, C., Malka, V. & Davoine, X. Numerical growth of emittance in simulations of laser-wakefield acceleration. *Phys. Rev. ST Accel. Beams* **16**, 021301, https://doi.org/10.1103/PhysRevSTAB.16.021301 (2013).

Acknowledgements

We acknowledge the support of the Knut and Alice Wallenberg Foundation, the Swedish Research Council, the Swedish Foundation for Strategic Research and Laserlab-Europe (EU-H2020 654148). The simulations were performed on resources provided by the Swedish National Infrastructure for Computing (SNIC) at Lunarc.

Author Contributions

H.E., M.H. and O.L. conceived the numerical experiment, H.E. conducted and analyzed the simulations and wrote the manuscript, X.D. co-developed the code CALDER-CIRC and suggested modifications, X.D. and O.L. supervised the project. All authors have contributed to the interpretation and discussed the results. All authors reviewed the manuscript.

Additional Information

Competing Interests: The authors declare that they have no competing interests.

Publisher's note: Springer Nature remains neutral with regard to jurisdictional claims in published maps and institutional affiliations.

Paper V

Effects of the dopant concentration in laser wakefield and direct laser acceleration of electrons

I. Gallardo González, H. Ekerfelt, M. Hansson, T. L. Audet, B. Aurand, F. G. Desforges, S. Dobosz Dufrénoy, A. Persson, X. Davoine, C.-G. Wahlström, B. Cros and O. Lundh.

New J. Phys. **20**, 053011 (2018).

IOP Publishing New J. Phys. 20 (2018) 053011 https://doi.org/10.1088/1367-2630/aabe14

New Journal of Physics
The open access journal at the forefront of physics

Deutsche Physikalische Gesellschaft DPG
IOP Institute of Physics

Published in partnership with: Deutsche Physikalische Gesellschaft and the Institute of Physics

OPEN ACCESS

RECEIVED
24 November 2017

REVISED
26 March 2018

ACCEPTED FOR PUBLICATION
13 April 2018

PUBLISHED
4 May 2018

PAPER

Effects of the dopant concentration in laser wakefield and direct laser acceleration of electrons

I Gallardo González[1], H Ekerfelt[1], M Hansson[1], T L Audet[2], B Aurand[1,5], F G Desforges[2], S Dobosz Dufrénoy[3], A Persson[1], X Davoine[4], C-G Wahlström[1], B Cros[2] and O Lundh[1]

[1] Department of Physics, Lund University, PO Box 118, SE-22100 Lund, Sweden
[2] LPGP, CNRS, Université Paris-Sud, Université Paris-Saclay, F-91405 Orsay, France
[3] LIDYL, CEA, CNRS, Université Paris-Saclay, CEA-Saclay, F-91191 Gif-sur-Yvette, France
[4] CEA, DAM, DIF, F-91297 Arpajon, France
[5] Present address: Heinrich-Heine-University Düsseldorf, Düsseldorf, Germany.

E-mail: isabel.gallardo@fysik.lth.se

Keywords: laser–plasma interaction, laser wakefield acceleration, direct laser acceleration, ionization-induced trapping

Abstract

In this work, we experimentally study the effects of the nitrogen concentration in laser wakefield acceleration of electrons in a gas mixture of hydrogen and nitrogen. A 15 TW peak power laser pulse is focused to ionize the gas, excite a plasma wave and accelerate electrons up to 230 MeV. We find that at dopant concentrations above 2% the total divergence of the electrons is increased and the high energy electrons are emitted preferentially with an angle of ± 6 mrad, leading to a forked spatio-spectral distribution associated to direct laser acceleration (DLA). However, electrons can gain more energy and have a divergence lower than 4 mrad for concentrations below 0.5% and the same laser and plasma conditions. Particle-in-cell simulations show that for dopant concentrations above 2%, the amount of trapped charge is large enough to significantly perturb the plasma wave, reducing the amplitude of the longitudinal wakefield and suppressing other trapping mechanisms. At high concentrations the number of trapped electrons overlapping with the laser fields is increased, which rises the amount of charge affected by DLA. We conclude that the dopant concentration affects the quantity of electrons that experience significant DLA and the beam loading of the plasma wave driven by the laser pulse. These two mechanisms influence the electrons final energy, and thus the dopant concentration should be considered as a factor for the optimization of the electron beam parameters.

1. Introduction

Laser wakefield acceleration (LWFA) stands out as a promising mechanism to complement other kind of electron accelerators, providing a new and more compact source of relativistic electrons [1]. In this acceleration scheme [2], an ultra-short laser pulse is focused to a peak intensity above 10^{18} W cm^{-2} in a gas, which becomes ionized at the front of the pulse. As a result, the remainder of the laser pulse, including the peak, interacts with an under-dense plasma. The ponderomotive force exerted by the large intensity gradients perturbs the electron density and creates a relativistic plasma wave. The electron density perturbation results in strong longitudinal fields up to hundreds of GV m^{-1}. If the laser pulse is intense enough and matches with the plasma parameters, the electrons are completely blown out from the path of the laser pulse, forming a bubble in the so called blowout regime [3]. An electron located in this region with sufficient velocity is trapped in the wave and accelerated to relativistic energies of few hundreds of MeVs in only a few hundreds of micrometers.

In the presence of a strong quasistatic electric and/or magnetic field, as the generated in the plasma bubble, energetic electrons undergo transverse oscillations. These are known as betatron oscillations [4] and generate x-ray pulses with a synchrotron-like spectral distribution and photon energies in the keV range [5]. If the betatron transverse motion of the electrons is in resonance with an overlapping laser field, the electrons can gain a significant transverse momentum from the electric field in the laser polarization direction. This gain in

transverse momentum is then transferred into longitudinal momentum via the magnetic part of the Lorentz force, which can accelerate the electrons in the longitudinal direction. This mechanism is known as direct laser acceleration (DLA) [6, 7]. A laser wakefield accelerator creates a scenario in which, provided that there is an overlap between the laser pulse and the trapped electrons, DLA can coexist and contribute directly to the total energy gained by the electron in the plasma wave [8–11].

DLA was first experimentally studied in such schemes where the laser pulse duration extended to several plasma wavelengths [12–14]. However, DLA in the LWFA quasi-blowout regime was initially investigated only numerically by particle-in-cell (PIC) simulations [8, 9, 11]. Recently, experimental work has finally identified in this regime an imprint of DLA in the accelerated electrons [15]. The dispersion of the electrons through a magnet in the direction perpendicular to the laser polarization showed a forked structure in the electron spatio-spectral distribution, with two symmetrical peaks along the divergence of the high energy electrons. The origin of this structure will be discussed in more detail later in this paper.

Together with the spatial overlap with the laser fields, electrons must be trapped in the plasma wave with significant transverse momentum in order to experience noticeable DLA [9, 16]. Electrons can be self-trapped if the plasma wave becomes highly nonlinear and eventually breaks, but other trapping mechanisms have been developed [17–21]. In particular, the mixture of gases can lead to ionization-induced trapping by combining a low percentage of a high-Z gas dopant, such as nitrogen, with a low-Z gas, such as hydrogen [22, 23]. While the plasma wave is formed by the background electrons of hydrogen and the outer electrons of nitrogen, the two electrons from the K shell of nitrogen are released only around the peak intensity of the laser pulse, due to over-the-barrier ionization. These electrons also get, during the nitrogen ionization process, a certain momentum in the laser polarization direction, and are more easily trapped in the wake potential at the back of the first plasma wave period or bubble, closer to the laser pulse in comparison to self-injected electrons. Ionization-induced trapping is then a very convenient mechanism to explore DLA [8, 11]. In addition, the dopant concentration in the gas mixture allows to change the number of electrons trapped in the plasma bubble without modifying neither the background electron number density n_e or the parameters of the incoming laser pulse.

Here we present a parametric experimental study of ionization-induced trapping of electrons for different concentrations of hydrogen and nitrogen in the gas mixture. Our work shows that the number of electrons accelerated to high energy and large transverse momentum along the laser polarization increases with the nitrogen concentration and the electron density in the target. Quasi-cylindrical PIC simulations with CALDER-Circ support that the amount of ionization-induced trapped electrons increases for higher nitrogen concentration, and thereby also increases the number of accelerated electrons in the bubble that overlap with the laser electromagnetic fields. The transverse fields of the laser influence the acceleration of electrons, showing both, experimentally and in the simulations, the mentioned forked structure. This effect of DLA is experimentally enhanced when reducing the size of the plasma bubble, by increasing the background electron density. The control of the nitrogen concentration and the electron number density can affect the DLA contribution to the LWFA accelerated electrons and decrease or increase the electrons transverse momentum in the laser polarization direction.

2. Experimental method

The experimental data was acquired at the Lund Laser Centre in Sweden, using the multi-terawatt laser system. Pulses of 585 mJ at 800 nm central wavelength were delivered on target, with a pulse duration of $\tau_L = 37$ fs full width at half maximum (FWHM). The laser was linearly polarized. A 775 mm focal length off-axis parabolic mirror (OAP) focused the beam to a FWHM spot size of 17 μm after wavefront optimization with a deformable mirror. The image of the spatial intensity distribution in the focal plane together with the measured pulse energy and duration gave an estimated peak intensity in vacuum of 3.0×10^{18} W cm^{-2}, corresponding to a peak normalized vector potential $a_0 = 1.2$. The peak power $P_L \simeq 15$ TW of the laser pulse was higher than the critical power for relativistic self-focusing $P_{\rm crit} = (8\pi\epsilon_0 m_e^2 c^5)/e^2 \times (n_c/n_e) = 3.2$ TW where $n_c = (\omega_0^2 \epsilon_0 m_e)/e^2 \simeq 1.75 \times 10^{21}$ cm^{-3} is the critical density of the plasma. Nonlinear effects are then expected to happen during the propagation of the laser beam in the plasma, including self-focusing and self-compression of the laser pulse, that can locally increase the normalized vector potential. In order to improve the beam pointing stability of the system, the transverse position of the focal spot was actively corrected with the image of a focused leak of the last mirror before the OAP. The position of the centre of the spot was used to control the response of a piezo-actuated mirror just after the compressor. The correction was made between the full power shots using a train of pulses with MHz repetition rate and a few μJ per pulse that propagated collinearly with the high energy pulse.

The electrons were accelerated by focusing the laser pulse to the entrance of a gas cell, filled by a mixture of hydrogen and a chosen concentration χ of nitrogen. The gas mixture was enclosed in a cylindrical cell with a

IOP Publishing New J. Phys. 20 (2018) 053011 I Gallardo González et al

fixed inner length of 800 μm. Two 500 μm thick sapphire plates with 200 μm diameter holes were placed at the entrance and output of the cell, through which the laser pulse and the accelerated electrons propagated. The gas was stored in a reservoir connected to the cell by an electrovalve. The valve was opened 40 ms before each laser pulse arrived in order to reach a stationary gas density distribution. Inside the cell, the gas density is essentially constant. However, due to the aperture of the sapphire plates, a density gradient was formed at the entrance and the output of the gas cell. The density gradient length was calculated using computational fluid dynamics simulations (COMSOL CFD) to be around 0.6 mm. Different percentages χ of nitrogen were added to the hydrogen for the gas mixture: 0.1%, 0.5%, 2.0% and 5.0%. Note that the parameter χ accounts for the percentage of nitrogen molecules in the gas mixture, and not for the percentage of *K* shell electrons with respect to the background electrons in the later formed plasma. Comparison of the accelerated electron beam parameters for nitrogen concentration of 0.0% (pure hydrogen) and 1.0% can be found in a previously published work [21].

The spectrum and charge of the accelerated electrons were calculated from the dispersion of the electrons through a 100 mm long permanent magnet with a peak magnetic field strength of 0.7 T on a Kodak Lanex Regular scintillation screen. The magnet was placed so that the electrons were dispersed in the direction perpendicular to the polarization plane of the laser pulses. The full acceptance angle of the electron spectrometer was approximately 60 mrad. The divergence of the electrons introduces an uncertainty in the electron energy calculated from the screen signal. 150 MeV electrons with an angle of ± 3 mrad are estimated to introduce an uncertainty of ± 8.4 MeV, corresponding to $\pm 5.6\%$. Due to the geometry of the diagnostics only electrons with an energy above approximately 45 MeV were detected. The scintillation emission was recorded by a 16 bit CCD camera, from which the charge is calculated by using published calibration factors of the screen [24]. An aluminium plate covering the front part of the screen blocked any laser light reaching the detector.

The molecular density in the gas cell used in the experiment was previously characterized by interferometry for both gases in the mixture independently, at backing pressures ranging from 200 mbar to 1 bar. The background electron density is calculated for each gas mixture by considering that all hydrogen is fully ionized and nitrogen releases five electrons per atom, up to the fifth ionization state, by the leading edge of the laser pulse. The intensity required to ionize N^{4+} corresponds to a normalized vector potential $a_0^{N^{5+}} = 0.08$, more than one order of magnitude lower than the peak normalized vector potential of the laser in vacuum.

3. Experimental results

The features of the accelerated electrons, such as collected charge, energy spectrum and divergence were explored by scanning the gas cell backing pressure for different nitrogen concentrations in the gas mixture. The results are sorted into values of electron number density within $\pm 1\%$, ranging from 8.1×10^{18} to 9.5×10^{18} cm^{-3}. No data was collected at 8.1×10^{18} and 8.6×10^{18} cm^{-3} at a nitrogen concentration of 5% as the minimum backing pressure explored produced an electron number density already above these values. Though the data with 0.1% at 8.1×10^{18} cm^{-3} was collected, it is not included as its finite energy spread indicates that the charge was not continuously trapped by the ionization of the *K* shell electrons. As such, it should not be compared to data where that was the case.

Figure 1(a) shows the collected charge of the dispersed electrons. The charge increases with the density, as the laser group velocity becomes slower which lowers the trapping threshold. The addition of nitrogen in the gas mixture increases the accelerated charge up to a maximum before decreasing for higher nitrogen concentrations. This maximum is reached for lower nitrogen percentage as the electron number density increases. Thus the maximum collected charge depends on both, the electron number density and the nitrogen concentration. For the explored parameters, the charge is maximum with 26 pC at a nitrogen concentration of 0.5% and an electron number density of 9.5×10^{18} cm^{-3}.

The experimental results also show that electrons experience lower acceleration with higher concentration of nitrogen in the gas, see figure 1(b). The maximum energy is obtained creating a dQ_{max}/dE vector from the reconstructed spatio-spectral charge distribution, finding the maximum value of charge at each energy level. From this vector, the maximum energy is defined for when the signal is at least five times the minimum signal above the noise level. Figure 1(b) shows that the maximum energy varies around similar values independently of the electron number density, but decreases when the nitrogen concentration χ increases to 5%. In fact, the error bars for the different electron number densities overlap in more or less degree, and the maximum energy decreases from around 250 MeV at $\chi = 0.1\%$ to around 188 MeV at $\chi = 5\%$.

The electron spectra obtained for a fixed electron density $n_e = 9.5 \times 10^{18}$ cm^{-3} as a function of the nitrogen concentration are shown in figure 2(a). Each plot is an average of the reconstructed spectrum after five consecutive acquisitions. In order to make the charge distribution of high energy electrons visible, the colour-scale for $\chi = 0.1\%$ and $\chi = 0.5\%$ are saturated. An example of the stability of the electron beams can be found

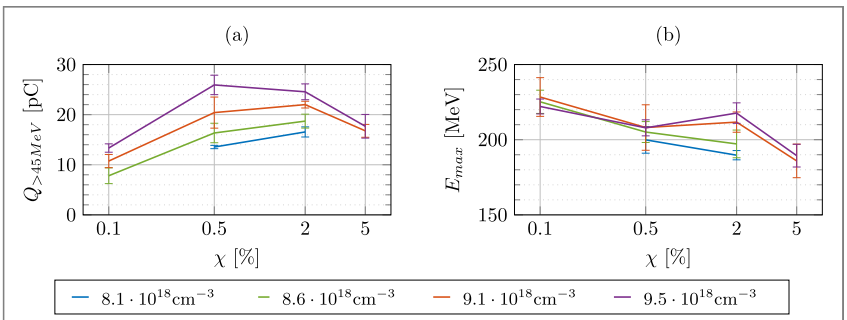

Figure 1. (a) Electron beam charge and (b) electron maximum energy as a function of the nitrogen concentration χ. Each data point is the average of five consecutive measurements and the standard deviation of those five values is shown by the error bars. The colour lines correspond to different background electron number densities given in the legend underneath the figures.

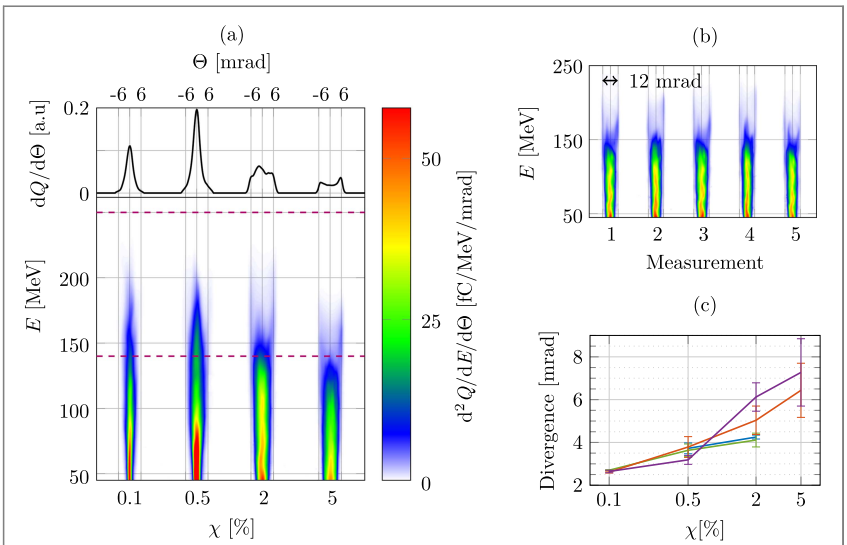

Figure 2. (a) Average of five electron spectra at an electron number density of 9.5×10^{18} cm^{-3} as a function of the nitrogen concentration χ. The inset plot shows the integrated charge between 140 and 250 MeV along the divergence axis, in the laser polarization plane. The energy limits are marked with the dashed lines on the electron spectra. (b) Five consecutive measurements at $\chi = 2\%$ and $n_e = 9.5 \times 10^{18}$ cm^{-3} and averaged in (a) with the same colour-scale. (c) FWHM divergence of the electron beams as a function of the nitrogen concentration. Each colour line corresponds to the same electron number densities given in the legend of figure 1.

in figure 2(b) with five consecutive measurements obtained for $\chi = 2\%$ and averaged in figure 2(a). The general distribution of charge along the energy and angular dispersion axes is consistent in all shots. This stability of the beams is similar in all the studied cases. However the averaging in electron spectra in figure 2(a) smears out some details of the transverse distribution of the accelerated charge.

The divergence of the electron beams is calculated as FWHM of the integrated charge along the energy dispersion. Figure 2(c) shows the divergence as a function of the gas mixture for the same electron densities as in figure 1. The total divergence of the electron beam along the laser polarization plane increases with the concentration of nitrogen. This is observed directly from the spectra in figure 2(a), which also shows that the growth in divergence occurs for the whole electron energy range. Back to figure 2(c), the electron number density has a smaller impact on the divergence of the electron beam. The presence of more nitrogen in the gas mixture seems to increase the transverse momentum of the electron beam. In terms of shot-to-shot stability, the

IOP Publishing New J. Phys. 20 (2018) 053011 I Gallardo González et al

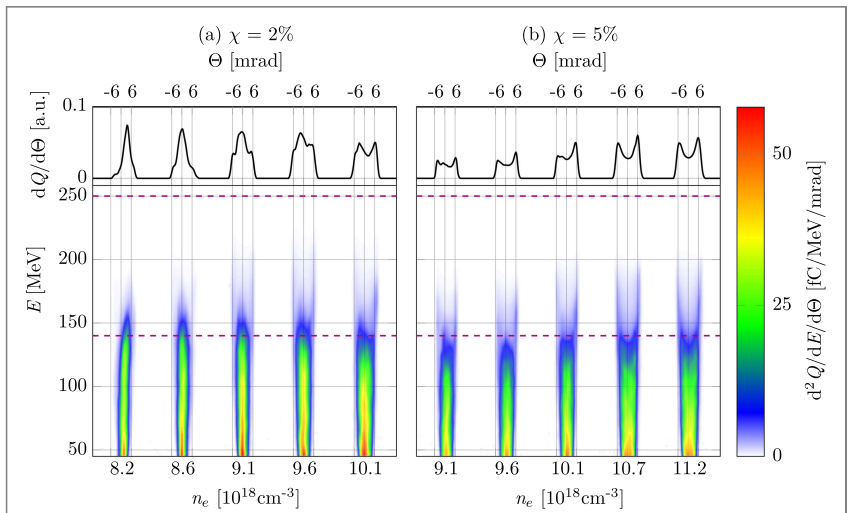

Figure 3. Averaged electron spectra at increasing electron densities for (a) 2% and (b) 5% of nitrogen in the gas mixture. The inlet plot on the top shows the corresponding charge integrated between 140 and 250 MeV, which values are represented by the dashed lines.

measurements of charge, maximum energy, and divergence vary within a maximum of 20%, 7% and 13% respectively, although their reproducibility also depends on the concentration and electron number density as shown in each case by the error bars.

The transverse spectral distribution is noticeably different for the different nitrogen percentages. In particular, at high concentrations of nitrogen the distribution of charge for high electron energies becomes preferentially off-axis and accumulates at non-zero divergence. The high energy electrons are then preferentially emitted at an angle. This forked structure is akin to the one associated to DLA [15]. To emphasize it, the inset in figure 2(a) shows the electron charge integrated between energies from 140 to 250 MeV, which levels are marked with the dashed lines. Although for $\chi = 0.1\%$ and $\chi = 0.5\%$ the angular distribution of the charge gathers in the electron beam axis, at higher concentrations of nitrogen the off-axis charge grows around ± 6 mrad while the on-axis charge gradually decreases. It is found that there is always a non-zero charge at ± 6 mrad at energies above 140 MeV for any nitrogen concentration, including 0.1% and 0.5%. Even so, this is not the case when replacing the gas mixture by pure hydrogen. It therefore seems that the increase in transverse momentum associated with DLA affects more electrons when increasing the nitrogen concentration.

The increase in nitrogen is not the only factor inducing a larger transverse momentum of the electron beam. Figure 3 shows the averaged electron spectra obtained as a function of the electron number density n_e for nitrogen concentrations of (a) 2% and (b) 5%. Note that the colour-scale is the same as in figures 2(a), (b). The presence of high energy electrons with the forked structure becomes more prominent when increasing the electron density n_e, while the on-axis high energy charge decreases. Again, charge integrated between 140 and 250 MeV is shown in the inset above the electron spectra. The high energy electrons clearly peak at ± 6 mrad for high electron densities, being dominant over the on-axis charge for electron number density above 10.1×10^{18} cm^3 for $\chi = 2\%$, but already from $n_e = 9.1 \times 10^{18}$ cm^3 for $\chi = 5\%$. The main part of the high energy charge is there distributed off-axis, with certain angular dispersion. We observe then a growth in the electrons transverse momentum in the direction of the laser polarization, that is only visible with gas mixtures and that is enhanced for a higher electron number density, i.e. for smaller plasma wavelength λ_p as $\lambda_p \simeq 2\pi \times c/\omega_p \propto \sqrt{1/n_e}$.

4. CALDER-Circ simulations

We compare the experimental data with PIC simulations performed with CALDER-Circ to get a better understanding of the electron acceleration dynamics. The code CALDER-Circ uses cylindrical coordinates, but decomposes the fields into azimuthal Fourier modes. Only a small number of modes are required in order to correctly describe the non-cylindrical features of LWFA such as a linearly polarized laser pulse. The Fourier expansion can thus be truncated which significantly reduces the computational load of the simulations. In

comparison with full 3D codes CALDER-Circ has shown a solid reproduction of the laser–plasma interaction [25], including nonlinear effects occurring to the laser pulse during its propagation in the plasma.

In our simulations, the laser pulse is represented by a linearly polarized Gaussian beam with a spot size of 18 μm FWHM. Its normalized vector potential a_0 and temporal duration τ_L varies for different simulations and it is described for each case below. The gas density profile reproduces the estimated density gradient described in section 2, with density ramps 650 μm long and a density plateau of 500 μm. The laser pulse is focused at the beginning of the plateau of the gas cell. The background electron number density in the plateau corresponds to 10^{19} cm^{-3}, created by a preformed plasma with both, hydrogen and nitrogen *L* shell electrons. In the following, the axis will be appointed as *x* for the longitudinal direction (laser propagation), *y* for the transverse direction parallel to the polarization of the laser electric field, and *z* for the transverse direction perpendicular to the polarization. The plane $x = 0$ corresponds to the beginning of the density up-ramp. The code considers the background hydrogen ions immobile and the nitrogen ions mobile, and includes Ammosov–Delone–Krainov-based strong-field ionization modules [26] to compute the ionization that release the *K* shell electrons of the nitrogen. Simulations are performed applying the scheme proposed by Lehe *et al* [27] to avoid numerically overestimation of the betatron oscillations due to spurious Cherenkov radiation. The spatial cells are set to be 16 nm long in the direction of the laser propagation, and 127 nm long in the transverse radial direction, with 32 macro-particles per cell representing background electrons and two macro-particles per cell representing N^{5+} ions. The time step corresponds to 52 as, and three Fourier modes are used for the fields in the azimuthal direction. Furthermore it has been shown that the interpolation of the magnetic field in the PIC lattice can induce a spurious force that increases the transverse momentum of the accelerated particles that propagate inside the plasma wave [28]. To avoid these non-physical forces, the second-order time-interpolation method used by Lehe *et al* [28] is applied here.

A set of four simulations are performed to compare the laser–plasma interaction for different nitrogen concentrations. The simulations consider a mixture of hydrogen and 0.1%, 0.5%, 2% and 5% of nitrogen in the gas forming the plasma, similar to the gas mixtures studied experimentally. The electrons contributing to the background plasma density are differentiated to the ones released from the *K* shell of the nitrogen around the peak intensity of the laser pulse. The laser beam has a peak normalized vector potential of $a_0 = 1.08$ and the FWHM laser pulse duration is 37 fs. The simulations show that for all concentrations, a_0 evolves due to self-compression and self-focusing of the laser beam and exceeds the peak normalized potential corresponding to the ionization intensity required to release the innermost *K* shell electron $a_0^{N^{7+}} = 2.75$ just at the beginning of the density plateau, remaining mainly above this value until 200 μm after the beginning of the density down-ramp. The evolution is similar at all concentrations and achieves a maximum peak normalized vector potential $a_0 = 3.4$.

Figures 4(a)–(d) show the electron density distribution and laser field in a snapshot of the simulations in the density plateau of the gas cell $x = 970$ μm for (a) 0.1%, (b) 0.5%, (c) 2% and (d) 5% of nitrogen in the gas mixture. The longitudinal field originated in the plasma wave is plotted on the electron density distribution in violet. Simulations show that with $\chi = 2\%$ and $\chi = 5\%$, there is so much ionization-induced trapped charge already before the beginning of the density plateau that beam loading strongly influences the formation of the plasma wave. In this case, as electrons are trapped in the density up-ramp, the charge clusters at the rear part of the bubble before the density plateau. This charge drives its own wake and expels the background electrons in the back of the first plasma period. It also flattens and reduces the amplitude of the longitudinal field in the rear part of the bubble. However, the simulations performed for lower nitrogen concentrations (0.1% and 0.5%) agree with our previous study [21]. Along the plateau of the electron density distribution most of the accelerated charge comes from ionization-induced trapped electrons in the first plasma period. During the density down-ramp at the exit of the gas cell, both electrons from the background and electrons from the *K* shell of the nitrogen become trapped in the rear part of the plasma bubble, behind the charge accelerated in the plateau. Thence the maximum energy at which electrons are accelerated decreases as the beam loading increases with the dopant concentration, as shown in figure 4(e) by the purple diamonds, in agreement with the tendency observed during the experiment in figure 1(b).

For this reason, despite a larger amount of *K* shell electrons available for ionization-induced trapping, at higher nitrogen concentrations the LWFA is not always able to efficiently accelerate the charge to energies above 45 MeV.The bar graph in figure 4(e) compares the total charge accelerated at the end of the simulations (left bars, light colours) and the fraction of this total charge above 45 MeV (right bars, dark colours) as a function of χ. In each bar, the blue colour represents accelerated background electrons while the nitrogen *K* shell electrons are represented in green. Although the total charge increases with the nitrogen concentration, the charge above 45 MeV is maximum for 2% of nitrogen in the gas mixture and then decreases for 5%. This represents the same trend as observed in the experimental results for an electron number density $n_e = 9.1 \times 10^{18}$ cm^{-3} in figure 1(a). In addition, the acceleration of background electrons in the laser–plasma interaction quickly

IOP Publishing New J. Phys. 20 (2018) 053011 I Gallardo González et al

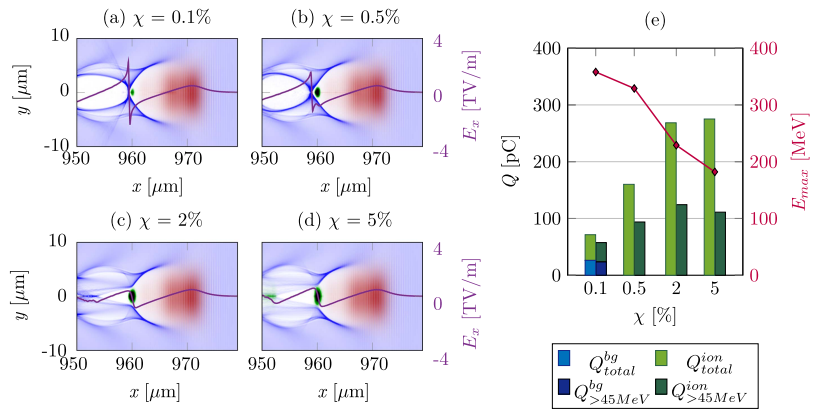

Figure 4. (a)–(d) Snapshots from the simulations for different nitrogen concentrations χ. Details on the simulations parameters can be found in the text. The blue scale represents background electrons, the green scale electrons released from the *K* shell of the nitrogen, and the red scale the intensity of the laser beam. The violet curve corresponds to the on-axis wakefield. (e) Bar chart: comparison of the charge accelerated at the end of the simulation (left) in total, and (right) above 45 MeV for the different gas mixtures. Accelerated background electrons are represented in blue, and the ones from the *K* shell of nitrogen are in green. Diamonds: maximum electron energy.

decreases with the nitrogen concentration, as described before, and becomes zero for nitrogen concentrations $\chi = 0.5\%$ and above. The fact that the simulated laser pulse has a Gaussian temporal and spatial distribution implies a more efficient self-compression and self-focusing than for our real laser pulse. This produces a stronger wakefield that can increase the total accelerated charge and energy of accelerated electrons when comparing with the experimental results [29]. We believe that this might originate the mismatch of accelerated charge and maximum electron energy between simulations and the experiment, but the trend of the charge above a certain energy threshold for different concentrations qualitatively reproduces the experimental observations.

A new simulation is performed where the pulse duration of the laser is increased to 45 fs FWHM to get a better observation of the effect of the overlap of the trapped electrons with the laser fields. To keep consistency of the total energy of the laser pulse with respect to our previous simulations, the normalized vector potential is decreased to $a_0 = 0.9$. The plasma density is the same as in the previous simulations, with a nitrogen concentration of $\chi = 5\%$. 10% of the macro-particles accelerated over 4 MeV were tracked during the simulation.

Figures 5(a), (b) show the transverse phase space of the tracked macro-particles with longitudinal momentum above 145 $m_e c$, corresponding approximately to 75 MeV, before exiting the density down-ramp $x = 1.44$ mm. The macro-particles are coloured according to their longitudinal momentum p_x. In the laser polarization transverse phase space, figure 5(a), the electrons distribution forms a ring. It can be seen that the electrons with higher longitudinal momentum are also the ones in the outer part of the ring. Nevertheless these particles have a very different distribution in the transverse phase space perpendicular to the laser polarization, figure 5(b). There, most of the electrons have an almost null transverse momentum, and are localized close to the axis independently on their longitudinal momentum. The rest of tracked particles with $p_x < 145\ m_e c$ and not shown in the figure, are however distributed homogeneously along a larger transverse position $\pm 6\ \mu$m, and a narrower transverse momentum $\pm 5\ m_e c$ for both axis y and z.

Figure 5(c) shows the p_x/p_y histogram of the accelerated electrons at the end of the simulation, after exiting the density down-ramp $x = 1.8$ mm. The distribution with maximum longitudinal momenta p_x is less dense around $p_y = 0$, and clusters at the sides of the axis, forming the forked structure. Charge along the transverse momentum p_y is integrated in figure 5(d) in analogy to the inset of figures 2(a) and 3. The charge is maximum for $p_y = \pm 5.5\ m_e c$, and drops in the centre of the transverse axis. The shape is alike to the experimentally observed integrated charge of the high energy electrons for similar nitrogen concentration and electron number density in figure 3(b). The phase space trajectories of four of these macro-particles accelerated to high final energies are shown in figure 5(e). The particles are chosen in the leading part of the accelerating electrons, closer to the laser pulse, with final longitudinal and transverse momenta over 250 $m_e c$ and 6 $m_e c$ respectively. The particles start being tracked at around 4 MeV but soon increase their longitudinal momentum. This can be seen looking at the distance between the equally spaced time-steps represented by the points and defining the trajectories. The

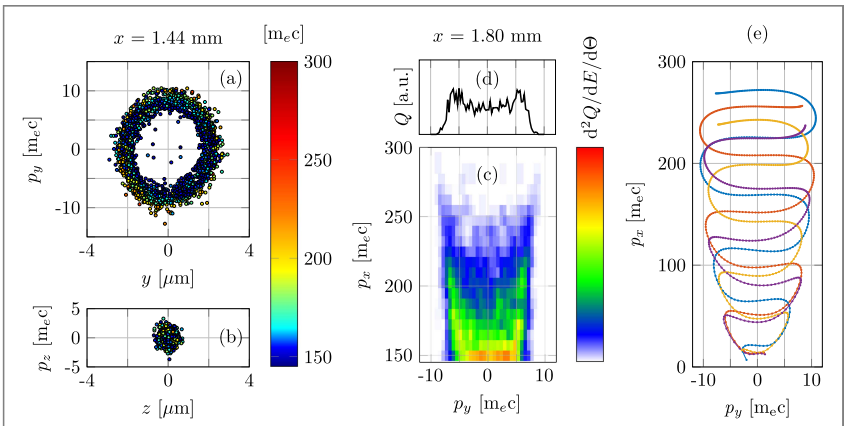

Figure 5. Results from the simulation after tracking electrons interacting with laser pulse of 45 fs FWHM, with $\chi = 5\%$. Transverse phase space of the electrons with $p_x > 145\ m_e c$ in the electron density down-ramp in (a) the laser polarization axis, and (b) the perpendicular direction. The colorscale corresponds with the longitudinal momentum p_x. (c) Histogram of the phase space p_x/p_y at the end of the simulation. (d) Integrated charge along the transverse momentum p_y parallel to the laser polarization from (c). (e) Trajectory in the phase space of four of the high energy electrons from the simulation.

longitudinal momentum gain is more significant where the absolute value of transverse momentum is large, while it can slightly decreases while the transverse momentum changes sign. The transverse momentum p_y changes sign periodically during the trajectory indicating betatron oscillations of the electrons, and increases gradually the maximum absolute value in each period. The particle spends more time in the regions where the transverse momentum is non-zero, as can be seen from the larger distance between time-steps around the p_y axis. Our interpretation is that regardless the transverse position of the electrons, it is more probable that the electrons close to the laser pulse have a non-zero transverse momentum when leaving the plasma wake, originating the forked shape.

5. Discussion

The fact that ionization-induced trapped electrons show a larger divergence along the laser polarization axis has been observed since the first experimental studies of ionization-induced trapping [22]. Momentum conservation imposes that the electrons released by ionization within the laser field are emitted with a certain momentum in the laser polarization direction. Although this entails an intrinsic asymmetrical divergence in beams generated by ionization-induced trapping, this effect does not depend on the nitrogen concentration χ. The observed electron divergence dependence on χ in the laser polarization axis, and shown in figure 2(c), is reproduced also in the simulations presented in figure 4. The increase in divergence is only visible in the direction of the laser polarization and grows with the trapped charge, which suggests that it is related to the laser fields and to the beam loading occurring in the bubble when more electrons are trapped, but not necessarily by DLA. However, as explained below, the preferential angle the high energy electrons are emitted with can only be attributed to DLA.

Simulations of different nitrogen concentrations in figures 4(a)–(d) show that at 2% and 5% of nitrogen in the gas mixture, there is a significant amount of charge trapped by ionization of the N^{5+} and N^{6+} ions already at the beginning of the density plateau. This charge is trapped in the first plasma bubble. As the amount of trapped charge increases, the number of electrons in the leading part of the electron beam also increases. Thus there are more electrons overlapping with the laser fields than in the case of 0.1% or 0.5% percentages of nitrogen, where the ionized *K* shell electrons get trapped in a slower ratio. The increase of trapped charge induces also an increase in the beam loading of the wakefield. Due to beam loading, the most accelerated electrons are closer to the laser pulse and are subjected to DLA, while the heavy perturbation of the already trapped electrons suppresses electron trapping in the density down-ramp. In contrast, at 0.1% and 0.5%, even though existent, the charge subjected to DLA is much lower than for higher concentrations. As mentioned in section 3, at these dopant concentrations we experimentally find a non-zero charge distributed as a forked structure, but the charge in this region is much lower than on-axis. Besides, as beam loading is weaker for these cases, the wake can accelerate the

charge to higher energies and there is the chance of trapping electrons in the density down-ramp, reducing the relative contribution of DLA.

As already referred, higher dopant concentration leads to more ionization-induced trapping, which also implies a larger beam loading effect. Both simulations and experimental results display a net reduction in the maximum energy at which the electrons are accelerated as the nitrogen percentage is increased to 5%. It is also seen that the electron charge accelerated above 45 MeV, which is the lower limit defined by the geometry of the electron spectrometer, decreases at higher nitrogen concentrations despite more charge is trapped in the plasma wave. At 2% and 5% of nitrogen the electron beam is strong enough to drive its own wake in the plasma wave, reducing the longitudinal wakefield and hence the energy to which the electrons are accelerated.

As a result, the forked structure found in the spatio-spectral charge distribution and originated by the preferential angular emission of the high energy electrons subject to DLA, is more visible at high concentrations of nitrogen, when the number of electrons affected by DLA is larger and the electrons accelerated by the wakefield and emitted on-axis achieve lower energies.

The simulation summarized in figure 5 shows the effect of the laser pulse fields on the electron momenta. Electrons with the highest longitudinal momentum appear to be entangled in a driven harmonic oscillator potential in the laser polarization axis phase space, forming a ring along y/p_y. Those with a higher longitudinal momentum are besides located in the outer part of the ring, thus achieving the largest transverse momentum, as observed in figure 5(c). In addition, the ring shape of the y/p_y phase space implies that the majority of the high energy particles have a non-zero transverse momentum, as exhibit in figure 5(d). The high energy electrons, despite located around the optical axis within a narrow space, are emitted preferentially with an angle. The angular emission forms the fork structure and corresponds qualitatively to the experimental observations. The fact that this angular distribution is visible at high nitrogen concentrations, when more charge is trapped at the beginning of the density plateau, and at high electron densities, when the decrease of the plasma wavelength enhances the overlap between the laser fields and the trapped electrons, reinforces that the effect is produced by DLA, and agrees with a previous experimental study [15].

Other studies on DLA have modified either the plasma wave structure or the laser pulse temporal shape to change the DLA contribution to the electron acceleration [8, 9, 11, 13–16]. In those cases a dopant was added only when ionization-induced trapping was required, but not as a variable that affects DLA. However, in this work the dopant concentration allows to influence the DLA contribution to the electrons energy while keeping the same plasma wave and laser pulse parameters. There are several properties of DLA that could be explored by modifying the dopant concentration. Since the first experimental studies, the enhancement of the betatron oscillations attributed to the overlap of electrons and laser pulse in DLA has brought interest for the amplification of the betatron x-ray yield, as the total number of x-ray photons scales with the betatron oscillation amplitude [14]. The dopant concentration might increase the total number of x-ray photons by increasing both, the number of accelerated electrons and their betatron oscillation amplitude.

6. Conclusions

We have shown that the dopant concentration in the gas target for LWFA alters the ratio of ionization-induced trapping of electrons which significantly affects the acceleration mechanism and electron parameters. PIC simulations support that by increasing the amount of nitrogen in the gas mixture, the charge is trapped earlier in the plasma wave and can experience DLA by the overlap with the laser fields, while beam loading decreases the maximum energy of the accelerated electrons and cancels other trapping mechanisms. Our experimental results show that for a given electron number density and laser parameters, electrons emitted from a higher doped gas show a larger total divergence in the direction of the laser polarization and, at concentrations above 2%, the high energy electrons >145 MeV are emitted with a preferential angle ± 6 mrad, producing a forked structure in the charge's spatio-spectral distribution which is an indication of DLA. This is the first time to our knowledge that the dopant concentration is contemplated as a factor that influences contribution of DLA in a LWFA. Our results open the possibility of using the dopant concentration to control or study other effects of DLA, as the increase in amplitude of the electron betatron oscillations, as well as its influence on the x-ray betatron emission.

Acknowledgments

We acknowledge the support of the Swedish Research Council, the Knut and Alice Wallenberg Foundation, the Swedish Foundation for Strategic Research, the Triangle de la Physique (contract no. 2012-032TELISA) and LASERLAB-EUROPE (grant agreement no. 284464, EU FP7). The simulations were performed on resources provided by the Swedish National Infrastructure for Computing (SNIC) at Lunarc.

ORCID iDs

I Gallardo González https://orcid.org/0000-0003-1390-0262
M Hansson https://orcid.org/0000-0001-5813-7040

References

[1] Hooker S M 2013 *Nat. Photon.* **7** 775–82
[2] Tajima T and Dawson J M 1979 *Phys. Rev. Lett.* **43** 267
[3] Lu W, Huang C, Zhou M, Mori W B and Katsouleas T 2006 *Phys. Rev. Lett.* **96** 165002
[4] Corde S, Ta Phuoc K, Lambert G, Fitour R, Malka V and Rousse A 2013 *Rev. Mod. Phys.* **85** 1
[5] Fourmaux S *et al* 2011 *New J. Phys.* **13** 033017
[6] Pukhov A, Sheng Z M and Meyer-ter-Vehn J 1999 *Phys. Plasmas* **6** 2847
[7] Pukhov A 2002 *Rep. Prog. Phys.* **66** 47
[8] Shaw J L, Tsung F S, Vafaei-Najafabadi N, Marsh K A, Lemos N, Mori W B and Joshi C 2014 *Plasma Phys. Control. Fusion* **56** 084006
[9] Zhang X, Khudik V N and Shvets G 2015 *Phys. Rev. Lett.* **114** 184801
[10] Shaw J L, Lemos N, Marsh K A, Tsung F S, Mori W B and Joshi C 2016 *Plasma Phys. Control. Fusion* **58** 034008
[11] Zhang X, Khudik V N, Pukhov A and Shvets G 2016 *Plasma Phys. Control. Fusion* **58** 034011
[12] Gahn C, Tsakiris G D, Pukhov A, Meyer-ter-Vehn J, Pretzler G, Thirolf P, Habs D and Witte K J 1999 *Phy. Rev. Lett* **83** 4772–5
[13] Mangles S P D *et al* 2005 *Phys. Rev. Lett.* **94** 245001
[14] Kneip S *et al* 2009 *Proc. SPIE* **7359** 73590T
[15] Shaw J L, Lemos N, Amorim L D, Vafaei-Najafabadi N, Marsch K A, Tsung F S, Mori W B and Joshi C 2017 *Phys. Rev. Lett.* **118** 064801
[16] Arefiev A V, Robinson A P L and Khudik V N 2015 *J. Plasma Phys.* **81** 475810404
[17] Bulanov S, Naumova N, Pegoraro F and Sakai J 1998 *Phys. Rev.* E **58** R5257
[18] Hansson M, Aurand B, Davoine X, Ekerfelt H, Svensson K, Persson A, Wahlström C-G and Lundh O 2015 *Phys. Rev. ST Accel. Beams* **18** 071303
[19] Esarey E, Hubbard R F, Leemans W P, Ting A and Sprangle P 1997 *Phys. Rev. Lett.* **79** 2682
[20] Hansson M, Aurand B, Ekerfelt H, Persson A and Lundh O 2016 *Nucl. Instrum.* **829** 99–103
[21] Hansson M *et al* 2016 *Plasma Phys. Control. Fusion* **58** 055009
[22] Pak A, Marsh K A, Martins S F, Lu W, Mori W B and Joshi C 2010 *Phys. Rev. Lett.* **104** 025003
[23] McGuffey C, Thomas A G R, Schumaker W, Matsuoka T, Chvykov V, Dollar F J, Kalintchenko G, Yanovsky V, Maksimchuk A and Krushelnick K 2010 *Phys. Rev. Lett.* **104** 025004
[24] Buck A *et al* 2010 *Rev. Sci. Instrum.* **81** 033301
[25] Lifschitz A F, Davoine X, Lefebvre E, Faure J, Rechatin C and Malka V 2009 *J. Comput. Phys.* **228** 1803–14
[26] Nuter R, Gremillet L, Lefebvre E, Lévy A, Ceccotti T and Martin P 2011 *Phys. Plasmas* **18** 033107
[27] Lehe R, Lifschitz A, Thaury C and Malka V 2013 *Phys. Rev. ST Accel. Beams* **16** 021301
[28] Lehe R, Thaury C, Guillaume E, Lifschitz A and Malka V 2014 *Phys. Rev. ST Accel. Beams* **17** 121301
[29] Ferri J, Davoine X, Fourmaux S, Kieffer J C, Corde S, Ta Phuoc K and Lifschitz A 2016 *Sci. Rep.* **6** 27846

Paper VI

Electron acceleration in merging laser wakefields

I. Gallardo González, H. Ekerfelt, J. Björklund Svensson, G. Gatti, A. Gonoskov, D. Guénot, M. Hansson, M. Marklund, J. A. Pérez-Hernández, C. Salgado, E. Wallin, G. Zeraouli and O. Lundh.

(2019) *Submitted to Phys. Rev. Lett.*

Electron acceleration in merging laser wakefields

I. Gallardo González,[1] H. Ekerfelt,[1] J. Björklund Svensson,[1] G. Gatti,[2] A. Gonoskov,[3,4,5] D. Guénot,[1] M. Hansson,[1] M. Marklund,[3] J. A. Pérez-Hernández,[2] C. Salgado,[2] E. Wallin,[6] G. Zeraouli,[2] and O. Lundh[1,*]

[1] *Department of Physics, Lund University, PO Box 118, SE-22100, Lund, Sweden*
[2] *Centro de Láseres Pulsados (CLPU), Parque Científico, E-37185 Villamayor, Salamanca, Spain*
[3] *Department of Physics, University of Gothenburg, SE-41296 Gothenburg, Sweden*
[4] *Institute of Applied Physics, Russian Academy of Sciences, Nizhny Novgorod 603950, Russia*
[5] *Lobachevsky State University of Nizhny Novgorod, Nizhny Novgorod 603950, Russia*
[6] *Department of Physics, Chalmers University of Technology, SE-41296 Gothenburg, Sweden*

(Dated: June 27, 2019)

(this document is not included due to copyright)

(this document is not included due to copyright)

(this document is not included due to copyright)

(this document is not included due to copyright)

Paper VII

Analysis of electron injection in laser wakefield acceleration using betatron emission in capillary tubes

F. G. Desforges, B. S. Paradkar, M. Hansson, T. L. Audet, J. Ju, I. Gallardo González, B. Aurand, P. Lee, L. Senje, A. Persson, S. Dobosz Dufrénoy, O. Lundh, G. Maynard, P. Monot, J.-L. Vay, C.-G. Wahlström and B. Cros.

Proc. of SPIE **9514**, 95140Z-1 (2015).

Analysis of Electron Injection in Laser Wakefield Acceleration Using Betatron Emission in Capillary Tubes

F. G. Desforges[a], B. S. Paradkar[a], M. Hansson[b], T. L. Audet[a], J. Ju[a], I. Gallardo-González[b], B. Aurand[b], P. Lee[a], L. Senje[b], A. Persson[b], S. Dobosz Dufrénoy[c], O. Lundh[b], G. Maynard[a], P. Monot[c], J. L. Vay[d], C.-G. Wahlström[b] and B. Cros[a]

[a]Laboratoire de Physique des Gaz et des Plasmas, CNRS-Université Paris-Sud , 91405, Orsay, France
[b]Department of Physics, Lund University, P.O. Box 118, S-22100 Lund, Sweden
[c]Laboratoire Interactions, Dynamique et Lasers, CEA Saclay, 91191 Gif-sur-Yvette, France
[d]Lawrence Berkeley National Laboratory, Berkeley, California 94720, USA

ABSTRACT

The dynamics of ionization-induced electron injection in the high density ($\sim 1.2 \times 10^{19}\mathrm{cm}^{-3}$) regime of Laser Wakefield Acceleration (LWFA) was investigated by analyzing betatron X-ray emission inside dielectric capillary tubes. A comparative study of the electron and betatron X-ray properties was performed for both self-injection and ionization-induced injection. Direct experimental evidence of early onset of ionization-induced injection into the plasma wave was obtained by mapping the X-ray emission zone inside the plasma. Particle-In-Cell (PIC) simulations showed that the early onset of ionization-induced injection, due to its lower trapping threshold, suppresses self-injection of electrons. An increase of X-ray fluence by at least a factor of two was observed in the case of ionization-induced injection due to an increased trapped charge compared to self-injection mechanism.

Keywords: Laser-wakefield acceleration, betatron radiation, self-injection, ionization-induced injection

1. INTRODUCTION

Since the theoretical prediction[1] of electron acceleration in a plasma wave driven by a laser pulse, evidence of large amplitude electric field (100 GV/m) and subsequent electron acceleration to MeV energies have been reported from numerous experiments[2–4] . More recently[5–7] , production of quasi-monoenergetic GeV electrons have been demonstrated in the bubble regime[8] , where an ion cavity is formed by the near-total expulsion of electrons initially located in the path of the laser. For adequate laser-plasma parameters[9] , self-injection may occur: electrons from the background plasma are injected into the bubble, then accelerated to relativistic energies. During their acceleration, electrons are subjected to the radial focusing force existing inside the cavity[10] which leads to a transverse oscillatory betatron motion, and so emission of radiation in the X-ray domain. Electron acceleration in the bubble regime is a very promising technique aiming at various applications, such as the development of the next generation of compact X-ray sources with femtosecond pulse duration and micron source size. Typically, current experiments[11–15] are able to produce up to $\sim 10^9$ photons per pulse with peak spectral brightness in the range of $10^{20} - 10^{22}$ photons/(s mm^{2}mrad^{2}0.1%BW) using 50 - 100 TW laser systems.

For a successful realization of a practical LWFA based X-ray source, it is crucial to improve the efficiency of X-ray generation. Since X-ray fluence is proportional to charge[15] , increasing the amount of trapped and accelerated electrons for constant laser parameters would be a significant step toward an efficient compact femtosecond X-ray source. This can be achieved in two ways:

Send correspondence to:
F. G. Desforges .: E-mail: frederic.desforges@u-psud.fr, Telephone: +33 (0)1 69 15 81 76
or, B. Cros: E-mail: brigitte.cros@u-psud.fr, Telephone: +33 (0)1 69 15 81 77

Laser Acceleration of Electrons, Protons, and Ions III; and Medical Applications of Laser-Generated Beams of Particles III, edited by Kenneth W. D. Ledingham, Eric Esarey, Klaus Spohr, Carl B. Schroeder, Paul McKenna, Florian J. Grüner, Paul R. Bolton, Proc. of SPIE Vol. 9514, 95140Z · © 2015 SPIE · CCC code: 0277-786X/15/$18 · doi: 10.1117/12.2178654

1. The trapped charge is maximum when the LFWA is operated near the beam loading limit, where the amplitudes of the laser wakefield and the electron bunch wakefield are comparable. For the laser pulses commonly used in LWFA experiments, beam loading occurs in the high density operation regime: $n_{e0} \sim 10^{19}\,\mathrm{cm}^{-3}$.

2. The ionization-induced injection mechanism[16–20] offers an attractive alternative to the self-injection mechanism for the optimization of X-ray generation. In this mechanism, inner shell electrons of high atomic number gas are ionized near the laser peak intensity, and preferentially trapped in the plasma wave. The electron injection starts for lower laser intensity compared to self-injection, resulting in an earlier time of injection onset. This increases the time during which electrons radiate, and leads to a higher X-ray fluence.

We report here a comparative study of electron and X-ray properties for both self-injection and ionization-induced injection mechanisms in the high density regime near beam-loading threshold. By analyzing betatron radiation, we give an experimental demonstration of the early onset of the ionization-induced injection due its lower injection threshold compared to self-injection. This result is obtained by using a technique similar to pinhole imaging of the betatron radiation inside a long dielectric capillary tube[15,21,22] . Previous experiments[16–19] have demonstrated ionization-induced injection by operating below the self-injection threshold. With the help of numerical simulations, we demonstrate that this early ionization-induced injection of electrons in the ion cavity suppresses subsequent self-injection. We also report a significant increase, by at least a factor of two, of the X-ray fluence when ionization-induced injection is used compared to self-injection. The improvement of the X-ray yield is pre-dominantly due to an increase of trapped charge. The remaining part of this paper is organized as follows: the experimental arrangement is described in Sec. 2, while the results on accelerated electrons and emitted X-rays are presented in Sec. 3. PIC simulations using the WARP code were performed, their results are reported and used to discuss experimental results in Sec. 4.

2. EXPERIMENTAL SETUP

2.1 Laser Beam

Experiments were performed at the Lund Laser Centre (LLC) in Sweden using a multi-terawatt laser. The scheme of the layout of the experimental chamber is represented in Fig. 1. A titanium-doped sapphire (Ti:Sa) laser delivers pulses with FWHM duration of 40 fs at a wavelength of 800 nm by using chirped pulse amplification (CPA). The laser radial profile is corrected by a deformable mirror before focusing by a $f = 78$ cm off-axis parabola. This produces beams with gaussian-like transverse profile, as seen in Fig. 2(a). The profile of the laser intensity distribution in the focal plane, measured in vacuum with a CCD camera, is represented by the blue crosses. The blue solid line represents the best fit of the experimental points to a gaussian function. As part of the signal in the wings was not detected by the camera, only the central part of the laser intensity distribution was used for the fitting. The laser transverse size w_0 at waist, *i.e.* radius at e^{-2}, is measured to be about 17 µm (black vertical line). The energy on target is measured to be $E_L = (830 \pm 30)$ mJ and its proportion contained within a circle having a radius equal to w_0 is 88%. The laser peak intensity is thus estimated to be $I_{peak} = (3.8 \pm 0.2) \times 10^{18}\,\mathrm{W/cm^2}$ giving a normalized vector potential of $a_0 = eA/m_e c^2 \approx 1.3 - 1.4$. An active system for stabilizing the laser pointing, developed[23] at LLC, was used in this experimental campaign, giving a standard deviation of the laser pointing of ≈ 4 µrad and improving the electron properties as well as extending the lifetime of capillary tubes.[24]

2.2 Electron and X-ray Diagnostics

Spectra of accelerated electron bunches were studied using a 12 cm long dipole magnet with a peak field of 0.7 T, located 13 cm after the capillary entrance. After being deflected by the magnet, the electrons drifted 16 cm before impinging on a scintillating screen (Kodak Lanex Regular). The radiation emitted by the lanex was imaged by a 16-bit CCD camera located outside of the vacuum chamber. Both the energy and the divergence spectra of bunches were obtained from the analysis of the distribution of the lanex emission. The lowest energy that could be measured with this setup was about 40 MeV. The charge Q_e was calculated from the image of the scintillating screen using published calibration factors[25] . Finally, the average full width at half maximum (FWHM) divergence ($\langle \theta_e^{FWHM} \rangle$) of the electron bunches was estimated as follows: (i) Both the charge (dQ_e/dE_e) and the FWHM

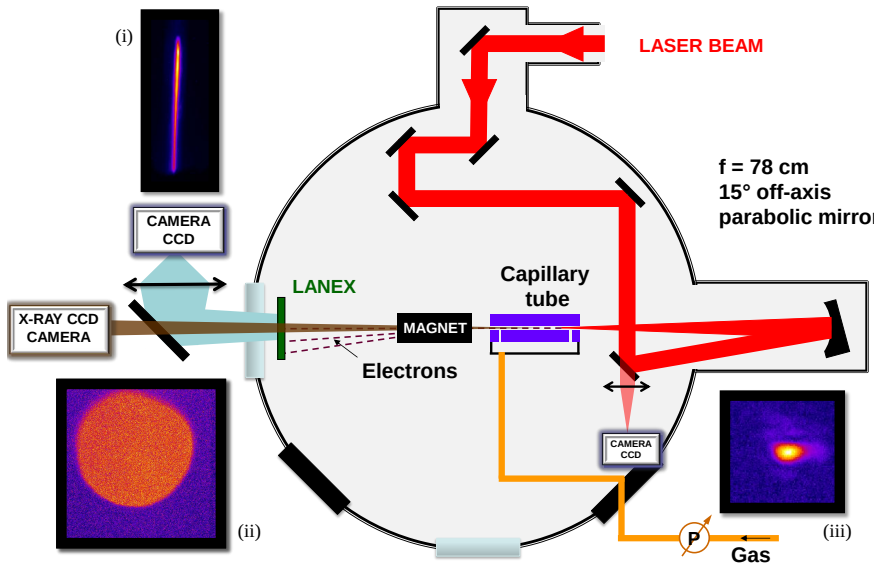

Figure 1. Layout of the experimental chamber implemented for the experimental campaign at the Lund Laser Centre. A multi-terawatt laser system, including a deformable mirror and an active system stabilizing the laser pointing (not represented on this scheme), was employed. (i) Typical radiation emitted by the scintillating screen, *i.e.* electron energy distribution when the magnet is on axis, (ii) typical betatron radiation exiting by the hole of the capillary tube, and (iii) typical laser focal spot are shown. For clarity of the scheme, the electron dispersion is drawn horizontally whereas they were deflected downward during the experiment.

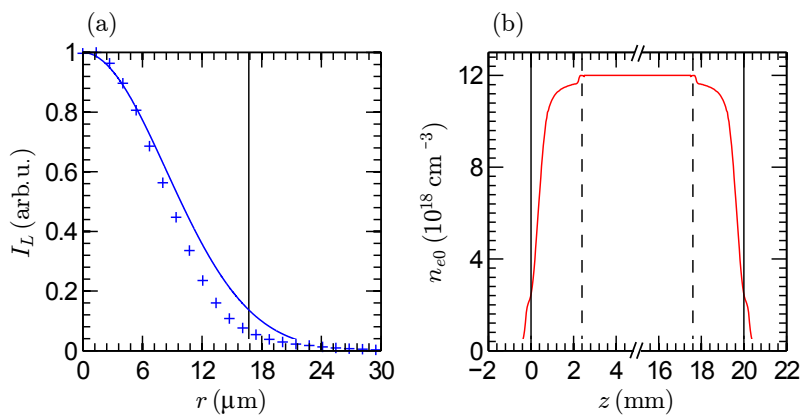

Figure 2. (a) Experimental radial profile (blue crosses) of the laser intensity (I_L), in vacuum, at the focal plane. The solid blue line indicates the best fit of the central part of the experimental points with a gaussian function. The vertical black solid line defines the laser size at waist w_0. (b) Electron number density (red solid line) as a function of the longitudinal position z, within a 20 mm long, 152µm diameter dielectric capillary tube. The locations of the capillary exits and the slits are indicated by the vertical solid and dashed lines, respectively.

divergence (θ_e^{FWHM}) are calculated in term of the electron energy (E_e), (ii) the average FWHM divergence is determined using the formula :

$$\langle \theta_e^{FHWM} \rangle = \frac{\int \theta_e^{FWHM}(E_e) \frac{dQ_e}{dE_e} dE_e}{\int \frac{dQ_e}{dE_e} dE_e} \quad (1)$$

The X-ray emission was recorded with a 16-bit X-ray CCD camera, its features have been characterized by Fullagar *et al.*[26] . An array of thin metallic filters was positioned in front of the camera in order to estimate the critical energy using the method of Ross' filters, assuming a synchrotron-like spectrum.

2.3 Gas Target: Dielectric Capillary Tubes

A glass capillary tube, with length of $L_{cap} = 20\,\text{mm}$, and inner radius $r_{cap} = 73\,\mu\text{m}$, was used to confine and control the gas distribution. It was mounted in a motorized holder allowing its accurate alignment, in vacuum, on the laser axis. The gas used for studying self-injection was pure hydrogen (H_2), and two gas mixtures for ionization-induced injection. We name these mixtures as nitrogen (N_2) mixture and argon (Ar) mixture, which are composed of $99\%H_2 + 1\%N_2$ and $99\%H_2 + 1\%Ar$, respectively. The gas was let in through two slits located at 2.5 mm from the tube exits, providing a 15 mm long plateau with constant pressure between the two slits. The molecular density inside the capillary tubes was adjusted by a gas regulator controlling the upstream reservoir pressure. The gas density was calibrated off-line by interferometric studies[27] coupled with fluid simulations using the *sonicfoam* solver of OpenFOAM code[28,29] . The simulated longitudinal profile of the electron number density is represented in Fig. 2(b); the locations of the capillary exits and the slits are indicated by the black solid and dashed lines, respectively. The electron number density of the plateau, with and without nitrogen or argon, is $n_{e0} = (12 \pm 2) \times 10^{18}\,\text{cm}^{-3}$, assuming complete ionization of the atoms.

3. EXPERIMENTAL RESULTS

3.1 Electron Acceleration

The energy spectra of electron bunches accelerated in pure H_2, nitrogen mixture and argon mixture media are given in Fig. 3(a), (b) and (c), respectively. These data were acquired from a sequence of 30 shots in the case of pure H_2 and nitrogen mixture, and a sequence of 8 shots when the argon mixture was employed. The mean spectra are represented by the solid lines whereas the dashed lines illustrate its standard deviation. For these experimental parameters, electron bunches with broad energy spectra were measured, suggesting continuous injection. The resulting detected charge (Q_e), with energy above 40 MeV, was estimated to be 55 ± 10 pC for pure H_2, 100 ± 20 pC for the nitrogen mixture, and 130 ± 40 pC for the argon mixture. It was found that the average energy is approximately 70 MeV for the three cases, giving a Lorentz factor (γ_e) of about 140.

Similarly, the divergence spectra of the electron bunches as a function of electron energy is plotted for pure H_2, nitrogen mixture and argon mixture media in Fig. 3(d), (e) and (f), respectively. In the case of pure H_2, the signal was too low to compute the FWHM divergence for energies higher than 130 MeV. Using Eq. 1, the FWHM divergence is estimated to be 6 ± 1 mrad for pure H_2, 23 ± 3 mrad for nitrogen mixture and 24 ± 5 mrad for argon mixture.

3.2 X-ray Generation

The characterization of the X-ray beams exiting the capillary tubes provides valuable insight on the electron injection and dynamics during acceleration. On one hand, it allows an estimate of the transverse amplitude of betatron oscillation, which is assumed to be the source size of the emitted X-ray radiation. On the other hand, it is possible to determine the profile of betatron emission which is directly linked to the dynamics of electron acceleration. The X-ray beams generated during the acceleration process are depicted by the typical image of the integrated X-ray beam shown in Fig. 1(ii). As the emission angle of the betatron radiation is much larger ($\sim 100\,\text{mrad}$) than the aperture angle of the capillary tubes ($\sim 10\,\text{mrad}$) in the present case, the X-ray beam will be cropped by the capillary walls. This allows the use of capillary tubes for pinhole imaging as discussed in Sec. 3.2.2. Moreover, published tables[30] indicate that the X-ray beams are not absorbed by the gas.

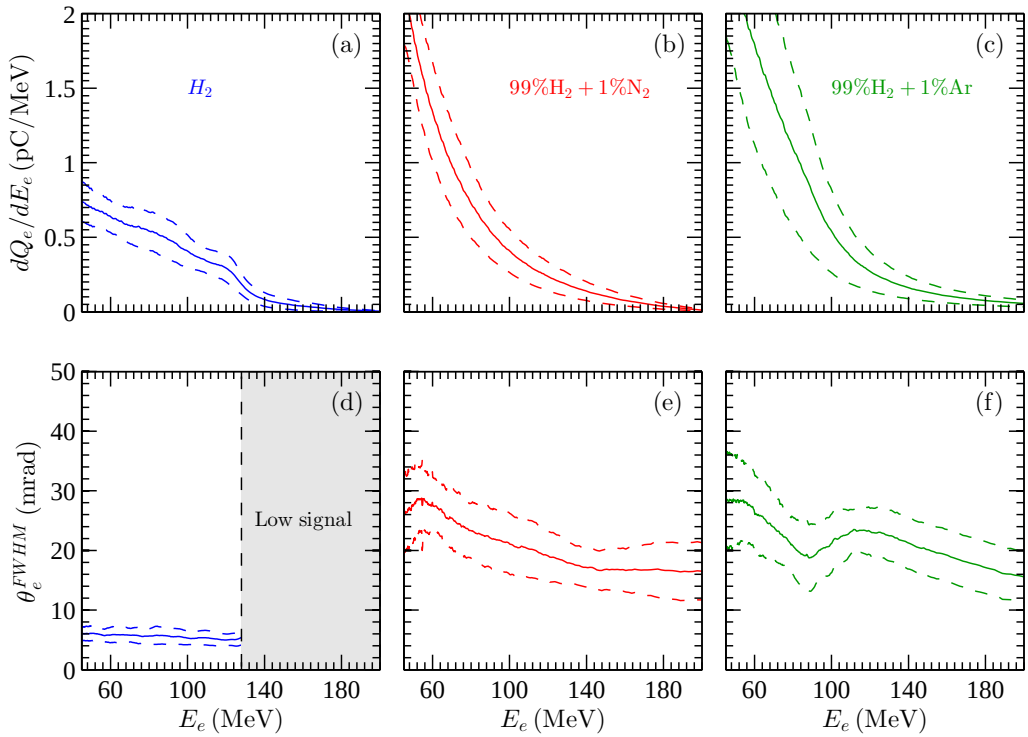

Figure 3. Mean energy spectra (solid curves) of electron bunches for a sequence of 30 shots performed at $n_0 = (12 \pm 2) \times 10^{18}\,\mathrm{cm}^{-3}$ with pure H_2 (a) , nitrogen mixture (b) and argon mixture (c). The dashed curves indicate the standard deviation from the mean spectra. (d-f) Corresponding FWHM divergence curves. The gray area shows the energy range where the signal was too low to compute the FWHM divergence.

3.2.1 Synchrotron Spectra and Critical Energy

Assuming a synchrotron-like spectrum[13] , the critical energy of an X-ray beam is given[31] in the wiggler regime as

$$E_c = \frac{3\gamma_e^2 r_\beta \hbar \omega_p^2}{2c}, \tag{2}$$

where r_β and ω_p are the source size and the plasma frequency, respectively. E_c was estimated from a least squares method using the transmission data of the filters and the sensitivity of the imaging system[14] . The critical energy was only determined for the pure H_2 and nitrogen mixture. It is found to be independent of the type of gas. The average critical energy for all the shots shown in Fig. 3(a) and (b) was computed to be $5.2 \pm 1.0\,\mathrm{keV}$, giving rise to an X-ray source size of $r_\beta \approx 2.2 \pm 0.5\,\mu\mathrm{m}$ (see Eq. 2). We assumed here the betatron radiation from the argon mixture medium to have a critical energy similar to the one measured for pure H_2 and nitrogen mixture media.

3.2.2 Profiles of X-ray Beams

The X-ray radiating zone along the capillary axis inside the plasma can be determined by analyzing the transverse spatial distribution of the cropped X-ray beam exiting the capillary tubes[21,22] . This method assumes that: (i) X-ray photons are emitted on the capillary axis, (ii) the radiation source is ponctual ($r_\beta \ll r_{cap}$). The radial

variation of the X-ray signal ($S_{chip}(r)$) in the detector plane can be transformed into the longitudinal intensity ($I(z)$) of the X-ray emission inside the plasma by using the following system of equations :

$$z = L_{cap} - D_X \frac{r_{cap}}{r}, \tag{3}$$

$$I(z) = -\frac{\partial S_{chip}(r)}{\partial r} \frac{r^2}{r_{cap} D_X}, \tag{4}$$

where $D_X = 1220\,\text{mm}$ is the distance between the X-ray source and the detector. The azimuthal average of the X-ray signal on the detector (Fig. 4(a)) shows that the peak value of the X-ray fluence for the nitrogen mixture (red solid line) and argon mixture (green dot-dash line) is twice that of pure H_2 (blue dashed line). The fluctuations of S_{chip} for $r < 2$ mm is attributed to X-ray reflection. This artefact has been highly mitigated by carefully chosing the region of interest used for plotting the radial profile, in such a way it does not affect the analysis of the betatron emission profiles. The peak fluence for the nitrogen mixture case is estimated to be $\sim 10^5\,\text{ph/mrad}^2$. Kostyukov *et al.* shows[10] that the fluence (Γ_X) of betatron radiation emitted by an electron bunch oscillating within an ion plasma channel is

$$\Gamma_X = 5.6 \times 10^{-3} \times N_\beta \gamma_e^2 Q_e\,. \tag{5}$$

The number of oscillations can be estimated as $N_\beta = L_\varphi/\lambda_\beta \propto n_0^{-1}\gamma_e^{-1/2}$, where L_φ is the dephasing length of electrons and λ_β the betatron oscillation wavelength. As γ_e and n_0 are similar for the three cases, the higher fluence observed in the presence of the mixture is pre-dominantly due to an increase of the electron bunch charge. The betatron emission profiles are plotted in Fig. 4(b) and give rise to two main conclusions:

1. Assuming that the start of charge trapping is similar to the onset of betatron emission, Fig. 4(b) shows that the onset of charge trapping occurs earlier with the presence of N_2 or Ar than with pure H_2. As the electron number density is similar for all the gases, the non-linear evolution of the laser pulse enveloppe during the propagation is similar for the three cases, as confirmed by simulations (Fig. 5(a)).
2. The emission length for both gas mixtures is about 5 mm whereas it is 3 mm for pure H_2. For all the gases, the X-ray emission length is significantly larger than the dephasing length which is estimated[32] to be

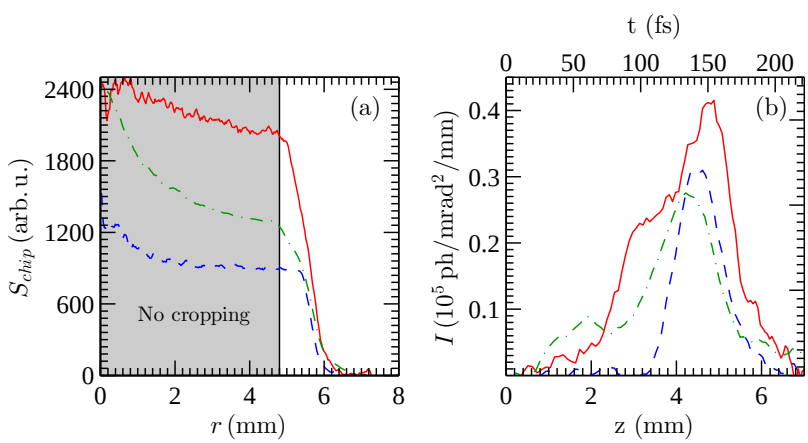

Figure 4. Typical experimental profiles of X-ray beams for pure H_2 (blue dashed line), nitrogen mixture (red solid line) and argon mixture (green dot-dash line) at $(11 \pm 1) \times 10^{18}\,\text{cm}^{-3}$: (a) Azimuthal average of the X-ray signal on the detector, and (b) corresponding calculated longitudinal profile of emission. The grey area represents the central part of the X-ray profile that is not cropped by the capillary tube.

$L_\varphi \simeq 400\,\mu$m. It indicates a continuous injection of electrons over the emission length. Assuming that the X-ray radiation source moves inside the plasma with the laser group velocity, we can estimate the temporal profile of the X-ray pulse using the transformation $t = z(v_g^{-1} - c^{-1})$ where v_g is the group velocity of the laser pulse. The corresponding time scale is shown on the top horizontal axis in Fig. 4(b).

The analysis of 10 shots shows that, on average, the FWHM of X-ray emission duration is 47 fs for pure H_2 and 53 fs for nitrogen mixture media. The corresponding peak brightness for nitrogen mixture case is estimated to be $\sim 5 \times 10^{20}$ photons/(s mm^{2}mrad^{2}0.1%BW) and the number of photons $\sim 10^9$.

4. PARTICLE-IN-CELL SIMULATIONS AND DISCUSSION

4.1 Simulation Settings

These experimental results are qualitatively analyzed using Particle-In-Cell (PIC) simulations in two dimensional cartesian geometry with the code WARP[33] . Ionization dynamics is described by a field ionization model[34] implemented in WARP. In order to identify the origin of trapped electrons, different electron species are created for each possible ionization state of hydrogen (H), helium (He), nitrogen (N) and argon (Ar). The corresponding ionization potentials (IP) are reported in Tab. 1. The cells are shaded according to the dynamics of the electrons after ionization, as discussed in Sec. 4.2; this is not based on the atomic structure. The cells colored in light gray, white and dark gray refer to, arbitrarily named, low IP (LIP), medium IP (MIP) and high IP (HIP), respectively. In the following discussion on gas mixture, LIP electrons will refer to a group of electrons including hydrogen electrons and those coming from the LIP shells of nitrogen or argon.

The glass capillary tube (dielectric constant = 2.25) is modelled by two dielectric slabs separated by a distance equal to the inner diameter of the capillary tube. As shown by the grey area in Fig. 5(a), the longitudinal profile of plasma density is set to be a linear density ramp near the capillary entrance followed by a plateau of density $n_0 = 11 \times 10^{18}\,\mathrm{cm}^{-3}$. The laser pulse with $a_0 = 1.3$, waist size $w_0 = 17\,\mu$m and duration (FWHM) $\tau_L = 40$ fs is focused at $z = 1$ mm. The grid resolution in Z and X directions is 0.04 µm and 0.33 µm, respectively, with 4 macro-particles per cell.

H	He	N	Ar
13.6	24.6	14.5	15.8
	54.4	29.6	27.6
		47.5	40.7
		77.5	59.8
		97.9	75.0
		552.1	91.1
		667.0	124.3
			143.5
			422.5
			478.7
			539.0
			618.3
			686.1
			755.7
			854.8
			918.0
			4121.0
			4426.0

Table 1. Table of ionization potentials in electron-volt for the hydrogen (H), helium (He), nitrogen (N) and argon (Ar). The light gray cells show the low ionization potential (LIP) for which electrons contribute to the plasma wake. No significant amount of these electrons are trapped and accelerated. The white cells contain the medium ionization potential (MIP). MIP electrons are potentially trapped by the plasma wave. The dark gray cells indicate the non-ionized argon shells with a high ionization potential (HIP).

4.2 Parameters of Laser Beam and Electron Bunches

The simulated evolution of the laser a_0 and accelerated charge Q (with energy above 40 MeV) along the longitudinal direction z is plotted in Fig. 5 for pure H_2 (blue dashed line), nitrogen mixture (red solid lines) and argon mixture (green dot-dash lines). In all cases, self-focusing of the laser pulse causes a_0 to increase above the thresholds of self-injection and ionization-induced injection (see Fig. 5(a)). Typically, for our operating conditions, ionization-induced injection is expected[20] to occur for $a_0 \approx 1.7$ whereas self-injection will occur for[32] $a_0 > 2$. The locations z where the laser intensity reaches the thresholds of self-injection and ionization-induced injection are shown by the dashed and solid black lines, respectively. The dynamics of electron injection is discussed for the three cases.

Firstly, we observe on Fig. 5(b) that, for the pure H_2 medium, the onset of hydrogen electron trapping is located at $z \approx 2.7$ mm. The corresponding intensity of the laser pulse is $a_0 = 3$, well above the theoretical threshold of self-injection.

Secondly, in the case of nitrogen mixture, the amount of trapped

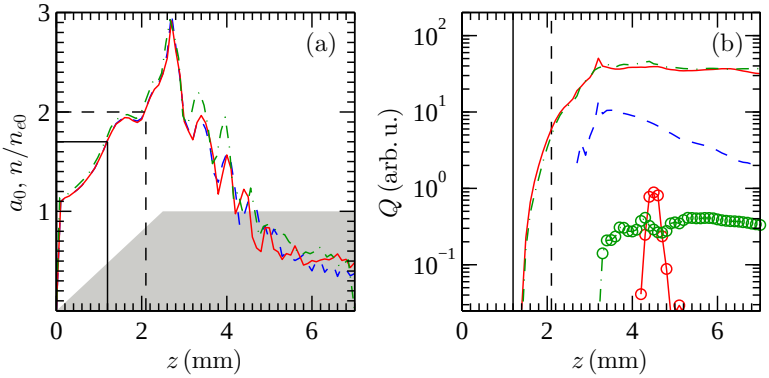

Figure 5. Simulated normalized vector potential a_0 of the laser beam and gas profile (grey area) (a), bunch charge (b) as functions of plasma length for pure H_2 (blue dashed line), nitrogen mixture (red solid lines) and argon mixture media (green dot-dash lines). The black dashed and solid lines indicate the theoretical thresholds of self-injection and ionization-induced injection, respectively. In case of mixture, the lines with and without circles represent the trapped charge coming from LIP and MIP, respectively.

LIP and MIP electrons are represented in Fig. 5(b) by a red solid line with and without circles, respectively. It shows that the amount of MIP electrons is two orders of magnitude higher than that of accelerated electrons with a LIP, which confirms that more electrons are trapped when nitrogen mixture is employed (see Fig. 3(a),(b)). As electron injection starts at $z \approx 1.4\,\text{mm}$, a position where laser intensity ($a_0 \approx 1.8$) is below the self-injection threshold, it shows that the injection of MIP electrons can only be attributed to ionization-induced injection. However, as soon as the laser intensity is above the self-injection threshold ($z > 2.1\,\text{mm}$), the two mechanisms are possibly in competition. Previous work[35] showed that, in the case of nitrogen mixture, self-injection of LIP electrons is suppressed by the ionization-induced injection of MIP electrons. The LIP electrons coming transversely to the axis are repelled by the presence of longitudinally injected MIP electrons near the axis. This suppression is possible because, for our experimental conditions, the evolution of a_0 is such that the onsets of self-injection and ionization-induced injection are clearly separated in space and time, as it can be seen by comparing the two vertical lines in Fig. 5(a). The threshold for ionization-induced injection is reached before the trapping of self-injected electrons could take place. It was found that ionization-induced injection starts at ~ 1 mm before self-injection (Fig. 5(b)) which is consistent with the experimental results (see Fig. 4(b)). The continuous injection of MIP electrons is possible over a longer distance than the dephasing length, it results in the increase of radiating charge in ionization-induced injection compared to the self-injection process.

Thirdly, a trend similar to the nitrogen case is observed when the argon mixture is employed. The amount of trapped LIP and MIP electrons is plotted in Fig. 5(b) by a green solid line with and without circles, respectively. We note that the intensity of the laser pulse did not reach a peak value high enough[36] ($a_0 > 20$ for $\tau_L = 40\,\text{fs}$) to ionize the argon HIP electrons. As suggested by the experimental results on X-ray emission (Fig. 4), the simulation shows that the amount of trapped charge, as well as the dynamics of electron injection, is similar to the nitrogen case. This observation may differ at higher laser intensity. McGuffey *et al.* reported a different electron injection dynamics for a $a_0 = 4$ and $n_{e0} = 10^{19}\,\text{cm}^{-3}$ in a $95\%\text{He} + 5\%\text{N}_2$ medium: LIP and MIP electrons were indifferently and transversely injected. This is infered to result from an ionization of MIP electrons located at the front of the laser pulse where the residual transverse momentum given to them is high. As argon MIP electrons have a different IP range compared to nitrogen MIP electrons (Tab. 1), this change in electron injection scheme may occur at a different laser intensity for argon mixture. Dynamics of argon electron injection will be the topic of future investigations.

5. CONCLUSION

Through an experimental study of betatron radiation, as well as two dimensional PIC simulations, we demonstrate the early onset of ionization-induced injection in a LWFA regime in which both ionization-induced injection and self-injection are possible. We find that a higher X-ray fluence ($\sim 10^5$ ph/mrad^2) is achieved in the case of ionization-induced injection compared to the case of self-injection. This is inferred to be the consequence of the increased amount of trapped charge observed in presence of ionization-induced injection, resulting from a longer injection length due to a lower injection threshold. Finally, we observe that the early onset of ionization-induced injection suppresses the transverse self-injection process in the regime where both self-injection and ionization-induced injection can occur.

ACKNOWLEDGMENTS

This project has benefited from financial support from the Triangle de la Physique, the Labex PALM, ARC, the Swedish Research Council, the Knut and Alice Wallenberg Foundation, the Swedish Foundation for Strategic Research, the Lund University X-ray Centre (LUXC), Laserlab-Europe/CHARPAC (Grant agreement 284464, EC's 7th Framework Programme), EuCARD2/ANAC2 (Grant agreement 312453, ECs 7th Framework Programme) and US-DOE (Contracts DE-AC02-05CH11231). J. Ju acknowledges financial support from the Chinese Scholarship Council (CSC).

REFERENCES

[1] T. Tajima and J. M. Dawson, "Laser electron accelerator," *Phys. Rev. Lett.* **43**, pp. 267–270, Jul. 1979.

[2] A. Modena, Z. Najmudin, A. Dangor, C. Clayton, K. A. Marsh, C. Joshi, V. Malka, C. Darrow, C. Danson, D. Neely, and F. Walsh, "Electron acceleration from the breaking of relativistic plasma waves," *Nature* **377**, pp. 606–608, Oct. 1995.

[3] K. Nakajima, D. Fisher, T. Kawakubo, H. Nakanishi, A. Ogata, Y. Kato, Y. Kitagawa, R. Kodama, K. Mima, H. Shiraga, K. Suzuki, K. Yamakawa, T. Zhang, Y. Sakawa, T. Shoji, Y. Nishida, N. Yugami, M. Downer, and T. Tajima, "Observation of ultrahigh gradient electron acceleration by a self-modulated intense short laser pulse," *Phys. Rev. Lett.* **74**, pp. 4428–4431, May 1995.

[4] D. Umstadter, S.-Y. Chen, A. Maksimchuk, G. Mourou, and R. Wagner, "Nonlinear optics in relativistic plasmas and laser wake field acceleration of electrons," *Science* **273**, pp. 472–475, Jul. 1996.

[5] J. Faure, Y. Glinec, A. Pukhov, S. Kiselev, S. Gordienko, E. Lefebvre, J.-P. Rousseau, F. Burgy, and V. Malka, "A laser-plasma accelerator producing monoenergetic electron beams," *Nature* **431**, pp. 541–544, Sept. 2004.

[6] C. G. R. Geddes, C. Toth, J. van Tilborg, E. Esarey, C. B. Schroeder, D. Bruhwiler, C. Nieter, J. Cary, and W. P. Leemans, "High-quality electron beams from a laser wakefield accelerator using plasma-channel guiding," *Nature* **431**, pp. 538–541, Sept. 2004.

[7] S. P. D. Mangles, C. D. Murphy, Z. Najmudin, A. G. R. Thomas, J. L. Collier, A. E. Dangor, E. J. Divall, P. S. Foster, J. G. Gallacher, C. J. Hooker, D. A. Jaroszynski, A. J. Langley, W. B. Mori, P. A. Norreys, F. S. Tsung, R. Viskup, B. R. Walton, and K. Krushelnick, "Monoenergetic beams of relativistic electrons from intense laser-plasma interactions," *Nature* **431**, pp. 535–538, Sept. 2004.

[8] A. Pukhov and J. Meyer-ter Vehn, "Laser wake field acceleration: the highly non-linear broken-wave regime," *Applied Physics B* **74**, pp. 355–361, Apr. 2002.

[9] S. P. D. Mangles, G. Genoud, M. S. Bloom, M. Burza, Z. Najmudin, A. Persson, K. Svensson, A. G. R. Thomas, and C.-G. Wahlström, "Self-injection threshold in self-guided laser wakefield accelerators," *Phys. Rev. ST Accel. Beams* **15**, p. 011302, Jan. 2012.

[10] I. Kostyukov, S. Kiselev, and A. Pukhov, "X-ray generation in an ion channel," *Physics of Plasmas (1994-present)* **10**, pp. 4818–4828, Nov. 2003.

[11] S. Corde, C. Thaury, A. Lifschitz, G. Lambert, K. Ta Phuoc, X. Davoine, R. Lehe, D. Douillet, A. Rousse, and V. Malka, "Observation of longitudinal and transverse self-injections in laser-plasma accelerators," *Nat. Commun.* **4**, p. 1501, Feb. 2013.

[12] A. Rousse, K. T. Phuoc, R. Shah, A. Pukhov, E. Lefebvre, V. Malka, S. Kiselev, F. Burgy, J.-P. Rousseau, D. Umstadter, and D. Hulin, "Production of a kev x-ray beam from synchrotron radiation in relativistic laser-plasma interaction," *Phys. Rev. Lett.* **93**, p. 135005, Sept. 2004.

[13] S. Fourmaux, S. Corde, K. T. Phuoc, P. M. Leguay, S. Payeur, P. Lassonde, S. Gnedyuk, G. Lebrun, C. Fourment, V. Malka, S. Sebban, A. Rousse, and J. C. Kieffer, "Demonstration of the synchrotron-type spectrum of laser-produced betatron radiation," *New J. Phys.* **13**, p. 033017, Mar. 2011.

[14] S. Kneip, S. R. Nagel, C. Bellei, N. Bourgeois, A. E. Dangor, A. Gopal, R. Heathcote, S. P. D. Mangles, J. R. Marqus, A. Maksimchuk, P. M. Nilson, K. T. Phuoc, S. Reed, M. Tzoufras, F. S. Tsung, L. Willingale, W. B. Mori, A. Rousse, K. Krushelnick, and Z. Najmudin, "Observation of synchrotron radiation from electrons accelerated in a petawatt-laser-generated plasma cavity," *Phys. Rev. Lett.* **100**, p. 105006, Mar. 2008.

[15] J. Ju, K. Svensson, H. Ferrari, A. Dopp, G. Genoud, F. Wojda, M. Burza, A. Persson, O. Lundh, C.-G. Wahlström, and B. Cros, "Study of electron acceleration and x-ray radiation as a function of plasma density in capillary-guided laser wakefield accelerators," *Phys. Plasmas* **20**, p. 083106, Aug. 2013.

[16] M. Chen, Z.-M. Sheng, Y.-Y. Ma, and J. Zhang, "Electron injection and trapping in a laser wakefield by field ionization to high-charge states of gases," *J. Appl. Phys.* **99**, p. 056109, Mar. 2006.

[17] C. McGuffey, A. G. R. Thomas, W. Schumaker, T. Matsuoka, V. Chvykov, F. J. Dollar, G. Kalintchenko, V. Yanovsky, A. Maksimchuk, K. Krushelnick, V. Y. Bychenkov, I. V. Glazyrin, and A. V. Karpeev, "Ionization induced trapping in a laser wakefield accelerator," *Phys. Rev. Lett.* **104**, p. 025004, Jan. 2010.

[18] C. E. Clayton, J. E. Ralph, F. Albert, R. A. Fonseca, S. H. Glenzer, C. Joshi, W. Lu, K. A. Marsh, S. F. Martins, W. B. Mori, A. Pak, F. S. Tsung, B. B. Pollock, J. S. Ross, L. O. Silva, and D. H. Froula, "Self-guided laser wakefield acceleration beyond 1 gev using ionization-induced injection," *Phys. Rev. Lett.* **105**, p. 105003, Sept. 2010.

[19] A. Pak, K. A. Marsh, S. F. Martins, W. Lu, W. B. Mori, and C. Joshi, "Injection and trapping of tunnel-ionized electrons into laser-produced wakes," *Phys. Rev. Lett.* **104**, p. 025003, Jan. 2010.

[20] M. Chen, E. Esarey, C. B. Schroeder, C. G. R. Geddes, and W. P. Leemans, "Theory of ionization-induced trapping in laser-plasma accelerators," *Phys. Plasmas* **19**, p. 033101, Mar. 2012.

[21] G. Genoud, K. Cassou, F. Wojda, H. Ferrari, C. Kamperidis, M. Burza, A. Persson, J. Uhlig, S. Kneip, S. Mangles, A. Lifschitz, B. Cros, and Wahlström, C.-G., "Laser-plasma electron acceleration in dielectric capillary tubes," *Applied Physics B* **105**, pp. 309–316, Apr. 2011.

[22] S. Corde, K. T. Phuoc, R. Fitour, J. Faure, A. Tafzi, J. P. Goddet, V. Malka, and A. Rousse, "Controlled betatron x-ray radiation from tunable optically injected electrons," *Phys. Rev. Lett.* **107**, p. 255003, Dec. 2011.

[23] G. Genoud, F. Wojda, M. Burza, A. Persson, and C.-G. Wahlström, "Active control of the pointing of a multi-terawatt laser," *Rev. of Sci. Instrum.* **82**, p. 033102, Mar. 2011.

[24] M. Hansson, L. Senje, A. Persson, O. Lundh, C.-G. Wahlström, G. Desforges, F. J. Ju, L. Audet, T. B. Cros, S. Dobosz Dufrénoy, and P. Monot, "Enhanced stability of laser wakefield acceleration using dielectric capillary tubes," *Phys. Rev. ST Accel. Beams* **17**, p. 031303, Mar. 2014.

[25] A. Buck, K. Zeil, A. Popp, K. Schmid, A. Jochmann, S. D. Kraft, B. Hidding, T. Kudyakov, C. M. S. Sears, L. Veisz, S. Karsch, J. Pawelke, R. Sauerbrey, T. Cowan, F. Krausz, and U. Schramm, "Absolute charge calibration of scintillating screens for relativistic electron detection," *Rev. Sci. Instrum.* **81**, p. 033301, Mar. 2010.

[26] W. Fullagar, J. Uhlig, M. Walczak, S. Canton, and V. Sundstrom, "The use and characterization of a backilluminated charge-coupled device in investigations of pulsed x-ray and radiation sources," *Rev. Sci. Instrum.* **79**, p. 103302, Oct. 2008.

[27] J. Ju and B. Cros, "Characterization of temporal and spatial distribution of hydrogen gas density in capillary tubes for laser-plasma experiments," *J. Appl. Phys.* **112**, p. 113102, Dec. 2012.

[28] H. G. Weller, G. Tabor, H. Jasak, and C. Fureby, "A tensorial approach to computational continuum mechanics using object-oriented techniques," *Computers in physics* **12**, pp. 620–631, Aug. 1998.

[29] "Openfoam documentation, http://www.openfoam.com/," 2014.

[30] B. Henke, E. Gullikson, and J. Davis, "X-ray interactions: Photoabsorption, scattering, transmission, and reflection at e = 50-30,000 ev, z = 1-92," *Atomic Data and Nuclear Data Tables* **54**, pp. 181–342, July 1993.

[31] E. Esarey, B. A. Shadwick, P. Catravas, and W. P. Leemans, "Synchrotron radiation from electron beams in plasma-focusing channels," *Phys. Rev. E* **65**, p. 056505, May 2002.

[32] W. Lu, M. Tzoufras, C. Joshi, F. S. Tsung, W. B. Mori, J. Vieira, R. A. Fonseca, and L. O. Silva, "Generating multi-gev electron bunches using single stage laser wakefield acceleration in a 3d nonlinear regime," *Phys. Rev. ST Accel. Beams* **10**, p. 061301, Jun. 2007.

[33] J.-L. Vay, D. P. Grote, R. H. Cohen, and A. Friedman, "Novel methods in the particle-in-cell accelerator code-framework warp," *Comput. Sci. Disc.* **5**, p. 014019, Dec. 2012.

[34] G. L. Yudin and M. Y. Ivanov, "Nonadiabatic tunnel ionization: Looking inside a laser cycle," *Phys. Rev. A* **64**, p. 013409, Jun. 2001.

[35] F. G. Desforges, B. S. Paradkar, M. Hansson, J. Ju, L. Senje, T. L. Audet, A. Persson, S. Dobosz-Dufrénoy, O. Lundh, G. Maynard, P. Monot, J.-L. Vay, C.-G. Wahlström, and B. Cros, "Dynamics of ionization-induced electron injection in the high density regime of laser wakefield acceleration," *Phys. Plasmas (1994-present)* **21**, p. 120703, Dec. 2014.

[36] L. Keldysh, "Ionization in the field of a strong electromagnetic wave," *Sov. Phys. JETP* **20**, pp. 1307–1314, Nov. 1965.

Paper VIII

Optimization of soft X-ray phase-contrast tomography using a laser wakefield accelerator

K. Svendsen, I. Gallardo González, M. Hansson,
J. Björklund Svensson, H. Ekerfelt, A. Persson and O. Lundh.

Opt. Express, **26**, 33930 (2018).

Research Article | Vol. 26, No. 26 | 24 Dec 2018 | OPTICS EXPRESS 33930

Optics EXPRESS

Optimization of soft X-ray phase-contrast tomography using a laser wakefield accelerator

K. Svendsen,* I. Gallardo González, M. Hansson, J. Björklund Svensson, H. Ekerfelt, A. Persson, and O. Lundh

Department of Physics, Lund University, P.O Box 118, S-22100, Lund, Sweden

*kristoffer.svendsen@fysik.lth.se

Abstract: X-ray phase-contrast imaging allows for non-invasive analysis in low-absorbing materials, such as soft tissue. Its application in medical or materials science has yet to be realized on a wider scale due to the requirements on the X-ray source, demanding high flux and small source size. Laser wakefield accelerators generate betatron X-rays fulfilling these criteria and can be suitable sources for phase-contrast imaging. In this work, we present the first phase-contrast images obtained by using ionization injection-based laser wakefield acceleration, which results in a higher photon yield and smoother X-ray beam profile compared to self-injection. A peak photon yield of 1.9×10^{11} ph/sr and a source size of 3 μm were estimated. Furthermore, the current laser parameters produce an X-ray spectrum mainly in the soft X-ray range, in which laser-plasma based phase-contrast imaging had yet to be studied. The phase-contrast images of a Chrysopa lacewing resolve features on the order of 4 μm. These images are further used for a tomographic reconstruction and a volume rendering, showing details on the order of tens of μm.

1. Introduction

X-ray phase-contrast imaging (PCI) gives great contrast compared to X-ray absorption imaging in lowly absorbing samples, such as soft tissue or small objects and has previously been used in biomedical applications such as in vivo mammography [1, 2], imaging human joints [3] as well as material science, among others. This method relies on measuring the phase-shift induced by the sample, instead of absorption, which traditional radiography relies on. The phase shift is measured as an intensity modulation at a detector and is obtained by applying a phase-retrieval algorithm. Further post-processing allows for calculations of the projected thickness, making the images suitable for standard tomography to obtain a 3D reconstruction of the sample.

back projIn-line, or propagation based, phase-contrast imaging (PB-PCI) requires no optical components, which simplifies the experimental set-up. With appropriate propagation distances, the phase-shift will by itself evolve into a measurable intensity modulation. The drawback of PB-PCI is that it requires a more complex phase-retrieval method compared to other techniques, such as grating based PCI (where the phase-shift may be obtained directly) [4].

Several factors impact the image quality, such as contrast, signal-to-noise ratio (SNR) and resolution. These quantities are all associated, forcing a compromise between them, and several reports discuss the process of optimizing PB-PCI [5–8]. For example, greater contrast results in lower SNR. Soft X-rays (energy less than 5 keV) yield greater contrast (as the phase contrast is proportional to the phase-shift which is proportional to the wavelength) compared to hard X-rays; this will also increase the average absorption in the object, resulting in lower SNR [5]. For very small/thin samples, the absorption is also small as it scales exponentially with the optical depth according to the Beer-Lambert law. In such cases, soft X-ray PB-PCI may be advantageous over hard X-ray PB-PCI due to its increase in contrast without significantly degrading the SNR. By choosing geometrical parameters that maximize SNR while maintaining the highest possible contrast, a soft X-ray source may be optimal for PB-PCI of thin samples.

#349377 https://doi.org/10.1364/OE.26.033930
Journal © 2018 Received 29 Oct 2018; revised 2 Nov 2018; accepted 2 Nov 2018; published 12 Dec 2018

Research Article | Vol. 26, No. 26 | 24 Dec 2018 | OPTICS EXPRESS 33931
Optics EXPRESS

Lower energetic X-rays are preferentially absorbed over higher energies in the sample, resulting in the X-ray beam having a higher mean energy after the sample compared to before, this is referred to as beam hardening. This can lead to artifacts in the tomographic reconstruction when using a polychromatic source. These artifacts appear as either dark streaks going through brighter areas (streaking artifacts) or an increased brightness at the edges of an object (cupping artifacts). Beam hardening becomes less prominent for smaller samples as there is less absorption. On the other hand, it increases for a softer polychromatic X-ray source as this leads to more absorption in the sample.

The X-ray source size will determine the optimal magnification and therefore influences the overall resolution [6]. In general, a smaller source size performs better but to properly determine the experimental parameters, this size has to be known and a source size measurement is needed.

Although small commercial X-ray sources with a few μm in size are readily available in microfocus X-ray tubes, they have a limited flux. Furthermore, they produce a continuous beam which limits the possibilities for temporally resolved studies. The X-ray source generated by laser wakefield acceleration (LWFA) can be very small, and was recently shown to be suitable for PB-PCI [9–12]. LWFA give high flux in relation to the source size and the X-rays are generated in very short pulses (fs), allowing for time-resolved studies of ultra-fast phenomena.

In LWFA, the production of X-rays is accomplished by focusing a high-power laser pulse onto a gas target. As the intensity at the focus is very high (on the order of 10^{18} W/cm^2), a plasma will be generated. The main part of the pulse is, due to the ponderomotive force, pushing electrons out from high intensity regions which creates a void of electrons inside the plasma. Within this electron void, referred to as a "plasma bubble", a very strong electrostatic potential gradient is formed (on the order of 1 TV/m) [13–21] and some of the electrons trapped within may be accelerated to hundreds of MeV. Electrons not located on the optical axis in the plasma bubble will, due to the focusing force of the plasma, start to oscillate. These oscillations of electrons lead to the generation of X-rays, and the size of the X-ray source which is a few μm, is smaller than the plasma bubble diameter.

Synchrotron radiation is produced whenever a charged particle is accelerated perpendicular to its velocity and, for relativistic electrons the radiation spectrum is in the X-ray range. For a single relativistic particle, this radiation becomes highly directed, having an opening angle that is inversely proportional to the Lorentz factor, as $\phi = 2/\gamma$. In LWFA, a group of particles (an electron bunch), is oscillating within an envelope, and the X-ray beam divergence depends on the maximum envelope amplitude r_β, plasma wavelength λ_p and electron energy as $\theta \propto \sqrt{(2/\gamma)} \cdot r_\beta/\lambda_p$ [22]. The generated X-ray spectrum is synchrotron-like [23–25] and, as such, the spectrum is broadband and may be characterized by its critical energy, E_c, i.e. the median energy for which 50 % of the total number of photons have an energy below E_c. In a LWFA, $E_c \propto n_e \gamma^2 r_\beta$, where, n_e is the electron density in the plasma.

This is to our knowledge the first time a laser-plasma accelerator using ionization injection has been used for PB-PCI. Previous works have been done using self-injection [26] which relies on the self-evolution of the laser pulse to break the plasma wave and thereby inject electrons into the plasma bubble. Ionization injection [27] allows for a more controlled injection mechanism by using a gas mixture, e.g. helium and nitrogen. Electrons are continuously injected as long as the peak intensity of the laser is above a certain threshold or until the bubble is fully loaded with charge. This leads to a broad spectrum and it has been shown that ionization injection increases the accelerated charge and the X-ray yield compared to self-injection [28, 29].

The injection method will impact the characteristics of the X-ray beam and, ionization injection has shown to be less sensitive to laser energy and beam-size variations as well as producing an X-ray beam with a higher, more stable flux. It also shows a more stable divergence and critical energy compared to self-injection [28, 30]. Since the electrons are injected close to the peak of the laser pulse, they also have a preferred direction of oscillation, resulting in an X-ray beam

Research Article | Vol. 26, No. 26 | 24 Dec 2018 | OPTICS EXPRESS 33932
Optics EXPRESS

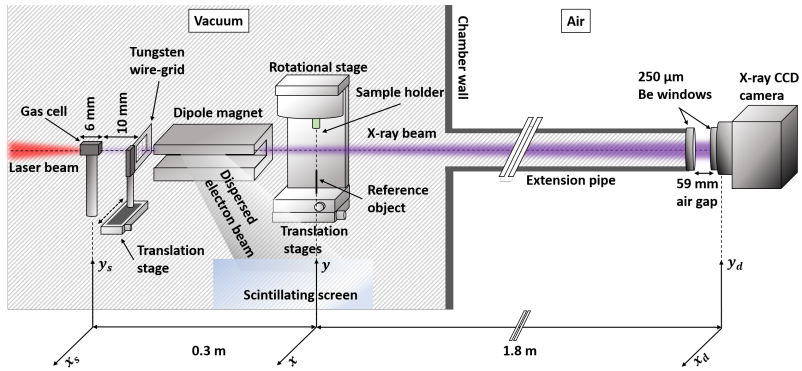

Fig. 1. Schematic of the experimental setup showing the most relevant components. The laser pulse propagates from left to right and is focused on the entrance of the gas cell. Electrons are accelerated and generate X-ray radiation which co-propagates with the electrons and the laser pulse. The wire grid is used to determine the X-ray source size and is not present during the tomographic image acquisition. The dipole magnet disperses the electron beam onto a scintillating screen to monitor the energy. The X-rays propagate to the sample, mounted on a rotational stage. The X-rays are then allowed to propagate a large distance and are finally detected by the CCD. The coordinates (x_s, y_s), (x, y) and (x_d, y_d) refer to the transverse plane of the X-ray source, sample and detector respectively.

with a polarization ratio up to 80 % and an asymmetric divergence [29].

2. Experimental method

The experiment was performed at the Lund Laser Center using a chirped-pulse-amplification-based multi-terawatt laser system with titanium-doped sapphire as the amplifying medium. In this experiment the laser was set to deliver pulses with an energy of 730 mJ on target with a duration (FWHM) of 37 fs, as measured using an intensity autocorrelator, at a central wavelength of 800 nm. The final compression is done in a grating-based compressor in vacuum and is fine-tuned using an acousto-optic programmable dispersive filter (Fastlite Dazzler) in the front-end of the laser system. After temporal compression the pulses are sent through vacuum tubes to the main experimental vacuum chamber.

The main parts of the experimental setup are illustrated in Fig. 1. The temporally compressed laser pulses are focused using an off-axis parabolic mirror with an effective focal length of 775 mm onto the entrance of a 6-mm-long gas cell. The diameter of the laser pulse in the focal plane is approximately 13 µm (FWHM), leading to an estimated peak intensity of 6.5×10^{18} W/cm^2 in vacuum, corresponding to a peak normalized vector potential of $a_0 = 1.7$.

The gas cell is filled with a mixture of helium and nitrogen with a ratio of 1:99 a few tens of milliseconds before the arrival of each laser pulse. This mixture is chosen to allow for a substantial ionization injection of electrons to be accelerated [31]. The backing pressure used for filling the gas cell is set using an electrically controlled gas regulator. Previous studies on similar gas cells showed a filling factor of 90%. The repetition rate of the laser system is 10 Hz but the effective repetition rate is closer to 0.1 Hz, as the residual gas needs to be evacuated prior to the next arriving laser pulse. For the peak normalized vector potential reached in vacuum, the helium atoms are fully ionized and the nitrogen atoms ionized to N^{5+} long before the arrival of the peak of the laser pulse. The released electrons, together with the ions, constitute the

Research Article | Vol. 26, No. 26 | 24 Dec 2018 | OPTICS EXPRESS 33933
Optics EXPRESS

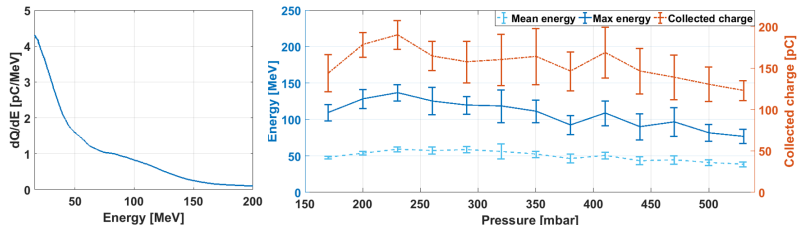

Fig. 2. (a) A typical electron spectrum for a backing pressure of 230 mbar. The spectrum is broad and decays exponentially towards higher energies. The mean (gray dashed line) and maximum energy (solid blue line) are shown in b), the error bars represent the standard deviation over 10 different spectra. The collected charge (dotted orange line) shows a maximum at a backing pressure of 230 mbar.

background plasma which the main part of the laser pulse interacts with.

The ratio between the peak power and the critical power for self-focusing [32, 33] in the linear regime is approximately 9, and thus the laser pulse is expected to be guided over a much longer distance than the Rayleigh range and at the same time reaching much higher a_0 than the estimated value in vacuum. Thus, the threshold for ionization of nitrogen to the second highest level is expected to be reached after some propagation in the plasma and only close to the peak of the laser pulse. The electrons released here are more easily trapped and accelerated in the following plasma wave driven by the laser pulse.

The electrons accelerated in the interaction exit the cell along the optical axis and are dispersed according to their energy using a 20 cm long dipole magnet with a peak magnetic field of 0.8 T, before impacting on a scintillating screen (Kodak Lanex Regular). The scintillating screen is imaged from the back side using a 16-bit scientific CMOS camera (Andor Zyla 4.2 Plus). By numerically tracing electrons of different energies through a measured map of the magnetic field, the relation between electron energy and position on the scintillating screen along the dispersed direction is determined. Furthermore, the response of the full imaging system is calibrated and used together with previously published calibration factors for the scintillating screen [34] to determine the amount of charge detected at each position. This enables the reconstruction of the energy spectrum of the accelerated electrons. Figure 2(a) shows a typical spectrum for a backing pressure of 230 mbar. The mean electron energy remains fairly constant over the range of scanned pressure, see Fig. 2(b). The maximum electron energy, defined here as the energy at 10% of the peak charge-per-energy, dQ/dE, shows a stronger trend to decline towards higher pressure and the maximum of the collected charge coincides with the maximum photon yield.

The dipole magnet is used to separate the electrons from the laser beam and the beam of X-rays generated in the acceleration process. The X-ray beam exits the experimental chamber through a 250 µm thick beryllium window and enters the vacuum chamber housing the CCD-chip of the X-ray camera (Andor iKon-L SO), sensitive to X-ray up to 20 keV, through a beryllium window of the same thickness. The X-ray CCD has 2048×2048 square pixels with a size of 13.5 µm. This detector is positioned 2.1 m from the front of the gas cell. The separation of the two beryllium windows is 6 cm over which the X-ray beam propagates in air.

To characterize the flux distribution and energy distribution of the X-ray pulse, a Ross-filter array [35, 36] was inserted into the X-ray beam close to the exit of the experimental chamber. The filter array used was composed of intersecting strips of the elements Cu, Sn, Zr, Fe, Ni, and V, of thickness 25, 3, 3, 3, 5 and 3 µm, respectively. The average signal values in the image behind each strip provide samples of the X-ray spectrum to which an assumed synchrotron-like

Research Article | Vol. 26, No. 26 | 24 Dec 2018 | OPTICS EXPRESS 33934
Optics EXPRESS

spectrum is fitted and allows for determination of the critical energy.

This way, the critical energy was determined while varying the background electron number density by changing the backing pressure to the gas cell. The result is shown in Fig. 3(a), together with the peak photon yield and mean photon yield. The error bars indicate the standard deviation within the average of 10 different X-ray pulses. The photon yield has a broad maximum centered around 230 mbar with a maximum value of 1.9×10^{11} ph/sr, corresponding to an electron number density of 1×10^{19} cm^{-3}. The critical energy at these pressures is approximately 2.4 keV. The X-ray beam divergence was estimated by fitting a Gaussian function to the X-ray intensity profile on the CCD camera. It was estimated to be 48 (vertical) and 67 mrad (horizontal) FWHM at 230 mbar. The divergence remained unchanged up until 400 mbar.

Results

A source size measurement was performed by placing a grid of 25 μm thick tungsten wires in the X-ray beam, 10 mm from the exit of the gas cell. As there was some concern for the durability of the 25 μm wires, the thicker 50 μm wires were also included in the grid. Having wires in both the vertical and horizontal plane allowed for a size measurement in both planes. The resulting diffraction patterns were fitted to simulated data that was obtained by the use of the equation [37]

$$I_s(x_d) = \int B(x_s)\bar{I}(x_d + x_s\frac{r_2}{r_1})\mathrm{d}x_s, \tag{1}$$

where x_s and x_d are the coordinates in the source plane and detector plane respectively. r_1 is the source-sample distance and r_2 is the sample-detector distance. $B(x_s)$ is the spatial distribution of the source which was assumed to be Gaussian and $\bar{I}(x_d)$ is the spectrally weighted average of

$$I(x_d, \lambda) = \left|\sqrt{\frac{r}{i\lambda r_1 r_2}}\int \exp\left(\frac{-i\pi}{\lambda r_2}(2xx_d - \frac{r}{r_1}x^2 - \frac{r_1}{r}x_d^2)\right)\cdot q(x,\lambda)\mathrm{d}x\right|^2 \tag{2}$$

where x is the object plane coordinates. The total propagation distance is $r = r_1 + r_2$. The wire's transmission function q is given by $q(x,\lambda) = e^{-\mu(\lambda)\cdot 2\sqrt{R^2-x^2}}$, where R is the wire radius and $\mu(\lambda)$ the attenuation coefficient. The weights w_λ used for the spectral average was determined by the spectral probability distribution by considering the synchrotron-like spectrum of the source at $E_c = 2.4$ keV, the quantum efficiency of the X-ray CCD, the photon absorption through the two beryllium windows and the air gap to the detector. The intensity distribution $I(x_d, \lambda)$ is Figure 3(b) shows the best fit for the horizontal and vertical source size respectively for the 25 μm thick tungsten wire. This results in a vertical size of approximately 3.6 ± 0.2 μm and a horizontal size of 2.6 ± 0.2 μm (FWHM).

To determine optimal r_1 and r_2 that result in the best SNR for PB-PCI, the findings by Ya. I. Nesterets *et al.* [5] were implemented. The procedure maximizes SNR with respect to the optimal magnification for a symmetrical Gaussian feature of a homogeneous object, wavelength, source size and detector resolution. For a source size of 2.6 μm, pixel size of 13.5 μm and a magnification that yields the best detector resolution results in $r_1 = 0.6$ m and $r_2 = 1.7$ m. This was further investigated by performing Fresnel-Kirchoff diffraction simulations and analyzing the contrast using different distances. The simulations gave better SNR with a magnification larger than what was obtained via the optimization procedure developed by Nesterets *et al*. This, in combination with the limited space inside the experimental chamber, motivated the use of a smaller r_1, and the final distances were $r_1 = 0.3$ m and $r_2 = 1.8$ m.

The detected image, I_0, is processed before any further calculations by subtracting a dark field image I_d and normalizing to a flat field image, I_f, as $I = (I_0 - I_d)/(I_f - I_d)$. This flat and dark field correction constitutes an issue as the flat field changes from shot-to-shot, is non-uniform, and it is not possible to simultaneously acquire a flat field and a corresponding sample image.

Research Article | Vol. 26, No. 26 | 24 Dec 2018 | OPTICS EXPRESS 33935
Optics EXPRESS

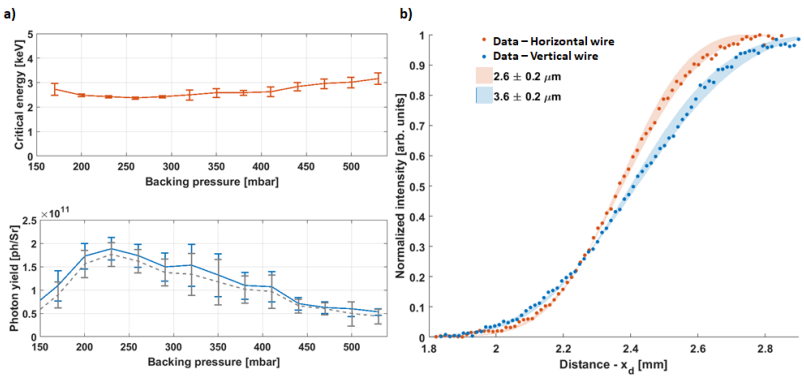

Fig. 3. (a) Critical energy and X-ray photon yield obtained from the Ross filter measurements. Maximal photon yield is obtained at a backing pressure of 230 mbar, corresponding to an electron number density of 1×10^{19} cm^{-3}. At this pressure, a critical energy of 2.4 keV is obtained. Error bars represent the standard deviation within the average of 10 X-ray pulses. The backing pressure used during the tomographic scan resulted in a peak photon yield of approximately 1.9×10^{11} ph/sr, a divergence of 48×67 mrad^2 in the vertical and horizontal direction respectively and a critical energy of 2.4 keV. (b) knife edge measurement of the source size, using a 25 μm tungsten wire. The obtained data (dots in b)) was compared to simulated values (shown as a shadow), resulting in a vertical source size of 2.6 ± 0.2 μm and a horizontal source size of 3.6 ± 0.2 μm.

By taking the average pixel value at several positions in the image and generating an cubical interpolated mesh, I_g, one obtains an approximated image background gradient, which results in a more representative image. This was implemented for the phase-contrast images of the Chrysopa specimen, Fig. 4(c).

All single-shot phase retrieval algorithms make some assumption on absorption and A. Burvall *et al.* gives a good overview on these [38]. The soft X-ray spectrum is subject to some absorption in the sample which limits the choice to Paganins single-material algorithm [39], since it does not require absorption close to zero. Instead, one assumes the absorption to be proportional to the refractive index decrement, δ. For a monochromatic source of wavelength λ, the projected thickness of the sample is [39]

$$t(\vec{r}_\perp) = -\frac{1}{\mu} \ln\left(\mathcal{F}^{-1}\left(\mu \frac{\mathcal{F}(I(\vec{r}_\perp, r_2))}{r_2 \delta |\vec{k}_\perp|^2 + \mu}\right)\right) \tag{3}$$

where $\vec{r}_\perp$ is the position vector perpendicular to propagation, $\mathcal{F}$ denotes the 2D Fourier transform, $\vec{k}_\perp$ is the spatial frequency vector, $\vec{k}_\perp = (u, v)$, so that $|\vec{k}_\perp|^2 = u^2 + v^2$. The spatial frequencies, u, v, were calculated as $M \cdot F(-1/2 + (n_i - 1)/(n-1))$, where M is the magnification, F the number of pixels per unit length, n_i the pixel number and n total number of pixels in the corresponding dimension [40]. $I(\vec{r}_\perp, r_2)_\lambda$ is the normalized and background subtracted PCI.

As the X-ray source is polychromatic, the effective refractive index decrement was calculated as the spectrally weighted average $\delta_{eff} = \int w_\lambda \delta_\lambda \mathrm{d}\lambda / \int w_\lambda \mathrm{d}\lambda$ and the effective attenuation coefficient μ_{eff} was calculated in the same way. The projected thickness was calculate by Eq. (3) using δ_{eff} and μ_{eff}.

Two different samples were used; a 100 μm thick plastic line (CH-line) tied in a reef-knot and

Research Article | Vol. 26, No. 26 | 24 Dec 2018 | OPTICS EXPRESS 33936
Optics EXPRESS

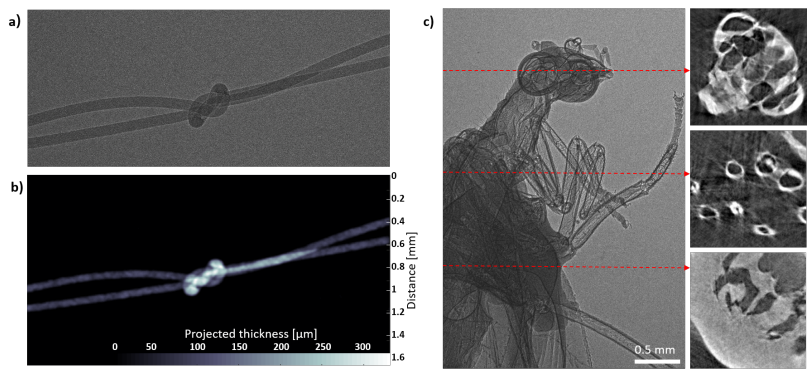

Fig. 4. (a) shows a raw PCI of a 100 μm thick CH-line with some visible edge enhancement due to the phase-contrast effect. The projected thickness of the same CH-line, obtained by using Eq. (3), is shown in (b). (c) shows a PCI of the Chrysopa specimen accompanied by three tomographic slices, the location of these at the specimen is indicated by the red dashed arrows.

a small green lacewing of the Chrysopa genus. For each of these samples, 900 images were taken, divided into 5 images at each angle over 180 degrees in 1 degree increments. Each set of 5 images were averaged to increase the SNR. The last set of images obtained at 180 degrees are not necessary for the tomographic reconstruction but were used to find the center of rotation by overlapping with the set of images at 0 degrees.

As some shot-to-shot pointing fluctuation is present in the laser system and, a general pointing drift, i.e. the laser focus drifts toward a general direction over time, the image will move on the detector. Taking an average of several images would diffuse any details and decrease the contrast. To account for this, a method of aligning the images before averaging was adapted by using a stationary reference object positioned in the plane of the sample. By performing edge-detection and cross-correlation computations the images were translated to cancel the pointing drift. The alignment can be sub-pixel accurate by interpolating either the images or the cross-correlation matrix.

Applying the procedure for background correction described earlier and calculating the projected thickness using Eq. (3) on a sample of known thickness, the 100 μm thick CH-line, showed good agreement. Figure 4(b) shows the projected thickness of this CH-line. This thickness varied along the line but this was believed to be due to the manufacturing process or possibly the process of tying the knot, which may have deformed the wire to some degree.

The tomographic images were reconstructed by the filtered backprojection from sinograms, which in turn were generated from the projected thickness data set. The tomographic reconstruction assumed parallel beam geometry and using the open-source software 3D Slicer [41–46], a volume rendering was made of the sample from the tomographic images.

Here we present a single PCI of the Chrysopa specimen sample, Fig. 4(c), along with tomographic images. Location of the cross-section is indicated by a red dashed arrow. In the PCI, some very fine details are visible such as the hairs, estimated to be 4 μm thick. The tomographic images were reconstructed by averaging and aligning 5 shots for each angle, calculating the projected thickness using Paganin's algorithm, Eq. (3), and applying the filtered backprojection formula to the sinograms. The finer details are lost when calculating the projected thickness as Eq. (3) also acts as a low-pass filter. Finally, we present the volume rendering, shown in Fig. 5.

Research Article | Vol. 26, No. 26 | 24 Dec 2018 | OPTICS EXPRESS 33937
Optics EXPRESS

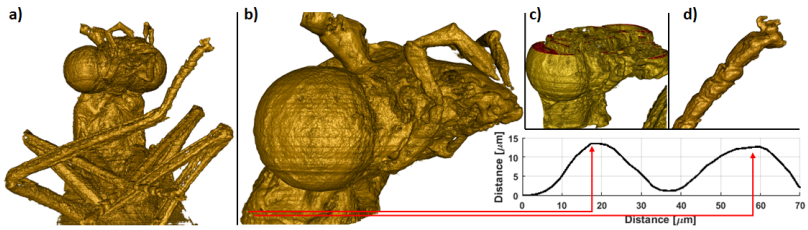

Fig. 5. The volume rendering of the Chrysopa specimen is shown here, a) shows the upper part. (b) shows the head where some finer details are resolved, such as the follicles. These are located within the red circle and a line-out plot is shown of two such follicles, showing them to be on the order of 30 μm in width and 10 μm in height. (c) shows a section of the head, which has hollow chambers and (d) shows a close up of the tarsus (leg) where two hooks can be seen at the tip.

In these images, the finest details visible are the small follicles at the neck. These are roughly 30 μm in diameter and 13 μm in height.

3. Discussion

The X-ray yield has a broad maximum centered around a backing pressure of 230 mbar which coincides with the maximum collected charge in the electron beam. The electron spectra exhibits a Maxwellian-like distribution which is most likely due to the continuous injection and the fact that the length of the gas cell is much longer than the dephasing length. To be able to continuously operate at the optimal electron density, the plasma density needs to be consistent. However, at a constant gas cell backing pressure, the plasma density might be decreased due to the decrease of the filling factor after a few hundred laser pulses due to ablation of the entrance and exit holes in the gas cell. This might be overcome by using gas cells with an entrance hole for the laser pulse that does not ablate easily. The peak photon yield and mean photon yield are close in magnitude, indicating a smooth beam profile. The X-ray beam divergence was observed to be fairly constant over the range of 150 – 400 mbar along with the critical energy.

The source was measured to be $(2.6 \pm 0.2) \times (3.6 \pm 0.2)$ μm, with the horizontal size being the larger of the two. This asymmetry was expected and the size is larger in the direction of the polarization of the laser pulse (horizontal polarization). It has previously been observed that the accelerated electrons, when overlapping with the laser pulse tail, oscillate with larger amplitudes along the laser polarization [31, 47]. Consequentially, this creates a larger X-ray source in this direction. The influence of the laser beam on the electron beam is reported to decrease as the laser pulse is made shorter [48]. Thus, a shorter pulse would be preferable to decrease the source size, assuming the photon flux does not decrease.

The SNR could be improved by introducing additional filters and/or increasing the number of shots averaged. An increase in the laser and gas injection repetition rate would facilitate this. The calculated thickness of the sample depends strongly on the ability to detect diffraction fringes in the X-ray beam, making the detector resolution a crucial aspect of the setup [5]. To further improve, a detector with higher pixel density would be mandatory, this may however decrease the SNR due to the smaller pixel size.

The tomographic reconstruction could be further improved as parallel beam geometry was assumed. This was not the case as the beam is divergent (estimated to about 60 mrad). This would result in a rhombus distortion in the sinogram, introducing some error in the reconstruction if not taken into account. The beam divergence is still relatively small, hence the error will not

Research Article | Vol. 26, No. 26 | 24 Dec 2018 | OPTICS EXPRESS 33938
Optics EXPRESS

be significant, but the reconstruction would still be improved if assuming a cone beam geometry.

4. Conclusions

It has been shown that ionization injection-based LWFA can provide sufficient X-ray flux and beam quality for high-resolution PCI by using ionization injection at a suitable plasma electron density. This allows for rapid data collection at high-repetition rate systems and the sample is only illuminated during data acquisition, minimizing the applied radiation dose. The phase contrast images resolve features on the order of 4 μm and the final 3D volume rendering shown in Fig. 5, resolves details on the 10 μm scale such as the follicles, indicated by the red arrows. Despite the sample having a considerable thickness and absorption at the photon energies used, soft X-ray PB-PCI provides good resolution and seems to be limited primarily by the source size. To further decrease the source size, the oscillation amplitude of the accelerated electrons would need to be decreased. This would also decrease the critical energy of the emitted X-ray spectrum which is proportional to the oscillation amplitude. As such, this may be a possibility to gain a tunable X-ray source by using clever injection methods that allow for injection at a certain transverse position, thereby controlling the amplitude.

Using lower energetic X-rays improves the contrast but it also decreases the SNR due to the increased absorption. By using a thinner sample, the increase in contrast remains but as the absorption decreases, the SNR improves, and in the extreme case for a pure phase-object (no absorption) softer X-rays will always be more beneficial over hard X-rays. There is some loss in detail as the projected thickness is calculated, which is needed to perform the tomographic reconstruction, but one may view this as complementary data to the PCI. The volume rendering creates a full 3D object which can be manipulated and analyzed by a number of different tools and software packages, providing a valuable workspace.

This technique is intriguing since it allows for X-ray imaging of small objects that generally have low absorption, along with the possibility to fully 3D render the object. The advantage of using laser-plasma produced X-rays is the compactness of the system compared to a synchrotron source, its small source size and relatively high flux. An additional advantage is the automatic synchronization. By extracting part of the laser beam, one may easily construct a pump-probe experiment with accurate timing (assuming the laser beam has enough energy to spare). Furthermore, the ultra-short X-ray pulse duration, which is on the order of fs, allows for temporally resolved experiments. The X-ray beam divergence allows for a compact setup when imaging mm-sized objects as the distances needed for the beam to expand and cover the full sample are relatively small. Smaller samples, especially ones exhibiting ultra-fast dynamics (such as chemical reactions or molecular vibrations) might require some focusing optics in order to achieve a satisfactory X-ray flux on the sample. Such small systems would on the other hand benefit from the increase in contrast due to using soft X-rays and this method may have a large impact in other fields such as micro- and nano-structures, cell biology and aerosol studies.

Author contributions statement

K.S., I.G.G., O.L and M.H planned and performed the experiments. I.G.G., K.S., A.P., J.B.S. and H.E. prepared the experimental setup. K.S., I.G.G and J.B.S. analyzed the data and K.S and M.H wrote the manuscript. K.S., I.G.G., M.H. and O.L. discussed and interpreted the results. All authors reviewed the manuscript.

Funding

Knut and Alice Wallenberg Foundation (KAW 20140170); The Swedish Research Council (VR 201503749); The Swedish Radiation Safety Authority (SSM 20172478); The Crafoord

Research Article | Vol. 26, No. 26 | 24 Dec 2018 | OPTICS EXPRESS 33939
Optics EXPRESS

Foundation (20130712); The European Union's Research and Innovation programme under Laserlab-Europe (EU-H2020 654148); ARIES (EU-H2020 730871).

Acknowledgments

The authors would like to thank Mikael Sörensson, PhD student at the division of Functional Zoology, who helped identify the species of the fly.

Disclosures

The authors declare no competing interests.

References

1. E. Castelli, M. Tonutti, F. Arfelli, R. Longo, E. Quaia, L. Rigon, D. Sanabor, F. Zanconati, D. Dreossi, A. Abrami, E. Quai, P. Bregant, K. Casarin, V. Chenda, R. H. Menk, T. Rokvic, A. Vascotto, G. Tromba, and M. A. Cova, "Mammography with synchrotron radiation: First clinical experience with phase-detection technique," Radiology **259**, 684–694 (2011).
2. G. Tromba, R. Longo, A. Abrami, F. Arfelli, A. Astolfo, P. Bregant, F. Brun, K. Casarin, V. Chenda, D. Dreossi, M. Hola, J. Kaiser, L. Mancini, R. H. Menk, E. Quai, E. Quaia, L. Rigon, T. Rokvic, N. Sodini, D. Sanabor, E. Schultke, M. Tonutti, A. Vascotto, F. Zanconati, M. Cova, and E. Castelli, "The SYRMEP beamline of elettra: Clinical mammography and bio-medical applications," AIP Conf. Proc. **1266**, 18–23 (2010).
3. A. Momose, W. Yashiro, K. Kido, J. Kiyohara, C. Makifuchi, T. Ito, S. Nagatsuka, C. Honda, D. Noda, T. Hattori, T. Endo, M. Nagashima, and J. Tanaka, "X-ray phase imaging: from synchrotron to hospital," Philos. transactions. Ser. A, Math. physical, engineering sciences **372**, 20130023 (2014).
4. K. A. Nugent, "Coherent methods in the x-ray sciences," Adv. Phys. **59**, 1–99 (2010).
5. Y. I. Nesterets, S. W. Wilkins, T. E. Gureyev, A. Pogany, and A. W. Stevenson, "On the optimization of experimental parameters for x-ray in-line phase-contrast imaging," Rev. Sci. Instrum. **76**, 093706 (2005).
6. X. Wu, H. Liu, and A. Yan, "Optimization of x-ray phase-contrast imaging based on in-line holography," Nucl. Instrum. Methods B **234**, 563 – 572 (2005).
7. A. Pogany, D. Gao, and S. W. Wilkins, "Contrast and resolution in imaging with a microfocus x-ray source," Rev. Sci. Instrum. **68**, 2774 (1997).
8. A. Balles, S. Zabler, T. Ebensperger, C. Fella, and R. Hanke, "Propagator based formalism for optimizing in-line phase contrast imaging in laboratory x-ray setups," Rev. Sci. Instruments **87**, 093707 (2016).
9. S. Fourmaux, S. Corde, K. Ta Phuoc, P. Lassonde, G. Lebrun, S. Payeur, F. Martin, S. Sebban, V. Malka, A. Rousse, and J. C. Kieffer, "Single shot phase contrast imaging using laser-produced betatron x-ray beams," Opt. Lett. **36**, 2426 (2011).
10. J. Wenz, S. Schleede, K. Khrennikov, M. Bech, P. Thibault, M. Heigoldt, F. Pfeiffer, and S. Karsch, "Quantitative x-ray phase-contrast microtomography from a compact laser-driven betatron source," Nat. Commun. **6**, 7568 (2015).
11. J. M. Cole, J. C. Wood, N. C. Lopes, K. Poder, R. L. Abel, S. Alatabi, J. S. J. Bryant, A. Jin, S. Kneip, K. Mecseki, D. R. Symes, S. P. D. Mangles, and Z. Najmudin, "Laser-wakefield accelerators as hard x-ray sources for 3d medical imaging of human bone," Sci. Reports **5**, 13244 (2015).
12. A. Döpp, L. Hehn, J. Götzfried, J. Wenz, M. Gilljohann, H. Ding, S. Schindler, F. Pfeiffer, and S. Karsch, "Quick x-ray microtomography using a laser-driven betatron source," Optica **5**, 199–203 (2018).
13. S. Kneip, C. McGuffey, J. L. Martins, S. F. Martins, C. Bellei, V. Chvykov, F. Dollar, R. Fonseca, C. Huntington, G. Kalintchenko, A. Maksimchuk, S. P. D. Mangles, T. Matsuoka, S. R. Nagel, C. A. J. Palmer, J. Schreiber, K. T. Phuoc, A. G. R. Thomas, V. Yanovsky, L. O. Silva, K. Krushelnick, and Z. Najmudin, "Bright spatially coherent synchrotron x-rays from a table-top source," Nat. Phys. **6**, 980 (2010).
14. Z. Najmudin, S. Kneip, M. S. Bloom, S. P. D. Mangles, O. Chekhlov, A. E. Dangor, A. Döpp, K. Ertel, S. J. Hawkes, J. Holloway, C. J. Hooker, J. Jiang, N. C. Lopes, H. Nakamura, P. A. Norreys, P. P. Rajeev, C. Russo, M. J. V. Streeter, D. R. Symes, and M. Wing, "Compact laser accelerators for x-ray phase-contrast imaging," Philos. Trans. Ser. A **372**, 20130032 (2014).
15. T. Tajima and J. Dawson, "Laser electron accelerator," Phys. Rev. Lett. **43**, 267–270 (1979).
16. T. Tajima and J. Dawson, "Ultrahigh gradient particle acceleration by intense laser-driven plasma density waves," Nature **311**, 525–529 (1984).
17. S. P. D. Mangles, C. D. Murphy, Z. Najmudin, A. G. R. Thomas, J. L. Collier, A. E. Dangor, E. J. Divall, P. S. Foster, J. G. Gallacher, C. J. Hooker, D. A. Jaroszynski, A. J. Langley, W. B. Mori, P. A. Norreys, F. S. Tsung, R. Viskup, B. R. Walton, and K. Krushelnick, "Monoenergetic beams of relativistic electrons from intense laser - plasma interactions," Nature **431**, 535–538 (2004).
18. J. Faure, Y. Glinec, A. Pukhov, S. Kiselev, S. Gordienko, E. Lefebvre, J.-P. Rousseau, F. Burgy, and V. Malka, "A laser-plasma accelerator producing monoenergetic electron beams," Nature **431**, 541–544 (2004).

Research Article | Vol. 26, No. 26 | 24 Dec 2018 | OPTICS EXPRESS 33940

Optics EXPRESS

19. C. G. R. Geddes, C. Toth, J. van Tilborg, E. Esarey, C. B. Schroeder, D. Bruhwiler, C. Nieter, J. Cary, and W. P. Leemans, "High-quality electron beams from a laser wakefield accelerator using plasma-channel guiding," Nature **431**, 538–541 (2004).
20. M. Burza, A. Gonoskov, K. Svensson, F. Wojda, A. Persson, M. Hansson, G. Genoud, M. Marklund, C.-G. Wahlström, and O. Lundh, "Laser wakefield acceleration using wire produced double density ramps," Phys. Rev. Accel. Beams **16**, 011301 (2013).
21. M. Hansson, *Controlled Trapping in Laser Wakefield Accelerators* (Lund University, 2016).
22. S. Corde, K. Ta Phuoc, G. Lambert, R. Fitour, V. Malka, and A. Rousse, "Femtosecond x-rays from laser-plasma accelerators," Rev. Mod. Phys. **85**, 1–48 (2013).
23. D. Elder, A. Gurewitsch, R. Langmuir, and H. Pollock, "Radiation from electrons in a synchrotron," Phys. Rev. **71**, 829–830 (1947).
24. A. Rousse, K. Ta Phuoc, R. Shah, A. Pukhov, E. Lefebvre, V. Malka, S. Kiselev, F. Burgy, J.-P. Rousseau, D. Umstadter, and D. Hulin, "Production of a keV x-ray beam from synchrotron radiation in relativistic laser-plasma interaction," Phys. Rev. Lett. **93**, 135005 (2004).
25. S. Corde, K. Ta Phuoc, R. Fitour, J. Faure, A. Tafzi, J. P. Goddet, V. Malka, and A. Rousse, "Controlled betatron x-ray radiation from tunable optically injected electrons," Phys. Rev. Lett. **107**, 255003 (2011).
26. A. Modena, Z. Najmudin, A. Dangor, C. E. Clayton, K. A. Marsh, C. Joshi, V. Malka, C. Darrow, C. Danson, D. Neely, and F. N. Walsh, "Electron acceleration from the breaking of relativistic plasma waves," Nature **377**, 606–608 (1995).
27. C. McGuffey, A. G. R. Thomas, W. Schumaker, T. Matsuoka, V. Chvykov, F. J. Dollar, G. Kalintchenko, V. Yanovsky, A. Maksimchuk, K. Krushelnick, V. Y. Bychenkov, I. V. Glazyrin, and A. V. Karpeev, "Ionization induced trapping in a laser wakefield accelerator," Phys. Rev. Lett. **104**, 025004 (2010).
28. A. Döpp, B. Mahieu, A. Lifschitz, C. Thaury, A. Doche, E. Guillaume, G. Grittani, O. Lundh, M. Hansson, J. Gautier, M. Kozlova, J. P. Goddet, P. Rousseau, A. Tafzi, V. Malka, A. Rousse, S. Corde, and K. Ta Phuoc, "Stable femtosecond x-rays with tunable polarization from a laser-driven accelerator," Light. Sci. & Appl. **6**, e17086 (2017).
29. F. G. Desforges, B. S. Paradkar, M. Hansson, J. Ju, L. Senje, T. L. Audet, A. Persson, S. Dobosz-Dufrénoy, O. Lundh, G. Maynard, P. Monot, J.-L. Vay, C.-G. Wahlström, and B. Cros, "Dynamics of ionization-induced electron injection in the high density regime of laser wakefield acceleration," Phys. Plasmas **21**, 120703 (2014).
30. M. Hansson, T. L. Audet, H. Ekerfelt, B. Aurand, I. Gallardo González, F. G. Desforges, X. Davoine, A. Maitrallain, S. Reymond, P. Monot, A. Persson, S. Dobosz Dufrénoy, C.-G. Wahlström, B. Cros, and O. Lundh, "Localization of ionization-induced trapping in a laser wakefield accelerator using a density down-ramp," Plasma Phys. Control. Fusion **58**, 055009 (2016).
31. I. Gallardo González, H. Ekerfelt, M. Hansson, T. L. Audet, B. Aurand, F. G. Desforges, S. Dobosz Dufrénoy, A. Persson, X. Davoine, C.-G. Wahlström, B. Cros, and O. Lundh, "Effects of the dopant concentration in laser wakefield and direct laser acceleration of electrons," New J. Phys. **20**, 053011 (2018).
32. G. Sun, E. Ott, Y. C. Lee, and P. Guzdar, "Self-focusing of short intense pulses in plasmas," The Phys. Fluids **30**, 526–532 (1987).
33. P. Sprangle, C.-M. Tang, and E. Esarey, "Relativistic self-focusing of short-pulse radiation beams in plasmas," IEEE Trans. Plasma Sci. **15**, 145–153 (1987).
34. A. Buck, K. Zeil, A. Popp, K. Schmid, A. Jochmann, S. D. Kraft, B. Hidding, T. Kudyakov, C. M. S. Sears, L. Veisz, S. Karsch, J. Pawelke, R. Sauerbrey, T. Cowan, F. Krausz, and U. Schramm, "Absolute charge calibration of scintillating screens for relativistic electron detection," Rev. Sci. Instrum. **81**, 033301 (2010).
35. P. Kirkpatrick, "Theory and use of ross filters. II," Rev. Sci. Instrum. **15**, 223 (1994).
36. P. Ross, "A new method of spectroscopy for faint x-radiations," J. Opt. Soc. Am. **16**, 433–437 (1928).
37. I. N. Tilikin, T. A. Shelkovenko, S. A. Pikuz, and D. A. Hammer, "Determination of the size of a radiation source by the method of calculation of diffraction patterns," Opt. Spectrosc. **115**, 128–136 (2013).
38. A. Burvall, U. Lundström, P. A. C. Takman, D. H. Larsson, and H. M. Hertz, "Phase retrieval in x-ray phase-contrast imaging suitable for tomography," Opt. Express **19**, 10359 (2011).
39. D. Paganin, S. C. Mayo, T. E. Gureyev, P. R. Miller, and S. W. Wilkins, "Simultaneous phase and amplitude extraction from a single defocused image of a homogeneous object," J. Microsc. **206**, 33–40 (2002).
40. K. Svendsen, *In-line Phase Contrast Tomography using Betatron X-rays Produced by a Laser-Plasma Accelerator* (Lund University, 2017).
41. 3DSlicer, "A multi-platform, free and open source software package for visualization and medical image computing," https://www.slicer.org.
42. A. Fedorov, R. Beichel, J. Kalpathy-Cramer, J. Finet, J.-C. Fillion-Robin, S. Pujol, and C. Bauer, "3d slicer as an image computing platform for the quantitative imaging network," Magn. resonance imaging **30**, 1323–1341 (2012).
43. S. Pieper, B. Lorensen, W. Schroeder, and R. Kikinis, "The NA-MIC kit: ITK, VTK, pipelines, grids and 3D slicer as an open platform for the medical image computing community," Proc. 3rd IEEE Int. Symp. on Biomed. Imaging: From Nano to Macro **1**, 698–701 (2006).
44. S. Pieper, M. Halle, and R. Kikinis, "3d slicer," Proc. 1st IEEE Int. Symp. on Biomed. Imaging: From Nano to Macro **1**, 632–635 (2004).
45. D. Gering, A. Nabavi, R. Kikinis, N. Hata, L. O'Donnell, W. Grimson, F. Jolesz, P. Black, and W. W. III, "An integrated visualization system for surgical planning and guidance using image fusion and an open MR," J. Magn. Reson. Imaging **13**, 967–975 (2001).

Research Article | Vol. 26, No. 26 | 24 Dec 2018 | OPTICS EXPRESS 33941

Optics EXPRESS

46. D. Gering, A. Nabavi, R. Kikinis, W. Grimson, N. Hata, P. Everett, F. Jolesz, and W. W. III, "An integrated visualization system for surgical planning and guidance using image fusion and interventional imaging," Int Conf Med Image Comput. Comput. Assist. Interv. **2**, 809–819 (1999).
47. S. P. D. Mangles, A. G. R. Thomas, M. C. Kaluza, O. Lundh, F. Lindau, A. Persson, F. S. Tsung, Z. Najmudin, W. B. Mori, C.-G. Wahlström, and K. Krushelnick, "Laser-wakefield acceleration of monoenergetic electron beams in the first plasma-wave period," Phys. Rev. Lett. **96**, 215001 (2006).
48. J. L. Shaw, N. Lemos, L. D. Amorim, N. Vafaei-Najafabadi, K. A. Marsh, F. S. Tsung, W. B. Mori, and C. Joshi, "Role of direct laser acceleration of electrons in a laser wakefield accelerator with ionization injection," Phys. Rev. Lett. **118**, 064801 (2017).

Paper IX

Laser-wakefield accelerators for high-resolution X-ray imaging of complex microstructures

A. E. Hussein, N. Senabulya, Y. Ma, M. J. V. Streeter, B. Kettle, S. J. D. Dann, F. Albert, N. Bourgeois, S. Cipiccia, J. M. Cole, O. Finlay, E. Gerstmayr, I. Gallardo González, A. Higginbotham, D. A. Jaroszynski, K. Falk, K. Krushelnick, N. Lemos, N. C. Lopes, C. Lumsdon, O. Lundh, S. P. D. Mangles, Z. Najmudin, P. P. Rajeev, C. M. Schlepütz, M. Shahzad, M. Šmíd, R. Spesyvtsev, D. R. Symes, G. Vieux, L. Willingale, J. C. Wood, A. J. Shahani and A. G. R. Thomas.

Sci. Rep. **9**, 3249 (2018).

www.nature.com/scientificreports

OPEN

Laser-wakefield accelerators for high-resolution X-ray imaging of complex microstructures

ed: 3 December 2018
ed: 29 January 2019
ed online: 01 March 2019

A. E. Hussein[1], N. Senabulya[2], Y. Ma[1,3,4], M. J. V. Streeter[3,4,5], B. Kettle[5], S. J. D. Dann[3,4], F. Albert[6], N. Bourgeois[7], S. Cipiccia[8], J. M. Cole[5], O. Finlay[3,4], E. Gerstmayr[5], I. Gallardo González[9], A. Higginbotham[10], D. A. Jaroszynski[4,11], K. Falk[12], K. Krushelnick[1], N. Lemos[6], N. C. Lopes[5,13], C. Lumsdon[10], O. Lundh[9], S. P. D. Mangles[5], Z. Najmudin[5], P. P. Rajeev[7], C. M. Schlepütz[14], M. Shahzad[4,11], M. Smid[12], R. Spesyvtsev[4,11], D. R. Symes[7], G. Vieux[4,11], L. Willingale[1], J. C. Wood[5], A. J. Shahani[2] & A. G. R. Thomas[1,3,4]

Laser-wakefield accelerators (LWFAs) are high acceleration-gradient plasma-based particle accelerators capable of producing ultra-relativistic electron beams. Within the strong focusing fields of the wakefield, accelerated electrons undergo betatron oscillations, emitting a bright pulse of X-rays with a micrometer-scale source size that may be used for imaging applications. Non-destructive X-ray phase contrast imaging and tomography of heterogeneous materials can provide insight into their processing, structure, and performance. To demonstrate the imaging capability of X-rays from an LWFA we have examined an irregular eutectic in the aluminum-silicon (Al-Si) system. The lamellar spacing of the Al-Si eutectic microstructure is on the order of a few micrometers, thus requiring high spatial resolution. We present comparisons between the sharpness and spatial resolution in phase contrast images of this eutectic alloy obtained *via* X-ray phase contrast imaging at the Swiss Light Source (SLS) synchrotron and X-ray projection microscopy *via* an LWFA source. An upper bound on the resolving power of $2.7 \pm 0.3\ \mu$m of the LWFA source in this experiment was measured. These results indicate that betatron X-rays from laser wakefield acceleration can provide an alternative to conventional synchrotron sources for high resolution imaging of eutectics and, more broadly, complex microstructures.

Laser-wakefield acceleration (LWFA) is a method for producing high-energy electron beams using the accelerating field structure produced in the wake of a high-power, ultrashort pulsed laser propagating through low density plasma. During wakefield acceleration, an electron bunch "surfs" on the electric wave generated by the light pressure of an intense laser pulse[1]. This wave induces a strong longitudinal electric field that remains in phase with the relativistic driver, enabling relativistic electrons to gain significant energy from the accelerating field over long distances. Due to the lack of a breakdown limit in a plasma accelerator, accelerating gradients 1000 times stronger than those produced in conventional sources can be produced[1,2] and the generation of high energy electron beams has been demonstrated experimentally[3–9]. Additionally, in the highly nonlinear regime, electrons undergo betatron oscillations in the strong focusing fields of the wakefield, emitting a bright source of X-rays with a source size as small as one micrometer[10–12]. Betatron X-ray beams produced *via* LWFA have been shown to produce

[1]Center for Ultrafast Optical Science, University of Michigan, Ann Arbor, MI, 48109-2099, USA. [2]Department of Materials Science and Engineering, University of Michigan, Ann Arbor, MI, 48109-2099, USA. [3]Physics Department, Lancaster University, Lancaster, LA1 4YB, UK. [4]The Cockcroft Institute, Keckwick Lane, Daresbury, WA4 4AD, UK. [5]The John Adams Institute for Accelerator Science, Imperial College London, London, SW7 2AZ, UK. [6]Lawrence Livermore National Laboratory, NIF and Photon Sciences, Livermore, CA, 94550, USA. [7]Central Laser Facility, STFC Rutherford Appleton Laboratory, Didcot, OX11 0QX, UK. [8]Diamond Light Source, Harwell Science and Innovation Campus, Fermi Avenue, Didcot, OX11 0DE, UK. [9]Department of Physics, Lund University, P.O. Box 118, S-22100, Lund, Sweden. [10]York Plasma Institute, Department of Physics, University of York, York, YO10 5DD, UK. [11]SUPA, Department of Physics, University of Strathclyde, Glasgow, G4 0NG, UK. [12]ELI Beamline, Institute of Physics of the ASCR, Na Slovance 2, Prague, 182 21, Czech Republic. [13]GoLP/Instituto de Plasmas e Fusão Nuclear, Instituto Superior Técnico, U.L., Lisboa, 1049-001, Portugal. [14]Swiss Light Source, Paul Scherrer Institute, CH-5232, Villigen, Switzerland. Correspondence and requests for materials should be addressed to A.E.H. (email: aehuss@umich.edu)

stable, bright X-ray beams capable of high resolution tomographic imaging[11,13–17]. The resultant beams have a low divergence (on the order of a few milliradians[18]) and ultrashort duration (less than 100 fs[19]), making them useful for a large range of applications across engineering, medicine, homeland security and science[11,12,14–17]. Moreover, the demonstration of micrometer scale, keV betatron X-ray beams using a single laser shot highlights the potential of these sources for imaging of complex objects in real time using high repetition rate laser systems[13].

One exciting application for these novel X-ray sources is as a diagnostic tool for additive manufacturing processes. Laser-aided solidification is an avenue of interest in manufacturing science that requires *in situ* measurements with high spatial and temporal resolution[20,21]. Such is the case for the solidification of eutectics, in which two (or more) solid phases grow simultaneously from a parent liquid phase[22–25]. Once solidified, eutectics act as *in situ* composite materials, providing outstanding mechanical and electrical properties that are not afforded by their constituent phases alone. It is for this reason that lightweight Al-Si alloys comprise over 90% of the total Al parts produced by the United States[26]. *Irregular* eutectics such as Al-Si are composed of one faceted phase (Si) and another non-faceted (Al) phase. Due to the stiffness of the faceted phase, irregular eutectics feature a non-periodic arrangement of lamellae (fine rods or sheets of adjacent material). The interfacial dynamics underlying irregular eutectic solidification (under relatively low cooling rates) has only recently been elucidated through synchrotron-based X-ray microtomography (denoted XRT), using conventional accelerators[27]. In general, the lamellar spacing (between Al and Si phases) can be as fine as 1 μm, thus requiring experimental probes that are capable of delivering high resolution information.

As noted above, synchrotron-based XRT in the micrometer range have been achieved using modern third generation light sources, such as the the beamline for TOmographic Microscopy and Coherent rAdiology experimenTs (TOMCAT) of the Swiss Light Source (SLS) at the Paul Scherrer Institut in Switzerland[28]. The TOMCAT beamline has been employed to produce high-resolution, multimodal X-ray tomographic images using monochromatic sources with energies between 8 and 45 keV, a source size of 127 μm (V) $\times$ 38 μm (H) (Full-Width-Half-Maximum) and a flux of $(0.5-2)\times10^{12}$ photons/sec/mm^2[29]. However, while conventional synchrotron light sources yield high average brightness, they are prohibitively large and expensive, limiting access to these facilities. The 1000 $\times$ stronger accelerating gradients in a LWFA enable miniaturization of the accelerator to a standard laboratory scale, potentially increasing the accessibility of advanced photon sources. And although compact synchotron sources have recently been developed[30], laser-driven sources also have the unique capability to be co-timed to other laser-initiated events. In this way, LWFA sources can be used for so called *pump-probe* experiments of laser-irradiated targets[16,19]. Additionally, while the source size of newest generation conventional beamlines has been reduced to the order of 10–20 μm, the resolution limit for X-ray imaging in a parallel beam geometry on these systems is dependent on the pixel size of the detector and the brightness of the source. Conversely, for a LWFA X-ray source, where the source size has been measured to be on the order of a few micrometers[11,13,15,17], high resolution measurements are obtained using a high geometric magnification, and the resolution requirements of the detector are relaxed (see *Methods*).

In this report, we investigated the potential of laser-based X-ray sources for the imaging of solid density targets. We present a comparison between the image sharpness and resolution of raw projection images of Al-Si alloys obtained *via* conventional synchrotron X-ray phase contrast imaging at the Swiss Light Source (SLS) and X-ray projection microscopy *via* a LWFA. The former experiment was conducted *ex situ* at the TOMCAT beamline of SLS (Paul Scherrer Institut, Switzerland)[28,29] in 2012. In these measurements, the sample was located 20 m from the source and the sample-to-detector distance was set to 11 cm for a monochromatic X-ray energy of 28 keV produced by a broad-band ($\Delta E/E\approx2\%$) W/Si multilayer monochromator, resulting in virtually no geometric magnification in the X-ray regime, i.e. a value of approximately 1. The X-ray radiographic image, which is produced by the absorption and refraction of the X-ray beam within the sample, was converted to visible light using a 100 μm thick LuAG:Ce scintillator. The corresponding visible light image was then optically magnified by a 10x microscope objective onto the imaging chip of a pco.2000 CCD camera with 7.5 μm pixel size, yielding an effective pixel size of 0.75 μm. Individual images were acquired with a 500 ms exposure time.

LWFA experiments were conducted using the Gemini laser at the Science and Technology Facilities Council (STFC), Rutherford Appleton Laboratory (RAL). The 40 fs FWHM laser pulse was focused using an *f*/40 parabolic mirror into a gas cell producing an electron beam. A schematic of the experimental setup at the Gemini laser system is given in Fig. 1(a). 3D printed two-stage gas cells have been shown to improve the stability, divergence and energy spread of LWFA electron beams[31], therefore a two-stage gas cell with a 3 mm first stage for injection and a 2–21 mm variable length second stage was employed in this experiment (see *Methods*). Plasma density was controlled by altering the pressure of the gas supply of each individual stage, and density measurements were made using Stimulated Raman Side Scattering (see *Methods*). The plasma density corresponding to the optimum betatron spectrum was $n_p=(4.1\pm0.45)\times10^{18}$ cm^{-3} in both stages at a length of 15.5 mm. For these densities, electron beams with average peak energies of (1000 ± 150) MeV were produced. Example electron beams are shown in Fig. 1(b), with a superimposed line-out of the spectrum, indicating a quasi-monoenergetic peak and a broad low-energy tail. Further discussion of electron spectra and beam stability is presented in *Methods*. The X-ray beam, which was assumed to be synchrotron-like as shown in Fig. 1(c), contained $1.94\pm1.24\times10^8$ photons above 5 keV, and is estimated to have a source size smaller than 3 μm, as discussed in *Results*. The LWFA X-ray beam has been found in similar experiments to have divergence on the order of a few millirads[15,17,18] and femtosecond duration[16,19]. The electron and X-ray measurements shown in Fig. 1(b,c) were not obtained simultaneously, but were taken at identical experimental conditions. In these experiments, the Al-Si sample was 19.3 cm away from the betatron source and an X-ray CCD camera with pixel size of 13.5 μm and a 100 ms exposure time was located 410 cm behind the sample (see *Methods*). A total of 136 single-shot images were acquired and no reconstructions were applied.

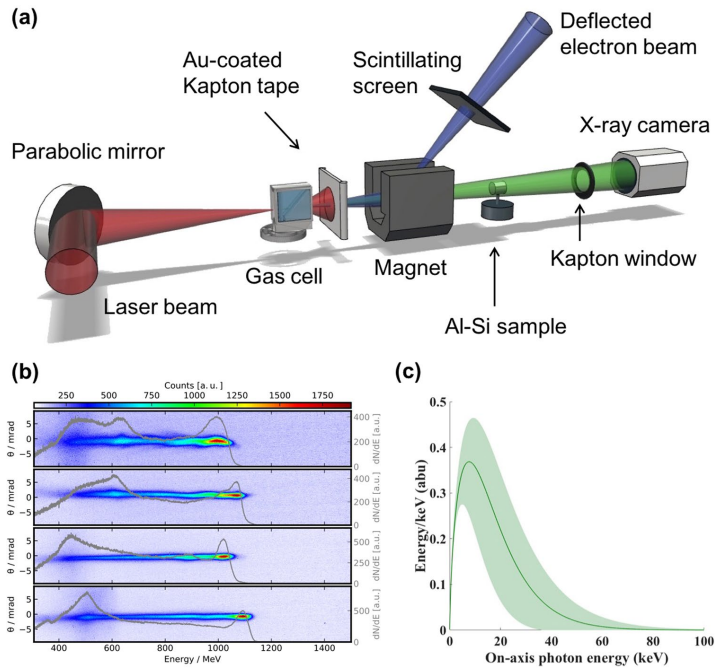

Figure 1. Experimental details for X-ray imaging using a laser wakefield accelerator. (**a**) Experimental layout. High energy electron and X-ray beams were produced by focusing the beam into a two-stage gas cell (see *Methods*). Gold-coated Kapton tape was used to block the laser pulse following the interaction, and was replaced on each shot. A 1 T magnet was used to disperse the electron beam onto a scintillating LANEX screen, from which the electron beam was imaged using a CCD camera. Betatron X-rays passed through the Al-Si sample, which was mounted on a rotation and translation stage at a distance of 19.3 cm from the source. Measurements were made through a kapton vacuum window onto an Andor iKon 2048 × 2048 pixel CCD camera at a distance of 410 cm from the Al-Si sample. (**b**) Samples of typical electron beams with a quasi-monoenergetic peak energy and broad low-energy tails. These measurements were obtained at the same experimental conditions as the phase contrast images and betatron spectrum. Electron beam divergence is plotted on the left axis and a line-out of the electron number density (right axis) is overlaid. (**c**) A best-fit to the betatron X-ray spectrum from an Andor iKon X-ray camera was obtained using a 9-element filter array (see *Methods*). Shaded error bars reflect the uncertainty in the critical energy over many shots due to shot-to-shot fluctuations in electron energy.

Results

Al-Si samples for phase contrast imaging were prepared by the Materials Preparation Center at Ames Laboratory, with a composition of 50 wt% Si for the LWFA experiment and 30 wt% for the SLS experiment. Although the Al-Si sample used in the LWFA experiment had 20% more Si than that used in the SLS experiment, this excess Si is associated not with the Al-Si eutectic but rather the primary (*i.e.*, pro-eutectic) Si phase. The larger mass fraction of this primary Si phase in the Al-Si alloy used in these experiments clouded the field-of-view in the X-ray images, limiting the eutectic — which is last to solidify — to a smaller region of the sample. However, this has little to no bearing on the development of the eutectic microstructure. Both alloys were cast in the exact same manner, and thus have comparable lamellar spacings (see *Methods*). For both experiments, the samples were machined into cylindrical samples of 1 mm thickness.

A microscope image of the 1 mm diameter machined sample is shown in Fig. 2(a) alongside an example image of the Al-Si microstructure obtained using X-rays from a LWFA in Fig. 2(b). The LWFA projection image was obtained using a nearly 22× magnification, and the banded or lamellar structure can be observed in the zoomed-in image, from which a line-out indicates that the LWFA source is successfully resolving features smaller than 3 μm. The resolution of these images is determined by the geometry of the imaging system, as discussed in *Methods*. The observed microstructure is consistent with that predicted for irregular eutectics, in which the lamellar spacing can be as fine as 1 μm (Fig. 2(c)). In this idealized schematic, the faceted phase β (e.g., Si) and the non-faceted phase α (e.g., Al) are shown, growing in a non-periodic manner into the liquid.

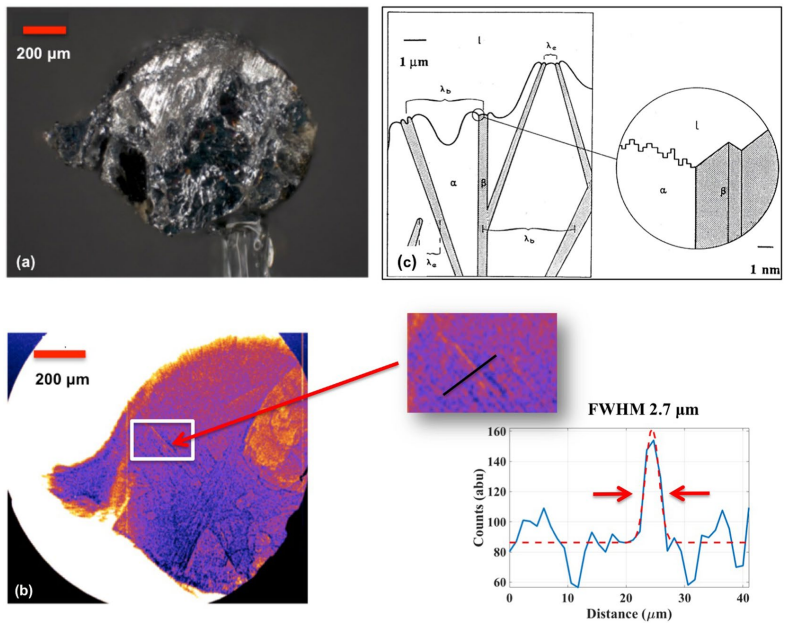

Figure 2. Al-Si sample investigated using a LWFA X-ray source. (**a**) Optical microscope image of the Al-Si cylindrical sample imaged in LWFA experiments. (**b**) X-ray phase contrast image obtained with a LWFA, revealing a lamellar microstructure with an interphase spacing on the order of 1–3 μm. A line-out from a region of interest in the phase contrast image is shown, indicating 2.7 ± 0.3 μm as an upper bound on the resolving power of this method. (**c**) A schematic showing growth of irregular eutectics where β represents the faceted phase (e.g., Si), α is the non-faceted, higher volume fraction phase (e.g., Al), and l is the melt ahead of the interface. The microstructure is deemed irregular due to the difficulty or "stiffness" in changing the growth direction of the faceted phase. The inset shows the atomically diffuse α phase and the defect growth mechanism for the faceted β phase. Retrieved with permission from ref.[73].

The quality of the SLS and LWFA projection images were compared according to two metrics: image sharpness and resolution. Image sharpness is closely related to the fineness of the resolvable details in an image (X-ray projection microscopic images in this case). An algorithm developed by Shaked and Tastl[32] was used to determine the overall sharpness of an image (see *Methods*). Spatial resolution was compared using a Fourier-based criterion[33] on raw projection images obtained *via* a LWFA source and the TOMCAT beamline at the SLS. In this analysis, image quality was computed for the interior regions of phase contrast images to compare areas of highest resolution.

Normalized sharpness estimates given in arbitrary units (1 ± 0.05 a.u. and 0.62 ± 0.05 a.u. for LWFA and SLS projection images, respectively) show that the LWFA projection images are comparable to the sharpness of projection images obtained at SLS (see *Methods*). In addition, Fig. 3 shows the calculation of the spatial resolution, where $|S(k)|^2$ is the spectral power of the detected signal and k_{res} is the maximum spatial frequency when the spectral power is twice the noise level (see *Methods*). The power spectral density (PSD) conveys the strength of the intensity variation in the image pixels as a function of frequency; it indicates the frequencies at which intensity variations are strong and those at which the variations are weak. In other words, the high frequency wavenumber for the PSD in the LWFA image is related to sharper variations in intensity values of the pixels in the image domain. Such variations occur in pixels near to an object edge, e.g., between different lamellae in the Al-Si eutectic.

The PSD shown in Fig. 3(a,b) have been calculated for line profiles in the images taken using the TOMCAT beamline and *via* LWFA, respectively. The PSD profiles, projected onto polar plots, were computed for lines arbitrarily drawn within the projection image at angles ranging from 0° to 90° with the horizon to ensure that the PSD over all pixel directions in the projection images were statistically represented. It can be observed that the LWFA image has a spatial resolution x_{res} which is comparable to the spatial resolution in the SLS image. According to the Wiener-Khintchine theorem[34], the autocorrelation function is the Fourier transform of the power spectral density. Accordingly, Fig. 3(b) shows a slightly higher autocorrelation at long wavelengths as evidenced by a higher k_{res} value of 1.017 ± 0.01 px^{-1} compared to 0.98 ± 0.01 px^{-1} for the SLS image, where LWFA images have been

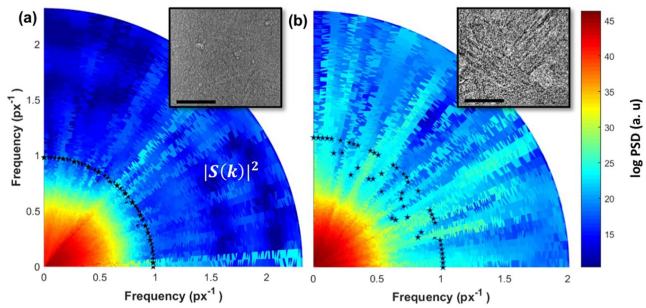

Figure 3. Measurement of the spatial resolution criterion for line profiles oriented from 0° to 90°. The spatial resolution criterion is projected onto polar plots in (**a**) SLS and (**b**) LWFA projection images. Projection images are shown as insets. $|S(k)|^2$ is the spectral power of the detected signal. Raw images were resized to match the dissimilar pixel resolutions for SLS and LWFA images, and PSD analysis was performed on projection images with equalized intensity histograms. For both cases, spatial frequencies are given in units of inverse pixels. The LWFA projection image has a spatial resolution that is comparable to the spatial resolution in the SLS projection image, as evidenced by the close to equal k_{res} values of $1.017 \pm 0.01\,\mathrm{px}^{-1}$ and $0.98 \pm 0.01\,\mathrm{px}^{-1}$ in the LWFA and SLS images, respectively. Stars represent the k_{res} spatial frequency value obtained along an arbitrary line in the projection image. Scale bar measures 70 μm.

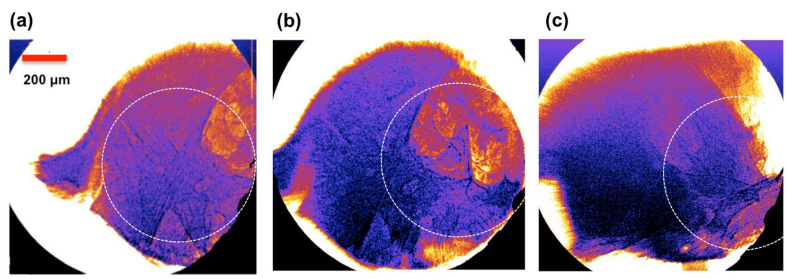

Figure 4. Blurring of LWFA X-ray images due to finite betatron emission length. Three LWFA phase contrast images of the Al-Si sample are shown. In (**a**,**b**) the sample is at the same orientation perpendicular to the laser axis. In image (**b**) the sample has been translated horizontally by approximately 30 μm. In (**c**) the sample has been rotated by 90 degrees about the vertical axis. Regions of sharpest resolution are circled with a dotted line, with a radius of approximately 600 μm at highest focus. In all images, blurring can be observed on the order of a millimeter away from the central point due to the emission length of the betatron source. Highest resolution imaging is obtained along the axis of the electron beam; only this section of the image is used for resolution analysis. Blurring due to the emission length of the X-ray source is not unique to betatron sources, also occurring with conventional synchrotron beams, but is exacerbated by high magnification in cases where the full beam is used for imaging.

rescaled to the effective pixel value for proper comparison. Errors in the measurement of image resolution arise from the absence of normalization by white- and dark-field images for the LWFA projections (Fig. 3(b)), which ultimately lead to intensity inhomogeneities on the detector plane.

Beyond sharpness and resolution, another consideration in the practical application of LWFA for X-ray imaging is blurring due to the non-zero emission length of the betatron source[35]. Betatron emission is highest at the location of high energy electrons, yielding a very small source size on the order of a few μm[11]. However, the emission length of a betatron source has been found to extend a few millimeters along the axis of laser propagation, resulting in blurring in X-ray images and decreased resolution[35,36]. This blurring can be observed in Fig. 4, where the image resolution is highest near the central axis of the X-ray beam (circled) and begins to blur towards the edges of the sample. It has also been found that the betatron emission length tends to increase with increasing plasma length[36], therefore longer plasma lengths are associated with lower resolution away from the central axis of the laser beam. Additionally, instability in beam pointing can result in variation of the location of highest resolution. For a plasma cell of length 15.5 mm, as employed in these experiments, the emission length of the betatron

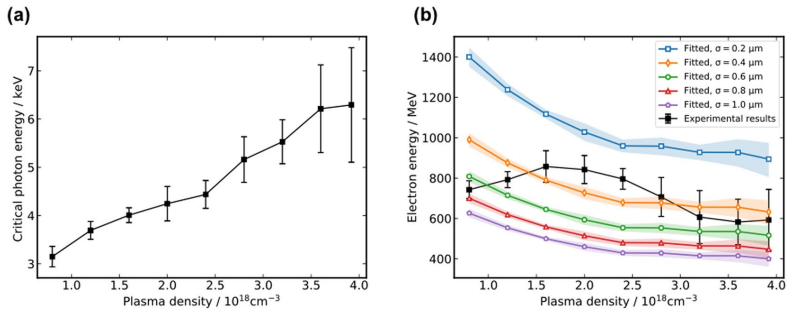

Figure 5. Critical energy of the LWFA betatron source. (**a**) Experimentally measured critical energy of the LWFA X-ray beam as a function of plasma density. (**b**) Theoretical predictions of the maximum electron energy corresponding to experimentally measured critical energy, shown for betatron source sizes of (0.2–1.0) μm along with experimentally measured maximum electron energies in the resultant LWFA beam (black).

source was found to be on the order of 5 mm. Image blurring is also a challenge with conventional synchrotron sources, where the emission length can be much longer (~m), versus ~mm for a LWFA source. However, the large divergence of the LWFA source makes this a concern when the full beam size is used for imaging. It is also important to note that blurring due to the emission length is exacerbated by high magnification. The relationship between plasma length and emission can inform optimization of the LWFA X-ray source for high resolution imaging.

For high contrast imaging of features in dense materials the critical energy of the X-ray beam must be on the order of several keV. In this experiment, the critical energy of the resultant X-ray beam is determined by comparing the transmission through an array of different elemental filters (see *Methods*). The critical energy as a function of plasma density was found to increase with increasing plasma density, as shown in Fig. 5(a), reaching a maximum critical energy of nearly 10 keV. These results indicate that LWFA X-ray sources can provide a tunable X-ray source for phase contrast imaging.

The critical photon energy of a LWFA source is related to the maximum energy of the electron beam, γ, and the plasma density, n_p, by[37–39]:

$$E_c = \frac{3}{2}\hbar\omega_\beta K\gamma^2 = \frac{3}{4}\hbar\frac{e^2}{\varepsilon_0 m_e c}\frac{\sigma}{2}n_p\gamma^2 \quad (1)$$

where $\sigma = 2r_\beta$ is the approximate betatron source size and r_β is the amplitude of betatron oscillations. From equation (1) the electron energy can be retrieved from the measured critical photon energy, the plasma density n_p and an assumed source size σ using $\gamma \propto \sqrt{2E_c/n_p\sigma}$. Figure 5(b) shows the retrieved electron energies with measured plasma densities and fitted source size σ of (0.2–1.0 μm). A plot of the experimentally measured peak electron energy is superimposed on retrieved electron energies, showing best agreement between theory and experimental data for betatron source size on the order of (0.4–1.0) μm.

For comparison with experimental results it is important to note that the critical photon energy in equation (1) is mainly determined by the maximum electron energy achieved during acceleration because of the γ^2 scaling. Therefore, the retrieved electron energies represent the maximum electron energies during the acceleration, which are not necessarily the same as those measured from the experiment. This is because for high plasma density (here, $n_p > 1.2 \times 10^{18}\,\mathrm{cm}^{-3}$) the dephasing length is shorter than the gas cell length and electron beams will experience dephasing. Currently, information about electron dephasing cannot be captured experimentally in a single shot, however novel techniques employing a transverse density gradient may provide single-shot diagnostic information of the temporal evolution of the betatron X-ray spectrum and electron acceleration[40].

Discussion

Thus far, Al-Si eutectics have only been investigated *via* conventional synchrotron-based phase contrast tomography (PCT)[41–43]. PCT enables the study of weakly absorbing samples, as well as materials systems consisting of elements with similar atomic numbers. This is because variations in the real valued refractive index are several orders of magnitude larger than the imaginary component[44,45]. In order to recover the microstructure from projection images obtained *via* PCT, phase-retrieval algorithms are first applied to the projection images[46,47]. Subsequently, a projection algorithm (*e.g.*, *filtered back projection*[48]) is used to reconstruct a three-dimensional (3D) map of the refractive index decrement (i.e., the difference between the sample's index of refraction and that of air). Image segmentation of the PCT reconstructions is crucial for quantitative analysis of interfacial properties, *e.g.*, orientations, velocities, curvatures, and *n*-point statistics[49,50]. However, sharp images taken at high resolution with sufficient contrast, such as those obtained with a LWFA source, can mitigate the challenges associated with low pass characteristics in projection images and in turn ease the data analysis process down-stream[41,51,52],

From the projection images obtained in the LWFA experiment the microstructural details can be measured straightaway and throughout the sample volume owing to the fact that the projection images were reasonably sharp. In particular, the spacing between neighboring Si lamellae was measured to be between 10 and 90 μm. Using the Jackson-Hunt relationships modified for irregular eutectics[22,24,53,54], the average lamellar spacing was correlated with an average growth rate and undercooling, estimated to be 0.35 ± 0.3 μm/s and 0.13 ± 0.03 K, respectively (see *Methods*). The combination of the two solidification parameters gave rise to the eutectic microstructure observed in the LWFA projection images. Additionally, the lamellar morphology as shown in Fig. 3(b), inset, exhibits a flake-like Si phase that is commonly found in irregular eutectics of undoped or unmodified alloys. This morphology is to be fully expected given the high purity of the constituent Al and Si powders, as discussed in *Methods*. The eutectic Si flakes extend laterally by a process known as twin plane re-entrant edge mechanism (TPRE), which was first introduced by Wagner[55] and Hamilton and Seindensticker[56]. Branching events between the Si flakes that are likewise facilitated by twins were also observed[57]. Altogether, these preliminary observations suggest the importance of growth twinning for the continued propagation of the faceted Si phase during solidification. A more conclusive argument for the growth mechanism of undoped and doped alloy samples cannot be made until a 4D (*i.e.*, space- and time-resolved) assessment of the microstructure is performed, which is the focus of future research.

The resolution limits of phase-contrast X-ray imaging experiments are set by the source size and the imaging geometry, which determines the magnification of the system, and the detector pixel size. For synchrotron beamlines, such as TOMCAT, the source size is much bigger than the desired resolution, but the distance from the source to the sample is typically much larger than the distance from the sample to the detector, effectively resulting in a large demagnification factor of the source size. Therefore, the effective pixel size of the detector (which includes the optical magnification provided by the visible light microscope coupling the scintillator to the detector's imaging chip) is the limiting factor for high-resolution imaging, and needs to be minimized for the highest possible resolution. Conversely, for LWFA sources, where the source size is much smaller than the pixel size of the detector, the high magnification in the X-ray imaging geometry reduces the resolution requirements of the detector. For high resolution phase contrast imaging, the conditions for detection of bright and dark phase contrast fringes are set by the detector resolution, and the bandwidth and size of the source[45].

A comparison of experimental parameters used in the SLS and LWFA experiments presented here indicates that these sources have comparable geometric resolution limits and both satisfy the criteria for fringe detection (see *Methods*). However, our analysis of the projection images shown in Fig. 3 indicates that the LWFA source has slightly greater sharpness and spatial resolution for these conditions and is able to resolve micrometer-scale lamellar features. The reason for resolution loss in the SLS projection image is likely due to vibrations in the experimental setup. At the time of the experiments, the relative sample to detector position could vibrate at an amplitude of up to 0.5–1 μm consequently resulting in a blurring of the projection images over the 500 milliseconds exposure time. Conversely, although LWFA experiments are prone to similar instabilities, the femtosecond timescale of the betatron source enables ultrafast imaging. Therefore, single-shot LWFA images are not subject to motion blur. In this way, the visibility of small-scale features such as lamellae is enhanced. It is also worth noting that the conditions for detecting phase contrast fringes for the LWFA experiments set an upper bound of 1 μm on the source size, indicating that betatron sources may be much smaller than previously noted.

Our results indicate that betatron X-rays from LWFA can be competitive with conventional synchrotron sources for the characterization of eutectic alloys and solid density materials. This opens the door to high-resolution materials diagnostics using laser-based sources, without needing to visit a synchrotron facility. Indeed, projection images of the Al-Si sample obtained using LWFA betatron X-rays were of comparable sharpness and spatial resolution to projection images obtained at SLS. Fine details of the lamellar microstructure were clearly resolved in LWFA projection images (Fig. 3(b) inset), indicating an upper bound of 2.7 μm on the resolving power of this method. Furthermore, the phase contrast spatial resolution criteria indicate that the LWFA source size may be much smaller than a micrometer, which is corroborated by the theoretical scaling of the betatron energy with plasma density in Fig. 5(b) in which the retrieved electron energy was most closely fit assuming betatron source sizes on the order of (0.4–1.0) μm. However, it is important to note that the enhanced spatial resolution reported in this paper is specific to the experimental conditions of these experiments, and that neither of the two experiments was optimized to obtain the ultimate spatial resolution. The ultrashort exposure time of betatron sources may also provide improved spatial resolution by enabling imaging on a timescale shorter than the frequency of vibrations in experimental setups.

As mentioned in the *Introduction*, one area in which we can demonstrate significant near-term impact of these LWFA sources is through the use of betatron X-rays as a diagnostic tool for real-time monitoring of additive manufacturing. In recent years, additive manufacturing has seen tremendous growth due to developments in processes and materials, as well as a greater understanding of the underlying design principles. It already has huge societal impacts through the ability to produce cheaper and customizable products, such as artificial hips and lightweight aircraft components[58–60]. As-solidified parts have traditionally been characterized by examining their microstructures following manufacturing, however such *post mortem* approaches lack the capability of tracking the interfacial dynamics during the solidification process. In fact, it is well known that quenching distorts the morphology of the solid-liquid interfaces, and thus the micrographs collected following manufacturing do not depict those same interfaces that are present during laser-aided processing. Moreover, the US National Institute of Science and Technology's "Measurement Science Roadmap for Metal-Based Additive Manufacturing" identifies *in situ* process monitoring and metrology *as a key barrier to additive manufacturing implementation*[61]. To address this confounding issue, a few investigators have recently employed synchrotron-based X-ray microtomography to track the microstructural evolution as a function of time[27,62]. High-speed synchrotron hard X-ray imaging on the nanosecond timescale has recently been demonstrated[20], however LWFA sources offer temporal resolution on the order of femtoseconds[16,63,64]. The realization of high-repetition rate laser drivers for LWFA[65–67] could enable

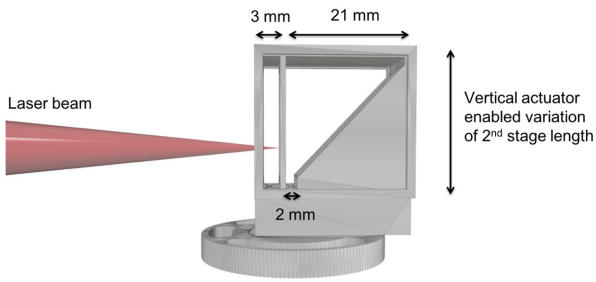

Figure 6. CAD model of the variable length two-stage gas cell used in LWFA experiments. A two-stage gas cell with a 3 mm first stage for ionization injection and a variable length second stage was used. A 45° wall in the second stage enabled variation of the length of the second stage (between 2 to 21 mm) using linear motor controls to vary the vertical position of the cell.

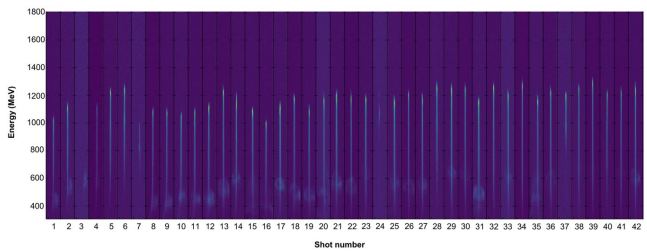

Figure 7. Electron beam profiles. Electron spectra obtained for 42 consecutive laser shots at identical experimental conditions.

dynamic measurements on an ultra-short timescale. Therefore, the micrometer-scale spatial resolution demonstrated in this paper, combined with femtosecond temporal resolution and high repetition capabilities, indicate that LWFA sources could be used for high-resolution dynamics measurements on an ultra-short timescale.

Methods

Laser. The LWFA experiments were carried out on the Gemini laser facility at the Science and Technology Facilities Council (STFC), Rutherford Appleton Lab (RAL), UK. The pulse for laser wakefield acceleration had a FWHM pulse duration of 40 ± 3 fs, a central wavelength of 800 nm, and was linearly polarized. The laser pulse with energy of 16.4 ± 0.6 J before the compressor, yielding approximately 8.4 ± 0.6 J on target. The pulse was focused by an $f/40$ off-axis parabolic mirror with a focal length of 6 m to a $1/e^2$ focal spot of 36.3 ± 0.8 μm, yielding a peak intensity of 1.0×10^{19} W/cm^2 ($a_0 = 2.0$) within the FWHM of the focal spot.

Gas target. The laser was focused into a 3D printed two-stage length gas cell, with mixed gas (2% nitrogen and 98% helium) in the first stage and helium gas in the second stage. The length of the first stage in the gas cell, used for ionization injection, was 3 mm, and the length of the second stage was varied between 2 and 21 mm using linear actuators to change the position of the laser relative to a 45° exit wall, as shown in Fig. 6. The thickness of the entrance and stage divider walls were 1 mm, and the exit wall was 2 mm thick. The plasma density was controlled by altering the backing pressure of the gas supply. Plasma density measurements were made using calibrated Stimulated Raman Side Scattering measurements[68] and yielded $n_p = (4.1 \pm 0.45) \times 10^{18}$ cm^{-3} in both stages at a cell length of 15.5 mm.

Electron and X-ray beam characterization. A 1 T magnet was used to disperse the electron beam onto a scintillating LANEX screen, from which the electron beam was imaged using a CCD camera. Particle tracing was performed with the measured magnet field map to calculate the electron energy as a function of the position on the lanex screen. A series of electron spectra from consecutive shots at identical experimental conditions is presented in Fig. 7, indicating good shot-to-shot reproducibility of accelerated beams at a plasma density of $n_p = (4.1 \pm 0.45) \times 10^{18}$ cm^{-3}. The average peak energy of the beams shown in Fig. 7 was (1200 ± 50) MeV, but for all spectra at these conditions the average peak energy was (1000 ± 150) MeV. Low energy features on the beams are likely untrapped energetic electrons, which have been found to form ring structures[69,70].

Material	Nb	Mo	Cu	Zn	Fe	Co	Sc	Ti	Pb
Thickness (μm)	24.5	20.0	9.2	10.0	5.6	5.4	26.7	17.3	503.8

Table 1. Thickness of filter array elements.

The X-ray beam was collected by an on-axis X-ray camera (model: Andor iKon-L SY DW936 BR-DD) with a 250 μm beryllium filter, placed 429.3 cm away from the source. In front of the X-ray camera a 9-element filter array composed of various materials with different K-edges was placed to characterize the X-ray spectral distribution[11,15]. The thickness of each filter element can be found in Table 1. The signal counts on camera can be estimated as[71]:

$$N_i = \eta \int_{E_{min}}^{E_{max}} S(E, E_{crit}) Q(E) T_i(E) dE \tag{2}$$

where η is a constant coefficient, $S(E, E_{crit}) \sim (E/2E_{crit})^2 K^2_{2/3}(E/2E_{crit})$ is the on-axis synchrotron spectrum with a critical energy of E_{crit}, $Q(E)$ is the quantum efficiency of the camera, T_i is the overall transmission of the filter i with the consideration of attenuation of other materials in the beam path. Fitting equation (2) with the measured signal counts on the camera for all the filters gives a best fitted E_{crit}.

It is important to note that characterizations of the electron and X-ray beams were not obtained from a single experimental day, but were compiled using data from experimental runs at the same conditions as the measurements that yielded the phase contrast images of complex microstructures presented in this paper. Simultaneous measurements of the electron beam with phase contrast imaging was not possible in these experiments due to the necessity of an additional "kicker" magnet to protect the sample by further deflecting the electron beam.

Image sharpness and resolution. The SLS projection image was normalized according to the standard procedure for synchotron experiments using dark images and flat-field corrections as follows:

$$\text{Normalized SLS image} = \frac{(\text{(Raw SLS projection image)} - \text{(average of 21 dark shots)})}{(\text{(average of 51 flat shots)} - \text{(average of 21 dark shots)})} \tag{3}$$

No such normalizations were applied to LWFA images.

An algorithm developed by Shaked and Tastl[32] was used to determine the overall sharpness of an image. Here, their global single parameter sharpness model is used, implemented as the ratio between the output energy of an ideal high pass filter and an ideal band pass filter[32], and described by

$$\text{Sharpness} = \frac{\int_{\bar{\xi} \in H} |M(\bar{\xi})|^2 d\bar{\xi}}{\int_{\bar{\xi} \in B} |M(\bar{\xi})|^2 d\bar{\xi}} \tag{4}$$

where the image is indicated by $m(x, y)$ and the Fourier transform of the image by $F(m) = M(\xi_x, \xi_y)$, the Cartesian frequency coordinates are defined as $\bar{\xi} = (\xi_x, \xi_y)$, and H and B are the high and low-band pass frequency ranges, respectively. The images were initially resized to match the dissimilar pixel resolutions (0.74 μm and 0.61 μm for SLS and LWFA experiments, respectively), and the intensity histogram in each image was scaled to lie within the same intensity range. Subsequently, a 2D high pass filter and 2D band pass filter were applied to the 2D Fourier transform of each image matrix and the image sharpness was calculated according to equation (4).

A Fourier-based spatial resolution criterion[33] was used on projection images obtained *via* a laser-wakefield accelerator system and the TOMCAT beamline at the Swiss Light Source. The power spectral density (PSD) profiles of lines arbitrarily drawn within the projection image at angles ranging from 0° to 90° with the horizon are computed. This was done to ensure that the power spectral density over all pixel directions in the projection images were statistically represented. The PSD values can then be projected onto polar plots to reveal the power spectral distribution at varying angular positions within the image. The PSD converges to a value defined as the "noise baseline" obtained in our calculations by taking the mean of the last fifty (50) power spectral density elements in the array of PSDs. According to the criterion put forward by ref.[33], spatial resolution is computed by taking twice the value of the PSD at the noise baseline, and matching this value to the corresponding maximum spatial frequency, k_{res}[33]. The spatial resolution x_{res} is related to the wavenumber k_{res} by:

$$x_{res} = \frac{2\pi}{k_{res}} \tag{5}$$

Resolution limits. The resolution in a lens-less X-ray image setup is determined by the imaging geometry and the detector, as shown in Fig. 8. For a source of size s_o at a distance of x_1 from an object, O, an image is formed at the detector, D. The distance from the object to the detector is x_2. In this configuration there are two limitations on the resolution dictated by source size and the detector resolution, both of which depend on the magnification of the system.

The geometric magnification of the system is related to the distances between the source and the object and the object and the detector using similar right angle triangles: $M = D/O = (x_1 + x_2)/x_1$. The transverse projection of a point in the object onto the detector determines the source-size limited resolution, $S_r = s_o x_2/x_1$. At the object plane, the resolution limit of the source is given by $S_r/M = s_o x_2/(x_1 + x_2)$. The resolution limit of the detector is set

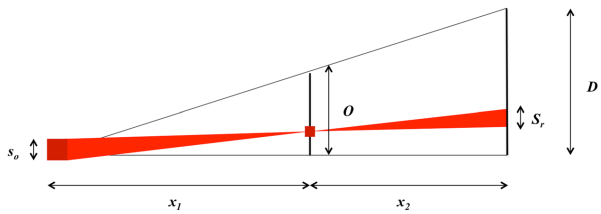

Figure 8. Geometric layout of a X-ray illumination setup without optics. The distance from the source, s_o to the object, O, is x_1, and the distance from the object to the detector, D, is x_2.

	SLS	LWFA
Source size, FWHM (s_0)	127 μm (H) × 38 μm (V)	<2.7 μm (1 μm assumed)
Detector pixel size (p)	0.75 μm	13.5 μm
Source to sample (x_1)	2000 cm	19.3 cm
Sample to detector (x_2)	11 cm	410 cm
Magnification (M)	≃1.01	22.2
Source size limited resolution at the object plane (S_r/M)	0.69 μm × 0.21 μm	0.96 μm
Detector resolution limit (p/M)	0.74 μm	0.61 μm
Total geometric resolution (r)	1.0 μm × 0.76 μm	1.1 μm
Phase contrast detector limit (z)	2.2 μm	21 μm
Critical energy (E_c)	28 keV	11.2 keV
Wavelength (λ)	4.4×10^{-11} m	1.1×10^{-10} m
Phase contrast source size limit (y)	≪400 μm	≪1 μm

Table 2. Comparison of resolution limits in X-ray imaging between the Swiss Light Source (SLS) and LWFA X-ray sources generated using the Gemini Laser at the Rutherford Appleton Lab (RAL). Errors on all measurements are approximately 10%.

by the pixel size, p, and therefore the lower bound on detector resolution is $D_r = p/M = px_1/(x_1 + x_2)$. The total resolution, r, can be considered as the 2-norm of these limits[72]:

$$r = \left(\left(\frac{s_o x_2}{x_1 + x_2} \right)^2 + \left(\frac{p x_1}{x_1 + x_2} \right)^2 \right)^{1/2} \tag{6}$$

The conditions for detecting fringes due to phase contrast imaging are set by the detector resolution, the wavelength bandwidth and the source size[45]. The X-ray detector must have sufficient resolution to resolve separate fringes, where the fringe spacing is given by $z \simeq \sqrt{x_2 \lambda}$ where λ is the wavelength of the critical energy of the source, given in Table 2. Using the values in Table 2, it is clear that this condition is satisfied in both the SLS and LWFA experiments. The condition on the longitudinal coherence of the source is given by $\Delta\lambda/\lambda \ll 2$. This conditions is rather weak and therefore can be assumed to be automatically satisfied for both sources[45].

The final condition on the resolution of phase-contrast imaging is set by the lateral coherence of the source, or the source size. A finite source size can be considered as a pair of point sources, separated by a finite distance, y. These two sources will each produce fringes at the detector. The shift between these fringes can result in blurring and decreased resolution. The limit on the source size for resolving individual fringes is given by $y \ll x_1\sqrt{\lambda/x_2}$. The parameters above are tabulated for the SLS and the LWFA generated X-ray source in Table 2.

Materials. The Al-Si targets for phase contrast imaging were prepared by the Materials Preparation Center at Ames Laboratory (Ames, IA, USA). High-purity powders (99.99% Al and 99.9999% Si) were prepared by melting three times in a low-pressure argon (Ar) atmosphere to mix and degas the melt. In this way, castings in the shape of buttons were produced with a composition of 50 wt% Si for the Rutherford Appleton Laboratory (RAL) experiment and 30 wt% for the Swiss Light Source (SLS) experiment. The as-cast buttons were machined into cylindrical samples of 1 mm diameter using Electrical Discharge Machining (EDM).

Lamellar spacing, growth rate, and undercooling. In measuring the growth rate and undercooling based on the interflake lamellar spacing, the following relationships based on the modified Jackson – Hunt eutectic theory[24,53,54] were employed:

$$\lambda^2 V = K_1 \text{ and } \Delta T = K_2 V^{0.53} \tag{7}$$

where $K_1 = 780.04$ and $K_2 = 0.24$. To solve for the growth rate, V, and undercooling, ΔT, the lamellar spacings λ were measured from the LWFA projection images as input. Values for λ ranged from approximately $10 \pm 0.5\,\mu$m to $90 \pm 0.5\,\mu$m. Errors in the measurement of the lamellar spacings arise due to the fact that only *projected* spacings can be measured in the projection images and may not represent the *true* spacing between lamellae, depending on whether the lamellar are tilted with respect to the plane perpendicular to the X-ray beam. Consequently, the growth rate was found to vary between $0.1 \pm 0.3\,\mu$m/s to $1.2 \pm 0.3\,\mu$m/s while the undercooling was found to vary between 0.065 ± 0.03 K to 0.25 ± 0.03 K. It is anticipated that a 3D microstructural analysis *via* phase contrast X-ray tomography in the laser wakefield accelerator setup could aid in the refinement of calculations of the lamellae spacing, growth rate, and undercooling and further enhance our understanding of the detailed morphology and topology of the Al-Si eutectic microstructure and other related alloys.

Data Availability

The authors confirm that all of the data used in this study are available without restriction. Data can be obtained by contacting aehuss@umich.edu.

References

1. Tajima, T. & Dawson, J. M. Laser electron accelerator. *Physical Review Letters* **43**, 215004 (1979).
2. Esarey, E., Schroeder, C. B. & Leemans, W. P. Physics of laser-driven plasma-based electron accelerators. *Reviews of Modern Physics* **81**, 1229–1285 (2009).
3. Modena, A. *et al*. Electron acceleration from the breaking of relativistic plasma waves. *Nature* **377**, 606 (1995).
4. Malka, V. *et al*. Electron acceleration by a wake field forced by an intense ultrashort laser pulse. *Science* **298**, 1596–1600 (2002).
5. Mangles, S. P. D. *et al*. Monoenergetic beams of relativistic electrons from intense laser-plasma interactions. *Nature* **431**, 535–538 (2004).
6. Faure, J. *et al*. A laser-plasma accelerator producing monoenergic electron beams. *Nature* **431**, 541–544 (2004).
7. Geddes, C. G. R. *et al*. High-quality electron beams from a laser wakefield accelerator using plasma-channel guiding. *Nature* **431**, 538–541 (2004).
8. Leemans, W. *et al*. Gev electron beams froma centimetre-scale accelerator. *Nature Physics* **2**, 696–699 (2006).
9. Wang, X. *et al*. Quasi-monoenergetic laser-plasma acceleration of electrons to 2 gev. *Nature Communications* **4** (2013).
10. Rousse, A. *et al*. Production of a keV X-Ray beam from synchrotron radiation in relativistic laser-plasma interaction. *Physical Review Letters* **93**, 135005 (2004).
11. Kneip, S. *et al*. Bright spatially coherent synchrotron X-rays from a table-top source. *Nature Physics* **6**, 980–983 (2010).
12. Albert, F. & Thomas, A. G. R. Applications of laser wakefield accelerator-based light sources. *Plasma Phys. Control. Fusion* **58** (2016).
13. Fourmaux, S. *et al*. Single shot phase contrast imaging using laser-produced betatron x-ray beams. *Optics Letters* **36**, 2426–2428 (2011).
14. Wenz, J. *et al*. Quantitative x-ray phase-contrast microtomography from a compact laser-driven betatron source. *Nature Communications* **6**, 7568 (2015).
15. Cole, J. *et al*. Laser-wakefield accelerators as hard x-ray sources for 3D medical imaging of human bone. *Scientific Reports* **5** (2015).
16. Wood, J. *et al*. Ultrafast imaging of laser driven shock waves using betatron x-rays from a laser wakefield accelerator. *Scientific Reports* **8**, 11010 (2018).
17. Cole, J. M. *et al*. High-resolution μCT of a mouse embryo using a compact laser-driven X-ray betatron source. *Proceedings of the National Academy of Sciences* **201802314** (2018).
18. Albert, F. *et al*. Angular dependence of betatron x-ray spectra from a laser-wakefield accelerator. *Physical Review Letters* **111**, 235004 (2013).
19. Mahieu, B. *et al*. Probing warm dense matter using femtosecond x-ray absorption spectroscopy with a laser-produced betatron source. *Nature Communications* **9**, 3276 (2018).
20. Zhao, C. *et al*. Real-time monitoring of laser powder bed fusion process using high-speed X-ray imaging and diffraction. *Scientific Reports* **7**, 3602 (2017).
21. Leung, C. L. A. *et al*. *In situ* X-ray imaging of defect and molten pool dynamics in laser additive manufacturing. *Nature Communications* **9**, 1–9 (2018).
22. Jackson, K. & Hunt, J. D. Lamellae and rod eutectic growth. *Trans. Met. Soc. AIME* **236**, 1129–1142 (1966).
23. Jackson, K. & Hunt, J. Lamellar and Rod Eutectic Growth. In *Dynamics of Curved Fronts*, vol. 236, 363–376 (1988).
24. Magnin, P. & Trivedi, R. Eutectic growth: a modification of the Jackson-Hunt theory. *Acta Metallurgica* **39**, 453 (1991).
25. Kang, J. L., Xu, W., Wei, X. X., Ferry, M. & Li, J. F. Solidification behavior of Co-Sn eutectic alloy with Nb addition. *Journal of Alloys and Compounds* **695**, 1498–1504 (2017).
26. Davis, J. R. *Aluminum and aluminum alloys* (ASM international, 1993).
27. Shahani, A. J., Xiao, X. & Voorhees, P. W. The mechanism of eutectic growth in highly anisotropic materials. *Nature Communications* **7**, 1–7 (2016).
28. Stampanoni, M. *et al*. Trends in synchrotron-based tomographic imaging: the sls experience. *Proc. of SPIE* **6318** (2006).
29. Stampanoni, M. *et al*. Hierarchical, multimodal tomographic X-ray imaging at a superbend. *Developments in X-Ray Tomography Vi* **7078**, 1–11 (2008).
30. Eggl, E. *et al*. The munich compact light source: initial performance measures. *Journal of Synchrotron Radiation* **23**, 1137–1142 (2016).
31. Vargas, M. *et al*. Improvements to laser wakefield accelerated electron beam stability, divergence, and energy spread using three-dimensional printed two-stage gas cell targets. *Applied Physics Letters* **104** (2014).
32. Shaked, D. & Tastl, I. Sharpness measure: Towards automatic image enhancement. *Proceedings - International Conference on Image Processing, ICIP* **1**, 937–940 (2005).
33. Modregger, P., Lübbert, D., Schäfer, P. & Köhler, R. Spatial resolution in Bragg-magnified X-ray images as determined by Fourier analysis. *Physica Status Solidi (A) Applications and Materials Science* **204**, 2746–2752 (2007).
34. Nobert, W. *Extrapolation, Interpolation, and Smoothing of Stationary Time Series* (Technology Press of Massachusetts Institute of Technology, 1964).
35. Corde, S. *et al*. Mapping the x-ray emission region in a laser-plasma accelerator. *Physical Review Letters* **107**, 215004 (2011).
36. Lopes, N. C. *et al*. Measurement of the lwfa betatron source length by cross-correlations over images of granular random targets. *Science and Technology Facilities Council - Central Laser Facility, Annual Report* (2015–2016).
37. Corde, S. *et al*. Femtosecond x rays from laser-plasma accelerators. *Reviews of Modern Physics* **85**, 1 (2013).

38. Thomas, A. G. R. Scalings for radiation from plasma bubbles. *Physics of Plasmas* **17**, 056708 (2010).
39. Esarey, E., Shadwick, B., Catravas, P. & Leemans, W. Synchrotron radiation from electron beams in plasma-focusing channels. *Physical Review E* **65**, 056505 (2002).
40. Ma, Y. *et al.* Angular streaking of betatron x-rays in a transverse density gradient laser-wakefield accelerator. *Physics of Plasmas* **25**, 113105 (2018).
41. Shahani, A. J., Begum Gulsoy, E., Gibbs, J. W., Fife, J. L. & Voorhees, P. W. Integrated approach to the data processing of four-dimensional datasets from phase-contrast x-ray tomography. *Optics Express* **22**, 24606 (2014).
42. Shahani, A. J. *et al.* The dynamics of coarsening in highly anisotropic systems: Si particles in Al-Si liquids. *Acta Materialia* **97**, 325–337 (2015).
43. Shahani, A. J., Gulsoy, E. B., Poulsen, S. O., Xiao, X. & Voorhees, P. W. Twin-mediated crystal growth: an enigma resolved. *Scientific Reports* **6**, 28651 (2016).
44. Cloetens, P., Barrett, R., Baruchel, J., Guigay, J. P. & Schlenker, M. Phase objects in synchrotron radiation hard x-ray imaging. *J. Phys. D Appl. Phys.* **29**, 133–146 (1996).
45. Margoritondo, G. *Elements of Synchrotron Light: for Biology, Chemistry, and Medical Research* (Oxford University Press, 2002).
46. Paganin, D., Mayo, S. C., Gureyev, T. E., Miller, P. R. & Wilkins, S. W. Simultaneous phase and amplitude extraction from a single defocused image of a homogeneous object. *J. Microsc.* **206**, 33–40 (2002).
47. Wu, X., Lu, H. & Yan, A. Phase-contrast x-ray tomography: Contrast mechanism and roles of phase retrieval. *Eur. J. Radiol.* **68S**, S8–S12 (2008).
48. Kak, A. C. & Slaney, M. *Principles of Computerized Tomographic Imaging* (IEEE, 1988).
49. Rowenhorst, D. J. & Voorhees, P. W. Measurement of interfacial evolution in three dimensions. *Ann. Rev. Mater. Res.* **42**, 105–124 (2012).
50. Sun, Y., Cecen, A., Gibbs, J. W., Kalidindi, S. R. & Voorhees, P. W. Analytics on large microstructure datasets using two-point spatial correlations: Coarsening of dendritic structures. *Acta Materialia* **132**, 374–388 (2017).
51. Irvine, S. C., M. Paganin, D., Dubsky, S., Lewis, R. A. & Fouras, A. Phase retrieval for improved three-dimensional velocimetry of dynamic x-ray blood speckle. *Appl. Phys. Lett.* **93**, 91–94 (2008).
52. Paganin, D., Gureyev, T. E., Pavlov, K. M., Lewis, R. A. & Kitchen, M. Phase retrieval using coherent imaging systems with linear transfer functions. *Opt. Commun.* **234**, 87–105 (2004).
53. Trivedi, R. & Kurz, W. Microstructure selection in eutectic alloy systems. *Solidification Processing of Eutectic Alloys* 3–34 (1988).
54. Jones, H. & Kurz, W. Relation of interphase spacing and growth temperature to growth velocity in fe-c and fe-fe3c eutectic alloys. *Zeitschrift fur Metallkunde* **72**, 792–797 (1981).
55. Wagner, R. S. On growth of germanium dendrites. *Acta Metallurgica* **8** (1960).
56. Hamilton, D. R. & Seidensticker, R. G. Growth Mechanisms of Germanium Dendrites: Kinetics and the Nonisothermal Interface. *Journal of Applied Physics* **34**, 1450–1460 (1963).
57. Hogan, L. & Shamsuzzoha, M. Crystallography of the flake-fibre transition in the al-si eutectic. *Materials Forum* **10**, 270–277 (1987).
58. Frazier, W. E. Metal additive manufacturing: A review. *Journal of Materials Engineering and Performance* **23**, 1917–1928 (2014).
59. Polozov, I., Sufiiarov, V., Borisov, E., Popovich, A. & Masaylo, D. Producing hip implants of titanium alloys by additive manufacturing. *International Journal of Bioprinting* **2**, 78–84 (2016).
60. Tofail, S. A. *et al.* Additive manufacturing: scientific and technological challenges, market uptake and opportunities. *Materials Today* **21**, 22–37 (2018).
61. *US National Institute of Science and Technology Measurement Science Roadmap for Metal-Based Additive Manufacturing* (Energetics Incorporated, Columbia, Maryland, 2013).
62. Moniri, S. & Shahani, A. J. Chemical modification of degenerate eutectics: A review of recent advances and current issues. *Journal of Materials Research* 1–15 (2018).
63. Kieffer, J.-C., Fourmaux, S. & Krol, A. The ultrafast high-peak power lasers in future biomedical and medical x-ray imaging. In *19th International Conference and School on Quantum Electronics: Laser Physics and Applications*, vol. 10226, 1022612 (International Society for Optics and Photonics, 2017).
64. McGuffey, C. *et al.* On the properties of synchrotron-like X-ray emission from laser wakefield accelerated electron beams. *Physics of Plasmas* **25** (2018).
65. Hooker, S. *et al.* Multi-pulse laser wakefield acceleration: a new route to efficient, high-repetition-rate plasma accelerators and high flux radiation sources. *Journal of Physics B: Atomic, Molecular and Optical Physics* **47**, 234003 (2014).
66. Cowley, J. *et al.* Excitation and control of plasma wakefields by multiple laser pulses. *Physical Review Letters* **119**, 044802 (2017).
67. Gustas, D. *et al.* High-charge relativistic electron bunches from a khz laser-plasma accelerator. *Physical Review Accelerators and Beams* **21**, 013401 (2018).
68. Matsuoka, T. *et al.* Stimulated raman side scattering in laser wakefield acceleration. *Physical Review Letters* **105**, 034801 (2010).
69. Zhao, T. *et al.* High-flux femtosecond x-ray emission from controlled generation of annular electron beams in a laser wakefield accelerator. *Physical Review Letters* **117**, 094801 (2016).
70. Pollock, B. *et al.* Formation of ultrarelativistic electron rings from a laser-wakefield accelerator. *Physical Review Letters* **115**, 055004 (2015).
71. Wood, J. *Betatron Radiation from Laser Wakefield Accelerators and its Applications*. Ph.D. thesis (Imperial College London, 2016).
72. Cole, J. *Diagnosis and Application of Laser Wakefield Accelerators*. Ph.D. thesis (Imperial College London, 2016).
73. Fisher, D. J. & Kurz, W. A theory of branching limited growth of irregular eutectics. *Acta Metallurgica* **28**, 777–794 (1980).

Acknowledgements

We acknowledge support of the UK STFC core grants ST/P002056/1 (Cockcroft Institute), ST/P000835/1 (John Adams Institute), and the United States Department of Energy Grant No. DE-NA0002372. This work was partially supported by EuPRAXIA (Grant No. 653782), EC's LASERLAB-EUROPE (Grant No. 654148), UK EPSRC Grant No. EP/J018171/1, EP/J500094/1 and EP/N028694/1), EuCARD-2 (Grant No. 312453), the Extreme Light Infrastructure (ELI) European Project, National Science and Engineering Research Council of Canada, and by FCT - Fundação para a Ciência e a Tecnologia, Ministério da Ciência e Ensino Superior, Portugal under the contract POCI/FIS/59574/2004 and by the auspices of the US Department of Energy by Lawrence Livermore National Laboratory under the contract DE-AC52- 07NA27344, as well as Lawrence Livermore National Security, LLC, and DOE Early Career Research Prog. SCW1575/1. LLNL- JRNL-742178. We acknowledge the Paul Scherrer Institut, Villigen, Switzerland for provision of synchrotron radiation beamtime at the TOMCAT beamline X02DA of the SLS and would like to thank Julie Fife for assistance. The authors also thank the staff at the Central Laser Facility, Rutherford Appleton Laboratory for their assistance.

Author Contributions

The experiment was conceived by A.E.H., A.G.R.T., A.J.S., F.A., S.P.D.M. and C.M.S. and was conducted by A.E.H., M.J.V.S., B.K. and Y.M., with assistance from S.J.D.D., N.B., S.C., J.M.C., E.G., I.G.G., N.L., N.C.L., C.L., M.S., M.S., R.S., D.R.S. and G.V. The data were analyzed by A.E.H., N.S., Y.M. and M.J.V.S., with assistance from J.C.W. and O.F. A.H., K.F., D.A.J., K.K., O.L., Z.N., P.P.R. and L.W. contributed to planning and interpretation. The manuscript was written by A.E.H., N.S., Y.M., A.J.S., C.M.S. and A.G.R.T. All authors reviewed the manuscript.

Additional Information

Competing Interests: The authors declare no competing interests.

Publisher's note: Springer Nature remains neutral with regard to jurisdictional claims in published maps and institutional affiliations.

Paper X

Highly efficient angularly resolving X-ray spectrometer optimized for absorption measurements with collimated sources

M. Šmíd, I. Gallardo González, H. Ekerfelt, J. Björklund Svensson, M. Hansson, J. C. Wood, A. Persson, S. P. D. Mangles, O. Lundh and K. Falk.

Rev. Sci. Instrum. **88**, 063102 (2017).

REVIEW OF SCIENTIFIC INSTRUMENTS **88**, 063102 (2017)

Highly efficient angularly resolving x-ray spectrometer optimized for absorption measurements with collimated sources

M. Šmíd,[1,a)] I. Gallardo González,[2] H. Ekerfelt,[2] J. Björklund Svensson,[2] M. Hansson,[2] J. C. Wood,[3] A. Persson,[2] S. P. D. Mangles,[3] O. Lundh,[2] and K. Falk[1]
[1]*Institute of Physics of the ASCR, ELI-Beamlines, 18221 Prague, Czech Republic*
[2]*Department of Physics, Lund University, P.O. Box 118, S-22100 Lund, Sweden*
[3]*John Adams Institute for Accelerator Science, Imperial College London, SW7 2AZ London, United Kingdom*

(Received 12 April 2017; accepted 3 June 2017; published online 19 June 2017)

Highly collimated betatron radiation from a laser wakefield accelerator is a promising tool for spectroscopic measurements. Therefore, there is a requirement to create spectrometers suited to the unique properties of such a source. We demonstrate a spectrometer which achieves an energy resolution of <5 eV at 9 keV ($E/\Delta E > 1800$) and is angularly resolving the x-ray emission allowing the reference and spectrum to be recorded at the same time. The single photon analysis is used to significantly reduce the background noise. Theoretical performance of various configurations of the spectrometer is calculated by a ray-tracing algorithm. The properties and performance of the spectrometer including the angular and spectral resolution are demonstrated experimentally on absorption above the K-edge of a Cu foil backlit by a laser-produced betatron radiation x-ray beam. *Published by AIP Publishing.* [http://dx.doi.org/10.1063/1.4986464]

I. INTRODUCTION

Betatron radiation generated by a Laser Wake Field Accelerator (LWFA)[1,2] is an x-ray source producing broadband radiation with synchrotron-like spectrum coming in ultrashort (<30 fs duration) and highly collimated beams (≈10–20 mrad). Its unique qualities make it an ideal probe for active time resolved diagnostics of ultrafast processes in mid-Z elements.[3] It could be used for x-ray absorption spectroscopy, most likely for observation of absorption lines to infer the ionization degree and temperature, or for the x-ray absorption near-edge spectroscopy (XANES) measurement to investigate the electronic density of states and therefore ionic correlation and structure of the matter.[4] However, the generally low flux of the beam produced using lasers with moderate power makes it very challenging for detection. Thus a highly efficient spectrometer is necessary for such applications.

XANES is a diagnostic method investigating the x-ray absorption just above the K-edge, i.e., capturing of x-rays in the process of photo-ionization of the 1*s* electrons. These electrons are ejected into the free (continuum) state with low residual energy, and they undergo scattering by surrounding ions. Therefore, the absorption cross section reflects the ionic structure of the matter.[4] Time resolved studies of K-edge in laser shocked Al with a 10 ps long backlighter have been used to determine the Warm Dense Matter (WDM) temperature.[5] The electronic structure during the creation of warm dense molybdenum was studied via the XANES spectroscopy and compared to theoretical calculations.[6] XANES of Fe can be used to investigate hydrodynamic conditions during shock compression.[7] The first use of a laser-driven betatron radiation beam as a backlighter for absorption studies did not provide sufficient number of detected photons.[8] This was caused mainly by a significant loss of photons during their refocusing and lower efficiency of the spectrometer compared to this work.

In this article, we present a design for a crystal spectrometer optimized for highly efficient detection of this kind of radiation. This spectrometer employs a mosaic Highly Oriented Pyrolitic Graphite (HOPG) crystal which guarantees extremely high reflectivity compared to more often used monocrystals. Though these crystals usually produce lower resolution spectrum, we have achieved a sufficient resolution for most diagnostic purposes mainly due to longer crystal to detector distance and by minimizing geometrical effects. A defocused regime of the von Hamos setup is proposed that provides angular resolution to resolve a probe and a reference beam spectrum at the same time.

A spectrometer design for LWFA betatron radiation has two significant requirements: high efficiency and suitability for highly collimated beams. Mosaic crystals are often used for high collection efficiency setups; however, they are usually placed close to the source to cover large solid angles. This close proximity to source negatively affects the spectral resolution and signal to background noise ratio. The collimation of the betatron beam allows the relatively small crystal to be placed further away from the source while maintaining overall collection efficiency and low geometric aberrations, common in larger focusing crystals.

The mosaic crystals are composed of a set of small crystallites whose surface is slightly inclined from the crystal surface. The crystals are characterized by their mosaic spread, which is the FWHM (full width at half maximum) of the angular distribution of the crystallites. The rocking curve and topography of large (5×10 cm) thin mosaic crystals in a similar configuration have previously been studied in detail, and these crystals were used for x-ray Thomson scattering measurements.[9–11]

a)michal.smid@eli-beams.eu

This kind of measurement is characterized by the need of high energy resolution and by the use of low intensity divergent sources. The spectral resolution was limited by focal aberrations due to the large collection angles. The HOPG crystal based spectrometers have also been used to obtain the angular resolution with divergent sources.[12]

The spectral resolution reported in previous works with this type of crystal is usually not so great.[10,13] Resolution of 8 eV FWHM was reported on similar crystal at 7.5 keV.[14] By increasing the crystal to detector distance[13] and exploiting the low Bragg angle in this configuration, it was possible to significantly improve the spectral resolution compared to previous work.

In the current article, the performance of the spectrometer is predicted for various configurations by the ray-tracing simulations. The most suitable configuration was experimentally demonstrated and evaluated by measuring absorption spectra using a betatron radiation source. The range of the measured spectra extends up till ≈150 eV above the edge; therefore, it contains both the XANES and EXAFS regions.[4] The experimental measurement of the spectral Point Spread Function (PSF) is shown. The spectral resolution and penetration depth of the radiation into the crystal is inferred from this measurement.

II. SPECTROMETER DESIGN

This section describes the principles and parameters of the spectrometer. It shows its basic properties like angular resolution and response function, and it presents the ray-tracing simulations and discusses the theoretical performance of the spectrometer.

A. Crystal

The crystal used was commercially available from the Optigraph company.[15] The mosaicity grade was ZYB with mosaic spread $m = 0.8°$. The size was 20 × 20 mm and its surface was cylindrically bent. The radius of the curvature was obtained by measuring the position of the focus of a divergent laser radiation reflected by the crystal as $r = 108 \pm 5$ mm. The uncertainty is so high because the focus is several millimeters large due to the irregularities of the crystal surface, which are common in HOPG crystals. The nominal radius given by the manufacturer is 115 mm.

B. Geometry

The presented spectrometer is based on the well known von Hamos geometry,[16] as illustrated in Fig. 1. The cylindrically curved crystal defines the axis of the cylinder. If the focused setup is used, both source and detector are located on this axis in opposite directions from the crystal. The radiation coming from the source is focused to the detector in one direction, forming a line with dispersion along its length. The dispersion is governed by various Bragg angles of reflection of different x-ray energies. However, due to the use of mosaic crystal, several significant differences to the scheme arise.

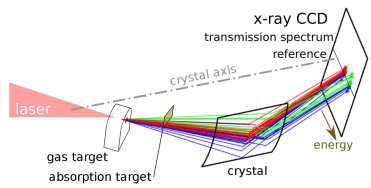

FIG. 1. Schematic of the spectrometer setup. The red and green lines denote x-rays going through the absorption target with two different energies. Both energies of x-rays propagating next to the target are marked in blue color and constitute the reference beam.

In a von Hamos scheme with a monocrystal, there is no focusing of the radiation along the dispersion direction, while in the perpendicular direction, both source and detector have to be placed on the center of the crystal curvature to obtain spatial focusing. When the mosaic crystal is used, the effect of *mosaic focusing*[13] focuses the radiation in the spectral direction like in the Rowland circle scheme. This means that the crystal works in a similar way as if it was toroidally bent with a large radius of curvature in the dispersion plane. On the other hand, the mosaicity includes randomness in the reflection angle. Therefore, the focusing in the spatial direction is not perfect.

We can define the ratio r_m for mosaic crystal spectrometers, which shows the relative importance of the mosaicity effects,

$$r_m = \frac{m}{\Delta\theta} \approx \frac{ml}{l_c \sin(\theta_0)}. \quad (1)$$

In this formula, m is the mosaic spread of the crystal, $\Delta\theta$ is the maximal difference between the angle of incidence of incoming radiation on various places on the crystal, l is the source to crystal distance, θ_0 is the central angle of incidence, and l_c is the crystal length.

If this ratio is high enough ($r_m \gg 1$), the mosaicity effects dominate over the variation of the angle of incidence over the crystal surface. This has two important consequences. First, the whole surface of the crystal reflects basically the same energies of radiation. This means that a ray with given energy can be reflected at any position within the crystal surface. However, the mosaic focusing guarantees that the photon is reflected to an angle based on its energy, therefore, impinging the detector at position given by the dispersion relation. Second, the spectral range is governed by the mosaicity, not by the variation of the incidence angle on the crystal (size of the crystal).

It is important to note that $\Delta\theta$ is the minimum of beam divergence and the crystal solid angle. Therefore, the ratio can never be small enough and the spectral range is usually governed by the mosaicity for highly collimated sources like the LWFA betatron beam. In the current setup, $m = 0.8°$, $l = 700$ mm, $l_c = 20$ mm, and $\theta_0 = 11.88°$; therefore, $\Delta\theta \approx 0.34°$ and the ratio was $r_m = 2.4$.

C. Angular resolution

If both the source and the detector would be located on the axis of the cylindrical crystal, any radiation coming from a

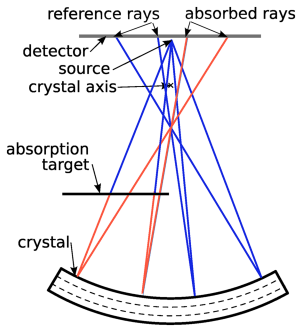

FIG. 2. Demonstration of the angular resolution. All rays (initially in blue color) are coming from a point source, half of them propagates through the absorption target (they become drawn with red color). Those rays hit the right side of the detector.

point source could be reflected to a thin spectrum on the detector. Any radiation emerging from a source positioned slightly off the axis would be reflected to a shifted position, giving rise to the typical *spatial* resolution. Since for the betatron backlit measurements we are interested in resolving different rays going from the same point-like source, this type of resolution is not useful. On the contrary, *angular* resolution is needed because it is resolving the x-rays passing through the sample from the reference part of the beam, see Fig. 2. The angular resolution with this type of spectrometer can be achieved when both the source and detector are located off the crystal axis, as illustrated in Figs. 1 and 2. The image of a point source is defocused and each position on the detector corresponds to a different emission angle from the source.

Mosaicity has a negative effect on this resolution. In the focused setup with a perfect monocrystal the width of the signal would correspond to the source size. The random orientation of the crystallites blurs this signal and increases its size to several millimeters, see the horizontal spread (green) in Fig. 3. This effect significantly degrades the angular resolution, but it is beneficial since it improves the dynamic range for single photon counting techniques as is discussed in greater detail in Sec. III A.

D. Ray-tracing

A new Monte Carlo ray-tracing code with the mosaicity effects included has been developed to model the properties of the spectrometer. The code is similar to the one developed by Zastrau *et al.*,[10] though the handling of radiation penetration through the crystal is different, as described below. This code generates a set of x-rays with random initial directions, lets them interact with the crystal and tracks their intersection with the defined detector plane. The interaction with the crystal is defined by two important functions defining the properties of the crystal: *penetration depth distribution* of the photons and the *mosaic spread function*, i.e., the angular distribution of the crystallites. The code selects the depth where each ray is reflected based on the

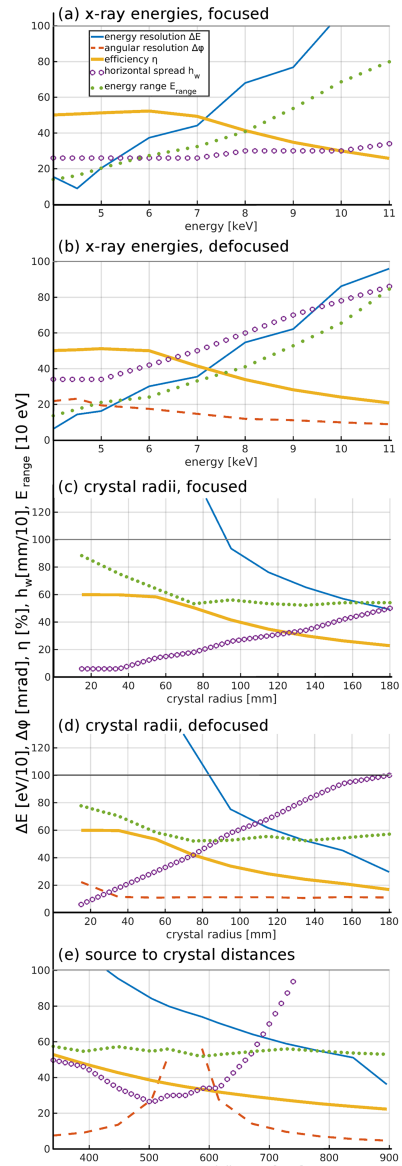

FIG. 3. Ray-tracing predicted performance of the spectrometer for various x-ray energies [(a) and (b)], crystal radii [(c) and (d)], and source–crystal distances (e). Calculated either for the focused setup [(a) and (c)] or defocused by 25%.

penetration depth distribution. This behavior simulates that the photon has to travel some unknown distance through the crystal until it finds the crystallite with appropriate orientation to be reflected. This distribution follows the exponential decay $e^{-\mu x}$ to mimic the absorption of x-rays in the matter. The

absorption length $1/\mu$ is generally not known. It is smaller compared to absorption in common graphite forms due to the structure of the crystal,[13] and it has to be inferred from experiments.

In the second step, the code randomly selects the orientation of the crystallite following the *mosaic spread function* and in a way that it fulfills the Bragg condition, which defines the angle between the crystallite and the ray. Finally, the angle of the reflected ray is calculated, and the intersection with detector is found. From a typical set of usually 10^5 photons, the synthetic detected image is formed and analyzed to provide the spectrometer characteristics described in Sec. II E.

E. Theoretical performance

The main aim of the ray-tracing simulations is to predict the performance of the spectrometer and thus to help with finding an optimal setup for given experimental requirements. The feasibility of the spectrometer for various x-ray energies was studied. Since the setup with Cu at 9 keV was found as suitable, the performance of crystal with various radii was investigated on this energy. As the energy and crystal radius was chosen, the effect of the distance l is studied. There are five performance parameters tracked by the ray-tracing simulations:

- *Spectral resolution [eV]*: the FWHM of the spectral point spread function (the simulation uses monochromatic signal).
- *Energy range [eV]*: the interval between the most and less energetic rays reflected by the crystal. Note that the efficiency is significantly dropping close to the edges of the range, thus the usable range is approximately half of this value.
- *Angular resolution [mrad]*: the horizontal FWHM of a perfectly collimated beam.
- *Horizontal spread [mm]*: the FWHM of the signal trace of a divergent beam in the direction of the angular resolution (perpendicular to the spectral one).
- *Efficiency [%]*: ratio of rays reflected by the crystal compared to all rays in a monoenergetic beam collimated to 20 mrad.

Figure 3(a) shows the variation of these parameters when the spectrometer is setup for different x-ray energies. The crystal dimensions are 2×2 cm, thickness 2 mm, and radius of curvature is set to $r = 115$ mm in the simulations. In general, HOPG crystals are suitable for range 2–11 keV; however, the setups with energies below 4 keV are considered unfeasible due to the increasing Bragg angle. The energy range is significantly dropping with decreasing energy, being only 180 eV at 4 keV. From Bragg law, it can be derived that the variation of energy for fixed variation of Bragg angle is close to $E_{\text{range}} \propto E^2$. The efficiency of the spectrometer is slightly decreasing with energy because the crystal is located further from the source making the effective solid angle smaller. The energy resolution is getting worse with increasing energy. The energy smearing by the effect of penetration depth is the dominant one. This effect gets stronger with increasing x-ray energy due to higher penetration depth; therefore, the resolution gets worse with energy [Figs. 3(a) and 3(b)]. On the other hand, the influence of this effect decreases with increasing crystal to detector distance; therefore, the spectral resolution improves with distance [Figs. 3(c)–3(e)].

The simulations in Figs. 3(a) and 3(c) were calculated in the focused geometry; therefore, the angular resolution is not present. Figures 3(b) and 3(d) show the configurations in the defocused regime. This was achieved by increasing both the source to crystal and crystal to detector distance by 25%. The angular resolution of approximately 10–30 mrad is obtained, the horizontal spread of the signal is more than doubled compared to its focused value, and the spectral resolution get slightly better due to the increased distances.

Figures 3(c) and 3(d) show setups for $E = 9$ keV and variable crystal radii for the focused and defocused regimes, respectively. The source to crystal distance is increasing linearly with the crystal radius ($L = r/\sin(\theta)$), which improves the energy resolution ($\Delta E \propto 1/L \propto 1/r$), increases the horizontal spread ($h_w = 2\sin(m)r$), and decreases the efficiency.

The performance of the setup for 9 keV radiation, $r = 115$ mm, and various source to crystal distances is shown in Fig. 3(e). The geometry becomes focused when both source and detector are located on the axis of the crystal cylinder, which happens at $l = 560$ mm. The regime defocused by 25% in distance has $l = 700$ mm. The angular resolution is improving with increasing distance from the focus. There is no angular resolution close the focused position. The focus is clearly seen as the minimum of the horizontal spread. The value of this minimum is given by the mosaicity of the crystal. The fact that the horizontal spread significantly increases for large distances to more than 10 mm is usually considered to be undesirable. However, this can reduce the flux on the detector to such values that the single photon counting method can be used, see Sec. III A. Similarly as in Figs. 3(a)–3(d), the efficiency is decreasing with distance due to smaller observation angle while the resolution improves. These better spectral and angular resolutions make the long distance setups more favorable, which is also beneficial in the experiment since longer distance significantly lowers background on the detector caused by the interaction of the accelerated electrons with surrounding material. The upper constraint for the distance is then given by the size of the detector which was 27 mm in our case. However, the limited size of the experimental chambers makes these setups very challenging and may limit their use.

F. Response function measurement on Cu Kα

The response function of the spectrometer was tested on a Cu Kα source. The x-ray source was a microfocus tube producing the Cu Kα doublet at $E = 8027$ and 8047 eV. It was running at power 4 W and produced a source size of 20 μm. The Kα_1 is narrow enough to be used as a quasimonochromatic source to evaluate the spectral resolution.

Figure 4 shows the experimentally measured Kα profile (red) alongside results of the ray-tracing simulations. The blue

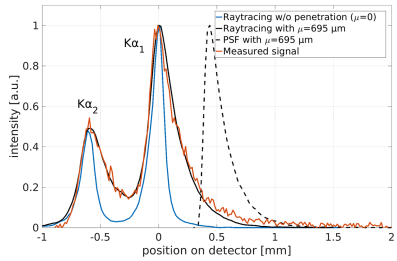

FIG. 4. Measured spectrum of Cu Kα compared with results of ray-tracing. The dashed line shows the calculated PSF of the spectrometer (drawn with horizontal offset).

line denotes a result when the penetration depth is neglected, i.e., all rays are expected to reflect from the crystal surface. The solid black line corresponds to a situation when the penetration depth $1/\mu$ was set to 695 μm to make the best fit with the experimental data. The dashed line presents the point spread function (PSF) of the spectrometer, i.e., the image of a monochromatic source, when this value is used in the ray-tracing. The asymmetric shape of this PSF reflects the penetration depth broadening.[17] The peak of the curve consists of the rays reflected from the surface of the crystal. The deeper the rays are reflected, the more they are shifted to the higher energy part of the PSF due to their extended trajectory in the crystal. This explains the sharpness of the left boundary and the exponential decay towards the right. The FWHM of this curve is 5.9 eV.

This penetration depth $1/\mu = 695$ μm is a fixed parameter of the crystal and photon energy and can be used for the ray-tracing simulations. Knowledge of the PSF is crucial for evaluation of the data. The predicted spectra should be convolved with this PSF prior to comparison with the measured data. Since this PSF is strongly asymmetrical the convolution with a Gaussian or Lorentzian function usually used for this purpose would not lead to a satisfactory agreement.

G. Efficiency

The efficiency calculated by the ray-tracing code is defined as a ratio of photons hitting the detector to the total number of photons at the central energy within the 20 mrad divergent cone. This efficiency is determined to be 30% for the setup used in the experiment described further below (photon energy 9 keV, crystal radius of curvature 115 mm, and source to crystal length 700 mm). The code expects that all photons which hit the crystal with suitable angle are reflected from it; therefore, this number has to be multiplied by the crystal peak reflectivity which is 52%.[18] The quantum efficiency of the CCD used in current experiment was 14% and the total transmission of used filters was 75%. The total efficiency is obtained by multiplying all these coefficients as 1.6%. This number relates the number of detected photons with certain energy to all photons with given energy produced by the x-ray source, assuming it has 20 mrad divergence.

III. EXPERIMENTAL RESULTS

The spectrometer was tested at the Lund Laser Centre using a multi terawatt laser operating at a central wavelength of 800 nm. The laser system produces 37 fs long pulses of up to 800 mJ after compression. The shape of the focal spot was optimized using deformable mirror to a size of ≈ 14 μm FWHM. The experimental setup is illustrated in Fig. 5. The laser pulse was focused onto an entrance of a 6 mm long 99% He and 1% N_2 mixture gas cell with a 775 mm focal length off-axis parabola. The electron density in the gas cell is 1×10^{19} cm^{-3}. During the interaction the laser drove a nonlinear plasma wave. The electric fields inside this wave accelerated electrons to ≈ 200 MeV, and the oscillatory movement of these electrons produced the betatron radiation which was collimated to ≈ 20 mrad and had a source size ≈ 10 μm. The critical energy of the x-ray spectrum was estimated as 2 keV by analysis of the transmission through Ross filters.[19]

A permanent magnet was placed after the gas cell to deflect the electrons to protect the crystal as well as to be used as electron spectrometer. The HOPG crystal was placed further down the x-ray beam to reflect the x-rays onto a direct detection Princeton Instruments PI-MTE CCD with chip size 27×27 mm and pixel size 13.5 μm. The absorption target was placed 3 cm behind the gas cell (before the magnet) in order to minimize the probed region. The spectrometer was set up for the Bragg angle $\theta = 11.88 \pm 0.07°$ corresponding to the Cu K-edge at 8980 eV. The source to crystal distance was set to $l = 697 \pm 3$ mm which is about 125% of the distance for focused geometry. The crystal was located on a motorized rotational stage in order to achieve high precision alignment.

Sections III A–III C draw three important conclusions about the spectrometer: the possibility of noise removal via single photon counting, the usability of angular resolution, and the evaluation of spectral resolution.

A. Single photon counting analysis

The large horizontal spread of the signal on the detector and the relatively low photon flux allowed us to use the single photon counting regime.[20] The signal of typically 33 000 photons per shot on the CCD was stretched over ≈ 2 cm^2, which corresponds to $\approx$ million pixels. Therefore, there was about 1 photon per 30 pixels, which is low enough to resolve single events. Higher fluxes might cause too many event overlapping making the data analysis more complicated.

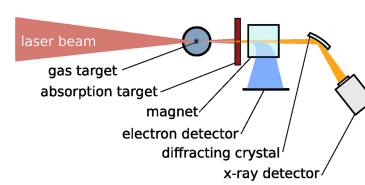

FIG. 5. A schematic of the experiment. The laser is focused to the gas target where the electron and x-ray beams are generated. The electron beam is deflected by the magnet to the scintillator. The x-ray beam propagates through the investigated absorption target is diffracted by the crystal and detected by the CCD.

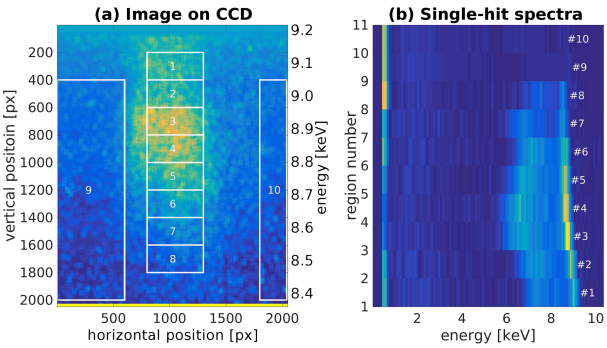

FIG. 6. Raw single shot data from the CCD with several selected regions (a) and x-ray spectra for those regions based on single photon counting (b). The shift of peak around 9 keV shows the dispersion of the spectrometer. Signal below 5 keV comes from experimental background.

There are ten regions marked in a single shot raw data in Fig. 6(a). Regions 1–8 correspond to part of the spectrum with various x-ray energies while regions 9 and 10 are areas without signal, having only background noise and scattered radiation. Figure 6(b) shows the broadband spectrum for each region obtained by the single photon counting analysis. All regions with data show a dominant peak around 9 keV. The dispersion of the spectrometer is clearly seen in the decrease of this peak energy with increasing index of the region. Regions 9 and 10 show almost no x-rays at this energy, while the low energy signal (below the threshold of 0.5 keV) and a broad peak around 2 keV are present almost homogeneously throughout the whole image. This signal is attributed to tertiary radiation produced by scattered electrons interacting with the vacuum chamber walls and surrounding material.

This analysis has three advantages:

1. The raw measurement of the energy of the signal can help during the alignment procedure.
2. The identification of the spectrum of background radiation can help to understand its origin and guide experimental shielding improvements.
3. Allows an effective background removal.

Figure 7 demonstrates the effect of this background removal technique. Figure 7(a) shows the raw data digitally accumulated over 315 shots. The inset presents a detail of a single shot image. The algorithm finds those events with energy around 9 keV (shown with red circles) and notes down their positions. The lists of all those positions for all shots in the series are merged, and a synthetic data image is constructed from them as a 2D histogram of the impact positions. This is shown in Fig. 7(b), where the same data are plotted for comparison in units of photons per pixel. The background which is quite strong especially in the bottom part of the figure has been effectively removed.

B. Angular resolution

The angular resolution of the spectrometer is demonstrated in Fig. 7. The energy dispersion direction is vertical on the image, and the instrument resolves angularly in the horizontal direction. Half of the beam corresponding to the right part of the figure was propagating through a 3 μm thick Cu foil, while the signal on the left was not obstructed and, therefore, can be used as a reference beam. The Cu K-edge can be clearly seen as a sharp horizontal line in the right part of the image. The uneven shape of the detected signal is caused by the irregularities of the crystal surface. The perfect straightness of the absorption edge however confirms that the effect of mosaicity focusing makes the spectral resolution insensitive to those irregularities.

For a quantitative analysis of the angular resolution, two series of shots were taken when either one or the other half of the beam was fully blocked. The horizontal lineouts of the signals integrated over the whole spectral range are presented in Fig. 8. The FWHM of the total signal is 9.2 mm and the difference between the peaks is 3.9 mm. The dashed line presents the

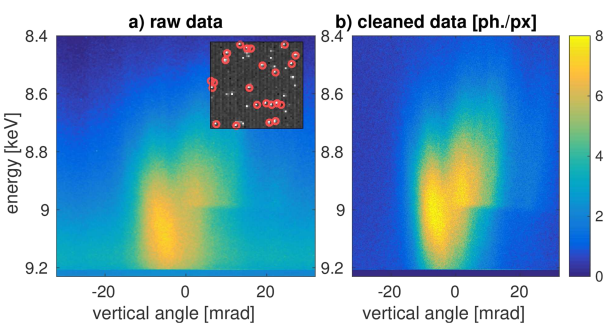

FIG. 7. Raw data from the CCD summed over 315 shots (a), the inset shows a single shot image where the 9 keV impacts are highlighted by red circles. (b) Image of the same data reconstructed by the single photon counting procedure.

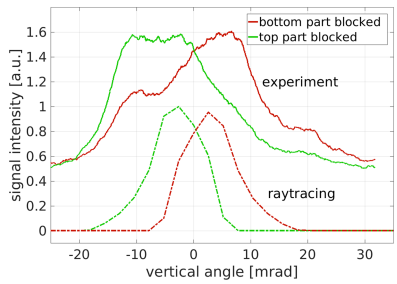

FIG. 8. Horizontal lineouts of the detected signal showing the angular resolution.

output of the ray-tracing algorithm which qualitatively agrees with the experiment. The overall width of the signal is however different. The same width of the signal was obtained when the crystal was illuminated by visible light, showing that this effect is caused by the imprecise surface of the crystal.

C. Spectral resolution

The experimentally observed absorption spectrum of a 3 μm thick Cu foil backlit with laser-produced betatron radiation can be seen in Fig. 9. 225 laser shots were accumulated, and each shot was saved in single CCD datafile and separately processed. The obtained positions of single photon events were gathered and used to plot the profile. The precise energy calibration is done by using the Cu K-edge.

The reference spectrum of polycrystalline Cu[21,22] is plotted as a thin gray line. It has been convolved with the ray-tracing modeled PSF (see Fig. 4) horizontally stretched to various FWHM. Results for 4, 5.5, and 7 eV FWHM are shown. The spectrum convolved with 5.5 eV wide PSF was selected as the best fit especially due to the agreement of the absorption feature at 9000 eV. Therefore, the FWHM resolution of the spectrometer is estimated to be ≈5.5 eV.

The PSF has strongly asymmetrical non-Gaussian shape with relatively sharp peak. The effective resolution can therefore be better for most applications, like observation of narrow features or estimation of spectral line positions. Another definition states that resolution is a wavelength of a sinusoidal signal which is transmitted through the system with 10% amplitude.[23]

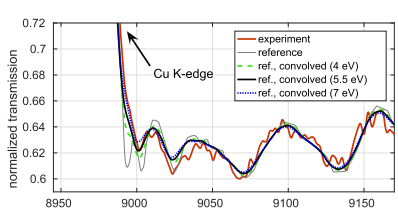

FIG. 9. Measured XANES spectra of a 3 μm thick Cu foil compared to a reference spectrum and to the convolution of this reference with the PSF with the given FWHM.

Numerical analysis of the PSF have shown that the spectral resolution is 4.8 eV when this definition is applied to the 5.5 eV FWHM resolution.

IV. CONCLUSIONS

We have designed and tested a novel HOPG spectrometer in von Hamos geometry optimized for effective use of low flux highly collimated beams. We have measured the XANES spectra of a 3 μm thick Cu foil backlit by a betatron radiation from a LWFA driven by 800 mJ laser, and the spectral peaks showing the crystallite structure of the material were resolved. Ray-tracing calculations show that 1.6% of photons generated by the source in 20 mrad cone are detected. This allowed 33 000 photons on the detector in the range 8.6–9.2 keV in each shot. Accumulation of ≈200 shots was sufficient to obtain enough photons to detect the narrow, low intensity XANES peaks. A separate experiment using a Cu Kα source confirmed the strongly asymmetrical PSF of the spectrometer as was predicted by the ray-tracing code. By comparing the measured spectra to reference data,[21,22] the spectral resolution we are able to infer was 4.8 eV at the wavelength of Cu K-edge (9 keV). We have demonstrated the angular resolution of the spectrometer which can be used to acquire both reference and data spectra at the same time, allowing accurate measurements of transmission. The developed ray-tracing code predicts the parameters of the spectrometer in various configurations and explains their behavior. This can help with adjustment of the setup for different experiments.

This spectrometer will be used in future x-ray absorption spectroscopy experiments on WDM targets backlit by LWFA produced betatron radiation. It is expected that a single shot spectrum could be obtained if the acceleration would be driven by ≈10 J laser system.

ACKNOWLEDGMENTS

The authors would like to thank Professor David Riley from the Queen's University Belfast for lending the crystal and the staff of Rigaku Innovative Technologies Europe s.r.o. for the calibration x-ray source. The research leading to these results has received funding from LASERLAB-EUROPE (Grant Agreement No. 654148, European Union's Horizon 2020 research and innovation programme), proposal No. LLC002259 and was supported by the project ELI (Extreme Light Infrastructure) –phase 2 (CZ.02.1.01/0.0/0.0/15_008/0000162) from European Regional Development Fund. This project has received funding from the European Research Council (ERC) under the European Union's Horizon 2020 research and innovation programme (Grant Agreement No. 682399). We acknowledge the support of the Swedish Research Council, the Crafoord Foundation and the Knut and Alice Wallenberg Foundation.

[1] A. Rousse, K. T. Phuoc, R. Shah, A. Pukhov, E. Lefebvre, V. Malka, S. Kiselev, F. Burgy, J.-P. Rousseau, D. Umstadter, and D. Hulin, Phys. Rev. Lett. **93**, 135005 (2004).
[2] S. Kneip, C. McGuffey, J. Martins, C. Bellei *et al.*, Nat. Phys. **6**, 980 (2010).
[3] F. Albert, A. G. R. Thomas, S. P. D. Mangles, S. Banerjee, S. Corde, A. Flacco, M. Litos, D. Neely, J. Vieira, Z. Najmudin, R. Bingham,

C. Joshi, and T. Katsouleas, Plasma Phys. Controlled Fusion **56**, 084015 (2014).
[4]J. J. Rehr and R. C. Albers, Rev. Mod. Phys. **72**, 621 (2000).
[5]F. Dorchies, F. Festa, V. Recoules, O. Peyrusse, A. Benuzzi-Mounaix, E. Brambrink, A. Levy, A. Ravasio, M. Koenig, T. Hall, and S. Mazevet, Phys. Rev. B **92**, 085117 (2015).
[6]F. Dorchies, V. Recoules, J. Bouchet, C. Fourment, P. M. Leguay, B. I. Cho, K. Engelhorn, M. Nakatsutsumi, C. Ozkan, T. Tschentscher, M. Harmand, S. Toleikis, M. Störmer, E. Galtier, H. J. Lee, B. Nagler, P. A. Heimann, and J. Gaudin, Phys. Rev. B **92**, 144201 (2015).
[7]M. Harmand, A. Ravasio, S. Mazevet, J. Bouchet, A. Denoeud, F. Dorchies, Y. Feng, C. Fourment, E. Galtier, J. Gaudin, F. Guyot, R. Kodama, M. Koenig, H. J. Lee, K. Miyanishi, G. Morard, R. Musella, B. Nagler, M. Nakatsutsumi, N. Ozaki, V. Recoules, S. Toleikis, T. Vinci, U. Zastrau, D. Zhu, and A. Benuzzi-Mounaix, Phys. Rev. B **92**, 024108 (2015).
[8]M. Z. Mo, Z. Chen, S. Fourmaux, A. Saraf, K. Otani, J. C. Kieffer, Y. Y. Tsui, A. Ng, and R. Fedosejevs, Rev. Sci. Instrum. **84**, 123106 (2013).
[9]S. H. Glenzer, G. Gregori, R. W. Lee, F. J. Rogers, S. W. Pollaine, and O. L. Landen, Phys. Rev. Lett. **90**, 175002 (2003).
[10]U. Zastrau, C. R. D. Brown, T. Döppner, S. H. Glenzer, G. Gregori, H. J. Lee, H. Marschner, S. Toleikis, O. Wehrhan, and E. Förster, J. Instrum. **7**, P09015 (2012).
[11]U. Zastrau, A. Woldegeorgis, E. Förster, R. Loetzsch, H. Marschner, and I. Uschmann, J. Instrum. **8**, P10006 (2013).
[12]E. García-Saiz, F. Y. Khattak, G. Gregori, S. Bandyopadhyay, R. J. Clarke, B. Fell, R. R. Freeman, J. Jeffries, D. Jung, M. M. Notley, R. L. Weber, L. van Woerkom, and D. Riley, Rev. Sci. Instrum. **78**, 095101 (2007).
[13]H. Legall, H. Stiel, M. Schnürer, M. Pagels, B. Kanngießer, M. Müller, B. Beckhoff, I. Grigorieva, A. Antonov, V. Arkadiev, and A. Bjeoumikhov, J. Appl. Crystallogr. **42**, 572 (2009).
[14]G. Ice and C. J. Sparks, Jr., Nucl. Instrum. Methods Phys. Res., Sect. A **291**, 110 (1990).
[15]See http://www.optigraph.eu/hopg.html for Optigraph GmbH: Conventional graphite monochromators, 2017.
[16]L. von Hamos, Ann. Phys. **409**, 716 (1933).
[17]A. Pak, G. Gregori, J. Knight, K. Campbell, D. Price, B. Hammel, O. L. Landen, and S. H. Glenzer, Rev. Sci. Instrum. **75**, 3747 (2004).
[18]A. K. Freund, A. Munkholm, and S. Brennan, Proc. SPIE **2856**, 68 (1996).
[19]F. G. Desforges, B. S. Paradkar, M. Hansson, J. Ju, L. Senje, T. L. Audet, A. Persson, S. Dobosz-Dufrénoy, O. Lundh, G. Maynard, P. Monot, J.-L. Vay, C.-G. Wahlstrom, and B. Cros, Phys. Plasmas **21**, 120703 (2014).
[20]A. Higginbotham, S. Patel, J. A. Hawreliak, O. Ciricosta, G. W. Collins, F. Coppari, J. H. Eggert, M. J. Suggit, H. Tang, and J. S. Wark, Rev. Sci. Instrum. **85**, 033906 (2014).
[21]See https://intranet.cells.es/Beamlines/CLAESS for CELLS: Alba beamline commissioning, 2016.
[22]See https://www.bnl.gov/ps/x18b/service.asp for Brookhaven national lab: Mail-in exafs service, accessed, 13 January 2017.
[23]S. W. Smith, *The Scientist and Engineer's Guide to Digital Signal Processing* (California Technical Publications, 1997), Chap. 25, ISBN: 0-9660176-3-3.